The Dissertation Committee for Ke-Yu Lai
Certifies that this is the approved version of the following dissertation:

Development of Electrode Materials with Matched Thermal Expansion for Solid Oxide Fuel Cells

APPROVED BY
SUPERVISING COMMITTEE:

Arumugam Manthiram, Supervisor

John B. Goodenough

Desiderio Kovar

Gyeong S. Hwang

Development of Electrode Materials with Matched Thermal Expansion for Solid Oxide Fuel Cells

by

Ke-Yu Lai

Dissertation

Presented to the Faculty of the Graduate School of

The University of Texas at Austin

in Partial Fulfillment

of the Requirements

for the Degree of

Doctor of Philosophy

The University of Texas at Austin

August 2018

Acknowledgements

I would like to express my true gratitude to my advisor, Dr. Arumugam Manthiram, for offering me an opportunity to pursue my Ph.D. degree with valuable supports. I sincerely appreciate my dissertation committee members, Dr. John B. Goodenough, Dr. Desiderio Kovar, and Dr. Gyeong Hwang, for their insightful comments and suggestions which have guided me to discover fundamental issues in my field and to design my experiments.

I would like to thank Dr. Daeil Yoon and Dr. Matthew West for teaching me several SOFC experimental techniques and training me various instrument. I would also like to thank my wonderful friends, Dr. Chih-Liang Wang, Dr. Sheng-Heng Chung, Dr. Veronica Augustyn, Robert Pipes, Kristofer B Ohlinger, Sanjay Nanda, Pauline Han, Chi-Hao Chang, Min-Je 'Daniel' Park, Martha Gross, Dr. Wang Hay Kan, Dr. Watchareeya Kaveevivichai, Dr. Shaofei Wang, Nora Colligan, and Andy Fang for their kindest assistance, interesting discussions, and sincere friendship. During my time in UT, they always offer me the most immediate care and help without any hesitance both on my personal and professional lives. My acknowledgements also go to Dr. James Knight, Dr. Zachary Moorhead-Rosenberg, Dr. Veronica Augustyn, and Robert Pipes again for working as lab managers with me, sharing the heavy duty of lab works, and solving many unexpected problems together. I gratefully acknowledge the financial support by the Welch Foundation to carry out my research work. I also appreciate the partial financial support by Taiwan government toward my living expenses during 2013 – 2015.

Lastly, I would like to thank my wife “Cassandra Chen”, parents, brothers, and parents-in-law for everything they have done for me with their warmest support and love. I am especially indebted to Cassandra for giving me endless joys every day and sharing my hard time with unconditional love. Thank you.

Abstract

Development of Electrode Materials with Matched Thermal Expansion for Solid Oxide Fuel Cells

Ke-Yu Lai, Ph.D.

The University of Texas at Austin, 2018

Supervisor: Arumugam Manthiram

Solid oxide fuel cells (SOFCs) are electrochemical energy conversion devices with a conversion efficiency of over 50 % from fuel to electricity. Their high operation temperature (600 – 1000 °C) enables SOFCs to directly utilize hydrocarbon fuels without an external fuel reforming system or precious-metal catalyst. However, several critical electrode challenges impede the mass commercialization, such as high thermal stress, electrode material decomposition, unwanted reactions between neighboring components, and impurity poisoning. A rapid SOFC failure during operation is mainly caused by the mismatch of thermal expansion coefficients (TECs) among device components. Unfortunately, few electrode materials with suitable TECs and adequate electrochemical activities have been reported. With the aim of achieving high phase stability and enhancing catalytic activity, new anode and cathode materials with compatible TECs are developed.

$YBaCo_4O_7$-based swedenborgite oxides with Y-site dopants (In^{3+} and Ca^{2+}) and Co-site dopants (Ga^{3+}, Al^{3+}, and Fe^{3+}) are investigated as cathode materials in intermediate-

temperature SOFCs (600 – 800 °C). The high-spin state of the Co cation in a tetrahedral coordination prevents spin transition at elevated temperatures and makes the TECs of $YBaCo_4O_7$-based materials much lower than those of Co-containing perovskite oxides. However, $YBaCo_4O_7$-based materials may decompose at > 600 °C. Hence, the cation doping effect on the long-term phase stability is examined with 50 compositions. The electrical conductivity, TECs, thermal behavior, catalytic activity toward the oxygen reduction reaction, and SOFC performance and stability are comprehensively evaluated.

A Co-doped chromite perovskite oxide with self-regenerating Co-Fe nanoparticles is utilized as a catalytically-active anode. The moderate TEC of the chromite perovskite oxide is slightly higher than the TECs of common electrolyte materials. Unlike the conventional Ni – electrolyte cermet anode, the oxide anode exhibits high redox phase stability without irreversible performance degradation during a reduction and oxidation (redox) cycle. The performance is significantly enhanced with exsolved Co-Fe nanocatalysts. The sulfur impurity tolerance and coking resistance are evaluated with an electrolyte-supported single cell by various fuels. Meanwhile, the self-regeneration behavior of exsolved nanoparticles on the oxide surface is described by carefully observing the surface evolution during a redox cycle at 700 and 800 °C.

Table of Contents

List of Tables

List of Figures

Chapter 1: Introduction

1.1 SOLID OXIDE FUEL CELLS

Solid oxide fuel cells (SOFCs) are high-temperature energy conversion devices which generate electricity directly through electrochemical reactions. Unlike conventional heat engines, the theoretical conversion efficiency of SOFCs is not limited by Carnot's cycle.[1,2] The conversion efficiency of SOFCs in practical applications is generally within the range of 45 – 55 %.[3] The overall system efficiency can achieve > 75 % by collecting waste heat with a combined heat and power (CHP) system.[4]

A high operation temperature within the range of 600 – 1000 °C facilitates an internal reforming process of hydrocarbon fuels without an external reforming system and noble metal catalysts.[1,5–7] Hence, a SOFC system minimizes the energy loss from a complex fuel pre-treatment and the high cost of electrode materials.[8] Based on its advantage of fuel flexibility, not only renewable energy resources, such as biogas, ethanol, and hydrogen, can be directly used in a SOFCs, but also conventional fossil fuels can be used. Overall, a SOFC system produces more electricity per unit fuel and reduces CO_2 emissions more per unit electricity than an internal combustion engine. The environmental impact of SOFCs is very low because NO_x and SO_x emissions and noise are eliminated to an insignificant level.[9] In addition, its compact size and modularity enable SOFCs to be sufficiently versatile to serve as a distributed power generator. Hence, the advantages of clean and efficient SOFC technology have attracted great interest from researchers and commercial sectors in the past few decades.

1.1.1 Basic principles of SOFCs

As an electrochemical device, SOFC consists of three major components, namely, an anode, electrolyte, and cathode, and all components are made of ceramic or cermet in order to withstand the high-temperature operation. The electron-conductive electrode materials in fuel cells work as catalysts in electrochemical reactions. Oxygen reduction reaction (ORR) and fuel oxidation reaction take place, respectively, on the cathode and anode, which are separated by an ion-conductive electrolyte. Figure 1.1 shows a schematic diagram of the SOFC operation principle. Firstly, fuel, as a source of energy, is oxidized on active sites of the anode surface with oxide ions, as written in eq. (1.1), and the generated electrons pass through an external circuit towards the cathode. Meanwhile, the ORR occurs on active sites of the cathode surface and generates oxide ions (O^{2-}) by combining the electron from the external circuit and oxygen in air, which is described by eq. (1.2). Then, the oxide ion in eq. (1.2) migrates through the electrolyte layer towards the anode to complete the overall reaction as shown in eq. (1.3). The reaction energy is released electrochemically in the form of electricity and heat.

Anode $H_2 + O^{2-} \rightarrow H_2O + 2e^-$ (1.1)

Cathode $O_2 + e^- \rightarrow 2O^{2-}$ (1.2)

Overall reaction $2H_2(g) + O_2(g) \rightarrow 2H_2O\ (g)$ (1.3)

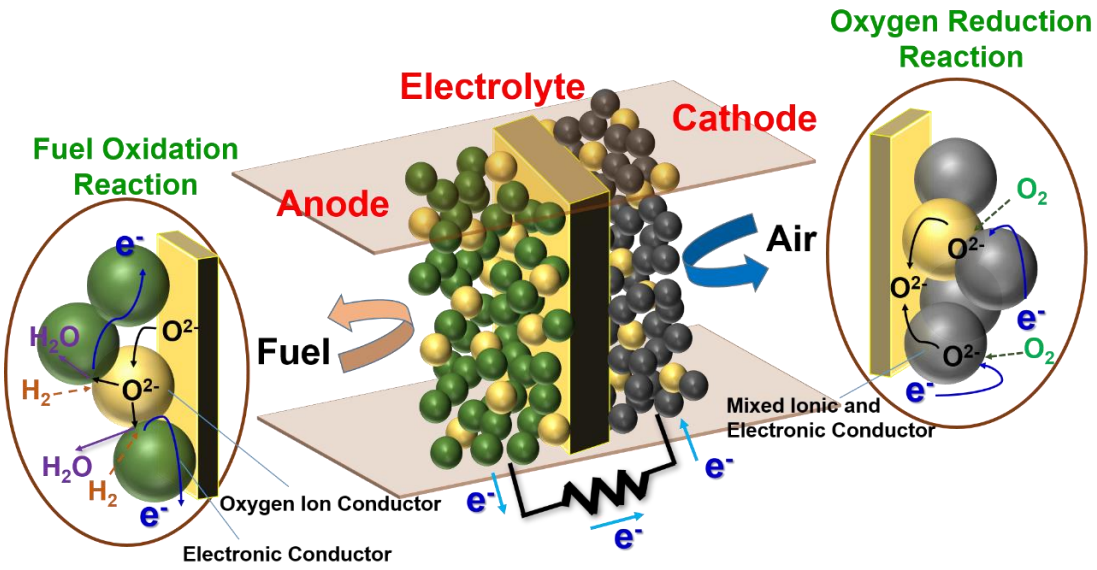

Figure 1.1 Schematic diagram of a SOFC and its operation principle.

When a hydrocarbon fuel (C_nH_{2n+2}) is used, an ideal electrochemical reaction on the anode side can be written as eq. (1.4). Here, methane is used as an example and the reaction is described as eq. (1.5).

Oxidation reaction of hydrocarbon fuel C_nH_{2n+2}

$$C_nH_{2n+2} + (3n+1)O^{2-} \rightarrow nCO_2 + (n-1)H_2O + (6n+2)e^- \quad (1.4)$$

Oxidation reaction of methane $$CH_4 + 4O^{2-} \rightarrow CO_2 + 2H_2O + 8e^- \quad (1.5)$$

However, the hydrocarbon fuel oxidation reaction on the anode side is extremely complex in practice. Mogensen and Kammer argued that it is very hard to achieve eq. (1.5) directly in one step and several steps have been proposed.[10] Many methane-related chemical and electrochemical reactions could occur on the anode side,[10–13] and some of the most important of these are listed below.

Partial oxidation reaction of methane $CH_4 + 3O^{2-} \rightarrow CO + 2H_2O + 6e^-$ (1.6)

Methane cracking reaction $CH_4 \leftrightarrow C + 2H_2$ (1.7)

Carbon oxidation reaction $C + 2O^{2-} \rightarrow CO_2 + 4e^-$ (1.8)

Carbon monoxide disproportionation reaction $2CO \leftrightarrow C + CO_2$ (1.9)

Dry reforming reaction of methane $CH_4 + CO_2 \leftrightarrow 2CO + 2H_2$ (1.10)

Steam reforming reaction of methane $CH_4 + H_2O \leftrightarrow CO + 3H_2$ (1.11)

Steam reforming reaction of carbon monoxide $CO + H_2O \leftrightarrow CO_2 + H_2$ (1.12)

In all of these reaction species, solid carbon should be avoided, because carbon deposition, which is also called coking, would inhibit fuel species transport to the active sites on the anode surface. The equilibrium among these reactions strongly depends on the operation temperature, anode composition, and reactant ratios. In addition, experimental evidence has showed that the carbon formation is mainly determined by kinetics.[1] Hence, the control of operational conditions and the selection of coking-resistant anode materials are both important to provide a highly stable performance with hydrocarbon fuels.

1.1.2 Thermodynamics and theoretical efficiency of SOFCs

Assuming that a system undergoes a reversible process under isothermal and isobaric conditions, the difference of Gibbs free energy (ΔG) between the initial state (reactants) and the final state (products) is equal to the work done by the system (-ΔW).[14]

$$\Delta G = -\Delta W \quad (1.13)$$

Here, this work described by the Nernst equation in eq. (1.14) is performed by electronic charge transport between two electrodes with a potential difference E.

$$\Delta G = -\Delta W_{ele} = -zFE \quad (1.14)$$

where z is the number of electrons participating in the reaction and F is Faraday's constant. When the chemical energy of the species in the reaction is considered, the Gibbs free energy (ΔG_T) and the corresponding reversible potential (E_T) at temperature T can be written, respectively, in eq. (1.15) and eq. (1.16).

$$aA + bB \leftrightarrow cC + dD$$
$$\Delta G_T = \Delta G_T^o + RT\, ln \frac{a_C^c\, a_D^d}{a_A^a\, a_B^b} \quad (1.15)$$

$$E_T = E_T^o - \frac{RT}{zF}\, ln \frac{a_C^c\, a_D^d}{a_A^a\, a_B^b} \quad (1.16)$$

ΔG_T^o and E_T^o are, respectively, the Gibbs free energy and reversible potential of a reaction when all reactant (A and B) and product (C and D) species are present an unit activity, and a is the activity of the species. Based on eq. (1.3), the reversible potential between the hydrogen fuel and oxygen oxidant is written in eq. (1.17).

$$E_T = E_T^o - \frac{RT}{2F}\, ln \frac{P_{H_2O}}{P_{H_2}\, P_{O_2}^{1/2}} \quad (1.17)$$

The theoretical fuel cell potential with hydrogen and oxygen at 800 °C is calculated here as an example. The standard Gibbs free energy of the reaction is taken from the appendix of reference 1. The reversible cell voltage in SOFCs with various fuels as a function of the operation temperature is shown in Figure 1.2.[1]

$$E_T^o = -\frac{\Delta G^o_{H_2(g)+0.5O_2(g)=H_2O(g)}}{zF}$$

$$E^o_{800\,℃} = -\frac{-188691\,J\,mol^{-1}}{2\times 96485\,C\,mol^{-1}} = 0.9778\,V$$

$$E_{800\,℃} = 0.9778 - \frac{(8.314)(1073.15)}{2(96400)}\,ln\frac{P_{H_2O}}{P_{H_2}\,P_{O_2}^{\frac{1}{2}}} = 0.9778 - 0.0463\,ln\frac{P_{H_2O}}{P_{H_2}\,P_{O_2}^{\frac{1}{2}}}$$

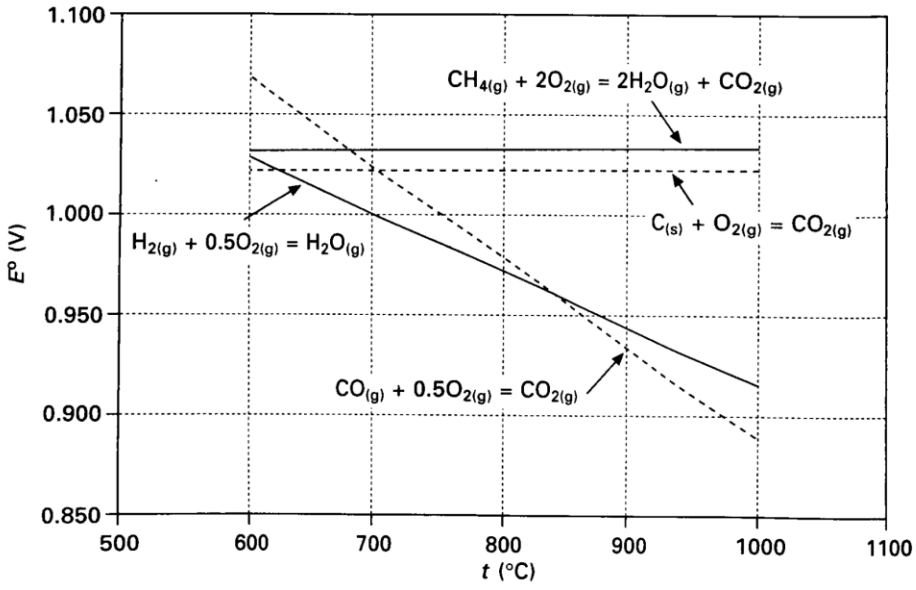

Figure 1.2 Reversible cell voltage in a SOFC with various fuels as a function of the operation temperature. Reprinted from reference 1 with permission from Elsevier.

The thermodynamic efficiency of a reversible reaction in a fuel cell at temperature T is calculated with enthalpy ΔH and entropy ΔS in eq. (1.18).

$$\varepsilon_{rev} = \frac{\Delta G_T}{\Delta H_T} = 1 - \frac{T \times \Delta S_T}{\Delta H_T} \quad (1.18)$$

Based on the thermodynamic data of selected chemical reactions in a SOFC, Figure 1.3 shows the thermodynamic efficiency with various fuels as a function of the operation temperature.[1] The high efficiency of the reactions with carbon or methane are a result of the relatively lower entropy term compared to the reaction enthalpy. The thermodynamic data can be found in the appendix of reference 1. However, it is worth noting that the practical efficiency is strongly affected by reaction kinetics. The overall efficiency of a fuel cell system should consider the fuel processing efficiency (if needed), practical fuel cell stack efficiency, and other energy loss due to the peripheral devices.

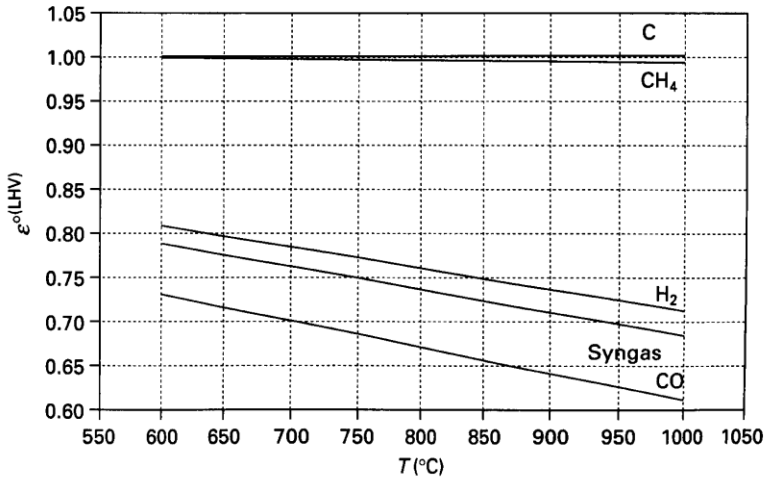

Figure 1.3 Thermodynamic efficiency of a reversible reaction with various fuels as a function of operation temperatures. Reprinted from reference 1 with permission from Elsevier.

1.1.3 Electrochemistry in SOFCs

The electrochemical property of SOFCs is evaluated by their current-voltage (I-V) relationship. An ideal fuel cell can convert the Gibbs free energy to electricity with a theoretical conversion efficiency, as described in section 1.1.2. The I-V curve of an ideal system is an almost flat curve, which means that the voltage does not change with a wide range of current as long as sufficient reactants are supplied.[15] However, ideal and non-polarized electrodes do not exist in a practical system. A series of steps is required to complete an electrochemical reaction, and irreversible voltage loss is caused by polarization during SOFC operation.

In fact, several physical, chemical, and electrochemical processes occur sequentially on the cathode:[16] (1) mass transport of oxygen molecules to the cathode surface region, (2) adsorption of an oxygen molecule on the cathode surface, (3) dissociation of an oxygen molecule on the cathode surface, (4) surface diffusion of an adsorbed oxygen species to the active site of ORR, (5) reduction of an adsorbed oxygen species with two electrons, and (6) incorporation of oxide ions into an ionic conductor and ion migration towards the electrolyte layer. Similar processes take place on the anode,[13] and hydrogen is taken as an example of fuel here: (1) mass transport of hydrogen molecules to the anode surface region, (2) adsorption of a hydrogen molecule on the anode surface, (3) dissociation of a hydrogen molecule on the anode surface, (4) surface diffusion of an adsorbed hydrogen species to the active site for hydrogen oxidation reaction, (5) hydrogen oxidation reaction, which combines two adsorbed hydrogen species and an oxide ion and generates two electrons, and (6) the desorption of water molecules from the active site and electron migration towards the external circuit.

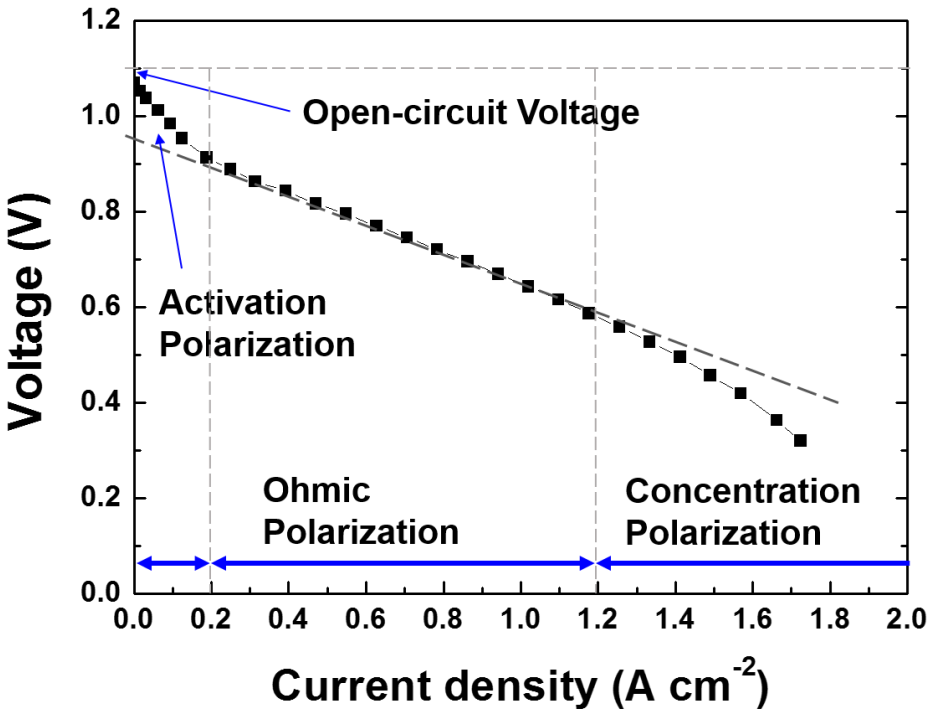

Figure 1.4 Typical I-V curve of a SOFC.

A typical I-V curve is shown in Figure 1.4. In the current case, the three operating ranges in the I-V curve are divided into (1) the activation polarization region ($i < 0.2$ A cm^{-2}), (2) ohmic polarization region (0.2 A cm^{-2} < i < 1.2 A cm^{-2}), and (3) concentration polarization region ($i > 1.2$ A cm^{-2}). The activation polarization is predominant on the low current region and is related to the kinetics of the electrochemical reactions on the electrode surface. The ORR has more sluggish kinetics compared to the fuel oxidation reaction in SOFCs, and it requires higher overpotential to drive the process effectively. Since the ORR is thermally activated, the activation polarization could be eliminated in a conventional high-temperature SOFCs (HT-SOFCs) operating at above 800 °C. However, activation polarization at a lower operation temperature causes more voltage loss. The relationship

between the electrode overpotential η^{act} of a charge transfer process and the current density i is generally described by the Bulter-Volmer equation as written in eq. (1.19).[1,15]

$$i = i_{ex}\left[\exp\left(\frac{(1-\beta)zF\eta^{act}}{RT}\right) - exp\left(-\frac{\beta zF\eta^{act}}{RT}\right)\right] \quad (1.19)$$

$$\alpha_a = (1-\beta)z \ and \ \alpha_c = \beta z$$

where i_{ex} is the exchange current density. α_a and α_b are, respectively, the transfer coefficient numbers for anodic and cathodic reactions. β is the symmetry factor ($0 \leq \beta \leq 1$), which indicates the fraction of the potential applied on the cathodic reaction, while z is the number of electrons transferred in the charge transfer reaction. In a high overpotential region (η^{act} > 100 mV), the Bulter-Volmer equation is simplified to eq. (1.20) and follows the Tafel relationship.[1,15]

$$\eta^{act} = \frac{RT}{\alpha zF} ln\left(\frac{i}{i_{ex}}\right) \quad (1.20)$$

Ohmic polarization in SOFCs is caused by the electronic resistance of two electrodes, the ionic resistance of the electrolyte, and the interface contact resistance between electrode and electrolyte layers. In addition, the resistance of the interconnect, current collector, metal wire, and interfaces between neighboring components is also parts of the total resistance in a stack. The component and contact resistances are strongly affected by materials, fabrication process, and device design. Unwanted side reactions on the interface should be avoided because electronic or ionic insulating phase formation increases ohmic polarization. Thus, the chemical compatibility between neighboring

components is one of the important factors in material selection. The voltage loss due to ohmic polarization is described as eq. (1.21).

$$\eta^{ohm} = iR_{tot} = i(R_{ionic} + R_{electronic} + R_{contact}) \quad (1.21)$$

An anode-supported single cell is currently the most popular device configuration because the ionic resistance is significantly reduced with a thin electrolyte layer (5 – 30 μm). The ohmic resistance of electrodes is relatively small due to the proper electrical conductivity.

The concentration polarization is the result of insufficient uncharged species reaching the active sites on the electrode surface. Fuel and oxidant should be continuously supplied, respectively, to the anode and cathode to generate electricity during SOFC operation. However, the consumption rate of the reactants rapidly increases in the region of high current density. Thus, the reactant concentration is gradually diluted by the fast generation of reaction products, such as water on the anode. The efficient mass transport of gas species in a solid porous electrode is crucial to maintain a stable performance with a high output of power. Since the convection is less effective inside the electrode layer due to a limited pressure difference, the ordinary molecular diffusion, Knudsen diffusion, and surface migration of gases play predominant roles in porous solid electrodes.[1] These mass transport mechanisms are affected by electrode geometry, such as porosity, tortuosity, pore size, and surface area.[17] Therefore, the electrode microstructure needs to be optimized to achieve effective mass transport and a high performance. In summary, the actual SOFC voltage can be written in eq. (1.22) by considering the accumulative contribution of the above polarization losses.

$$V_{actual} = E - \eta^{activation} - \eta^{ohmic} - \eta^{concentration} \quad (1.22)$$

1.2 MATERIALS OF CONVENTIONAL AND CONTEMPORARY SOFCS

The materials of functional components in SOFCs have to match many strict requirements to achieve a robust system with high performance and excellent stability for operating > 60,000 h, which is the minimum expected lifetime of a commercial SOFC device. The materials in a conventional HT-SOFC, which operates at > 800 °C, have been well-developed. However, low-cost metals cannot be used as interconnects in a stack because of their chemical incompatibility with other components and poor resistance to oxidation at such high temperatures. In addition, high degradation rate is generally observed due to the electrode microstructure coarsening and unwanted side reactions during long-term operation. Thus, the main goal of material research in the past decade has been to reduce the operation temperature to an intermediate range (IT) of 600 to 800 °C in order to extend the SOFC stack lifetime and reduce the material cost. Unfortunately, there are still many challenges at the lower operation temperature. The component requirement, common materials, and current challenges in IT-SOFCs are briefly reviewed and discussed below.[18]

1.2.1 Electrolyte

Excellent electrolyte material should include the following properties;

- High ionic conductivity; the transfer number of ionic conductivity should be equal or close to one
- Extremely low electronic conductivity

- High phase, chemical, thermal, and morphological stability in both highly reducing and oxidizing atmospheres
- Excellent chemical compatibility with anode and cathode materials
- Thermal-mechanical properties that match other components in a stack
- Proper sinterability to be fabricated as a highly dense membrane

The IT-SOFC performance is greatly influenced by the ohmic polarization of the electrolyte membrane. High ionic conductivity of the electrolyte is crucial to minimize the ohmic polarization, and the thickness of the electrolyte layer should be less than a few tens μm to reduce the ionic resistance. In addition, a fully dense electrolyte layer is necessary to prevent the crossover of reactants and oxidants. Some fluorite and perovskite oxides have been identified as oxide-ion conductors with adequate ionic conductivity at 600 – 1000 °C.[19] Figure 1.5 shows the ionic conductivity of the common oxide-ion conducting electrolyte materials.

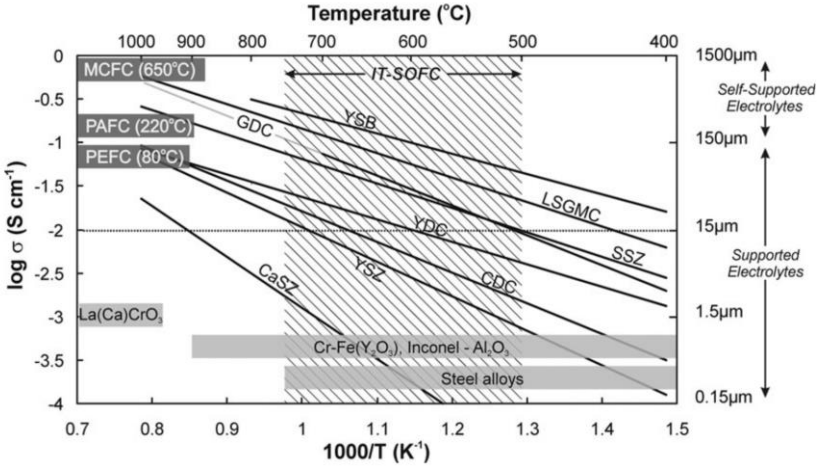

Figure 1.5 Oxide-ion conductivity of common electrolyte materials as a function of temperature. Reprinted from reference 20 with permission from Royal Society of Chemistry.

Yttria-stabilized zirconia (YSZ) is the state-of-the-art electrolyte material in conventional HT-SOFCs. Pure zirconia undergoes several phase transformations when the temperature increases, including monoclinic (≤ 1,170 °C), tetragonal (1,170 – 2,370 °C), and cubic fluorite (≥ 2,370 °C) structures. The acceptable oxide-ion conductivity is only provided by the cubic fluorite structure at above 800 °C. The cubic structure is stabilized at the SOFC operation temperature by doping an appropriate amount of aliovalent cations.[19] Since the oxidation state of dopants, such as Y^{3+} and Ca^{2+}, is lower than that of Zr^{4+}, oxygen vacancies are formed due to the charge imbalance, as written in eq. (1.23). The adequate amount of oxygen vacancies provides more channels for oxide ion migration and further enhances the ionic conductivity.

$$Y_2O_3 \xrightarrow{ZrO_2} 2Y'_{Zr} + 3O_O^{\times} + V_O^{\cdot\cdot} \quad (1.23)$$

The optimized ionic conductivity is achieved by doping 8 % of yttria, and the ionic transport number is > 0.99 at operational temperatures even in a reducing atmosphere. In addition, YSZ has excellent chemical stability and a good mechanical property. However, the thermally-activated ionic conductivity of YSZ becomes too low for IT-SOFCs at 600 – 800 °C. The ohmic polarization can be reduced by decreasing the thickness of the YSZ electrolyte layer to < 10 μm, but this makes the membrane fabrication process more complex.

Another promising electrolyte material is cerium oxide in the cubic fluorite structure. The oxygen vacancies in cerium oxide are formed by substituting trivalent rare earth cations or divalent alkaline earth cations for Ce^{4+}. The defect reaction of Gd substitution is described by eq. (1.24). The 10 - 20 % Gd-doped cerium oxides (GDCs) are the optimized compositions, and the ionic conductivity is > 0.01 S cm^{-1} at over 500 °C.[20]

$$Gd_2O_3 \xrightarrow{CeO_2} 2Gd'_{Ce} + 3O_o^{\times} + V_o^{\cdot\cdot} \quad (1.24)$$

GDC shows excellent compatibility and chemical stability with many electrode materials in both oxidizing and reducing atmospheres. However, ceria-based electrolyte materials suffer from the partial reduction of Ce^{4+} to Ce^{3+} at > 500 °C in a strong reducing atmosphere (low oxygen partial pressure). The partially mixed oxidation states of a ceria-based electrolyte induce electrical current leakage through the electrolyte layer and slightly decrease the open-circuit voltage of a SOFC.[18] Based on its high chemical compatibility and modifiable sintering behavior with sintering aids, GDC is commonly used as an electrolyte in anode-support IT-SOFCs. A common strategy to block the electrical current leakage is to use a YSZ-GDC bilayer electrolyte, but this generally requires a complex or high-cost membrane fabrication process.

Sr and Mg-doped $LaGaO_3$ (LSGM, $La_{0.8}Sr_{0.2}Ga_{0.8}Mg_{0.2}O_{3-\delta}$) perovskite oxide developed independently by the Ishihara group[21] and Goodenough group[22] also exhibits acceptable ionic conductivity at 600 – 800 °C. The substitution of Sr and Mg, respectively, for La and Ga enhances the oxygen vacancy formation. The defect reactions in LSGM are written in eq. (1.25) and (1.26);

$$2SrO \xrightarrow{La_2O_3\ in\ LaGaO_3} 2Sr'_{La} + 2O_o^{\times} + V_o^{\cdot\cdot} \quad (1.25)$$

$$2MgO \xrightarrow{Ga_2O_3\ in\ LaGaO_3} 2Mg'_{Ga} + 2O_o^{\times} + V_o^{\cdot\cdot} \quad (1.26)$$

Since all the cations in LSGM have only one oxidation state, the ionic transport number of LSGM is close to one in both reducing and oxidizing atmospheres. However, LSGM has poor chemical compatibility with conventional electrode materials. The high

reactivity impedes LSGM from co-sintering with an anode substrate and forming a dense membrane. Hence, LSGM is generally used as a self-standing electrolyte layer in electrolyte-supported SOFCs. A barrier layer, which is often a ceria-based material, is required between the LSGM electrolyte and cermet anode in practical applications. The SOFC fabrication process needs to be optimized by properly controlling the sintering behavior of each component during the co-sintering process in order to produce a mechanically reliable and robust SOFCs with a fully dense electrolyte membrane.

1.2.2 Cathode

Excellent cathode material should fulfill all of the following requirements;

- High catalytic activity towards ORR at the SOFC operation temperatures
- Acceptable electrical conductivity
- Acceptable oxide-ion conductivity
- High phase, chemical, thermal, and morphological stability in an oxidizing atmosphere
- Excellent chemical compatibility with electrolyte and interconnect materials
- Thermal-mechanical properties that match the other components in a stack
- Optimized microstructure with high porosity and large surface area to allow the diffusion of oxygen gas and provide large numbers of active sites

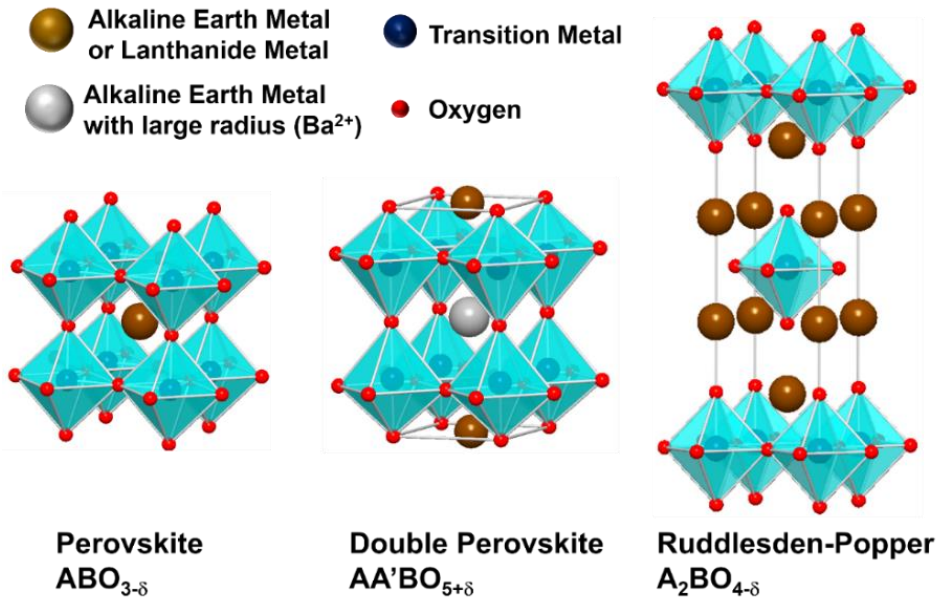

Figure 1.6 Crystal structures of perovskite, double perovskite, and Ruddlesden-Popper Oxides.

Many perovskite-related oxides have been studied as cathode materials for several decades because the structure is highly flexible and allows for various cation dopants.[23] Figure 1.6 shows common perovskite-related structures, such as simple perovskite (ABO_3), double perovskite ($AA'B_2O_6$), and Ruddlesden-Popper ($A_{n+1}B_nO_{3n+1}$). Alkaline earth or lanthanide metal cations with larger ionic radii generally sit in the A site with a 12-fold cuboctahedral coordination, and the transition metal cations in the B site with relatively smaller ionic radii are octahedral-surrounded by oxygen anions. $La_{0.8}Sr_{0.2}MnO_{3-\delta}$ (LSM) is the state-of-the-art cathode material in conventional HT-SOFCs with its high catalytic activity towards ORR, acceptable electrical conductivity, and matched thermal expansion coefficients (TECs) to YSZ at > 800 °C. However, LSM has limited oxide-ion conductivity because a small amount of oxygen vacancies (δ) exists in the lattice. Thus, a majority of ORR takes place at the triple-phase boundary (TPB), which is the interface of the electronic

conductor (LSM), ionic conductor (electrolyte), and reactant gas (O_2). An LSM – electrolyte composite cathode can increase the number of active sites for ORR, but unfortunately, the thermal-activated catalytic activity of an LSM composite cathode decreases rapidly below 800 °C. In addition, the side reaction between LSM and YSZ forms an insulting phase $La_2Zr_2O_7$, blocks the charge transfer, and irreversibly deteriorates the cathode performance.[24] Therefore, there is an urgent need for new cathode materials that fulfill all the requirements at 600 – 800 °C for IT-SOFCs.

Co-containing perovskite oxides are attractive cathode candidates in IT-SOFCs due to their high catalytic activity towards ORR.[23] Since oxygen vacancies are more easily formed in a Co-containing perovskite oxide compared to LSM, adequate oxide ionic conductivity is provided. Mixed ionic and electronic conductors (MIECs) significantly extend active sites for ORR because the reaction can take place directly on the MIEC surface and do not need to be limited by TPBs. The enhanced ORR activity is generally observed with the higher content of Co and oxygen vacancy in the perovskite lattice. $La_{1-x}Sr_xCo_{0.2}Fe_{0.8}O_{3-\delta}$ (LSCF) as an MIEC is a particularly promising cathode candidate in IT-SOFCs with the proper catalytic activity, acceptable electronic conductivity, and good chemical compatibility with several electrolyte materials. However, the spontaneous SrO phase segregation on the LSCF surface blocks the active sites and easily reacts with the poisoning chromia gases from the interconnect.[25] In addition, compared to the TECs of YSZ (10.5×10^{-6} K^{-1}), GDC (12.2×10^{-6} K^{-1}), and LSGM (11.0×10^{-6} K^{-1}), LSCF has a higher TEC of 16.7×10^{-6} K^{-1}. The TEC mismatch between cathode and electrolyte materials induces thermal stresses during the device fabrication process and system operation. Simulation results suggested that the thermal stresses of the LSCF cathode layer in a large-scale SOFC could be close to the layer characteristic strength, which may lead to mechanical failure, such as cracking, buckling, and delamination.[26] Although many Co-

containing perovskite oxides, such as $Ba_{0.5}Sr_{0.5}Co_{0.8}Fe_{0.2}O_{3-\delta}$ (BSCF)[27] and $SrCo_{0.9}Sb_{0.1}O_{3-\delta}$ (SCSb)[28], exhibit a higher ORR activity than LSCF, their TECs are even larger (> 20.0 × 10^{-6} K^{-1}) due to a higher content of Co and alkaline earth metal dopants. Such abnormally high TECs are a result of the reduction of Co cations and spin-state transition in the octahedral coordination at elevated temperatures, as shown in Figure 1.7. Thus, all perovskite-related oxides with high Co content may suffer from the high thermal stress due to their high TECs. Moreover, BSCF and SCSb both undergo spontaneous phase decomposition or phase transformation in air after tens of hours at 600 – 800 °C.[27,28] Therefore, it is crucial to develop an alternative cathode material with matched TECs, high phase stability, and adequate catalytic activity to achieve highly stable IT-SOFCs.

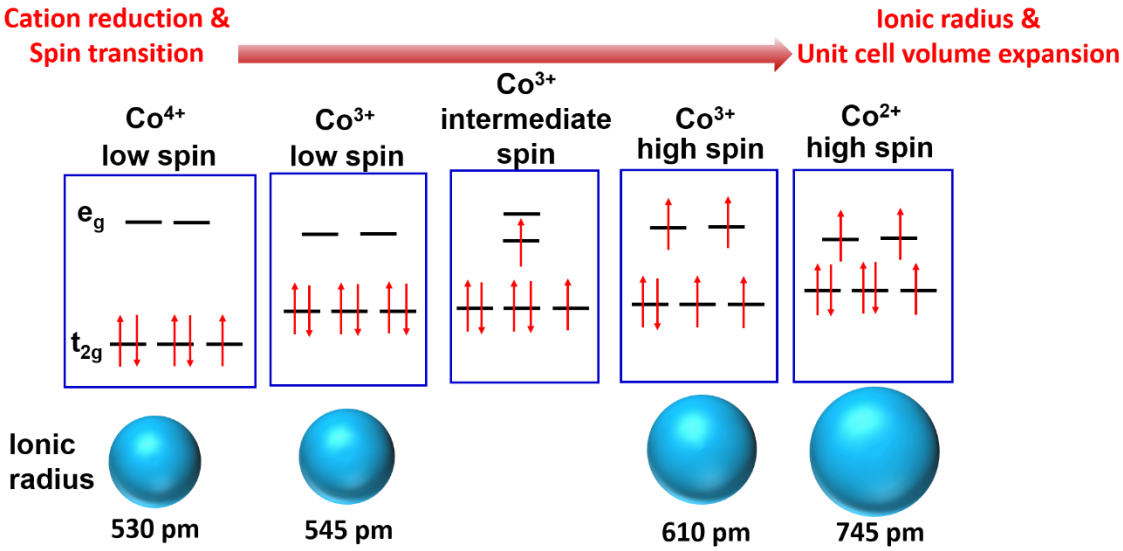

Figure 1.7 Schematic electronic configurations and ionic radii of Co cations with various oxidation states at elevated temperatures.

1.2.3 Anode

The following properties are essential for an outstanding anode material;

- High catalytic activity towards fuel oxidation reactions
- High coking resistance and adequate sulfur impurity tolerance
- Good redox stability when switching between reducing and oxidizing atmospheres
- Proper electrical conductivity and acceptable oxide-ion conductivity
- High phase, chemical, thermal, and morphological stability at a reducing atmosphere
- Excellent chemical compatibility with electrolyte and interconnect materials
- Thermal-mechanical properties that match the other components in a stack
- Optimized microstructure with high porosity and large surface area to allow fuel gas diffusion and provide large numbers of active sites

The SOFC anode is required to operate in a severe environment with highly reducing fuel, so excellent phase and chemical stability is an essential criterion. The current state-of-the-art cermet material, a Ni – electrolyte composite anode, performs efficient fuel oxidation reaction during long-term SOFC operation with an acceptable cost. Since the Ni metal and electrolyte oxide are, respectively, purely electrical and ionic conductors, homogenous mixing of these two materials propagates the total length of TPBs as active sites and increase the anode efficiency. The electrolyte materials, YSZ and GDC, are commonly composited with NiO as the anode precursor, and NiO is reduced to Ni metal during SOFC operation. The volume shrinkage from NiO to Ni metal makes the anode microstructure more porous, which is beneficial for the mass transport of fuel gases.

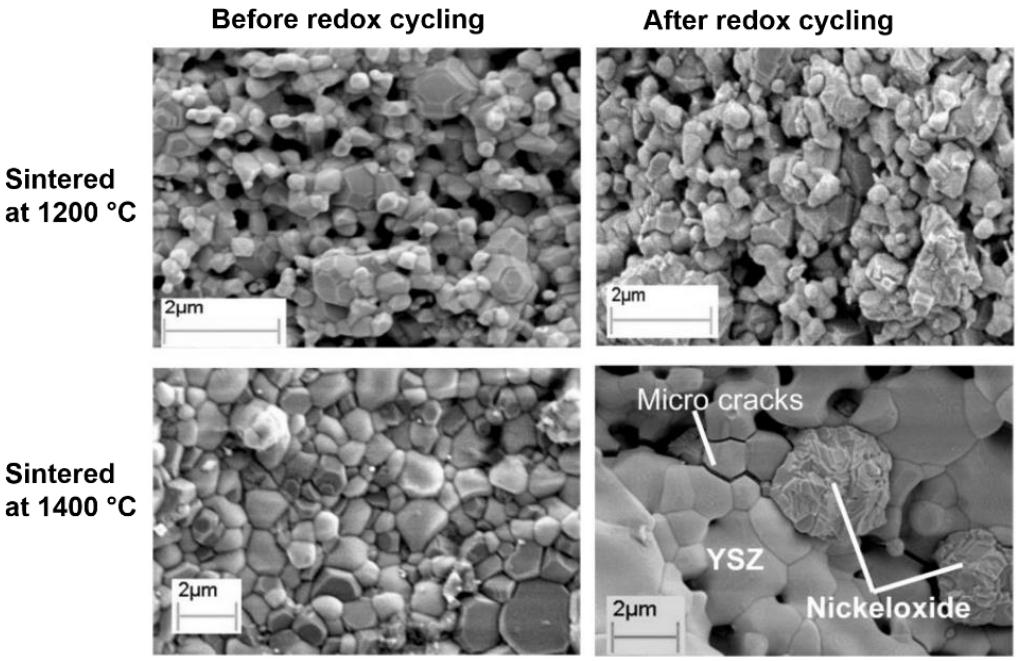

Figure 1.8 NiO – YSZ composite anode sintered at 1200 °C (above) and 1400 °C (below) in air. The anode microstructures before and after 4 redox cycles are, respectively, shown on the left and right. Adapted from reference 33 with permission from Springer Nature.

Although Ni is a good catalyst towards fuel oxidation reactions, several undesirable properties of Ni metal, such as severe carbon deposition, sulfur poisoning, redox instability, and Ni particle growth, lead to the anode performance degradation.[29] The carbon deposition is easily observed on the composite anode surface with hydrocarbon fuel due to a rapid hydrocarbon cracking reaction as shown in eq. (1.7), and inactive NiS_x phases quickly form on the Ni surface in the presence of H_2S impurities in the fuel. The coking and sulfur poisoning can be mitigated by partially or completely substituting Ni with other transition metals, but the anode activity decreases as a tradeoff.[30] GDC in the Ni – GDC composite anode is able to enhance the hydrocarbon fuel oxidation reaction and reduce the carbon deposition due to its mixed electronic and ionic conducting property in the reducing atmosphere; however, coking on the composite anode surface cannot be fully eliminated.

Furthermore, mechanical and microstructural instability occur inevitably during redox cycling, because the volume expansion from Ni to NiO causes stress on the Ni-electrolyte interface and generates micro-cracks at the grain boundary in the anode.[31,32] Figure 1.8 shows the microcracks in a Ni – YSZ composite anode before and after 4 redox cycles.[33] The Ni metal particles in a composite anode are commonly found to be agglomerated after long-term operation, and the particle growth rate of Ni increases with the operation temperature.[33] The above disadvantages of Ni composite anodes limit the SOFC's operational capability, such as the direct usage of hydrocarbon fuel and the carbon deposition removal through redox cycling.

Most alternative anode material development focus on perovskite-related oxides, including (1) chromite perovskite oxides[34], such as $La_{0.75}Sr_{0.25}Cr_{0.5}Mn_{0.5}O_{3-\delta}$[35] and $La_{0.33}Sr_{0.67}Fe_{0.67}Cr_{0.33}O_{3-d}$[36], (2) titanate perovskite oxides, such as $La_{1-x}Sr_xTiO_{3-\delta}$[37], and (3) double perovskite oxides, such as $Sr_2Mg_{1-x}Mn_xMoO_{5+\delta}$[38] and $PrBaMn_2O_{5+\delta}$[39]. Unlike Ni metal, these oxide anode candidates generally have the advantages of high redox stability, adequate sulfur tolerance, good coking resistance, and matched TECs to the electrolyte materials. However, the catalytic activity of these oxide anodes towards fuel oxidation reactions is much weaker than that of a Ni composite anode, and this relatively poor activity becomes more serious at lower operation temperatures (600 – 800 °C). Hence, oxide anodes have not been applied in practical IT-SOFCs because of their high activation polarization.

1.3 MOTIVATIONS AND OBJECTIVES

As highly efficient power generators, SOFCs aim to continuously operate for > 60,000 h with a minimum degradation rate. However, the cost of a commercial SOFC

system with or without a CHP system is currently still too high to compete with conventional power plants and other mature renewable energy conversion devices. Based on the analysis of Max Wei and his co-workers, a large SOFC system had a near-zero learning curve rate in the California market from 2005 to 2015.[40] The less expensive grid electricity and lower gas prices in the U.S. compared to Japan make SOFCs harder to enter the U.S. market. Therefore, reducing the cost is the most important factor for the mass commercialization of SOFCs. The cost reduction of the SOFC system can be effectively achieved by increasing performance, extending lifetime, improving reliability, and reducing the material and manufacturing costs. In terms of material selection, high catalytic activity, excellent chemical and phase stability, and matched thermal expansion are all essential properties of an excellent electrode to fabricate robust and efficient SOFCs. The matched thermal expansion behavior among the SOFC components is crucial to minimize thermal stress and increase the possibility of survival during operation and thermal cycles.

Here, alternative cathode and anode materials are designed to overcome the current challenges of electrode materials in IT-SOFCs. All the materials are carefully characterized, and the SOFC performance is evaluated with selected materials. In terms of the cathode, Co-containing perovskite materials have been shown to be very attractive to their catalytic activity towards ORR; however, intrinsically high TECs and phase instability of the perovskite oxides, such as BSCF and SCSb, impede their use in practical applications. Unlike the octahedrally-coordinated Co cations in perovskite-related oxides, Co in $YBaCo_4O_7$-based swedenborgite oxides is surrounded by oxygen anions in a tetrahedral coordination, as shown in Figure 1.9. The Co^{2+} and Co^{3+} cations in swedenborgite oxides will not undergo the spin transition because the electronic state constantly remains in the high spin state. Thus, the TECs of the $YBaCo_4O_7$-based swedenborgite oxides are much lower than those of the Co-containing perovskite oxides.

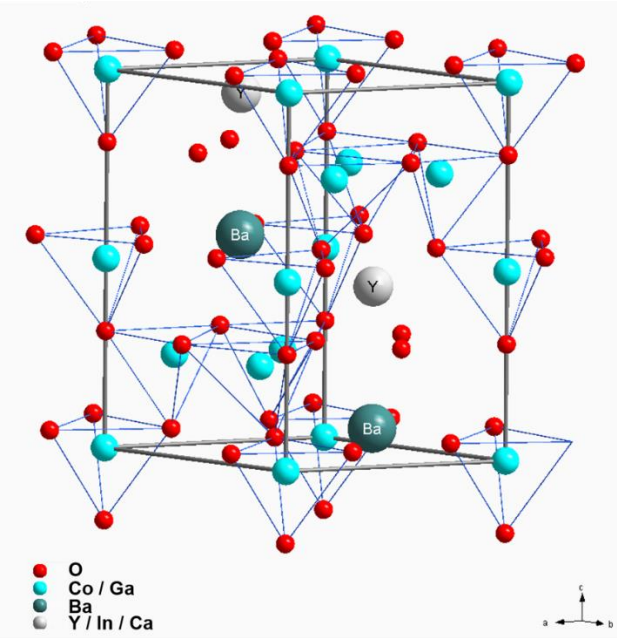

Figure 1.9 Crystal structure of $YBaCo_4O_7$-based swedenborgite oxides.

After Valldor and Andersson first reported $YBaCo_4O_7$[41], many compositions of $YBaCo_4O_7$-based swedenborgite oxides were synthesized.[42–48] Since the continuous oxygen absorption of $YBaCo_4O_7$ at > 600 °C leads to complete phase decomposition, many efforts have been made by Valldor, Hu, Karppinen, and Manthiram groups to stabilize the phase at high temperatures by doping with cations with an empty or full d-shell electron configuration.[49–61] However, the effect of the Y-site dopants (Ca^{2+} and In^{3+}) and Co-site dopants (Al^{3+}, Fe^{3+}, and Ga^{3+}) on the long-term stability has not yet been completely examined. Here, a comprehensive understanding of the cation effect on the phase stability, electrical conductivity, TEC, and electrochemical activity is presented as a guideline to design highly active and robust cathode materials.

In terms of the anode part, the catalytic activity improvement of $La_{0.3}Sr_{0.7}Cr_{0.3}Fe_{0.7}O_{3-\delta}$ cathode material is attempted by substituting Fe with Co and using

exsolved Co-Fe nanoparticles as catalysts. The easily reduced cations in a perovskite lattice will precipitate on the perovskite oxide surface as metallic catalysts in the reducing atmosphere, while the perovskite structure with an appropriate composition may remain stable.[62,63] The exsolved metal will reincorporate into the perovskite lattice in an oxidizing atmosphere and precipitate again in an reducing atmosphere. Thus, the exsolved nanoparticles are able to self-regenerate with control of the operational atmosphere. Although the strategy of catalytic activity enhancement with exsolved nanoparticles has been shown in several perovskite-related materials, the exsolving and self-regenerating temperatures in the literature are generally higher than 800 °C,[62–71] which is the upper temperature boundary of IT-SOFCs. As can be seen from the above discussion, irreversible performance degradation at relatively high operation temperature may be led by several mechanisms, such as microstructure coarsening, unwanted side reactions on the interface, and rapid oxidation of the metallic interconnect.

A perovskite oxide $La_{0.3}Sr_{0.7}Cr_{0.3}Fe_{0.6}Co_{0.1}O_3$ is designed and synthesized here as an anode material with the aim of reducing the self-regenerating temperature. Compared to Ti in perovskite oxides, Cr and Fe in a perovskite lattice allow the cation reduction and oxygen release at relatively lower temperatures, which may facilitate the cation exsolution process. The material is comprehensively characterized in reducing and oxidizing atmospheres, and the SOFC performance is evaluated with H_2, H_2 – 27 ppm of H_2S, and propane. The long-term performance stability and redox cycles are also tested to demonstrate the potential of this material in practical SOFC applications. Moreover, the self-regeneration behaviors of exsolved nanoparticles at 800 and 700 °C are carefully examined.

Chapter 2: Experimental Procedures

2.1 Material Synthesis

This chapter describes general experimental techniques in this dissertation. The swedenborgite oxides and chromite perovskite oxides with diverse dopants were all synthesized by a solid-state reaction (SSR). After properly mixing reagent chemicals with ethanol in a mortar and pestle, the raw materials were dried and calcined at 1000 °C. Then, the calcined powder was pressed into a pellet and sintered at an appropriate temperature with intermediate grinding and mixing to form a desired phase.

The NiO – GDC composite anode material for an anode-supported single cell was prepared by a glycine-nitrate combustion method[72] or a modified sol-gel method[73]. The combustion synthesis of GDC is taken as an example here, $Gd(NO_3)_3 \cdot 6H_2O$ and $Ce(NO_3)_3 \cdot 6H_2O$ were dissolved in deionized water with a molar ratio of 2 : 8. Then, glycine was added as the combustion fuel and complexing agent, and the stoichiometric ratio of glycine to nitrate was 1.67. After proper stirring and heating on a hotplate, the solution became a viscous gel and ignited spontaneously. The ash-like products were collected and calcined at 600 °C for 6 h to form single-phase powders. The NiO phase was formed by calcining the ash-like products at 850 °C for 6 h. In addition, the GDC powder was also used to fabricate an electrolyte membrane of an anode-supported substrate by a co-pressing method.

The surface-modified NiO – GDC composite anode powder was synthesized by a modified sol-gel method.[73] $Ni(NO_3)_2 \cdot H_2O$, $(NH_4)_2Ce(NO_3)_6$, and $Gd(NO_3)_3 \cdot 6H_2O$ were dissolved in deionized water in a molar ratio of 4.5 : 1 : 0.25, and

ethylenediaminetetraacetic acid (EDTA) and citric acid were added as chelating agents. The molar ratio of EDTA, citric acid, and total cations (Ni^{2+}, Gd^{3+}, and Ce^{4+}) was 1 : 1.5 : 1. After the pH of the solution was adjusted to 7 by NH_4OH, conventional anode powder consisting of ball-milled NiO (Alfa Aesar) and GDC (FuelCell Materials) in a weight ratio of 60 : 40 was added into the solution and stirred at room temperature for 12 h. Next, the solution was heated at 120 °C to slowly remove the excess water, and the dried product was calcined at 600 °C and 900 °C for 6 h each.

2.2 MATERIAL CHARACTERIZATION

2.2.1 Phase identification

The phase of powder materials was characterized by X-ray diffraction (XRD, Rigaku Miniflex 600 and Ultima IV) with a Cu Kα radiation, and the data were collected from 10° to 80° with a scanning step of 0.02° and a collection time of 2 sec per step. A XRD specimen was prepared by filling the sample powder into a cavity of a glass or aluminum sample holder. A crystal structure was determined by comparing the measured XRD pattern with those of known materials in databases of JADE software and Pearson's Crystal Data.

2.2.2 Rietveld refinement

The complete crystallographic parameters of synthesized materials in a crystal structure were determined by the conventional Rietveld method which applies a nonlinear least squares estimation to refine a theoretical pattern profile until it matches the measured

XRD pattern.[74] The XRD patterns were recorded by extending the collection time to 3 sec per scanning step to improve the signal-to-noise ratio. The General Structure Analysis System (GSAS) package with the graphical user interface (EXPGUI) was used as the refinement program.[75] The background, scale factor, zero-point position, cell parameters, atomic positions, thermal parameters, and profile coefficients for the Pseudo-Voigt / Finger-Cox-Jephcoat (FCJ) asymmetric peak shape function were refined until the convergence was achieved.

2.2.3 Iodometric Titration

The average oxidation state of the transition metal cations in the swedenborgite and perovskite oxides was measured by iodometric titration.[61,76] About 50 mg of oxide powder was dissolved in a mixed solution of (1) 10 ml of 10 wt. % KI solution and (2) 15 ml of 3.5 M $HCl_{(aq)}$ at room temperature. In order to prevent interference from oxygen in air, the sample solution was protected by purging with Ar gas during the titration process. Iodide (I^-) in the solution was oxidized to iodine (I_2) by transition metal cations. The solution was titrated against 0.015 M $Na_2S_2O_{3(aq)}$, and the solution color gradually changed from dark yellow to light yellow. Then, starch was added in the solution as an end-point indicator. The end point was reached when the solution color dramatically changed from dark purple to light pink. The average oxidation state of transition metal cations was calculated with the titrated mole amount of sodium thiosulfate. The oxygen content in a lattice was determined with the known oxide composition and the cation oxidation states.

2.2.4 Morphology Observation

The morphology and microstructure of various powder, dense pellet, and single cell samples were observed by scanning electron microscopies (SEMs, JEOL JSM-5610 and Hitachi S5500). In addition, energy dispersive X-ray spectroscopy (EDX, Oxford Inca X-act and Bruker Quantax 4010) was utilized for semi-quantitatively elemental analysis. In order to reveal the true nanoparticle morphology on an anode surface, 5 – 10 kV electron beam was used without depositing an electron-conductive Au layer on the sample surface.[77]

2.3 THERMAL ANALYSIS

2.3.1 Thermogravimetric analysis

Weight changes during heating and cooling processes were measured with a thermogravimetric analyzer (TGA, Netzsch STA 449 F3).[78] Differential scanning calorimetry (DSC) monitored the simultaneous heat change of a sample at elevated temperatures to determine chemical reactions and phase transformations. Since $YBaCo_4O_7$-based swedenborgite oxides have an unique oxygen storage capability at about 350 °C and a continuous oxygen adsorption above 600 °C, the reversibility of oxygen intake and release was evaluated from room temperature to 1000 °C at a rate of 1 °C min^{-1} with an air flow rate of 40 mL min^{-1}. The powder sample was pre-annealed with Ar at 500 °C for 6 h to eliminate the excess oxygen in the doped $YBaCo_4O_7$ lattice. The measured mass was corrected for buoyancy effect by subtracting a blank run of the empty platinum crucibles. The oxygen vacancy formation of perovskite oxides at high temperatures in reducing and oxidizing atmospheres was measured, respectively, with 5 % H_2 – Ar and air. The initial oxygen content at room temperature was calculated with the titration result, and

the oxygen content variation in the lattice as a function of temperature was determined with TGA data.

2.3.2 Electrical Conductivity

The electrical conductivity was measured by the van der Pauw method with a four-probe DC configuration as shown in Figure 2.1.[79–81] This technique is widely used to measure the resistivity of a sample with any arbitrary shape. The dense pellet samples were made by pressing the ball-milled materials into a desired shape and sintering at appropriate temperature with heating and cooling rates of 2 °C min^{-1}. The bulk density of these sintered samples was measured by the Archimedes method, and their relative density was over 90 % of the theoretical value. The pellet surface was polished to obtain a homogeneous thickness. Four silver wires were attached to four corners of a pellet sample with concentrated silver pastes (Fuelcell Materials) as four independent probes. The paste was dried at 100 °C and heated at 500 °C to provide sufficient mechanical strength. The voltage was monitored with applying a constant currency of 20 mA, and heating and cooling rates were 3 °C min^{-1}. The specific resistivity ρ of a flat sample can be calculated with eq. (2.1).

$$\rho = \frac{\pi d}{ln2}\frac{\left(R_{AB,CD} + R_{BC,DA}\right)}{2} f\left(\frac{R_{AB,CD}}{R_{BC,DA}}\right) \quad (2.1)$$

where d is pellet thickness and $R_{AB,CD}$ indicates the resistance calculated by the currency between A and B points and the voltage between C and D points. Here, the circle pellet is used and the four points are on the symmetrical positions. Thus, $R_{AB,CD}$ is identical to $R_{BC,DA}$, and the function of ($R_{AB,CD}$ / $R_{BC,DA}$) is equal to one.

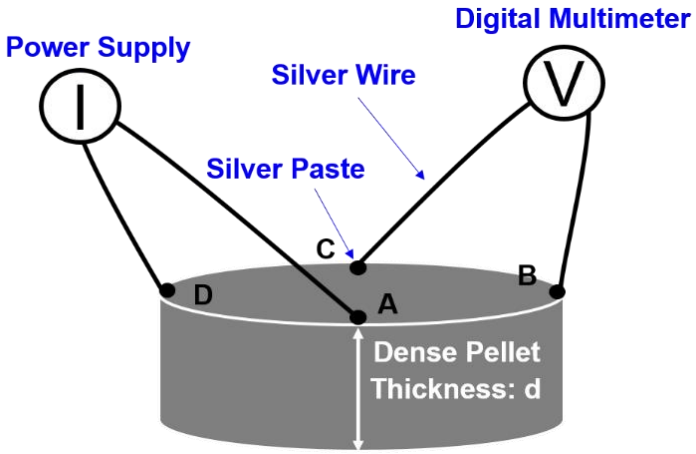

Figure 2.1 Schematic configuration of electrical conductivity measurement with the van der Pauw method.

2.3.3 Thermal Expansion Behavior

The thermal expansion behavior of the dense samples was collected with a dilatometer (Linseis L75H). The dense samples with a rod shape were prepared by the same procedure of the dense pellets in Chapter 2.3.2. The diameter and height of a rod were, respectively, about 3 mm and 10 mm. The top and bottom surfaces of a rod were polished. The rod height variation from room temperature to a specific temperature T at an oxygen partial pressure P_{O2} was monitored, and the TEC was calculated by eq. (2.2).

$$\alpha_{PO2} = \frac{1}{L_0}\left(\frac{dL}{dT}\right)_{PO2} \quad (2.2)$$

where L_0 is the height of a rod sample at room temperature. The expansion was measured from 80 to 900 °C at 3 °C min^{-1} rate in air and 5 % H_2 – Ar, respectively, as oxidizing and reducing atmospheres.

2.4 Electrochemical Analysis and Performance Evaluation

2.4.1 Electrochemical Impedance Spectroscopy

The polarization resistance of an electrochemical cell was measured by electrochemical impedance spectroscopy (EIS, Solartron 1260 FRA). Impedances of a system are determined by applying a small sinusoidal voltage perturbation and monitoring the current response from the system. Factors of the electrode and testing condition, such as composition, porosity, thickness, fabrication method, atmosphere, gas flow rate, and temperature, significantly affect the system impedance.

In order to understand the catalytic activity of cathode materials towards ORR, a symmetric cell consisted of two identical cathodes on two sides of a dense GDC electrolyte pellet was tested. The dense electrolyte pellet was made by uniaxially pressing GDC powder (FuelCell Materials) into a pellet and sintering it at 1450 °C for 12 h. The thickness of the sintered GDC pellet was about 1 mm. The swedenborgite oxide and commercial GDC in a weight ratio of 50 : 50 was ball-milled with ethanol for 24 h as the composite cathode material. The cathode slurry was made by mixing the composite cathode powder and an organic binder (Heraeus V006). After screen-printing the slurry on both sides of a polished GDC electrolyte pellet, the cathode was sintered at 950 °C for 2 h.

A thin layer of diluted silver pastes as a current collector was brushed on the electrode surface, and silver wire was attached to the current collector with concentrated silver pastes (Fuelcell Materials).[82] Three symmetric cells were tested at the same time on our homemade system, which improved the data validity. The testing temperature was from 500 to 800 °C at intervals of 50 °C in ambient air. The scanning frequency range of EIS was from 0.01 Hz to 1 MHz, and the signal amplitude was 10 mV under the open-circuit condition.

2.4.2 Single Cell Fabrication and Performance Measurement

The SOFC performance with selected cathode and anode materials was evaluated, respectively, with anode-supported and electrolyte-supported single cells. Schematic configurations of two types of single cells are shown in Figure 2.2.

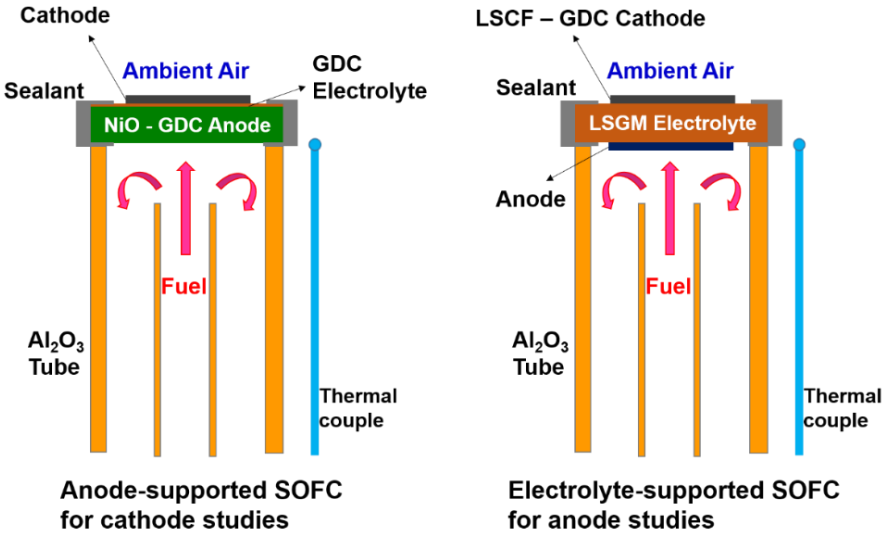

Figure 2.2 Schematic configuration of anode-supported and electrolyte-supported SOFCs.

The anode-supported single cell was prepared by dry-pressing. A mixture of the calcined anode powder with 10 wt. % rice starch was uniaxially pressed at 50 MPa to form a substrate. Then, GDC powder synthesized by the glycine-nitrate method was uniformly dispersed on the surface of the pre-pressed anode in the die. The GDC electrolyte layer and the anode substrate were co-pressed at 200 MPa, and the bi-layer pellet was sintered at 1350 °C for 3 h. The cathode was prepared on the sintered electrolyte surface by the same process in the symmetric cell fabrication. Ag paste was diluted and brushed on the cathode surface as the current collector, and Ag wire was attached to both the electrodes with

concentrated Ag paste. The active cathode area was 0.25 cm^2. The cathode was exposed to ambient air, and the H_2 flow rate on the anode side was 20 mL min^{-1}.

The electrolyte-supported solid oxide single cells were fabricated on a LSGM electrolyte thin disc. The LSGM powder (FuelCell Materials) was uniaxially pressed into a pellet and pre-sintered at 1200 °C to provide sufficient mechanical strength. The barrier-layer material $La_{0.4}Ce_{0.6}O_{2-\delta}$ (LDC) was synthesized by a glycine-nitrate process, which was described in Chapter 2.1. The ball-milled LDC was mixed with the organic binder (Heraeus V006) and screen-printed on one side of the pre-sintered LSGM pellet for preventing the interaction between the LSGM and the anode perovskite oxide.[83] The LDC-coated pellet was co-fired at 1450 °C for 6 h, and then the dense pellet was thinned and polished to about 250 μm from the non-LDC-coated side. The pristine perovskite oxides were ball-milled with commercial GDC in a 1 : 1 weight ratio for 24 h, and the electrode ink was prepared by mixing equal weights of the composite electrode powder and organic binder. The anode ink was printed on the LDC-coated side of the LSGM electrolyte support and sintered at 1150 °C for 2 h. Then, the LSCF – GDC composite cathode layer was prepared on the other side of the LSGM pellet with the same method as the anode layer and sintered at 950 °C for 2 h. The thickness of anodes and cathodes was, respectively, 20 and 30 μm. Then dilute Ag paste was brushed on both electrodes as the current collector and Ag wire was fixed with concentrated Ag paste. The active area of the two electrodes was 0.25 cm^2.

A single cell was mounted on an alumina tube with ceramic sealant (Aremco Ceramabond 552) and tested with our homemade system. The polarization curve and power density of a SOFC were obtained by measuring I-V curves at various operation temperatures.

Chapter 3: Phase Stability, Oxygen-storage Capability, and Electrocatalytic Activity in Solid Oxide Fuel Cells of (Y, In, Ca)$BaCo_{4-y}Ga_yO_{7+\delta}$

3.1 INTRODUCTION

$YBaCo_4O_{7+\delta}$-based materials have attracted much attention in the last 15 years because of their potential applications for oxygen storage and in SOFCs.[46] First, $YBaCo_4O_{7+\delta}$ can accept and release oxygen reversibly up to $\delta = 1.5$ in the temperature range of 200 – 400 °C.[42] Its oxygen-storage capability (OSC) at atmospheric pressure reaches $\delta = 1.1$, which is 30% higher than that found with the commercialized oxygen storage material $CeO_2 – ZrO_2$.[46,84] Secondly, $YBaCo_4O_{7+\delta}$ has relatively low thermal expansion coefficient (TEC), with an average TEC of 7.5×10^{-6} K^{-1} in the temperature range of 300 – 900 °C[44], and it matches well with the TECs of common oxide-ion electrolyte materials of SOFCs ($10 – 12.5 \times 10^{-6}$ K^{-1}).[22,85] However, the practical applications of this class of materials is impeded by the irreversible oxygen absorption and phase decomposition at 600 – 900 °C. The decomposition products, such as $BaCoO_3$, Y_2O_3, and Co_3O_4, are easily found after heating $YBaCo_4O_{7+\delta}$ to the decomposition temperature region.[42,51]

In order to eliminate the phase decomposition resulting from the irreversible oxygen absorption, various cationic substitutions have been carried out in the R sites and Co sites of the $RBaCo_4O_{7+\delta}$-based materials. The OSC and the irreversible oxygen absorption have been evaluated with thermogravimetric analysis (TGA). Valldor found that the $YBaCo_4O_{7+\delta}$ oxides exhibit high solubility for different dopants and $RBaM_4O_7$ (R = Ca, Y, In, Dy–Lu, M = Co, Al, Zn, and Fe) have been synthesized.[43] Furthermore, Kadota

---

Lai, K.-Y.; Manthiram, A. Phase Stability, Oxygen-Storage Capability, and Electrocatalytic Activity in Solid Oxide Fuel Cells of (Y, In, Ca)$BaCo_{4-y}Ga_yO_{7+\delta}$. *Chem. Mater.* 2016, **28**, 9077–9087. Manthiram, A. supervised the project.

et al. measured the OSC of $RBaCo_4O_{7+\delta}$ (R = Y, Dy, Ho, Er, Tm, Yb, and Lu) and suggested that the stable phase temperature window became wider with a larger ionic radius of the cation on the R site.[45] However, there was no significant reduction in the irreversible oxygen absorption above 600 °C with various R site substitutions. On the other hand, cationic substitutions on the Co-site, including Cu, Mn, Ni, Fe, Zn, Ga, and Al, have a larger influence both on the OSC and the phase stability.[48,50–52,56,57,86–90] Among those dopants, Ga, Al, and Zn have a greater stabilization effect against the phase decomposition because with a d^0 or d^{10} electronic configuration, they have a strong preference for tetrahedral coordination.[51,86,88,90,52,56,57] The complete elimination of high-temperature decomposition observed by TGA requires a substitution of, respectively, 20 or 25 atom % Ga[56,57] and Zn[86]. Al substitution alone could not provide the full stabilization as its solubility in $YBaCo_{4-y}Al_yO_{7+\delta}$ is limited to about 12 %[52,90], but a co-doping of 15 % of Al and Ga is able to completely suppress the phase decomposition.[57] Unfortunately, the oxygen-storage property and stability have an inverse relationship, as OSC decreases with increasing substitution in the M-site (Co-site).

Our group has further investigated the long-term stability of Zn-substituted $RBaCo_4O_{7+\delta}$ materials by annealing the samples at 600 – 800 °C for up to 120 h, and the electrochemical performance of the stabilized compositions were measured as cathode materials in SOFCs.[51,53–55,58–60] Although Hao *et al.*[86] did not observe any weight gain in the TGA results of $YBaCo_3ZnO_{7+\delta}$ above 600 °C, our group[54] found that $YBaCo_3ZnO_{7+\delta}$ decomposed after the long-term stability tests at 600 and 700 °C. Our previous work also revealed that high-temperature phase stability could be achieved by applying partial substitutions on the R site (*e.g.*, In or In-Ca) of $YBaCo_3ZnO_{7+\delta}$. Unfortunately, the electrochemical performance decreases with higher Zn or In content. Additionally, the oxygen-storage property was not studied due to the severe suppression of oxygen

absorption with Zn substitution. In the case of Ga-substituted and Al-substituted $RBaCo_4O_{7+\delta}$ materials, only the long-term stability (72 h) of $Y_{0.5}Ca_{0.5-x}In_xBaCo_{3.2}Ga_{0.8}O_{7+\delta}$ (x = 0 and 0.1) was tested, but the TGA results were not presented.[91] Therefore, the high-temperature stability and oxygen-storage properties of Ga-substituted $YBaCo_4O_{7+\delta}$ materials with R-site substitutions still lacks a comprehensive evaluation.

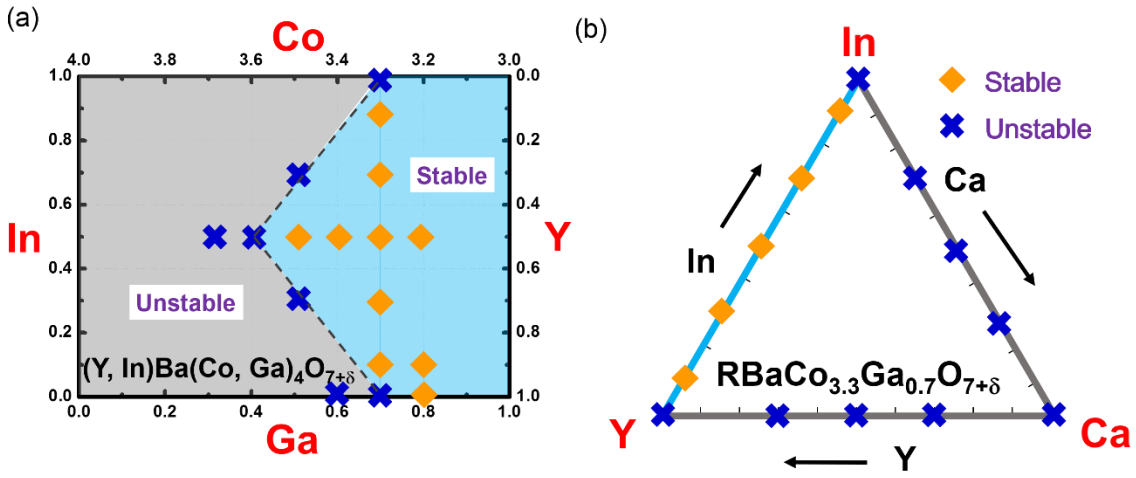

Figure 3.1 Schematic diagram indicating the synthesized compositions and their long-term stability at 600 – 800 °C: (a) (Y, In)Ba(Co, Ga)$_4O_{7+\delta}$ and (b) $RBaCo_{3.3}Ga_{0.7}O_{7+\delta}$ (R = Y-In, Y-Ca, and In-Ca) materials.

This present study aims to investigate the high-temperature phase stability of Ga-substituted $RBaCo_4O_{7+\delta}$, where R includes Y-In, Y-Ca, and Ca-In co-dopants. Twenty four compositions of (Y, In, Ca)Ba(Co, Ga)$_4O_{7+\delta}$ were synthesized and are shown in Figure 3.1 With the goal to enhance the oxygen storage capability at 200 - 400 °C and the electrochemical performance at the intermediate operating temperatures (600 – 800 °C) of SOFCs, the Ga content is kept as low as possible. Meanwhile, the optimization of the composition with R-site dopants is also considered. The phase stability is determined by

both TGA and long-term stability tests. Furthermore, the electrical conductivity and TEC of the stabilized materials are measured. For the electrochemical performance assessment, composites consisting of a mixture of $Ce_{0.8}Gd_{0.2}O_{2-\delta}$ (GDC) and the stabilized Ga-substituted $RBaCo_4O_{7+\delta}$ are applied as cathodes in intermediate-temperature SOFCs (IT-SOFCs). The performance of an anode-supported single cell is also presented.

3.2 EXPERIMENTALS

3.2.1 Powder Synthesis and Long-Term Stability Test

The (Y, In, Ca)Ba(Co, Ga)$_4O_{7+\delta}$ materials were synthesized by the traditional SSR of a stoichiometric mixture of Y_2O_3, In_2O_3, $CaCO_3$, $BaCO_3$, Co_3O_4, and Ga_2O_3.[51] These raw materials were mixed with ethanol in an agate mortar and pestle for one hour and calcined at 1000 °C for 12 h in air. The calcined powders were then mixed, ground, pressed into a pellet, and sintered at 1200 °C for 24 h. The product powder from the crushed pellet was characterized by XRD. The lattice parameters were calculated by the Rietveld refinement method with the GSAS program as described in Chapter 2.2.[75] The long-term phase stability of the (Y, In, Ca)Ba(Co, Ga)$_4O_{7+\delta}$ samples was assessed by annealing them separately at 600, 700, and 800 °C for 120 h. To prevent any side reaction between the samples and the alumina crucible, the powder samples were placed on the top of a pellet of the same material. The cathode materials and GDC electrolyte were mixed and heated at 1100 °C for analyzing the chemical compatibility.

3.2.2 Thermal Analysis and Electrochemical Evaluation

The detail of thermal analysis was described in Chapter 2.3. The oxygen absorption and desorption behaviors were evaluated by TGA. The sample was first annealed at 500 °C in Ar for 6 h in order to minimize its oxygen content, and the precise oxygen contents were determined by iodometric titration at room temperature.[92] The annealed samples were heated in the TGA from room temperature to 1000 °C at a rate of 1 °C min^{-1} with air.[61] The pellet and rod samples were made by pressing the ball-milled materials into the desired shapes and sintering at 1200 °C with a 2 °C min^{-1} heating and cooling rate. The thermal expansion behavior and electrical conductivity of the dense samples were collected at 80 – 900 °C at 3 °C min^{-1} rate in air.

The fabrication process of symmetric cells was detailed in Chapter 2.4. The composite cathode was made by ball milling (Y, In)Ba(Co, $Ga)_4O_7$ and GDC (Fuelcellmaterials) in a ratio of 50 : 50 wt.% for one day with ethanol. Then, the cathode slurry was prepared by mixing the composite cathode and an organic binder (Heraeus V006) and then screen-printed onto both sides of the GDC pellet as a symmetric cell. The cathode was sintered at 950 °C for 2 h. The polarization resistance of symmetric cells was measured with EIS from 500 to 800 °C at intervals of 50 °C in ambient air. The scanning frequency range of EIS was from 0.01 Hz to 1 MHz, and the signal amplitude was 10 mV under the open-circuit condition.

An anode-supported single cell was made by a co-pressing method, whose detail was described in Chapter 2.4. The NiO – GDC composite anode and GDC electrolyte materials of the single cell were all synthesized by the glycine-nitrate combustion method.[93] The electrochemical performance of the single cell was evaluated with a homemade testing system at 600 to 700 °C with an internal of 50 °C. The cathode was

exposed to ambient air, and the H_2 flow rate on the anode side was 20 mL min^{-1}. The microstructure was observed by SEM (JEOL JSM-5610) and EDX (Oxford Inca X-act).

3.3 Results and Discussions

3.3.1 Structural Characterization

Five series of Ga-substituted (Y, In, Ca)$BaCo_4O_{7+\delta}$ materials were synthesized in this study: $YBaCo_{4-y}Ga_yO_{7+\delta}$ (y = 0.6 – 0.8), $Y_{1-x}In_xBaCo_{3.3}Ga_{0.7}O_{7+\delta}$ (x = 0 – 1), $Y_{0.5}In_{0.5}BaCo_{4-y}Ga_yO_{7+\delta}$ (y = 0.3 – 0.8), $Y_{1-x}Ca_xBaCo_{3.3}Ga_{0.7}O_{7+\delta}$ (x = 0 – 1), and $In_{1-x}Ca_xBaCo_{3.3}Ga_{0.7}O_{7+\delta}$ (x = 0 – 1). The compositions of these single-phase materials are presented in Figure 3.1 The refinement results of all materials, including cell parameters, R_p, and χ^2 values, are given in the Appendix A (Figure A1 – A5). Most of the synthesized materials have the space group of *P31c*.[61] The only exception is $CaBaCo_{3.3}Ga_{0.7}O_{7+\delta}$ (see Figure A4(a)), which has the same space group (*Pbn21*) as $CaBaCo_4O_{7+\delta}$.[94,95] The un-doped $CaBaCo_4O_{7+\delta}$ is known to have two phases in the literature. The relatively high-temperature trigonal phase (*P31c*) of $CaBaCo_4O_{7+\delta}$ is composed of two types of corner-shared CoO_4 tetrahedra located along the c-axis on alternating triangular and Kagome layers. The Co^{2+} / Co^{3+} ions are distributed randomly on both the 2a and 6c sites in the trigonal unit cell. The low-temperature orthorhombic phase (*Pbn21*) of $CaBaCo_4O_{7+\delta}$ is a result of the distorted trigonal phase, and it implies a strong buckling of the CoO_4 tetrahedra on the Kagome layer.[94]

The phase transition generally takes place around or below room temperature.[95] Unlike the room temperature *P31c* space group of $CaBaCo_3ZnO_{7+\delta}$,[54], $CaBaCo_{3.3}Ga_{0.7}O_{7+\delta}$ does not experience a reduction in phase transition temperature below room temperature. Sarkar et al. suggested that an R-site cation with a larger ionic radius

benefits the orthorhombic phase. However, they did not discuss the influence of M-site dopants on the phase transition temperature. Therefore, the structural difference between $CaBaCo_3ZnO_{7+\delta}$ and $CaBaCo_{3.3}Ga_{0.7}O_{7+\delta}$ might be related to the valence state and ionic radius of the M-site dopants but the detailed mechanism is not yet clear.

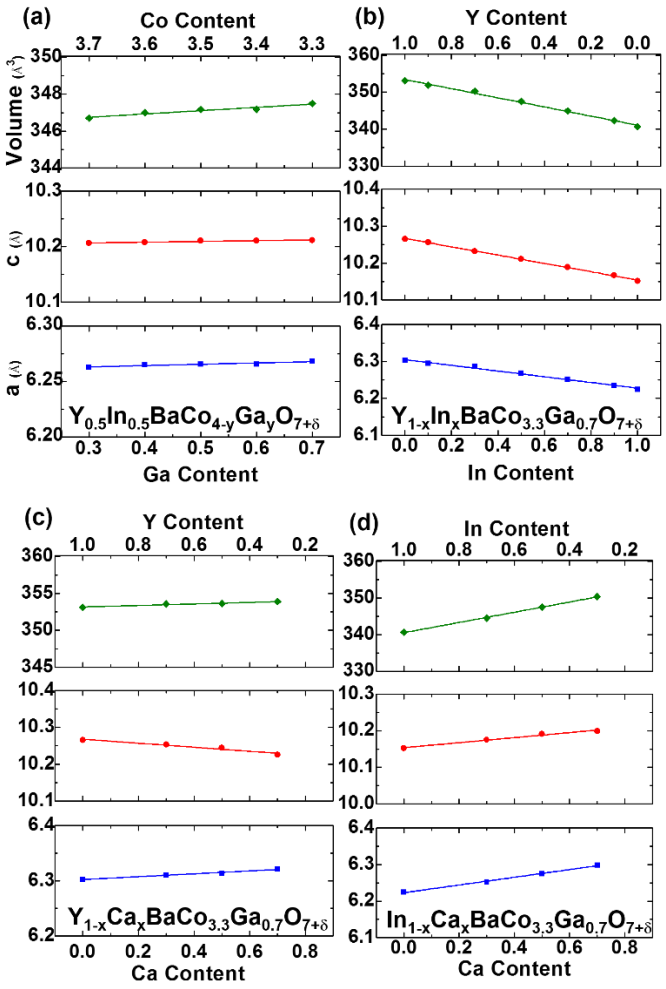

Figure 3.2 Lattice parameters of (a) $Y_{0.5}In_{0.5}BaCo_{4-y}Ga_yO_{7+\delta}$, (b) $Y_{1-x}In_xBaCo_{3.3}Ga_{0.7}O_{7+\delta}$, (c) $Y_{1-x}Ca_xBaCo_{3.3}Ga_{0.7}O_{7+\delta}$, and (d) $In_{1-x}Ca_xBaCo_{3.3}Ga_{0.7}O_{7+\delta}$. The cell parameters along with error bars determined by the Rietveld refinement are in Figures A1 – A5

Figure 3.2 illustrates the unit cell parameters of the $Y_{0.5}In_{0.5}BaCo_{4-y}Ga_yO_{7+\delta}$ (y = 0.3 – 0.8), $Y_{1-x}In_xBaCo_{3.3}Ga_{0.7}O_{7+\delta}$ (x = 0 – 1), $Y_{1-x}Ca_xBaCo_{3.3}Ga_{0.7}O_{7+\delta}$ (x = 0 – 0.7), and $In_{1-x}Ca_xBaCo_{3.3}Ga_{0.7}O_{7+\delta}$ (x = 0 – 0.7) samples. The exact values of the cell parameters along with the error bars determined by the Rietveld refinement[75] are given in Figures A1 – A5. The occupancies of oxygen at the 2a and 6c sites in the lattice are both 1.0 because all the materials have an oxygen content in excess of 7 in this study. The excess oxygen is commonly accepted to be located in the interstitial site with the samples treated at atmospheric pressures.[42,53,61] Therefore, the increase in oxygen content above the stoichiometric value of 7 was not considered in the refinement. The lattice constants and unit cell volumes of the $Y_{0.5}In_{0.5}BaCo_{4-y}Ga_yO_{7+\delta}$ series increase only slightly with increasing Ga content because the ionic radius of Ga^{3+} (0.47 Å)[96] is similar to that of of Co^{3+} in tetrahedral coordination. With the R-site dopants, the unit cell parameters consistently decrease with increasing In content in the Y-In and In-Ca co-doped materials due to the relatively small ionic radius of In^{3+} (0.62 Å) comparing to that of Y^{3+} (0.9 Å) and Ca^{2+} (1.0 Å). The unit cell volumes of the $Y_{1-x}In_xBaCo_{3.3}Ga_{0.7}O_{7+\delta}$ and $In_{1-x}Ca_xBaCo_{3.3}Ga_{0.7}O_{7+\delta}$ series have similar values since the ionic radii of Y^{3+} and Ca^{2+} are similar. However, a higher Ca content in the $Y_{1-x}Ca_xBaCo_{3.3}Ga_{0.7}O_{7+\delta}$ series leads to an increase in lattice parameter *a* and unit cell volume and a decrease in the lattice parameter *c*. In order to maintain charge neutrality, the Ca^{2+} substitution generates more Co^{3+} in the unit cell and further reduces the average Co-O bond length. The smaller CoO_4 tetrahedra on the triangular and Kagome layers lead to a smaller lattice parameter *c*. The larger effective ionic radius on the R-site has a stronger influence on the lattice parameter *a*, which is parallel to the layered plane. Combining the effects on the lattice parameters, the unit cell volume increases only slightly with Ca content.

3.3.2 Phase Stability

We aim to identify stable compositions with a lower Ga content by adjusting the R-site dopants to enhance the catalytic activity and OSC. The stable marks in Figure 3.1 indicate that no impurity peaks appeared in the XRD pattern after 120 h long-term tests at 600, 700, and 800 °C. Figure 3.3(a) – 3.3(d) show the XRD results of the materials with a single R-site dopant after the long-term tests. First, only $YBaCo_{3.2}Ga_{0.8}O_{7+\delta}$ in the $YBaCo_{4-y}Ga_yO_{7+\delta}$ (y = 0.6 – 0.8) series exhibits good stability, which is consistent with the TGA data of Rasanen *et al*.[56] Although the irreversible oxygen absorption peak of $YBaCo_{3.3}Ga_{0.7}O_{7+\delta}$ observed with TGA is at ~ 800 °C,[56] there are surprisingly no impurity peaks in the $YBaCo_{3.3}Ga_{0.7}O_{7+\delta}$ sample after testing at 800 °C. On the other hand, few $BaCoO_3$ impurity peaks are detected in the samples tested at 600 and 700 °C. Based on the long-term results, we suggest that Ga doping in $YBaCo_4O_{7+\delta}$ could reduce the temperature range of decomposition and improve the phase stability at 800 °C even with a lower amount of substitution. Second, Y was fully substituted with In or Ca to study the influence of R-site dopants on the phase stability with a reduced Ga content. Significant decomposition of $InBaCo_{3.3}Ga_{0.7}O_{7+\delta}$ takes place at 700 and 800 °C, and the products include Co_3O_4 and In_2O_3 with several unknown phases. However, the sample annealed at 600 °C remains stable without detectable impurities. On the other hand, instability of the $CaBaCo_{3.3}Ga_{0.7}O_{7+\delta}$ samples was found at all of the temperatures, and the decomposition becomes more severe than $YBaCo_{3.3}Ga_{0.7}O_{7+\delta}$ and $InBaCo_{3.3}Ga_{0.7}O_{7+\delta}$. The decomposition products mentioned above are consistent with the studies of $RBaCo_3ZnO_{7+\delta}$ (R = Y, In, and Ca)[51], and it indicates the driving force for phase decomposition is the instability of Co^{3+} in the tetrahedral sites and its preference for octahedral coordination.

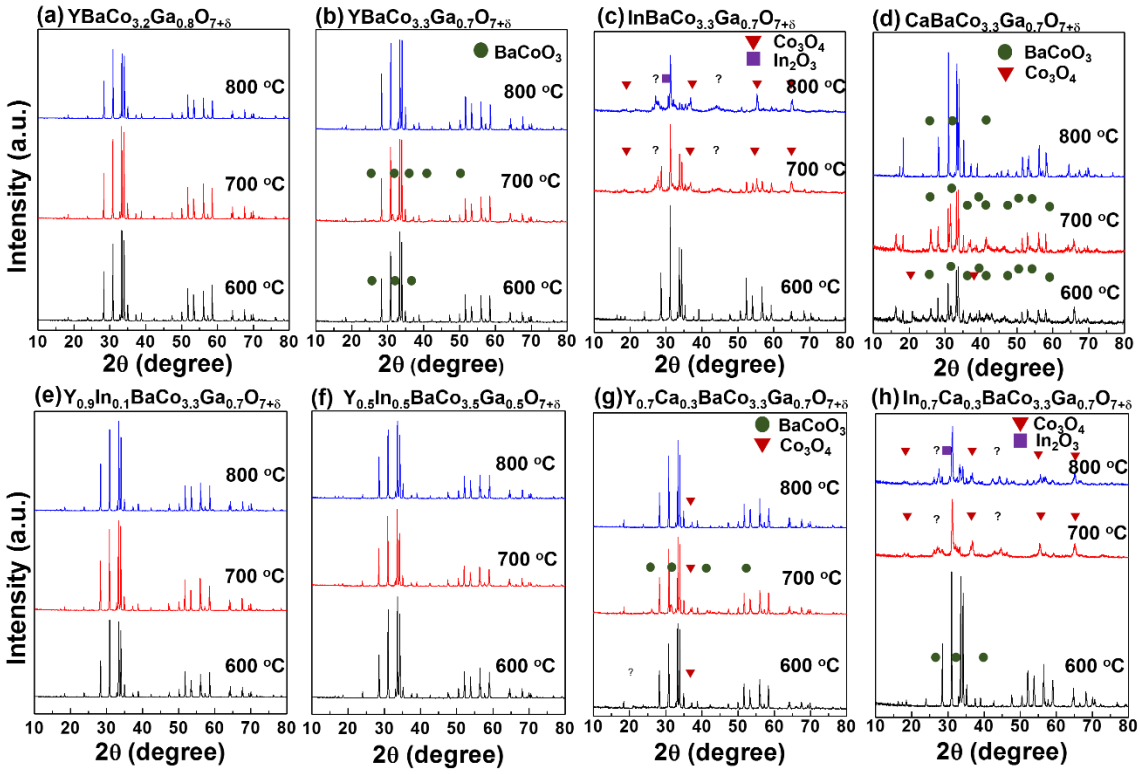

Figure 3.3 XRD patterns of (a) $YBaCo_{3.2}Ga_{0.8}O_{7+\delta}$, (b) $YBaCo_{3.3}Ga_{0.7}O_{7+\delta}$, (c) $InBaCo_{3.3}Ga_{0.7}O_{7+\delta}$, (d) $CaBaCo_{3.3}Ga_{0.7}O_{7+\delta}$, (e) $Y_{0.9}In_{0.1}BaCo_{3.3}Ga_{0.7}O_{7+\delta}$, (f) $Y_{0.5}In_{0.5}BaCo_{3.5}Ga_{0.5}O_{7+\delta}$, (g) $Y_{0.7}Ca_{0.3}BaCo_{3.3}Ga_{0.7}O_{7+\delta}$, and (h) $In_{0.7}Ca_{0.3}BaCo_{3.3}Ga_{0.7}O_{7+\delta}$ after the 120 h stability tests at 600, 700, and 800 °C.

The Y-In, Y-Ca, and In-Ca co-doped samples were also studied, and Figure 3.3(e) – 3.3(h) compare the XRD results of selected materials after the long-term tests. All $Y_{1-x}In_xBaCo_{3.3}Ga_{0.7}O_{7+\delta}$ ($x = 0.1 – 0.9$) materials remain stable. The results reveal that a partial substitution of In mitigates the phase decomposition, and the synergistic effect of In and Y could maximize the stability at a certain Ga content. Thus, the $Y_{0.5}In_{0.5}BaCo_{4-y}Ga_yO_{7+\delta}$ ($y = 0.3 – 0.8$) samples were analyzed to identify the minimum Ga content necessary for achieving a complete stabilization. These XRD results are shown in Figure 3.4. While decreasing the Ga content, $Y_{0.5}In_{0.5}BaCo_{3.5}Ga_{0.5}O_{7+\delta}$ still remains single phase at all tested

temperatures, but a tiny amount of impurity appears in the $Y_{0.5}In_{0.5}BaCo_{3.6}Ga_{0.4}O_{7+\delta}$ sample at 700 and 800 °C. Furthermore, the slight decomposition of $Y_{0.7}In_{0.3}BaCo_{3.5}Ga_{0.5}O_{7+\delta}$ and $Y_{0.3}In_{0.7}BaCo_{3.5}Ga_{0.5}O_{7+\delta}$ at 700 °C also provides evidence for the optimized synergistic effect of an equal ratio of Y and In.

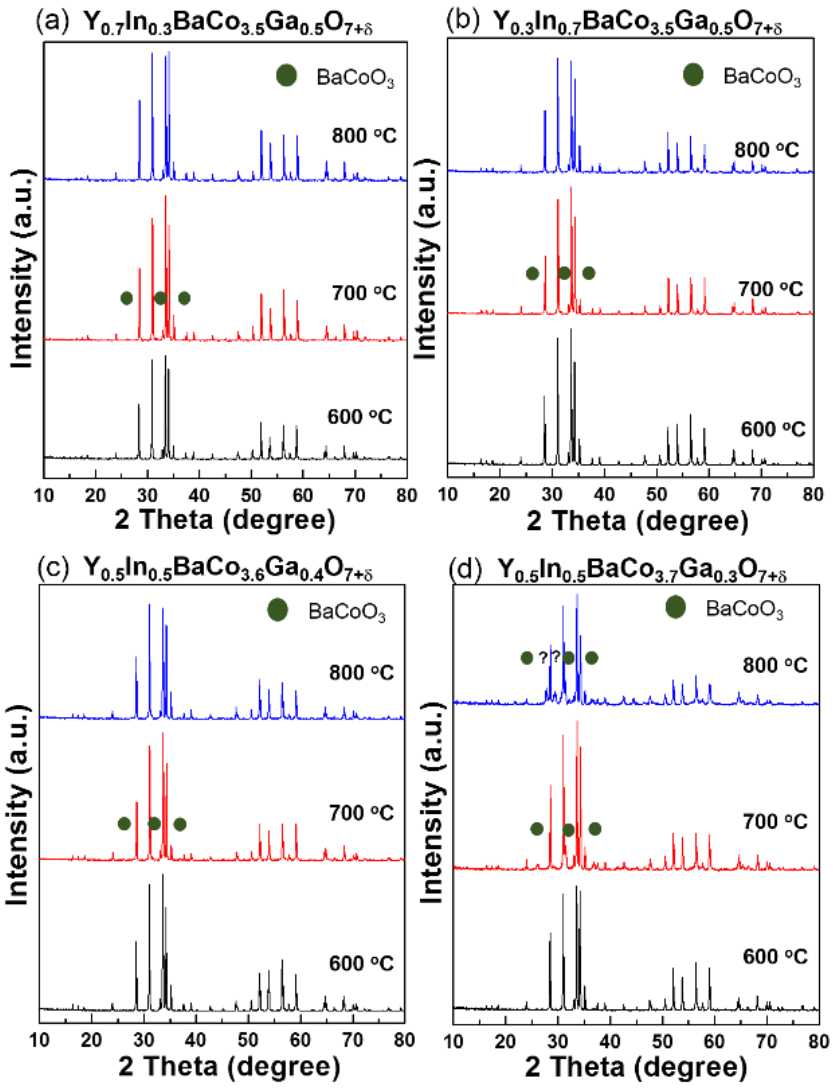

Figure 3.4 XRD patterns of (a) $Y_{0.7}In_{0.3}BaCo_{3.5}Ga_{0.5}O_{7+\delta}$, (b) $Y_{0.3}In_{0.7}BaCo_{3.5}Ga_{0.5}O_{7+\delta}$, (c) $Y_{0.5}In_{0.5}BaCo_{3.6}Ga_{0.4}O_{7+\delta}$, and (d) $Y_{0.5}In_{0.5}BaCo_{3.7}Ga_{0.3}O_{7+\delta}$ after the 120-hour stability tests at 600, 700, and 800 °C.

Finally, the $Y_{1-x}Ca_xBaCo_{3.3}Ga_{0.7}O_{7+\delta}$ and $In_{1-x}Ca_xBaCo_{3.3}Ga_{0.7}O_{7+\delta}$ samples were tested to reveal the stabilization effect of Ca. Unfortunately, none of the Ca-substituted materials passed the long-term stability test because of severe decomposition. $Y_{0.7}Ca_{0.3}BaCo_{3.3}Ga_{0.7}O_{7+\delta}$ displays a lower amount of decomposition than $In_{0.7}Ca_{0.3}BaCo_{3.3}Ga_{0.7}O_{7+\delta}$ in Figure 3.3(g) and 3.3(h). It suggests that Ca hinders the phase stability regardless of the other dopant on the R site, and there is no synergistic effect of In and Ca co-dopants. Recall that the lattice parameters of $Y_{1-x}In_xBaCo_{3.3}Ga_{0.7}O_{7+\delta}$ and $In_{1-x}Ca_xBaCo_{3.3}Ga_{0.7}O_{7+\delta}$ are in the same range, but their long-term stability results are clearly different. As a result, the lattice parameters and unit cell volume have no direct relationship to the high-temperature phase stability in this study.

3.3.3 Oxygen-storage Capability and Thermal Behavior

Figure 3.5 illustrates the thermal behaviors of the (Y, In, Ca)$BaCo_{3.3}Ga_{0.7}O_{7+\delta}$ samples measured with TGA with an air flow. The starting materials were annealed at 500 °C in Ar for 6 h in order to minimize the oxygen content. The precise oxygen contents were determined by iodometric titration at room temperature, and the OSC below 400 °C was calculated by the maximum amount of absorbed oxygen (maximum non-stoichiometric value of oxygen, δ). The OSC of $Y_{1-x}In_xBaCo_{3.3}Ga_{0.7}O_{7+\delta}$ is suppressed with increasing In content. The highest and lowest OSC values are 0.4 and 0.05, respectively, for $YBaCo_{3.3}Ga_{0.7}O_{7+\delta}$ and $InBaCo_{3.3}Ga_{0.7}O_{7+\delta.}$ The OSC of $Y_{0.9}In_{0.1}BaCo_{3.3}Ga_{0.7}O_{7+\delta}$ ($\delta = 0.37$) is the highest value among the high-temperature-stable $Y_{1-x}In_xBaCo_{3.3}Ga_{0.7}O_{7+\delta}$ materials. In the $Y_{0.5}In_{0.5}BaCo_{4-y}Ga_yO_{7+\delta}$ series, the OSC increases with decreasing Ga content. The OSC of $Y_{0.5}In_{0.5}BaCo_{3.5}Ga_{0.5}O_{7+\delta}$ was 0.3,

which is slightly lower than that of $Y_{0.9}In_{0.1}BaCo_{3.3}Ga_{0.7}O_{7+\delta}$. The balance between In and Ga content is critical to achieve phase stability and maintain the OSC at the same time.

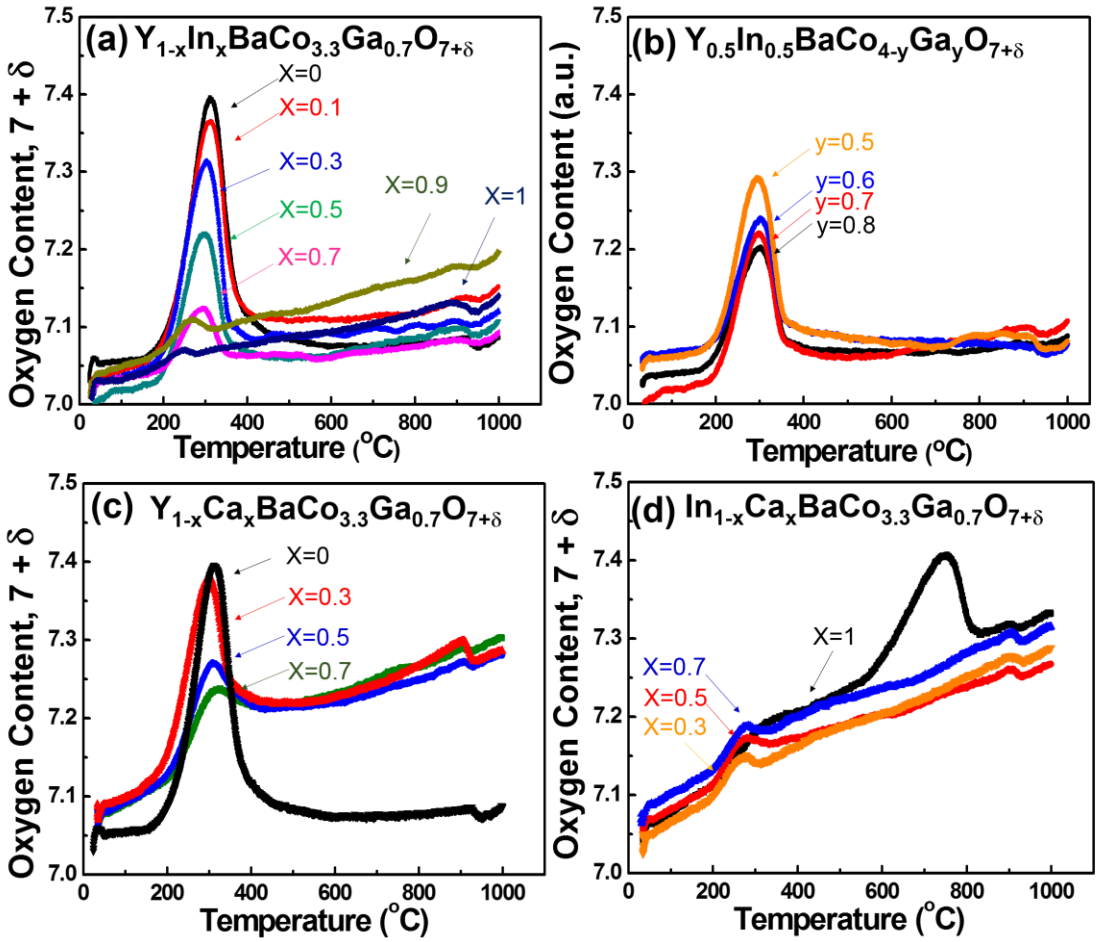

Figure 3.5 Representative TGA plots of the (a) $Y_{1-x}In_xBaCo_{3.3}Ga_{0.7}O_{7+\delta}$, (b) $Y_{0.5}In_{0.5}BaCo_{4-y}Ga_yO_{7+\delta}$, (c) $Y_{1-x}Ca_xBaCo_{3.3}Ga_{0.7}O_{7+\delta}$, and (d) $In_{1-x}Ca_xBaCo_{3.3}Ga_{0.7}O_{7+\delta}$ samples in air with a heating rate of 1 °C min^{-1}. The starting materials were annealed at 500 °C in Ar for 6 h before the TG measurement.

In Figure 3.5(a), the thermal behavior of $Y_{1-x}In_xBaCo_{3.3}Ga_{0.7}O_{7+\delta}$ also provides evidence for the synergistic effect on phase stabilization with the proper Y and In contents. The potential phase decomposition of $Y_{0.1}In_{0.9}BaCo_{3.3}Ga_{0.7}O_{7+\delta}$ and $InBaCo_{3.3}Ga_{0.7}O_{7+\delta}$ is led by a continuous oxygen absorption above 300 °C. The difference in their oxygen content at high temperature results from the difference in their OSC even though the irreversible oxygen absorption rate is similar. The rest of the materials (x = 0.1 – 0.7) maintain relatively small variations in the oxygen content above 400 °C.

The incomplete desorption and continuous oxygen absorption take place in all Ca-containing materials above 350 °C. Figure 3.5(c) indicates that less than half of the absorbed oxygen is released from the $Y_{1-x}Ca_xBaCo_{3.3}Ga_{0.7}O_{7+\delta}$ samples at 400 °C. The continuous oxygen absorption starts at about 500 °C and continues for the rest of the heating process. The thermal behavior in $In_{1-x}Ca_xBaCo_{3.3}Ga_{0.7}O_{7+\delta}$ is similar with the characteristics in $Y_{1-x}Ca_xBaCo_{3.3}Ga_{0.7}O_{7+\delta}$. Although Ca substitution increases the unit cell volume, the oxygen absorption of the $In_{1-x}Ca_xBaCo_{3.3}Ga_{0.7}O_{7+\delta}$ is still limited. In short, the TGA results reveal that Ca doping dramatically deteriorates the oxygen-storage ability and phase stability even with the assistance of Y or In substitutions.

The oxygen absorption above 600 °C is generally considered as evidence of irreversible phase decomposition, but we found the kinetics of phase decomposition cannot be explained only by TGA. For example, $Y_{0.1}In_{0.9}BaCo_{3.3}Ga_{0.7}O_{7+\delta}$ and $InBaCo_{3.3}Ga_{0.7}O_{7+\delta}$ show a small amount of oxygen absorption above 400 °C in Figure 3.5(a). However, only the $InBaCo_{3.3}Ga_{0.7}O_{7+\delta}$ sample decomposes in the long-term tests at 700 and 800 °C in Figure 3.3(c). Additionally, the $Y_{1-x}Ca_xBaCo_{3.3}Ga_{0.7}O_{7+\delta}$ and $Y_{1-x}Ca_xBaCo_{3.3}Ga_{0.7}O_{7+\delta}$ series exhibit similar continuous oxygen absorption behavior in Figure 3.5(c) and 3.5(d), but the degree of decomposition is different in the long-term tests. For instance, small impurity peaks are found in $Y_{0.7}Ca_{0.3}BaCo_{3.3}Ga_{0.7}O_{7+\delta}$ at 600 – 800 °C

in Figure 3.3(g), but $In_{0.7}Ca_{0.3}BaCo_{3.3}Ga_{0.7}O_{7+\delta}$ experiences severe decomposition at 700 and 800 °C in Figure 3.3(h). Consequently, the TGA data provides the potential temperature windows of phase decomposition, and the long-term stability test further identifies the kinetic aspect of phase instability at different temperatures. With the combination of TGA and long-term tests, the whole picture of phase decomposition can be described more comprehensively.

3.3.4 Thermal Expansion Properties and Electrical Conductivity

The characteristics of the $Y_{1-x}In_xBaCo_{3.3}Ga_{0.7}O_{7+\delta}$ and $Y_{0.5}In_{0.5}BaCo_{4-y}Ga_yO_{7+\delta}$ series were investigated as candidates for cathode materials for SOFCs due to their high-temperature stability. Figure 3.6 illustrates the temperature dependence of their thermal expansion behavior. The TECs of the studied materials are all in the range of 7.0 – 9.2 × 10^{-6} K^{-1} at 200 – 900 °C. The TEC exhibits a small increase with increasing In content, and an opposite trend occurs with Ga substitution. In addition, the Ga-doped (Y, In)$BaCo_4O_{7+\delta}$ has TECs similar to Zn-doped (Y, In)$BaCo_4O_{7+\delta}$ (9.0 – 11.0× 10^{-6} K^{-1}).[51,55] The relatively low TEC values are a result of Co^{2+} / Co^{3+} ions in the tetrahedral sites, which do not encounter spin-state transitions in the $RBaCo_4O_7$-based materials. On the contrary, the spin-state transition of Co^{3+} in perovskite oxides makes the TECs too high to match with the TECs of common electrolyte materials (10 – 12.5 × 10^{-6} K^{-1})[22,85] at the SOFC operation temperature. For example, the TECs of $Ba_{0.5}Sr_{0.5}Co_{0.8}Fe_{0.2}O_{3-\delta}$[97] and $NdBa_{0.5}Sr_{0.5}Co_2O_{5+\delta}$[98] are, respectively, 21.4 × 10^{-6} and 25.4 × 10^{-6} K^{-1} at 800 °C. As a result, the series of $Y_{1-x}In_xBaCo_{3.3}Ga_{0.7}O_{7+\delta}$ and $Y_{0.5}In_{0.5}BaCo_{4-y}Ga_yO_{7+\delta}$ materials are able to mitigate the thermal stress and high-temperature mechanical aging in practical applications due to their relatively low TECs.

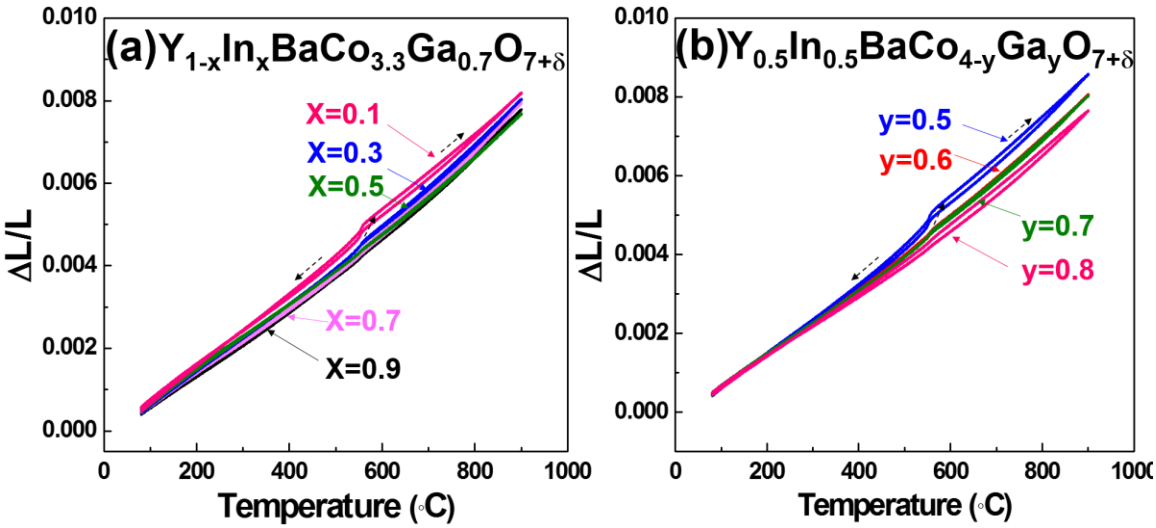

Figure 3.6 Thermal expansion curves of (a) $Y_{1-x}In_xBaCo_{3.3}Ga_{0.7}O_{7+\delta}$ and (b) $Y_{0.5}In_{0.5}BaCo_{4-y}Ga_{0y}O_{7+\delta}$ in air with a heating and cooling rate of 3 °C min^{-1}.

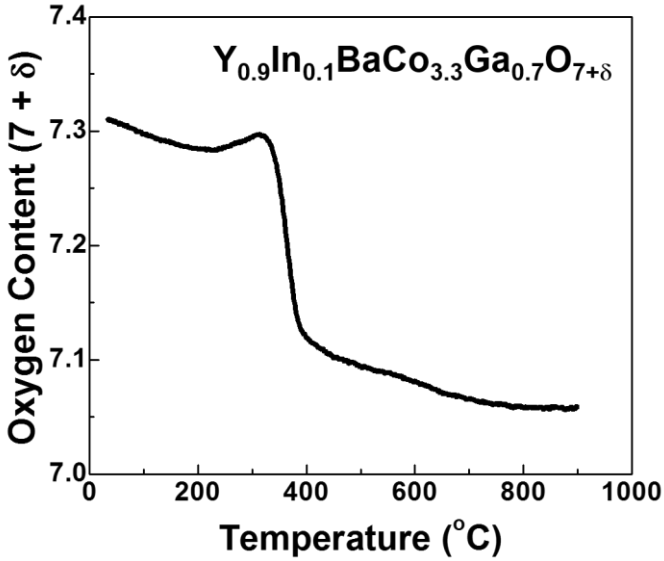

Figure 3.7 TGA plot of the $Y_{0.9}In_{0.1}BaCo_{3.3}Ga_{0.7}O_{7+\delta}$ sample conducted in air at a heating rate of 3 °C min^{-1}. In order to simulate the oxygen content of a bulk sample used in the thermal expansion measurement, the pellet sample was cooled from 1200 °C in air at a cooling rate of 2 °C min^{-1} and crushed into powders before the TGA measurement.

A small abrupt expansion in $Y_{0.9}In_{0.1}BaCo_{3.3}Ga_{0.7}O_{7+\delta}$ and $Y_{0.5}In_{0.5}BaCo_{3.5}Ga_{0.5}O_{7+\delta}$ occurred at ~ 550 °C during the heating process as shown in Figure 3.6. In order to reveal the reason behind this phenomenon, the thermal behavior of $Y_{0.9}In_{0.1}BaCo_{3.3}Ga_{0.7}O_{7+\delta}$, which had the same preparation process as the bulk sample for the thermal expansion measurement, was further investigated. Figure 3.7 shows the TGA plot of the $Y_{0.9}In_{0.1}BaCo_{3.3}Ga_{0.7}O_{7+\delta}$ sample, which was prepared by cooling from 1200 ^oC in air at a rate of 2 $^oC\ min^{-1}$. The initial room-temperature oxygen content was determined to be 7.31 by iodometric titration, which is much higher than the value of 7.03 for the sample annealed in Ar as shown in Figure 3.5(a). The excess oxygen is caused by the kinetically sluggish desorption process below 300 ^oC while cooling the sample during synthesis. In Figure 3.7, the slow oxygen loss from 30 to 300 ^oC also verifies the sluggish desorption process discussed above. Therefore, the small change in the oxygen content below 300 ^oC explains the smooth change in the thermal expansion at the temperature of reversible oxygen absorption (~ 300 ^oC).

Even though the oxygen desorption temperature starts from about 400 ^oC in Figure 3.7, the thermal expansion changes smoothly at this temperature. It might be due to the differences between the powder sample used for TGA and a highly-dense pellet sample used for thermal expansion. The oxygen release rate of the dense bulk sample might be limited by the oxygen desorption rate. According to our previous work[51], the oxygen penetration flux of $YBaCo_3ZnO_7$ is only $3 - 4 \times 10^{-10}$ mol cm^{-2} s^{-1} at 700 ^oC. The $Y_{0.9}In_{0.1}BaCo_{3.3}Ga_{0.7}O_{7+\delta}$ sample belonging to the same family could have the same order of oxygen penetration rate, and it is not surprising to have a much slower rate below 600 ^oC. Thus, the discontinuity in the thermal expansion at about 550 ^oC might be a result of the delayed oxygen release from the highly dense bulk sample. Moreover, the abrupt

change in the thermal expansion is eliminated in the materials with the smaller OSC value as shown in Figure 3.6 when In or Ga content increases. This is due to the smaller amount of oxygen loss from the material during heating from 350 to 600 ºC.

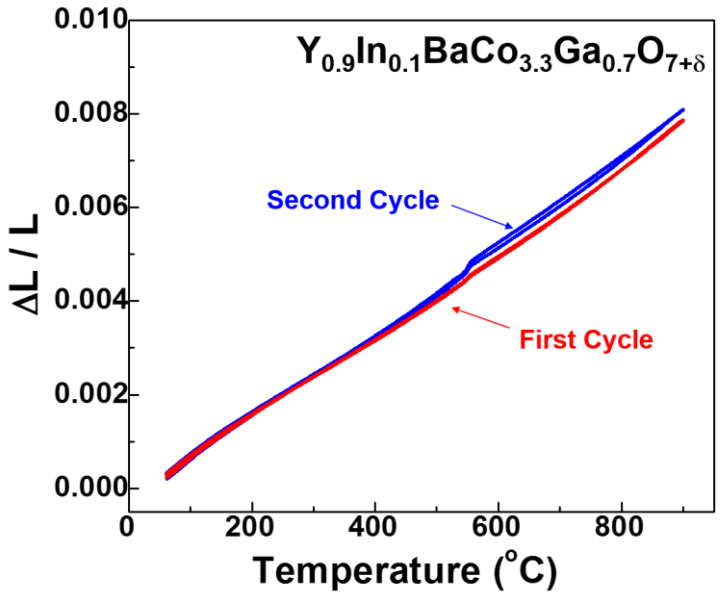

Figure 3.8 Thermal expansion curve of $Y_{0.9}In_{0.1}BaCo_{3.3}Ga_{0.7}O_{7+\delta}$ with two cycles of heating and cooling processes at a rate of 3 °C min^{-1}. The bar sample was annealed in Ar at 500 °C for 24 h before the measurement of thermal expansion behaviors.

In order to verify the above hypothesis further, the thermal expansion of the $Y_{0.9}In_{0.1}BaCo_{3.3}Ga_{0.7}O_{7+\delta}$ bulk sample, which was annealed in Ar at 500 °C for 24 h, is illustrated in Figure 3.8. The first cycle of the heating and cooling process has no obvious discontinuity because of the low initial oxygen content at room temperature and less oxygen loss above 350 °C. However, the second heating process exhibits the discontinuity when the initial oxygen content becomes higher due to the first cooling process in air. The

result indicates the direct relationship between the thermal expansion behavior and the variation in the oxygen content.

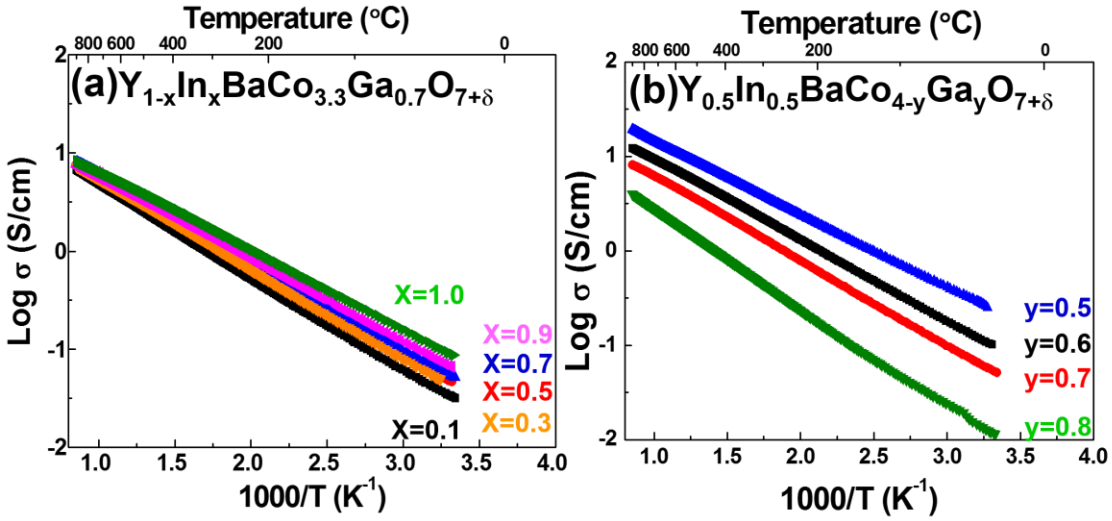

Figure 3.9 Electrical conductivity of (a) $Y_{1-x}In_xBaCo_{3.3}Ga_{0.7}O_{7+\delta}$ and (b) $Y_{0.5}In_{0.5}BaCo_{4-y}Ga_{0y}O_{7+\delta}$ in air with a heating rate of 3 °C min^{-1}.

Figure 3.9 compares the electrical conductivity of the $Y_{1-x}In_xBaCo_{3.3}Ga_{0.7}O_{7+\delta}$ and $Y_{0.5}In_{0.5}BaCo_{4-y}Ga_yO_{7+\delta}$ series in the temperature range of 100 - 900 °C. All samples show a rise in electrical conductivity with temperature, indicating a thermally activated polaron behavior.[51] In the $Y_{1-x}In_xBaCo_{3.3}Ga_{0.7}O_{7+\delta}$ samples, the electrical conductivity increases slightly and the activation energy decreases with increasing In content. Therefore, the $Y_{1-x}In_xBaCo_{3.3}Ga_{0.7}O_{7+\delta}$ materials have similar conductivity above 400 °C. Meanwhile, the conductivity of the $Y_{1-x}In_xBaCo_{3.3}Ga_{0.7}O_{7+\delta}$ samples decrease with increasing Ga content. The reason for the reduction in conductivity with Ga substitution is that the fully filled d orbital of the Ga^{3+} ion impedes the electron hopping pathway. Nonetheless, all materials

display adequate electrical conductivity (3 – 20 S cm^{-1}) when the temperature exceeds 500 °C.

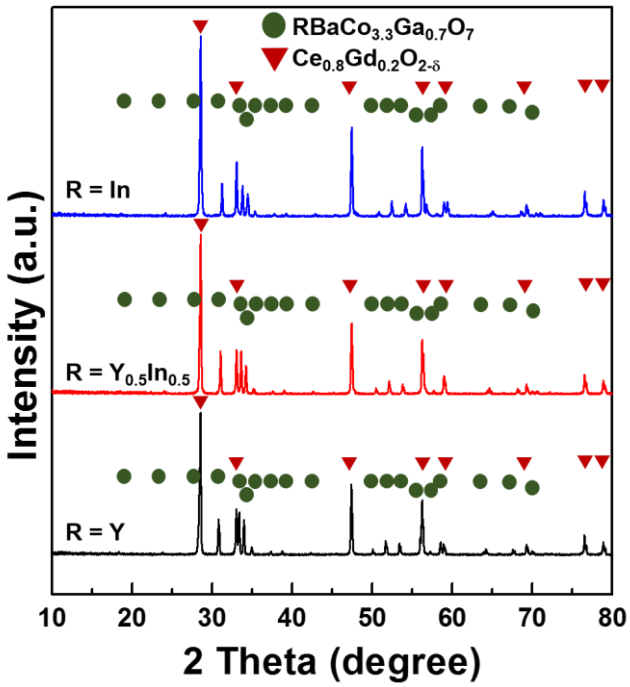

Figure 3.10 XRD patterns of $RBaCo_{3.3}Ga_{0.7}O_{7+\delta}$ (R = Y, $Y_{0.5}In_{0.5}$, and In) – GDC with a 50 : 50 wt.% after heating at 1100 °C for 3 h.

3.3.5 Chemical Compatibility and Electrochemical Properties

The chemical compatibility between the (Y, In)$Ba(Co, Ga)_4O_{7+\delta}$ materials and the GDC electrolyte was examined by annealing the mixtures at 1100 °C for 3 h, and a cooling rate of 5 °C min^{-1} was applied to avoid interference from self-decomposition of the (Y, In)$Ba(Co, Ga)_4O_{7+\delta}$ materials. Figure 3.10 shows the XRD results of $YBaCo_{3.3}Ga_{0.7}O_{7+\delta}$, $Y_{0.5}In_{0.5}BaCo_{3.3}Ga_{0.7}O_{7+\delta}$, and $InBaCo_{3.3}Ga_{0.7}O_{7+\delta}$ with GDC after the heat treatment, and no impurity peaks were identified in all of the mixtures. Although Kim *et al.*[53] reported

that small amounts of side-reaction products were found after the mixture of $InBaCo_3ZnO_{7+\delta}$ and GDC was heated at 1000 °C, our results indicate that $InBaCo_{3.3}Ga_{0.7}O_{7+\delta}$ is stable in contact with GDC. The difference might originate from the higher phase stability imparted by Ga-substitution.

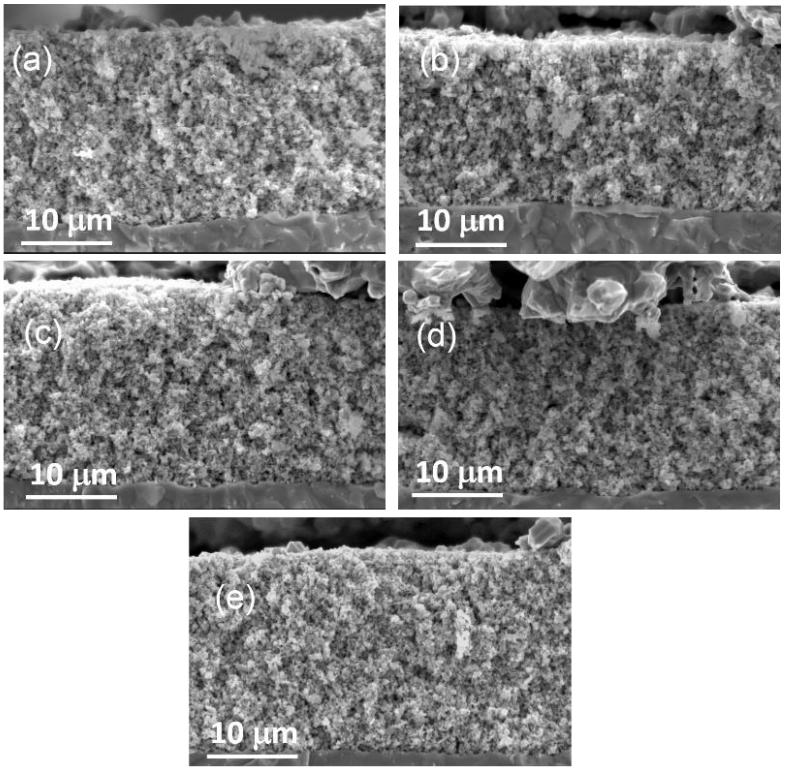

Figure 3.11 Cross-section SEM images of the tested symmetrical cells with (a) $Y_{0.9}In_{0.1}BaCo_{3.3}Ga_{0.7}O_{7+\delta}$ – GDC, (b) $Y_{0.7}In_{0.3}BaCo_{3.3}Ga_{0.7}O_{7+\delta}$ – GDC, (c) $Y_{0.5}In_{0.5}BaCo_{3.3}Ga_{0.7}O_{7+\delta}$ – GDC, (d) $Y_{0.3}In_{0.7}BaCo_{3.3}Ga_{0.7}O_{7+\delta}$ – GDC, and (e) $Y_{0.1}In_{0.9}BaCo_{3.3}Ga_{0.7}O_{7+\delta}$ – GDC composite cathodes.

The electrocatalytic activity for the ORR was evaluated by symmetric cells in air. According to previous research[51], the smaller polarization resistance (R_p) of the symmetric cell is achieved with a composite material containing equal masses of active material and

GDC electrolyte. The composite cathode provides an extended three-phase boundary as the active sites for the oxygen reduction reaction, and the oxygen ionic conductivity is improved by the addition of GDC. Furthermore, the composite material has better compatibility of TECs with the GDC electrolyte. The cross-section SEM images of the tested symmetric cells are shown in Figure 3.11. The microstructure of the composite cathodes, whose thickness is about 20 μm, contains particles of similar size and porosity. Figure 3.12 illustrates the cathodic polarization resistance (Rp) of the composite materials at various temperatures. The area-normalized R_p, also known as area specific polarization (ASR), can be calculated by the difference between the high-frequency and low-frequency intercepts at the real axis in the EIS plots. Similar to the Zn-substituted (Y, In)$BaCo_4O_{7+\delta}$ samples, the R_p increases with amount of In or Ga at a specific temperature. Among all the tested materials, the $Y_{0.9}In_{0.1}BaCo_{3.3}Ga_{0.7}O_{7+\delta}$ – GDC composite cathode exhibits the lowest ASR values of 0.24, 0.07, and 0.03 ohm cm^2 at, respectively, 600, 700, and 800 °C.

Meanwhile, the ASR values of the $Y_{0.5}In_{0.5}BaCo_{3.5}Ga_{0.5}O_{7+\delta}$ – GDC composite cathode are 0.30, 0.11, and 0.035 ohm cm^2 at, respectively, 600, 700, and 800 °C. Although 50 % of In substitution reduces the Ga content to 0.5 and offers high-temperature phase stability, the higher In amount in $Y_{0.5}In_{0.5}BaCo_{3.5}Ga_{0.5}O_{7+\delta}$ makes the R_p higher than that of $Y_{0.9}In_{0.1}BaCo_{3.3}Ga_{0.7}O_{7+\delta}$. The composition $Y_{0.9}In_{0.1}BaCo_{3.3}Ga_{0.7}O_{7+\delta}$ reaches an optimized balance between the Ga and In contents for maintaining high-temperature phase stability and achieving higher electrochemical performance. The ASR values of the $Y_{0.7}In_{0.3}BaCo_{3.3}Ga_{0.7}O_{7+\delta}$ cathode are close to those of $Y_{0.5}In_{0.5}BaCo_{3.5}Ga_{0.5}O_{7+\delta,}$ and this might be due to the relatively thinner electrode layer (18 μm) of the $Y_{0.7}In_{0.3}BaCo_{3.3}Ga_{0.7}O_{7+\delta}$ cathode in comparison to the other 20-μm-thick layers as shown in Figure 3.11. In spite of the ASR deviation among the $Y_{0.7}In_{0.3}BaCo_{3.3}Ga_{0.7}O_{7+\delta}$ cathodes (x = 0.1 to 0.5), the effect of increasing ASR is clearly observed with higher In content.

Compared to the activation energy of the Zn-substituted (Y, In)$BaCo_4O_{7+\delta}$ composite samples (~ 1.0 eV)[51,53–55,59], the (Y, In)Ba(Co, Ga)$_4O_{7+\delta}$ composite cathode materials have slightly lower activation energies in the range of 0.87 to 0.95 eV. To the best of our knowledge, the $Y_{0.9}In_{0.1}BaCo_{3.3}Ga_{0.7}O_{7+\delta}$ – GDC composite cathode has the lowest ASR among all the $YBaCo_4O_{7+\delta}$ –based materials investigated so far.

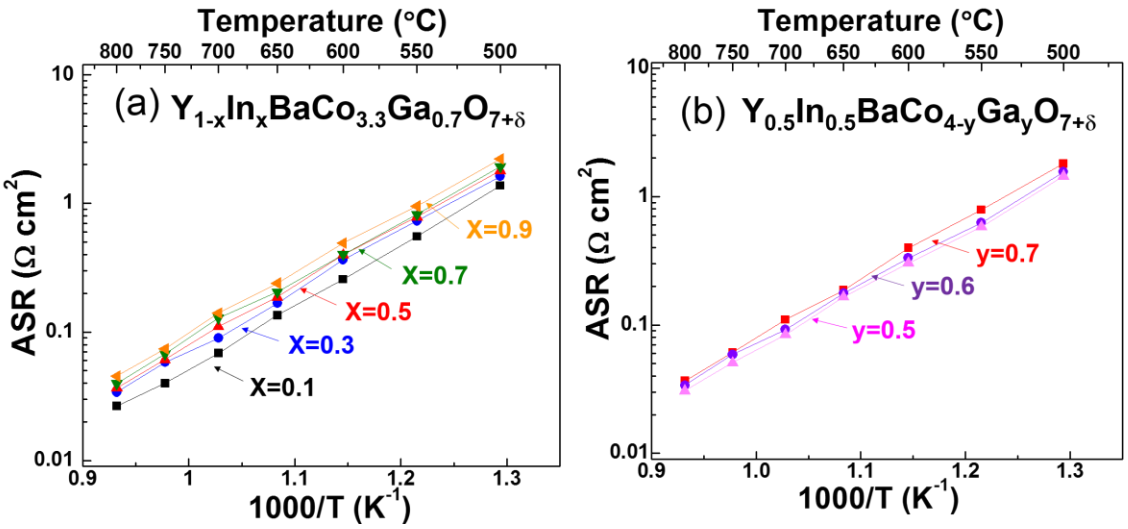

Figure 3.12 Temperature dependence of the polarization resistance of (a) $Y_{1-x}In_xBaCo_{3.3}Ga_{0.7}O_{7+\delta}$ – GDC and (b) $Y_{0.5}In_{0.5}BaCo_{4-y}Ga_yO_{7+\delta}$ – GDC composite cathodes at 500 – 800 °C.

In order to verify that the ASRs of the $Y_{0.9}In_{0.1}BaCo_{3.3}Ga_{0.7}O_{7+\delta}$ – GDC composite cathode are not affected by the Ag migration, the element distributions near the electrode-electrolyte interface of the tested symmetric cell were determined with energy dispersive X-ray spectroscopy (EDS). In Figure 3.13, the interface is clearly depicted by the selected elemental distributions of Co and Ce, and there is no obvious signal on the EDS mapping of Ag. Additionally, no distinguishable peak of silver $L_{\alpha 1}$ energy at 2.95 keV is observed

in comparison to the background intensity in the EDS spectrum in Figure 3.13 (e). In short, the silver content is lower than the EDS detection limit and the EIS results are not affected by Ag migration.

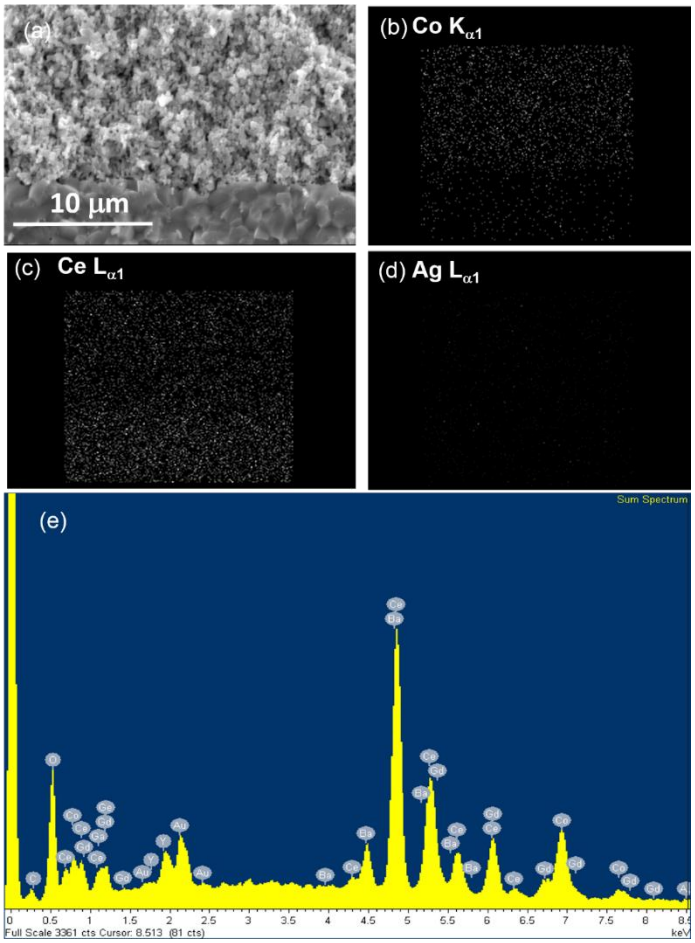

Figure 3.13 (a) Cross-section SEM image showing the electrode-electrolyte interface of the tested symmetrical cell with the $Y_{0.9}In_{0.1}BaCo_{3.3}Ga_{0.7}O_{7+\delta}$ – GDC composite cathode; EDS mapping result of the (b) Co distribution, (c) Ce distribution, and (d) Ag distribution and (e) the EDS spectrum of the mapping area.

3.3.6 Single-cell Performance

Among all the high-temperature stable materials in this study, the $Y_{0.9}In_{0.1}BaCo_{3.3}Ga_{0.7}O_{7+\delta}$ – GDC composite cathode demonstrates the lowest cathodic polarization resistance, and its fuel cell performance was evaluated by an anode-supported single cell at 600 – 700 °C. Figure 3.14 displays the cross-sectional microstructure of the anode-supported single cell with the $Y_{0.9}In_{0.1}BaCo_{3.3}Ga_{0.7}O_{7+\delta}$ – GDC composite cathode on the top part. The bottom part in Figure 3.14(a) is the porous substrate of the NiO – GDC composite anode, and the middle layer of the sandwich structure is the dense GDC electrolyte, which separates the anode and cathode layers. The thickness of the GDC electrolyte and the composite cathode layer is, respectively, about 20 μm and 35 μm. Figure 3.14(b) shows the higher magnification of the SEM image near the interface of the electrolyte and cathode. The cathode is composed of particles homogeneous in size and exhibits uniform porosity.

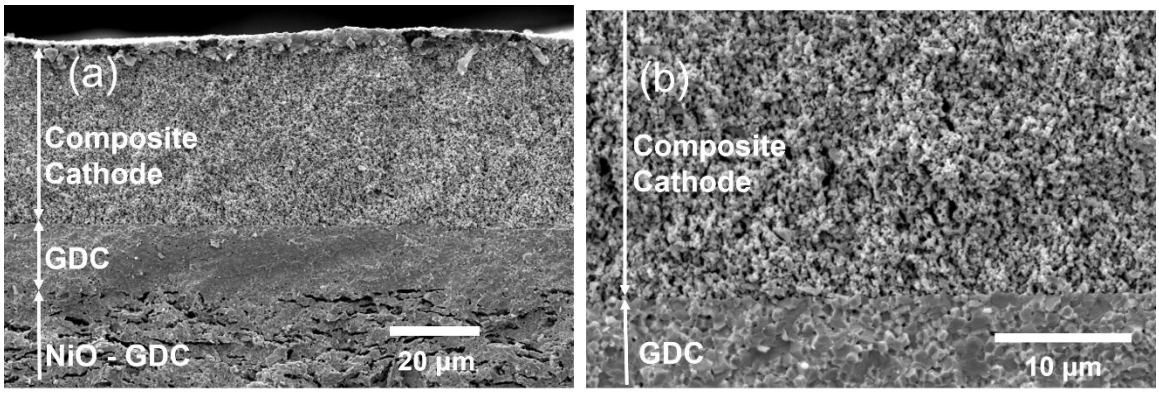

Figure 3.14 SEM images showing the cross section of (a) the anode-supported single cell with the $Y_{0.9}In_{0.1}BaCo_{3.3}Ga_{0.7}O_{7+\delta}$ – GDC composite cathode and (b) the interface between the $Y_{0.9}In_{0.1}BaCo_{3.3}Ga_{0.7}O_{7+\delta}$ – GDC composite cathode and GDC electrolyte.

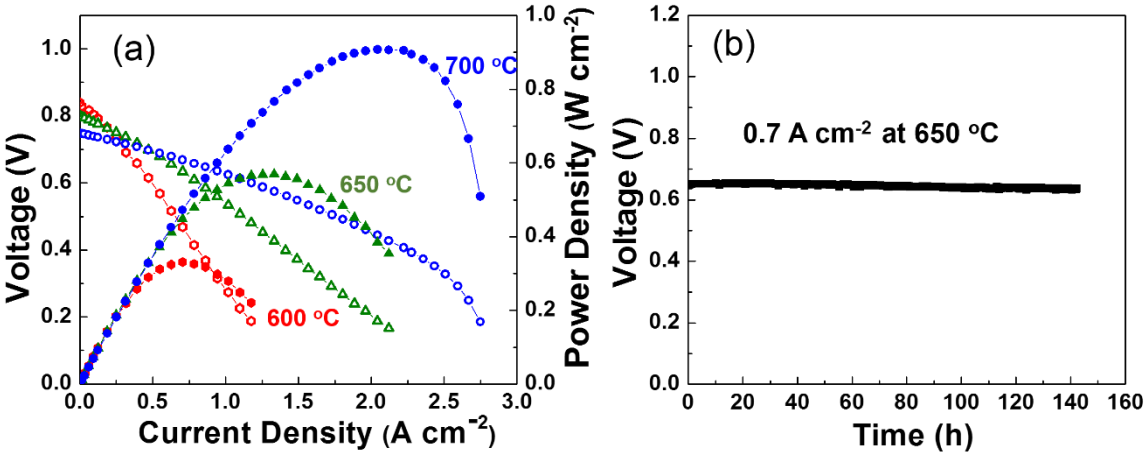

Figure 3.15 (a) Electrochemical performance and (b) long-term performance of the anode-supported single cell with the $Y_{0.9}In_{0.1}BaCo_{3.3}Ga_{0.7}O_{7+\delta}$ – GDC composite cathode.

In Figure 3.15, the electrochemical performance of the anode-supported single cell is shown. The open-circuit voltage of the single cell is only 0.84, 0.80, and 0.75 V, respectively, at 600, 650, and 700 °C. These values are much lower than the theoretical voltage calculated by the Nernst equation because of the increasing electronic conductivity of the GDC electrolyte due to the Ce^{4+} reduction at the higher operating temperatures. Nonetheless, the maximum power density reaches 0.33, 0.56, and 0.91 W cm^{-2}, respectively, at 600, 650, and 700 °C. With the benefits of low cathodic polarization resistance and the thin GDC electrolyte layer, the single-cell performance of the $Y_{0.9}In_{0.1}BaCo_{3.3}Ga_{0.7}O_{7+\delta}$ – GDC composite cathode is the highest among the other single-cell performances of the $YBaCo_4O_{7+\delta}$ –based materials reported previously in the literature. In order to evaluate the long-term performance, the single cell was tested with a constant current density of 0.7 A cm^{-2} at 650 °C in Figure 3.15(b). After operating for 140 h, the voltage remains stable without a significant degradation. The high stability of the single

cell performance tests points to the potential of the $Y_{0.9}In_{0.1}BaCo_{3.3}Ga_{0.7}O_{7+\delta}$ – GDC composite material as a cathode for IT-SOFCs.

3.4 CONCLUSIONS

The crystal chemistry, high-temperature phase stability, oxygen storage capacity, and electrochemical performance in IT-SOFCs of the Ga-substituted (Y, In, Ca)$BaCo_4O_{7+\delta}$ materials have been investigated comprehensively with various cationic substitutions. The behavior of phase decomposition was analyzed with TGA and long-term tests at 600 – 800 °C for 120 h. Although $YBaCo_{3.3}Ga_{0.7}O_{7+\delta}$ and $InBaCo_{3.3}Ga_{0.7}O_{7+\delta}$ suffered from decomposition at high temperatures, there were no impurities in the $Y_{1-x}In_xBaCo_{3.3}Ga_{0.7}O_{7+\delta}$ (x = 0.1 – 0.9) samples after the long-term stability test. Also, compared to $YBaCo_{3.2}Ga_{0.8}O_{7+\delta}$, the Ga content was able to be decreased from 0.8 to 0.5 due to the equal amounts of Y and In co-substitution. In contrast, Ca substitution deteriorated the phase stability of $Y_{1-x}Ca_xBaCo_{3.3}Ga_{0.7}O_{7+\delta}$ and $In_{1-x}Ca_xBaCo_{3.3}Ga_{0.7}O_{7+\delta}$ samples because of the incomplete oxygen desorption at 400 °C and continuous oxygen absorption above 500 °C. While the high-temperature phase stability was achieved with sufficient amounts of In and Ga substitutions, the oxygen storage capacity and electrochemical performance were also suppressed. By optimizing the composition, $Y_{0.9}In_{0.1}BaCo_{3.3}Ga_{0.7}O_{7+\delta}$ exhibited the highest OSC (δ = 0.37) and electrochemical performance (ASR of the composite cathode is 0.07 ohm cm^2 at 700 °C) among the materials in this study. The compatible TECs, high maximum power performance, and stable long-term performance demonstrate the advantages of $Y_{0.9}In_{0.1}BaCo_{3.3}Ga_{0.7}O_{7+\delta}$ as a potential cathode material for IT-SOFCs.

Chapter 4: Effect of Trivalent Dopants on Phase Stability and Catalytic Activity of $YBaCo_4O_7$-based Cathodes in Solid Oxide Fuel Cells

4.1 INTRODUCTION

SOFCs are promising energy conversion devices, which generate electricity directly from fuels at elevated temperatures with a high conversion efficiency, low emission, fuel flexibility, and stack scalability. Although a few companies, such as Kyocera, Bloom Energy, and Mitsubishi-Hitachi, have successfully commercialized their SOFC systems recently,[99,100] several development challenges still remain for achieving high production reliability, good durability during thermal cycling, and lifetime extension. Unlike the continuous but slow performance degradation of conventional perovskite cathodes due to phase segregation and chromium poisoning, sudden performance decay, cycling intolerance, and rapid failure are often related to the thermal stress in each SOFC stack component at higher operating temperatures. Internal stress in the ceramic components arises from the manufacturing process and the differential thermal expansion coefficients (TECs) among the cell component layers. External stresses are the result of operational atmosphere gradient, temperature gradient, and mechanical loading based on the stack design.[101–1032]

When the stress in a cell component exceeds its characteristic strength, the resulting interfacial cracks, buckling, or delamination will irreversibly lead to device failure. Simulation in a tubular SOFC has indicated that TEC mismatch between the cathode and the other cell layers generates a high tensile stress in the cathode layer.[103] The probability of survival decreased from 99.8 % to 97 % when the TEC of the cathode increased from

---

Lai, K.-Y.; Manthiram, A. Effect of Trivalent Dopants on Phase Stability and Catalytic Activity of $YBaCo_4O_7$-based Cathodes in Solid Oxide Fuel Cells *Submitted to J. Mater. Chem. A* 2018. Manthiram, A. supervised the project.

11.7×10^{-6} to 12.6×10^{-6} K^{-1}. Moreover, the probability of survival decreased with a larger size of SOFC.[101] In an anode-supported SOFC simulation with a planar size of 16 × 16 cm^2, a thin layer of $La_{0.6}Sr_{0.4}Co_{0.2}Fe_{0.8}O_{3-\delta}$ (LSCF) – $Ce_{0.8}Gd_{0.2}O_{1.9}$ (GDC) composite cathode experienced a maximal tensile stress of over 100 MPa at 700 - 750 °C even without considering a thermal gradient, and this thermal stress might be close to or above the estimated cathode strength.[26] Thus, developing new cathode materials with a high catalytic activity and a well-matched TEC is crucial to realize robust intermediate-temperature SOFCs (IT-SOFCs) (600 – 800 °C).

Figure 4.1 summarizes the TECs of common anode, electrolyte, and cathode materials. The TECs of $Zr_{0.84}Y_{0.16}O_{1.92}$ (YSZ), $La_{0.8}Sr_{0.2}Ga_{0.8}Mg_{0.2}O_{3-\delta}$ (LSGM), and GDC as electrolyte materials are, respectively, 10.5×10^{-6}, 11.0×10^{-6} , and 12.2×10^{-6} K^{-1}.[104,105,85] The conventional cathode material $La_{0.8}Sr_{0.2}MnO_{3-\delta}$ (LSM) has a slightly higher TEC than those of the electrolyte materials, but its poor performance below 800 °C impedes its application in IT-SOFCs.[106] LSCF is a well-studied cathode material with a moderate catalytic activity at 600 - 800 °C, and a LSCF-GDC composite cathode layer could mitigate the high TEC of LSCF (16.7×10^{-6} K^{-1}). However, the high possibility of mechanical failures with LSCF is still not avoidable.[26,107] Most recently developed cathodes in IT-SOFCs still focus on perovskite-related materials and many of them exhibit a promising catalytic activity for the ORR. Unfortunately, cobalt-containing simple perovskite oxides and double perovskite oxides always have high TECs in the range of $17 – 30 \times 10^{-6}$ K^{-1} due to the reduction of Co^{4+} to Co^{3+}/Co^{2+} and the spin-state transitions of Co^{3+} in the octahedral coordination with increasing temperature. Although cobalt-free ferrite perovskite oxides have relatively lower TECs than Co-containing perovskite oxides, their TECs are generally in a range of $15 – 20 \times 10^{-6}$ K^{-1}, which do not match well with the TECs of the SOFC electrolyte materials.

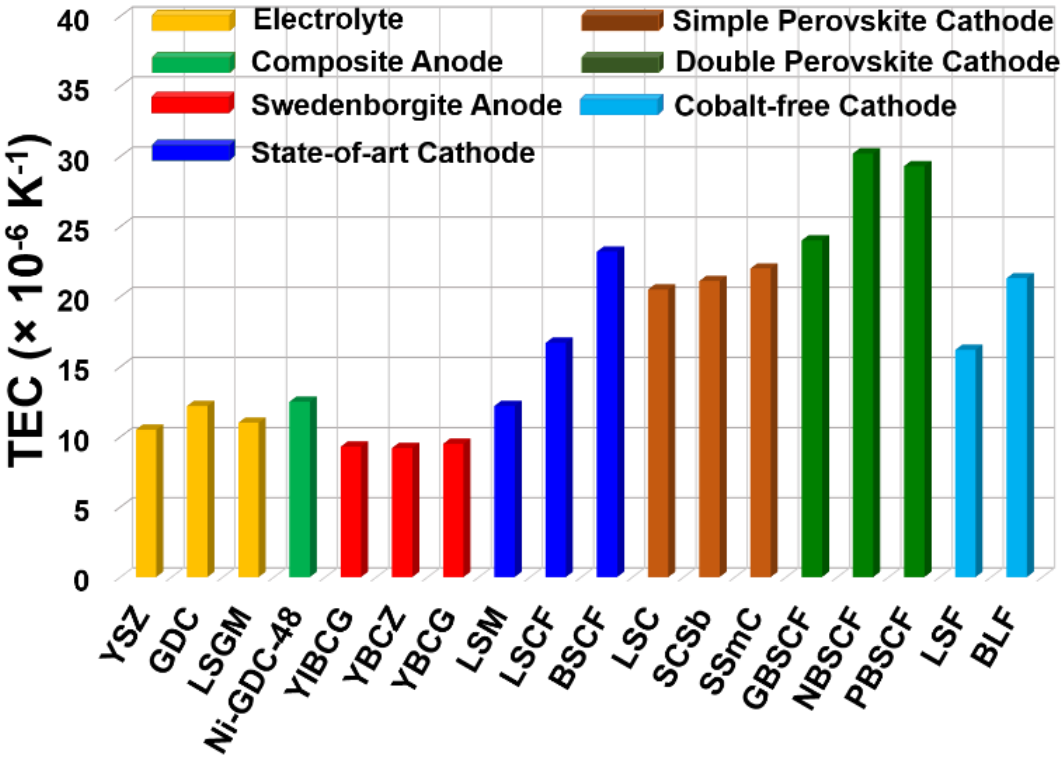

Figure 4.1 Summary of TECs of common electrolyte, anode, and cathode materials. The material compositions are listed: 48 vol.% Ni – GDC (Ni-GDC-48, porous, 75% theoretical density), $Y_{0.9}In_{0.1}BaCo_{3.3}Ga_{0.7}O_{7+\delta}$ (YIBCG), $YBaCo_3ZnO_{7+\delta}$ (YBCZ), $YBaCo_{3.2}Ga_{0.8}O_{7+\delta}$ (YBCG), $La_{0.8}Sr_{0.2}MnO_{3-\delta}$ (LSM), $La_{0.6}Sr_{0.4}Co_{0.2}Fe_{0.8}O_{3-\delta}$ (LSCF), $Ba_{0.5}Sr_{0.5}Co_{0.8}Fe_{0.2}O_{3-\delta}$ (BSCF), $La_{0.6}Sr_{0.4}CoO_{3-\delta}$ (LSC), $SrCo_{0.9}Sb_{0.1}O_{3-\delta}$ (SCSb), $Sr_{0.5}Sm_{0.5}CoO_{3-\delta}$ (SSmC), $GdBa_{0.5}Sr_{0.5}Co_{1.5}Fe_{0.5}O_{5+\delta}$ (GBSCF), $NdBa_{0.5}Sr_{0.5}Co_{1.5}Fe_{0.5}O_{5+\delta}$ (NBSCF), $PrBa_{0.5}Sr_{0.5}Co_{1.5}Fe_{0.5}O_{5+\delta}$ (PBSCF), $La_{0.6}Sr_{0.4}FeO_{3-\delta}$ (LSF), and $Ba_{0.95}La_{0.05}FeO_{3-\delta}$ (BLF).

Cobalt-containing swedenborgite oxides ($RBa(Co,M)_4O_{7+\delta}$) have the exclusive advantage of having relatively low TECs from 200 – 900 °C. The tetrahedrally-coordinated cations Co^{2+} and Co^{3+} in the swedenborgite oxide do not experience a spin-state transition at high temperatures as they are in the high-spin state, so the TECs of $YBaCo_4O_7$-based

materials are in the range of 7.0 – 11.0 × 10^{-6} K^{-1}, which matches well with those of common SOFC electrolytes.[61,51,76] In addition, the thermal stress of the cathode layer could be transformed from tensile to compressive stress due to the lower TEC of the swedenborgite cathode compared to the electrolyte, and the possibility of survival might increase due to the higher compressive strength than the tensile strength of ceramic materials.[108] Unfortunately, irreversible oxygen absorption of $YBaCo_4O_{7+\delta}$ above 600 °C leads to phase decomposition. Our group found that M-site dopants (Ga^{3+} and Zn^{2+}) have a higher impact on the phase stability than R-site dopants (In^{3+} and Ca^{2+}) by a 120 h phase stability evaluation at the intermediate operating temperature range of SOFCs and Ga^{3+} has a superior stabilization capability than Zn^{2+}.[51,54,55,59,76] Both Ga- and Zn-doped $YBaCo_4O_{7+\delta}$ showed high catalytic activity for ORR at 600 – 800 °C.[51,76] Although Fe only has a weak phase stabilization capability for $YBaCo_4O_{7+\delta}$, a moderate substitution of Zn by Fe improved the electrochemical performance as a stable cathode material.[60] Also, Kikkawa group and Karppinen group reported that low-cost Al has a high stabilization capability as an M-site dopant in $YBaCo_4O_{7+\delta}$ by thermogravimetric analysis (TGA), and the phase decomposition can be fully suppressed by Ga-Al co-dopants.[52,57,90] However, the long-term phase stability and the catalytic activity of Al-doped $YBaCo_4O_{7+\delta}$ materials have never been evaluated comprehensively.

This study focuses on the doping and co-doping effects of trivalent cations (Al^{3+}, Ga^{3+}, and Fe^{3+}) on the long-term phase stability of cobalt-containing swedenborgite materials. Nineteen compositions in the four series of $YBCo_4O_7$-based oxides, including $YBaCo_{4-x}Al_xO_{7+\delta}$, $YBaCo_{4-x-y}Ga_xAl_yO_{7+\delta}$, $YBaCo_{3.2}Ga_{0.8-x}Fe_xO_{7+\delta}$, and $YBaCo_{3.5-x}Al_{0.5}Fe_xO_{7+\delta}$, are synthesized and evaluated. To achieve better catalytic activity as cathode materials in IT-SOFCs, the content of cations with d^{10} and d^0 electronic configurations (Ga^{3+} and Al^{3+}) should be minimized.[76] After the phase stabilization capability of the

targeted cations is determined, the thermal behavior, electrical conductivity, TEC, and electrochemical performance of the stabilized materials are presented.

4.2 EXPERIMENTAL SECTION

4.2.1 Material Synthesis and Characterization

The four series of swedenborgite oxides were synthesized by SSR.[76] Stoichiometric amounts of Y_2O_3, $BaCO_3$, Co_3O_4, Ga_2O_3, Al_2O_3, and Fe_2O_3 reactants were mixed with ethanol in a mortar and then calcined at 1000 °C in air for 12 h. After mixing, grinding, and pressing into a pellet, the calcined samples were sintered at 1200 – 1300 °C for 24 h. The phase of the pulverized materials was characterized by XRD as described in Chapter 2.2. The long-term phase stability of the swedenborgite oxides was evaluated by analyzing the samples annealed for 120 h in ambient air at 600, 700, and 800 °C. The powder samples were placed on a pellet made of the same materials to prevent side reactions with the alumina crucible. The bulk samples for conductivity and thermal expansion measurement were made by pressing the ball-milled powder into a pellet or bar shape and sintering at 1200 – 1300 °C for 12 h. The thermal analysis, including the thermal behavior, electrical conductivity, and TEC, were measured at 100 to 900 °C, and the details were shown in Chapter 2.3.

4.2.2 Single Cell and Electrochemical Activity Evaluation

The electrochemical activity was evaluated by the polarization resistance of the symmetric cells by EIS from 500 to 800 °C under ambient air. The scanning amplitude was 10 mV with respect to the open-circuit voltage, and the sweeping frequency was from 0.1

Hz to 10^6 Hz. The substrate of a symmetrical cell was a dense GDC pellet, and the composite cathode layer was screen printed on the both sides of the polished GDC pellet and sintered at 950°C for 2 h. An anode-supported single cell with the selected cathode composite material was made by a co-pressing method, which was detailed in Chapter 2.4. In order to enhance the amount of three-phase boundary in the anode, the NiO-GDC composite anode of the single cell was prepared by a modified sol-gel method as described in Chapter 2.1.[73] The co-sintering temperature of the anode and electrolyte bilayer was 1350 °C for 3 h, and the cathode layer was sintered at the same temperature as the symmetric cell. The single cell performance was evaluated with our homemade system with ambient air and 20 sccm of H_2. The microstructure of the single cell was observed by SEM (JEOL JSM-5610) and EDX (Oxford Inca X-act).

4.3 Results and Discussion

4.3.1 Phase characterization and stability

Nineteen compositions of the swedenborgite oxides were synthesized in these studies. When over 12.5 % Co in $YBaCo_4O_{7+\delta}$ is substituted by Al, a Y_2O_3 impurity peak is observed at 29.1° in the XRD patterns, implying an incomplete SSR among the reactants. In order to achieve phase purity, the sintering process was repeated with an increase of sintering temperature from 1200 °C to 1300 °C at 50 °C intervals until the Y_2O_3 impurity peak was minimized. The sintering temperature of the $YBaCo_{4-x-y}Ga_xAl_yO_{7+\delta}$ and $YBaCo_{4-x-y}Ga_xAl_yO_{7+\delta}$ materials was fixed at 1200 °C. Figure 4.2 shows the room-temperature XRD (RT-XRD) results of the as-synthesized samples. Most of the materials are single phase with a trigonal structure with the P31c space group. Only $YBaCo_{3.2}Al_{0.8}O_{7+\delta}$ has a weak peak of the Y_2O_3 impurity phase even after undergoing the sintering process twice at

1300 °C. The impurity phase is consistent with the sol-gel synthesis results in the literature.[52,90] Although a single crystal of $YBaCo_3AlO_{7+\delta}$ could be synthesized in a floating-zone furnace[109], the high Al content in swedenborgite oxides seems to impede a homogeneous phase formation in the regular powder synthesis methods.

The long-term phase stability was evaluated by annealing the powder samples under ambient air at 600, 700, and 800 °C for 120 h, and the phase decomposition was determined by RT-XRD. Figure 4.3 summarizes the phase stability of the 19 swedenborgite materials. In the literature, the decomposition temperature was usually determined by the onset temperature of an irreversible oxygen absorption with TGA.[48,52,56,57,88,90,110] The decomposition temperature of $YBaCo_4O_{7+\delta}$ and $YBaCo_{3.5}Al_{0.5}O_{7+\delta}$ are reported, respectively, at 600 and 800 °C.[52,90] However, the observation of the thermal behavior cannot reveal the true long-term phase stability at high temperatures due to the slow kinetics of phase decomposition in these materials.

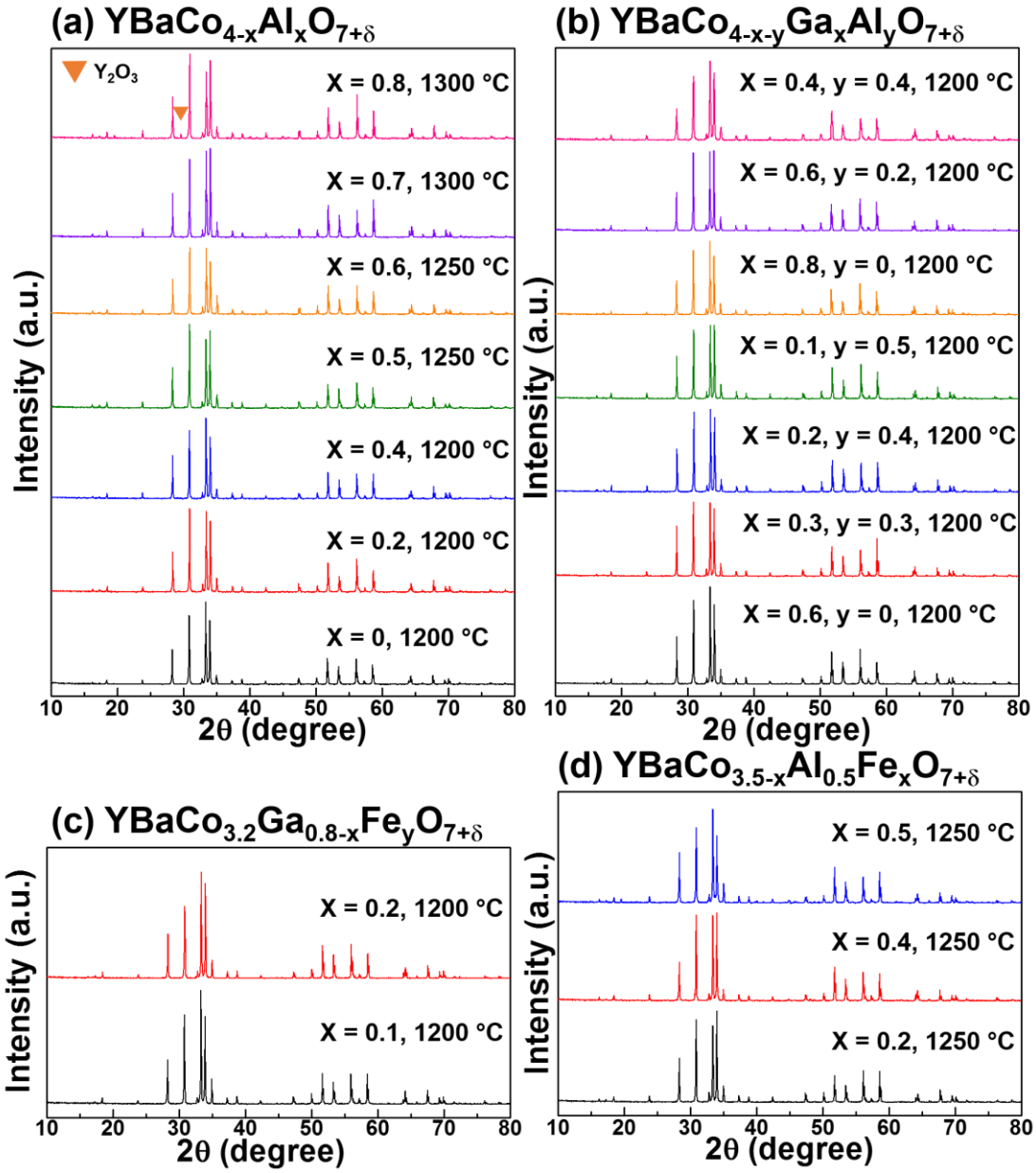

Figure 4.2. XRD patterns of as-synthesized (a) $YBaCo_{4-x}Al_xO_{7+\delta}$, (b) $YBaCo_{4-x-y}Ga_xAl_yO_{7+\delta}$, (c) $YBaCo_{4-x-y}Ga_xAl_yO_{7+\delta}$, and (d) $YBaCo_{3.5}Al_{0.5}Fe_xO_{7+\delta}$. The sintering temperature is 1,200 °C for $YBaCo_{4-x-y}Ga_xAl_yO_{7+\delta}$ and $YBaCo_{4-x-y}Ga_xAl_yO_{7+\delta}$. When the Al content in $YBaCo_{4-x}Al_xO_{7+\delta}$ and $YBaCo_{3.5}Al_{0.5}Fe_xO_{7+\delta}$ exceeds 0.5 in the formula, the final sintering temperature is over 1200 °C.

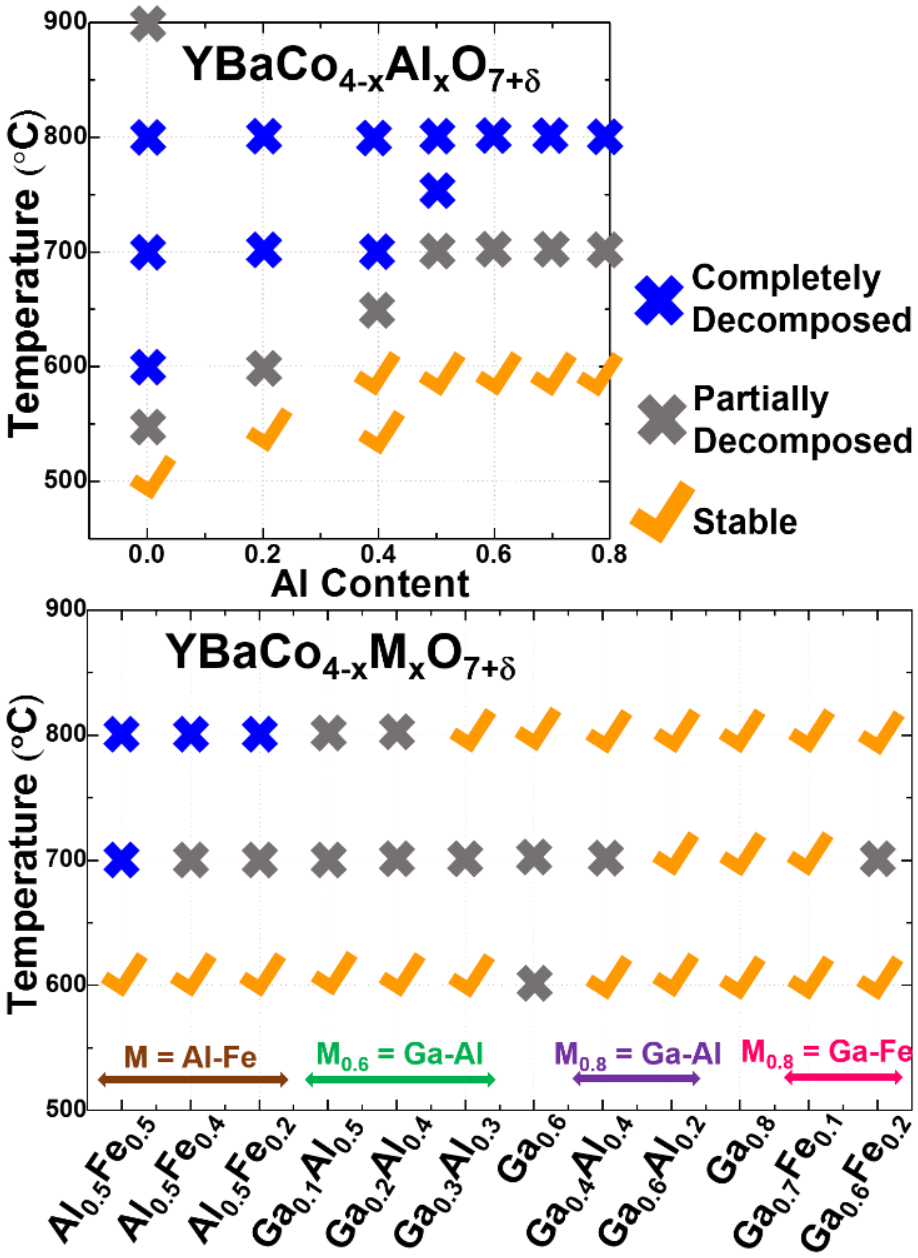

Figure 4.3 Summary of the phase stability of the 19 tested swedenborgite materials after annealing at 600, 700, and 800 °C for 120 h. Partial decomposition indicates that a small amount of impurity phases were found in RT-XRD. Complete decomposition indicates that the swedenborgite phase was not detected.

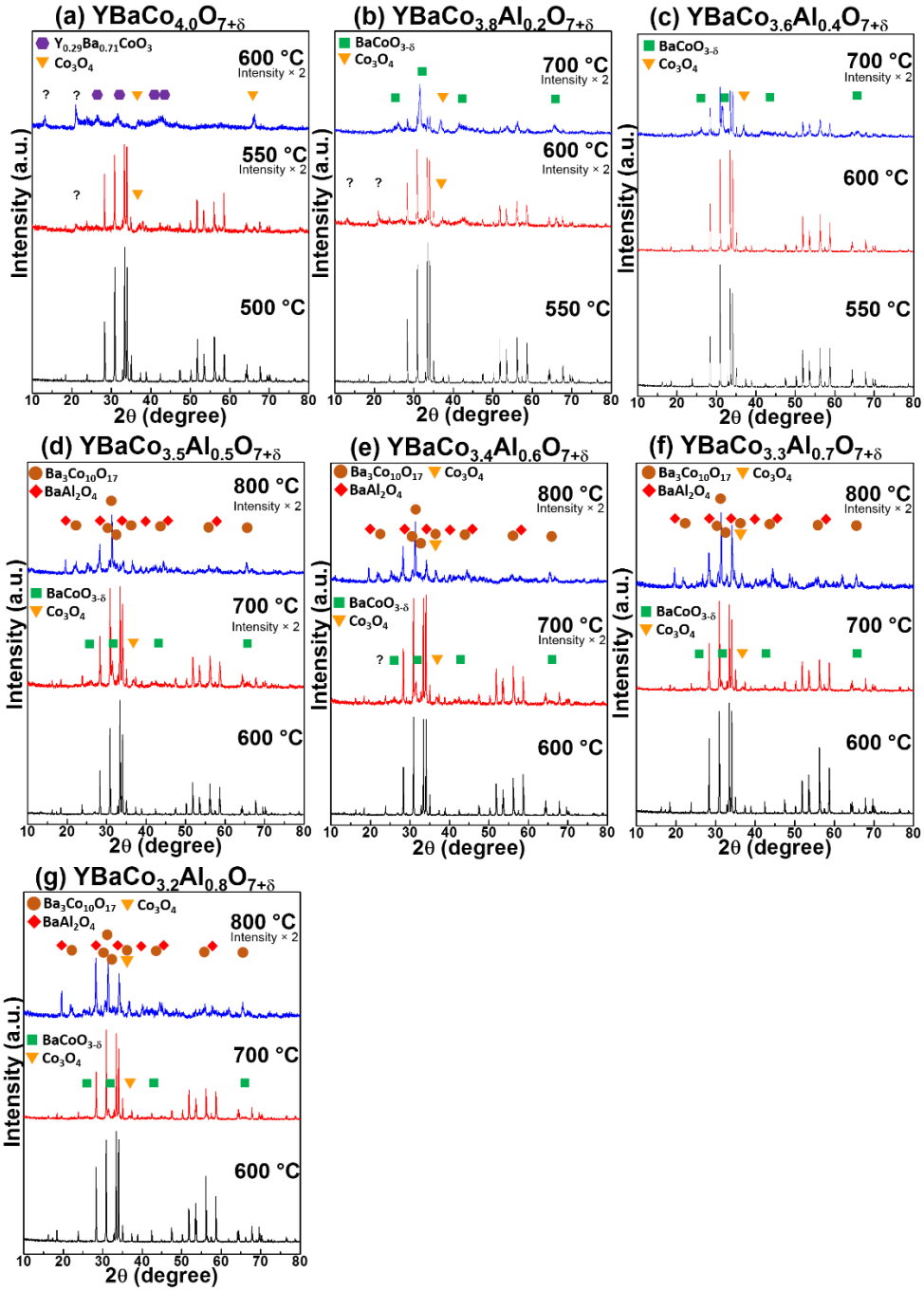

Figure 4.4 RT-XRD patterns of the (a) $YBaCo_4O_{7+\delta}$, (b) $YBaCo_{3.8}Al_{0.2}O_{7+\delta}$, (c) $YBaCo_{3.6}Al_{0.4}O_{7+\delta}$, (d) $YBaCo_{3.5}Al_{0.5}O_{7+\delta}$, (e) $YBaCo_{3.4}Al_{0.6}O_{7+\delta}$, (f) $YBaCo_{3.3}Al_{0.7}O_{7+\delta}$, and (g) $YBaCo_{3.2}Al_{0.8}O_{7+\delta}$ samples annealed at various temperatures for 120 h. Unknown impurity peaks are marked as "?".

Here, we accurately identify that the phase decomposition of $YBaCo_4O_{7+\delta}$ occurs at over 500 °C and the Al dopant slightly improves the phase stability up to 600 °C. In contrast to the literature results, the swedenborgite phase cannot be further stabilized by Al at over 650 °C even with a high amount of Al substitution. Figure 4.4 shows the RT-XRD patterns of the $YBaCo_{4-x}Al_xO_{7+\delta}$ samples annealed at the various temperatures for 120 h. $YBaCo_4O_{7+\delta}$ decomposes completely at 600 °C and its decomposition products are mostly not crystalline. When the Al content increases from 0.2 to 0.8, the swedenborgite phase becomes relatively stable at 700 °C but the phase instability is still observable. The decomposition products at different annealing temperatures, including $Y_{0.29}Ba_{0.71}CoO_{3-\delta}$ (PDF # : 01-078-5312), $BaCoO_{3-\delta}$ (PDF # : 01-071-2453), $Ba_3Co_{10}O_{17}$ (PDF # : 01-076-3359), and Co_3O_4 (PDF # : 01-074-1656), indicate that the driving force behind the phase decomposition might be Co cation instability in the tetrahedral coordination and its preference for the octahedral coordination. Although Al^{3+} has no d-shell electron and no preference for octahedral coordination, the Al dopant could not stabilize the swedenborgite structure at over 650 °C.

The long-term phase stability of $YBaCo_{4-x-y}Ga_xAl_yO_{7+\delta}$ was also evaluated because Karppinen's group reported by TGA data that $YBaCo_{3.4}Ga_{0.3}Al_{0.3}O_{7+\delta}$ was able to completely suppress the irreversible oxygen absorption at 600 to 900 °C. However, Figure 4.5 shows that none of the $YBaCo_{3.4}Ga_{0.6-x}Al_xO_{7+\delta}$ phases survives after the annealing test at 700 °C for 120 h. In addition, the phase decomposition of $YBaCo_{3.4}Ga_{0.6-x}Al_xO_{7+\delta}$ becomes more severe at 800 °C with a higher content of Al in Figure 4.5(b) – 4.5(d) On the other hand, the $YBaCo_{3.4}Ga_{0.6}O_{7+\delta}$ phase is only stabilized at 800 °C among the three annealing temperatures tested. Thus, the Al and Ga dopants, respectively, stabilize swedenborgite structure preferentially at 600 and 800 °C, and the stable $YBaCo_{3.4}Ga_{0.3}Al_{0.3}O_{7+\delta}$ phase at 600 and 800 °C is benefited by the co-doping effect.

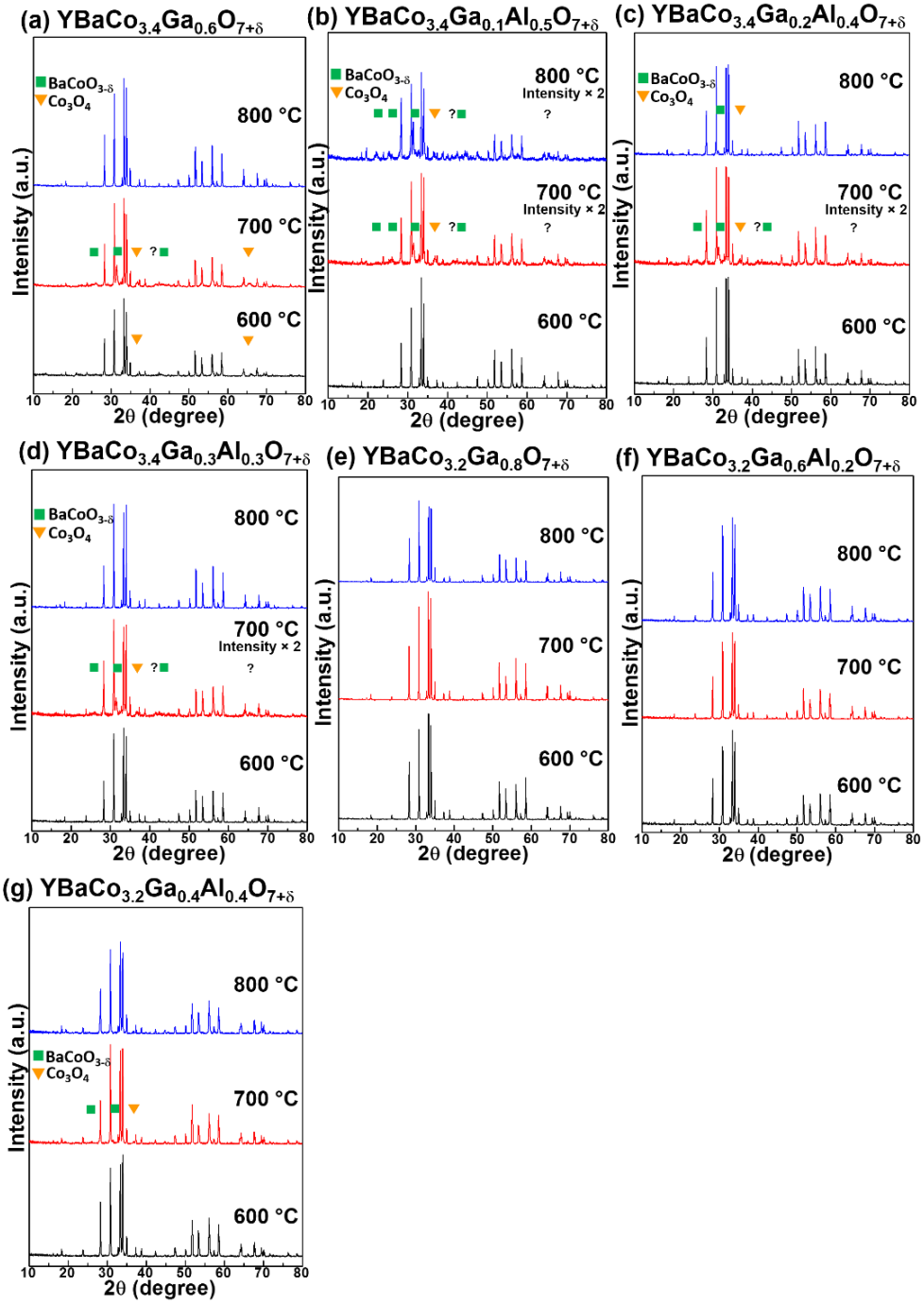

Figure 4.5 RT-XRD results of the (a) $YBaCo_{3.4}Ga_{0.6}O_{7+\delta}$, (b) $YBaCo_{3.4}Ga_{0.1}Al_{0.5}O_{7+\delta}$, (c) $YBaCo_{3.4}Ga_{0.2}Al_{0.4}O_{7+\delta}$, (d) $YBaCo_{3.4}Ga_{0.3}Al_{0.3}O_{7+\delta}$, (e) $YBaCo_{3.2}Ga_{0.8}O_{7+\delta}$, (f) $YBaCo_{3.2}Ga_{0.6}Al_{0.2}O_{7+\delta}$, and (g)$YBaCo_{3.2}Ga_{0.4}Al_{0.4}O_{7+\delta}$ samples annealed at 600 – 800 °C for 120 h. Unknown impurity peaks are marked as "?".

Furthermore, $YBaCo_{3.2}Ga_{0.8-x}Al_xO_{7+\delta}$ materials were studied to pursue the complete phase stabilization. While no impurity product is detected in the annealed $YBaCo_{3.2}Ga_{0.8}O_{7+\delta}$ and $YBaCo_{3.2}Ga_{0.6}Al_{0.2}O_{7+\delta}$ samples, a trace amount of $BaCoO_{3-\delta}$ and Co_3O_4 is found in the $YBaCo_{3.2}Ga_{0.4}Al_{0.4}O_{7+\delta}$ sample after the annealing process at 700 °C, as seen in Figure 4.5(e) – 4.5(g). The requirement of a higher Ga content for eliminating phase decomposition implies that Ga has a stronger stabilization capability than Al.

The weak stabilization capability of the Fe dopant in $YBaCo_4O_{7+\delta}$ has been reported in the literature due to the unchanged phase decomposition temperature[110,111], but Al-Fe and Ga-Fe co-doping effect on the long-term phase stability has not been discussed comprehensively. According to the Mossbauer spectroscopy and magnetization studies of $YBaCo_{4-x}Fe_xO_{7+\delta}$ ($x = 0 – 0.8$), all the Fe cations in swedenborgite structure are trivalent.[112] Thus, the substitution of Ga by Fe does not affect the Co average oxidation state. Phase stability results for the tested Ga-Fe and Al-Fe co-doped swedenborgite materials are displayed, respectively, in Figure 4.6 and Figure 4.7. In comparison to $YBaCo_{3.4}Ga_{0.6}O_{7+\delta}$ (Figure 4.5(a)), $YBaCo_{3.2}Ga_{0.6}Fe_{0.2}O_{7+\delta}$ has good stability at 600 °C, but a trace amount of a $BaCoO_{3-\delta}$ impurity phase is found after annealing at 700 °C for 120 h. The result indicates that Fe preferentially stabilizes swedenborgite structure at 600 °C, but the weak stabilization capability of Fe only allows small amounts of Fe doping in $YBaCo_{3.2}Ga_{0.7}Fe_{0.1}O_{7+\delta}$ to maintain the same excellent phase stability at 600 – 800 °C as with $YBaCo_{3.2}Ga_{0.8}O_{7+\delta}$. Since Al and Fe have a similar stabilization preference at 600 °C, Co was substituted by Fe in $YBaCo_{3.5-x}Al_{0.5}Fe_xO_7$ for a complete understanding of the stability effect of Fe. However, the phase decomposition of $YBaCo_{3.5-x}Al_{0.5}Fe_xO_7$ at both 700 and 800 °C is clearly observed. $YBaCo_{3.0}Al_{0.5}Fe_{0.5}O_{7+\delta}$ even experiences a complete decomposition at 700 °C, which is shown in Figure 4.7. Thus, Fe only shows a stabilization

capability with Ga co-dopant, and it does not improve the long-term phase stability when co-doped with Al.

The phase stabilization capability of the three trivalent dopants in the swedenborgite oxide is $Ga^{3+} > Al^{3+} > Fe^{3+}$, and only Ga^{3+} can achieve excellent phase stability as a single dopant at high temperatures. Although 19 compositions are evaluated in these studies, only three compositions do not display any decomposition product after the annealing tests at all three annealing temperatures: $YBaCo_{3.2}Ga_{0.8}O_{7+\delta}$ and $YBaCo_{3.2}Ga_{0.6}Al_{0.2}O_{7+\delta}$ in the $YBaCo_{3.2}Ga_{0.8-x}Al_xO_{7+\delta}$ series, and $YBaCo_{3.2}Ga_{0.7}Fe_{0.1}O_{7+\delta}$ in the $YBaCo_{4-x}Fe_xO_{7+\delta}$ series. The characteristics of materials in these two series determined the selection as candidate cathodes in SOFCs.

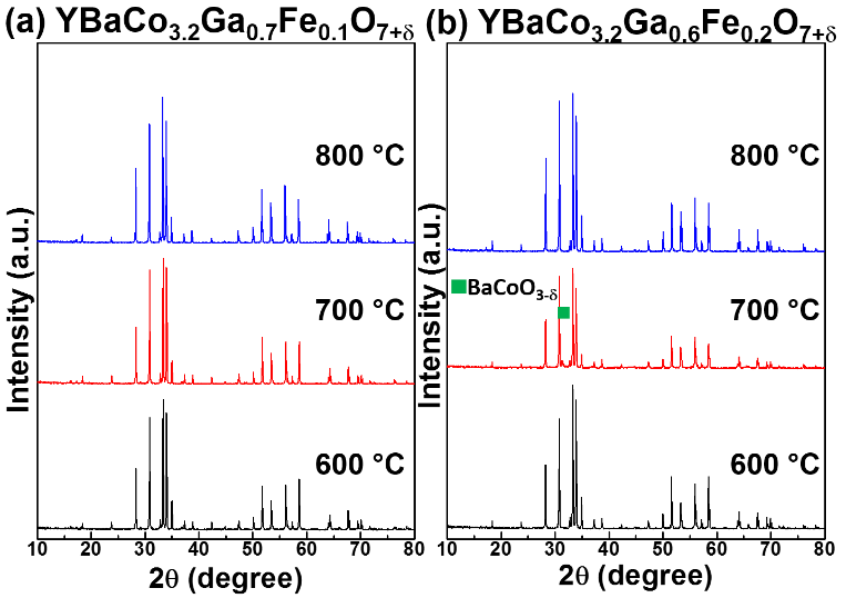

Figure 4.6 RT-XRD results of the (a) $YBaCo_{3.2}Ga_{0.7}Fe_{0.1}O_{7+\delta}$ and (b) $YBaCo_{3.2}Ga_{0.6}Fe_{0.2}O_{7+\delta}$ samples annealed at 600 – 800 °C for 120 h.

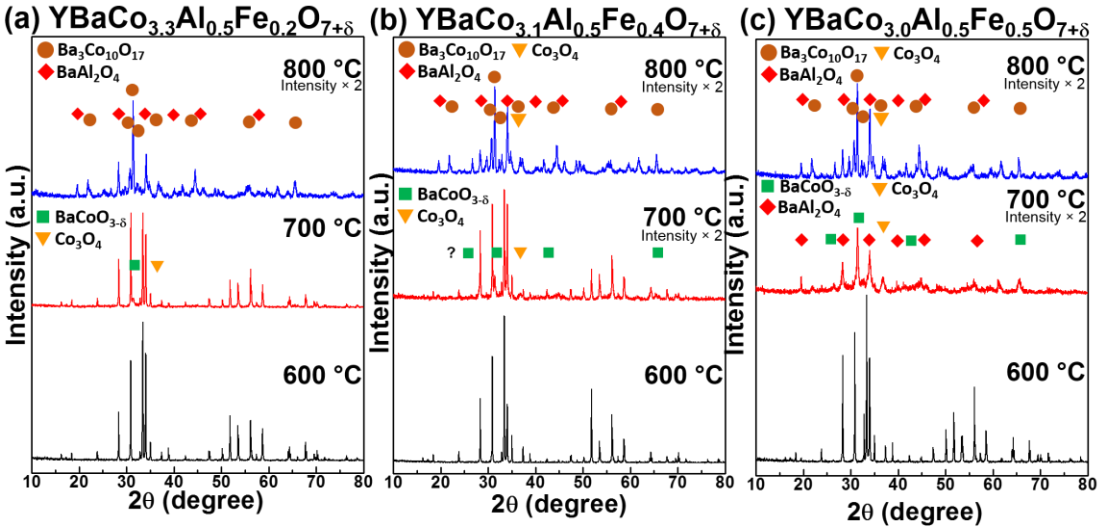

Figure 4.7 RT-XRD patterns of the (a) $YBaCo_{3.3}Al_{0.5}Fe_{0.2}O_{7+\delta}$, (b) $YBaCo_{3.1}Al_{0.5}Fe_{0.4}O_{7+\delta}$, and (c) $YBaCo_{3.0}Al_{0.5}Fe_{0.5}O_{7+\delta}$ samples annealed at 600 - 800 °C for 120 h. The intensities of the decomposed samples decrease significantly, so the intensity of some XRD pattern is doubled for clarity, which is noted in the figure.

4.3.2 Thermal Behaviors, Thermal Expansion Coefficients, and Electrical Conductivity

$YBaCo_4O_7$-based materials have a unique oxygen storage behavior at below 400 °C, and the reversible oxygen absorption and desorption does not lead to a phase decomposition as the continuous oxygen absorption does above 600 °C.[42] The oxygen storage capability (OSC) is determined by the maximum amount of the oxygen absorption (δ_{max}) about 320 °C, which depends strongly on the material composition. Figure 4.8 illustrates the thermal behavior of $YBaCo_{3.2}Ga_{0.8-x}Fe_xO_{7+\delta}$ and $YBaCo_{3.2}Ga_{0.8-x}Al_xO_{7+\delta}$ materials which is determined by TGA in air from 25 to 900 °C. Unlike the high OSC of up to $\delta_{max} = 1.0$ in $YBaCo_4O_{7+\delta}$, the $YBaCo_{3.2}Ga_{0.8-x}Fe_xO_{7+\delta}$ and $YBaCo_{3.2}Ga_{0.8-x}Al_xO_{7+\delta}$ materials have a much lower OSC of $\delta_{max} = 0.16 – 0.18$. When Ga is partially substituted

by Fe or Al, only a very small amount of OSC variation appears due to the strong suppression effect on OSC by Ga.[56,76] Meanwhile, the irreversible oxygen absorption above 600 °C is not found in any of the $YBaCo_{3.2}Ga_{0.8-x}Fe_xO_{7+\delta}$ and $YBaCo_{3.2}Ga_{0.8-x}Al_xO_{7+\delta}$ samples. However, according to the RT-XRD results discussed in the last section, the $YBaCo_{3.2}Ga_{0.6}Fe_{0.2}O_{7+\delta}$ and $YBaCo_{3.2}Ga_{0.4}Al_{0.4}O_{7+\delta}$ samples are partially decomposed after an annealing test at 700 °C. Thus, the phase decomposition of the swedenborgite oxides is kinetically slow due to the doping effect of Ga, Fe, and Al. Although the thermal behavior evaluation could clearly indicate the OSC at relatively lower temperatures, the long-term stability at high temperatures should be identified by annealing tests.

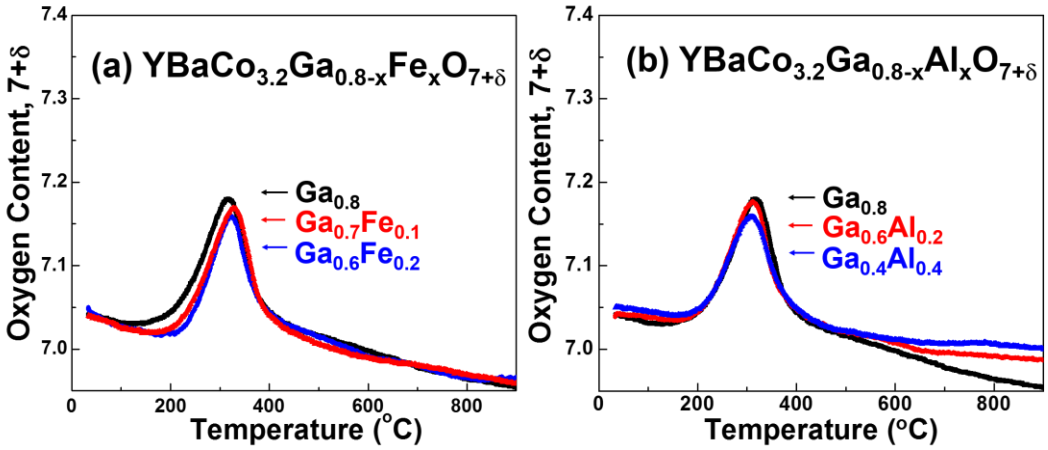

Figure 4.8 Oxygen content variation of (a) $YBaCo_{3.2}Ga_{0.8-x}Fe_xO_{7+\delta}$ and (b) $YBaCo_{3.2}Ga_{0.8-x}Al_xO_{7+\delta}$ with respect to temperature.

Figure 4.9 shows the thermal expansion curves of the $YBaCo_{3.2}Ga_{0.8-x}Fe_xO_{7+\delta}$ and $YBaCo_{3.2}Ga_{0.8-x}Al_xO_{7+\delta}$ materials in ambient air from 80 to 900 °C. The TECs of $YBaCo_{3.2}Ga_{0.8}O_{7+\delta}$ are 9.4×10^{-6} and 9.5×10^{-6} K^{-1} from 25 °C to, respectively, 600 and 900 °C. In comparison to the TECs of the perovskite cathode materials ($17 - 30 \times 10^{-6}$ K^{-}

[1]), the TEC of the swedenborgite cathode materials is a good match with those of the common electrolyte materials (10.5 – 12.2 × 10^{-6} K^{-1}) and that of the conventional composite anode with a porous microstructure (12.5 × 10^{-6} K^{-1}). In addition, the slightly lower TEC of the cathode layer compared to electrolyte and anode layers could transform the tensile stress in the cathode thin film to compressive stress, which might increase the possibility of survival of the SOFC stacks due to the nature of a higher compression strength than tensile strength in ceramics.[108] The TECs of the $YBaCo_{3.2}Ga_{0.8-x}Fe_xO_{7+\delta}$ and $YBaCo_{3.2}Ga_{0.8-x}Al_xO_{7+\delta}$ materials slightly decrease when more Ga is substituted by Fe or Al, and Al has a stronger suppression effect than Fe on the TEC. For example, the TECs of $YBaCo_{3.2}Ga_{0.6}Al_{0.2}O_{7+\delta}$ and $YBaCo_{3.2}Ga_{0.6}Fe_{0.2}O_{7+\delta}$ are, respectively, 8.0 × 10^{-6} K^{-1} and 8.9 × 10^{-6} K^{-1} from 25 °C to 600 °C. Although the Fe and Al dopants might cause the TECs of swedenborgite oxides to deviate from those of the common electrolyte materials, a composite cathode with GDC could further mitigate the TEC difference.

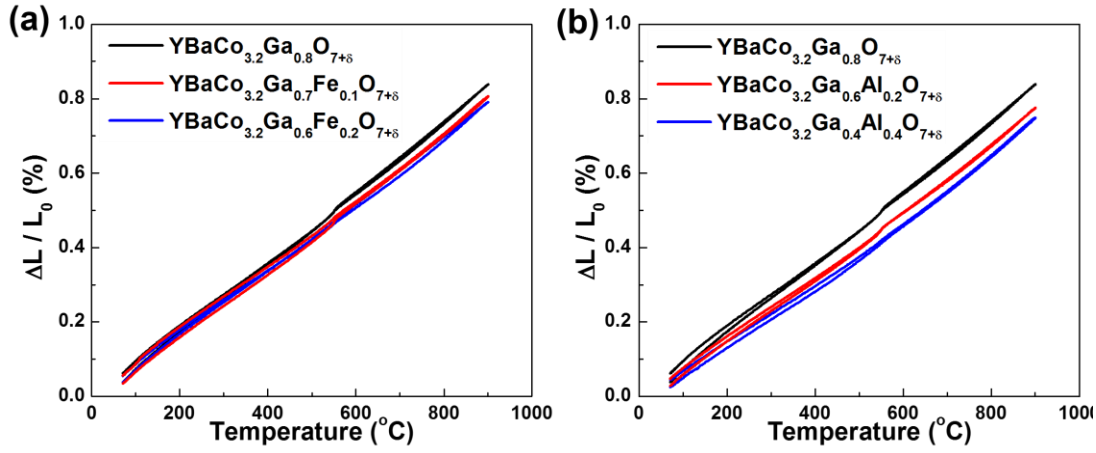

Figure 4.9 Thermal expansion curves of (a) $YBaCo_{3.2}Ga_{0.8-x}Fe_xO_{7+\delta}$ and (b) $YBaCo_{3.2}Ga_{0.8-x}Al_xO_{7+\delta}$ in ambient air from 80 to 900 °C.

Figure 4.10 illustrates the temperature-dependent electrical conductivity of the $YBaCo_{3.2}Ga_{0.8-x}Fe_xO_{7+\delta}$ and $YBaCo_{3.2}Ga_{0.8-x}Al_xO_{7+\delta}$ samples in ambient air from 100 to 900 °C. The electrical conductivity of the studied materials increases with temperature, and this suggests that the thermally activated small polaron mechanism dominates under the cathode operational atmosphere. The Ga^{3+} and Al^{3+} dopants without changeable oxidation states impede the hopping path due to, respectively, their fully-occupied and empty d-shell electronic configurations. Thus, the electrical conductivity decreases with a higher content of the Ga^{3+} or Ga^{3+} + Al^{3+} dopants, and it is clear that the conductivity of $YBaCo_{3.2}Ga_{0.8-x}Fe_xO_{7+\delta}$ slightly increases with increasing Fe content. In contrast, there is no noticeable conductivity difference in $YBaCo_{3.2}Ga_{0.8-x}Al_xO_{7+\delta}$ because the total content of Ga and Al remains unchanged.

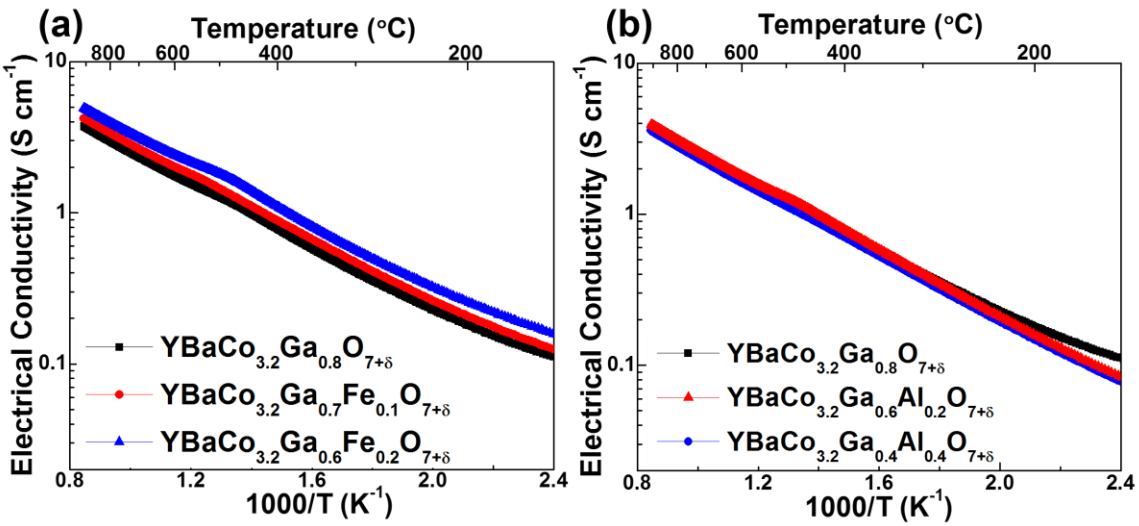

Figure 4.10 Electrical conductivity curves of (a) $YBaCo_{3.2}Ga_{0.8-x}Fe_xO_{7+\delta}$ and (b) $YBaCo_{3.2}Ga_{0.8-x}Al_xO_{7+\delta}$ in ambient air from 100 to 900 °C.

The thermally-activated conductivity can be described by the Emin–Holstein model with the as:

$$\sigma T = Ae^{-\Delta E_a / k_B T}$$

where σ, A, ΔE_a, and k_B are, respectively, the electrical conductivity, pre-exponential constant, activation energy, and Boltzmann constant. The activation energy slightly decreases with a substitution of Ga by Fe, and the opposite trend occurs with a higher content of Al. However, all the activation energies are in the range of 0.27 to 0.28 eV, which is higher than that of 0.20 eV in $YBaCo_{4.0}O_{7+\delta}$.[113] Nonetheless, the electrical conductivity of all the studied materials here is over 1 S cm^{-1} at > 500 °C, which fits the suggested requirement for the electrode.[114,115]

4.3.3 Catalytic Activity and Performance Evaluation

The catalytic activity for ORR was determined by the impedance of the symmetric cells with the $YBaCo_{3.2}Ga_{0.8-x}Fe_xO_{7+\delta}$ and $YBaCo_{3.2}Ga_{0.8-x}Al_xO_{7+\delta}$ composite cathodes under open-circuit voltage, and the results are displayed in Figure 4.11. The composite cathode is a mixture of the cathode material and GDC in a 1 : 1 wt. ratio, which could increase the reaction activity by extending the three phase boundary and enhancing the oxide-ionic conductivity.[51,76] In order to confirm the Ag current collector did not affect the data, the polarization resistance of a symmetric cell was measured twice from 500 to 800 °C at an interval of 50 °C. Consistency between the two data sets collected indicate no effect from the Ag current collector. The area-specific resistance (ASR) was calculated by normalizing the polarization resistance with the electrode area. The ASRs decrease with increasing Fe content in $YBaCo_{3.2}Ga_{0.8-x}Fe_xO_{7+\delta}$, and the $YbaCo_{3.2}Ga_{0.6}Fe_{0.2}O_{7+\delta}$ – GDC

composite cathode shows the lowest ASR values of 0.24, 0.12, and 0.07 Ω cm^2 at, respectively, 600, 650, and 700 °C. However, as previously described in Figure 4, a slight phase decomposition is detected in the annealed $YBaCo_{3.2}Ga_{0.6}Fe_{0.2}O_{7+\delta}$ sample, which might lead to long-term performance degradation as a cathode. Thus, the $YBaCo_{3.2}Ga_{0.7}Fe_{0.1}O_{7+\delta}$ – GDC composite cathode with the ASRs of 0.15 and 0.08 Ω cm^2, respectively, at 650 and 700 °C will be further tested as a cathode material in an anode-supported single cell. On the other hand, Figure 4.11(b) shows that the ASR values of the three $YBaCo_{3.2}Ga_{0.8-x}Al_xO_{7+\delta}$ – GDC composite cathodes are very close, and this suggests that the Al^{3+} and Ga^{3+} dopants have the similar effect on the catalytic activity due to their electronic configurations. Based on the Arrhenius equation, the activation energy of the studied composite cathodes is in the range of 0.94 to 0.99 eV, which agrees with those of the other $YBaCo_4O_{7+\delta}$–based composite cathodes.[51,76]

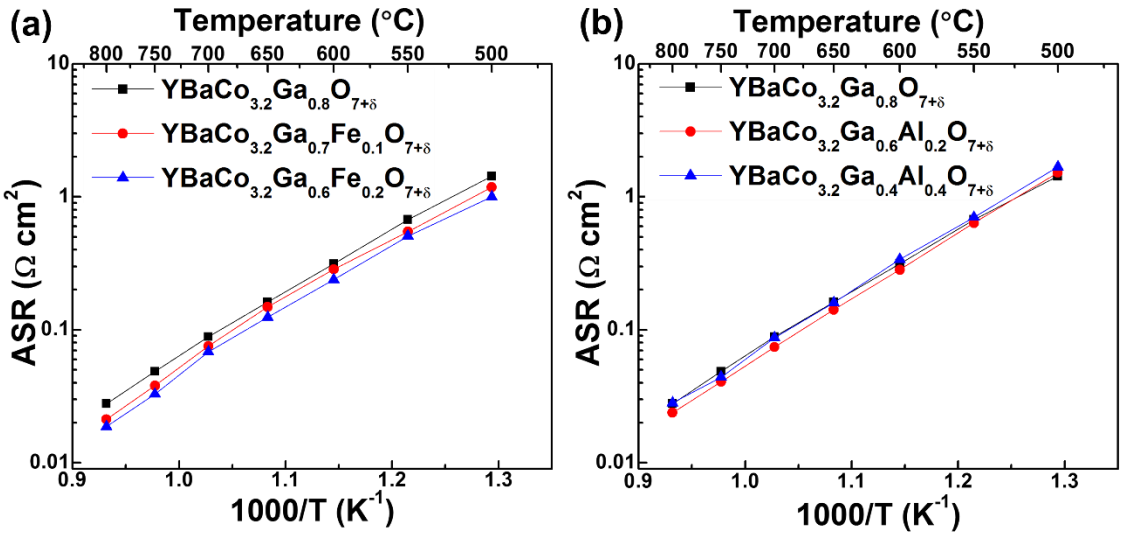

Figure 4.11 Temperature-dependent polarization resistance of (a) $YBaCo_{3.2}Ga_{0.8-x}Fe_xO_{7+\delta}$ + GDC and (b) $YBaCo_{3.2}Ga_{0.8-x}Al_xO_{7+\delta}$ + GDC composite cathodes in ambient air from 500 to 800 °C.

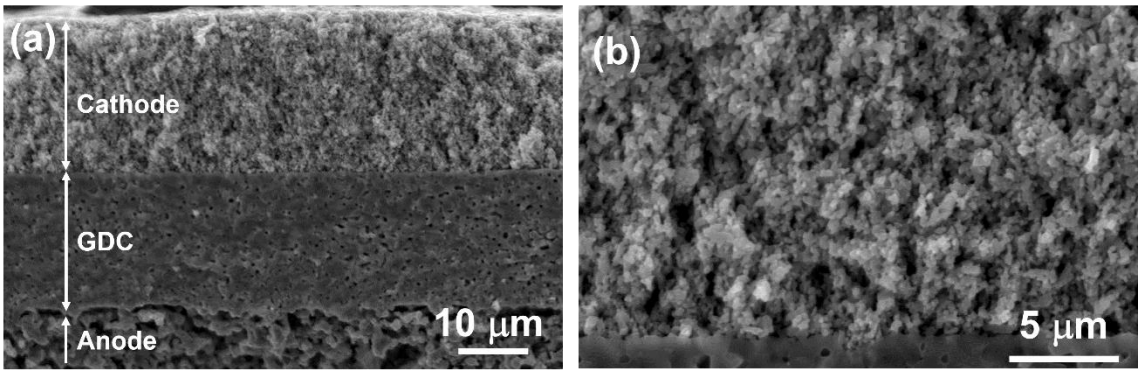

Figure 4.12 Cross-sectional SEM images of (a) an anode-supported single cell and (b) a composite cathode layer before performance evaluation.

Figure 4.12 shows the cross-sectional microstructure of the anode-supported single cell in a sandwich structure. The thickness of the porous composite anode, the dense electrolyte, and the porous composite cathode are, respectively, ~ 0.6 mm, ~20 μm, and ~20 μm. Although several closed pores are distributed in the GDC layer, there is no connected channel or crack, which would cause electrolyte deterioration. The composite cathode layer is composed of particles of homogeneous size and the interface between the cathode and the electrolyte exhibits a good contact without cracks. Figure 4.13 demonstrates the electrochemical performance of the anode-supported single cell with the $YBaCo_{3.2}Ga_{0.7}Fe_{0.1}O_{7+\delta}$ – GDC composite cathode. Since a partial reduction of Ce^{4+} in the GDC electrolyte has occurred noticeably above 500 °C in the reducing atmosphere, the open-circuit voltage of 0.84 V is much lower than the predicted voltage of above 1 V by Nernst equation at 600 °C. The maximum power density is 0.33, 0.65, and 1.00 W cm^{-2}, respectively, at 600, 650, 700 °C. Figure 4.13(b) shows the long-term performance stability of the anode-supported single cell, which was tested with a constant current density of 600

mA cm^{-2} at 650 °C. No significant degradation is observed after 120 h. This stable single-cell performance suggests the preliminary potential of the $YBaCo_{3.2}Ga_{0.7}Fe_{0.1}O_{7+\delta}$ – GDC composite materials as a candidate cathode in practical SOFC applications.

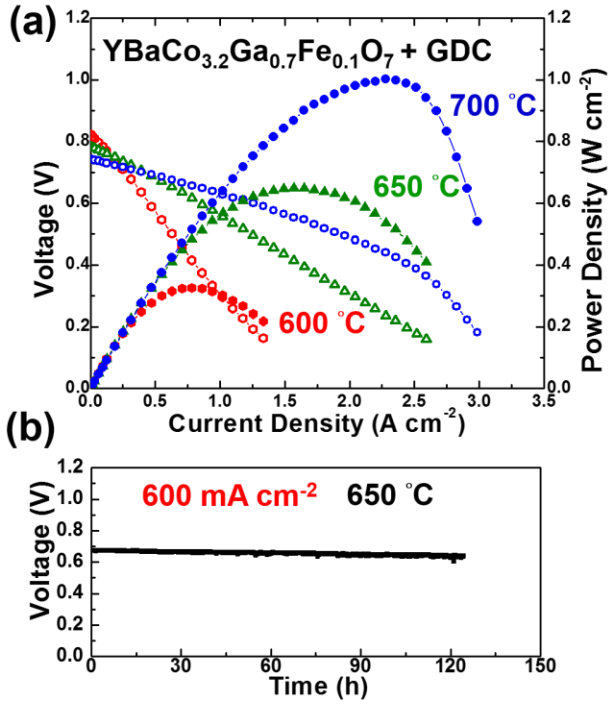

Figure 4.13 (a) Single-cell performance and (b) long-term performance evaluation of the anode-supported SOFC with the $YBaCo_{3.2}Ga_{0.7}Fe_{0.1}O_{7+\delta}$ + GDC composite cathode. The cathode was exposed to ambient air.

4.4 CONCLUSIONS

The doping and co-doping effects of three trivalent cations (Al^{3+}, Fe^{3+}, and Ga^{3+}) in $YBaCo_4O_{7+\delta}$ on the long-term phase stability, oxygen storage capability, thermal expansion behavior, electrical conductivity, and electrochemical activity have been comprehensively discussed in this study. The long-term phase stability at IT-SOFC

operational temperatures is clearly identified by the 120-h annealing test. This work identified that in long-term testing, Al is only able to stabilize the $YBaCo_4O_{7+\delta}$ swedenborgite phase up to 600 °C irrespective of the dopant content, in contrast to the reports in the literature that identified a high stabilization capability of Al by thermal behavior evaluation. Based on the phase stability evaluation results of the co-doped samples, $YBa(Co, Ga, Al, Fe)_4O_{7+\delta}$, the stabilization capability to the swedenborgite phase is summarized as $Ga^{3+} > Al^{3+} > Fe^{3+}$. When Ga in $YBaCo_{3.2}Ga_{0.8}O_{7+\delta}$ is substituted by Al, the TEC and electrical conductivity both decrease. On the other hand, Fe slightly improves the electrical conductivity. Nonetheless, the materials studied here all provide adequate electrical conductivity and well-compatible TECs to the common electrolyte materials. In comparison to the $YBaCo_{3.2}Ga_{0.8}O_{7+\delta}$ – GDC composite material, the $YBaCo_{3.2}Ga_{0.7}Fe_{0.1}O_{7+\delta}$ – GDC composite cathode shows improved catalytic activity for ORR, where the ASRs are 0.15 and 0.08 Ω cm^2, respectively, at 650 and 700 °C. In addition, the potential of the $YBaCo_{3.2}Ga_{0.7}Fe_{0.1}O_{7+\delta}$ composite material as a cathode candidate in IT-SOFCs is demonstrated by its high power and stable performance with an anode-supported single cell.

Chapter 5: Self-regenerating Co-Fe Nanoparticles on Perovskite Oxides as a Hydrocarbon Fuel Oxidation Catalyst in Solid Oxide Fuel Cells

5.1 INTRODUCTION

Metal nanoparticles decorated on oxide surfaces have been widely studied as catalysts in several chemical and electrochemical processes, including automotive emission control, synthesis gas generation, and SOFCs. The high surface-to-volume ratio of the nanoparticles enhances the overall catalytic activity by providing a large amount of active sites on the surface and potential synergistic effects on the interface between the metal and oxide phases.[116] In order to overcome the severe carbon build-up with hydrocarbon fuels and the microcrack formation during the reduction and oxidation (redox) cycles with the Ni cermet as the conventional anode material of SOFCs,[117] many oxide materials with high coking resistance and excellent redox stability have been investigated, but the poor catalytic activity of oxides limits the cell performance.[35,83,118,119] Performance improvements have been attempted by decorating precious metal nanoparticles on the oxide surface as active catalysts through a chemical deposition process, such as infiltration or electrodeposition.[120,121] However, the deposited nanoparticles often distribute closely and aggregate easily at high temperatures[120], and the nanoparticle coarsening leads to irreversible performance degradation.[3]

Metal nanoparticles exsolved from perovskite oxides have received much attention as alternative anode materials for SOFCs because of their highly dispersed distribution on the oxide surface with a size of tens of nm. The exsolution phenomenon involves the cations in the perovskite lattice precipitate *in-situ* on the oxide surface under reducing

---

Lai, K.-Y.; Manthiram, A. Self-regenerating Co-Fe Nanoparticles on Perovskite Oxides as a Hydrocarbon Fuel Oxidation Catalyst in Solid Oxide Fuel Cells. *Chem. Mater.* 2018. Manthiram, A. supervised the project.

conditions, and it avoids the time-consuming process and expensive precursors of the traditional infiltration process. The capability of cation precipitation is primarily determined by the intrinsic reducibility of the metal oxide and the non-stoichiometry of the perovskite oxide[66], so easily-reducible precious metals (Rh, Pt[63], Pd[122], and Ru[70]) and some first-row transition metals (Fe, Co[65], and Ni[123]) exsolved on perovskite oxides have been applied as catalytically active materials. As a result, the SOFC performance is greatly improved by the exsolved nanocatalysts. For example, the Barnett group has showed that the performance with a $La_{0.8}Sr_{0.2}Cr_{0.82}Ru_{0.18}O_3$ – $Gd_{0.2}Ce_{0.8}O_{1.9}$ (GDC) composite anode was 2 and 1.5 times of the performances of, respectively, the $La_{0.8}Sr_{0.2}CrO_3$ – GDC and $La_{0.8}Sr_{0.2}CrO_3$ – GDC – 5 % RuO_2 anodes.[70]

The strong interaction between the exsolved particles and their parent oxide provides better thermal stability and catalytic functionality. The nanocatalysts pinned on the oxide show better coking resistance and lower aggregation rate than the nanoparticles prepared by other chemical deposition processes.[67] Chen group demonstrated a Ruddlesden-Popper anode material, $Pr_{0.8}Sr_{1.2}(Co, Fe)_{0.8}Nb_{0.2}O_4$, with exsolved Co-Fe nanoparticles as a coking-resistant anode material with direct methane fuel, and the long-term performance with H_2 – 50 ppm of H_2S fuel further presented reasonable sulfur tolerance and excellent thermal stability of the composite anode. However, the degradation with hydrocarbon fuel was not negligible in the long-term test, which might be caused by the slow accumulation of carbon deposition.[65] Meanwhile, the Barnett group found that the significant particle growth of the exsolved nanoparticles is noticeable and it leads to performance degradation. The Ni nanoparticle size on $La_{0.8}Sr_{0.2}Cr_{0.82}Ni_{0.18}O_3$ increased from 5 to 60 nm after 300 h of reduction at 800 °C.[123] Thus, effective methods for catalytic reactivation and suppressed particle growth rate of exsolved nanoparticles are needed.

Self-regeneration of exsolved metal nanoparticles could overcome the above challenges by controlling the redox conditions.[62,64,124] In an oxidizing environment, the exsolved metal nanoparticles dissolve and reincorporate into the B site of the perovskite oxide lattice, and the easily-reduced cations precipitate on the surface again in reducing conditions. This reversible behavior benefits the catalytic recovery by reconstructing the surface morphology, and the unwanted carbon deposition could be removed by the oxidation process. However, the temperature of the self-regeneration process is generally reported to be at least 800 – 900 °C,[62–68,70,122,123] which might become an obstacle in practical SOFCs because irreversible performance degradation might be induced by the electrode microstructure coarsening and unwanted chemical reactions at the interface between the adjacent component materials in the system. The high operation or process temperatures also exclude low-cost Fe-Cr alloy as an interconnect material because the chromia insulator formation on the alloy surface and cathode poisoning effect by chromia vapor become more severe at higher operating temperatures.[125] Therefore, a lower temperature in the intermediate range of ≤ 700 °C for self-regeneration is preferred for extending the device lifetime.

Our goal is to explore the reversibility of the self-regenerating nanoparticles at relatively low temperatures and validate its application in SOFCs with hydrocarbon fuels. Here, we demonstrate a new perovskite anode material $La_{0.3}Sr_{0.7}Cr_{0.3}Fe_{0.6}Co_{0.1}O_{3-\delta}$ (LSCrFeCo10) with exsolved Co-Fe nanoparticles as electrochemically active catalysts. This material is derived from $La_{0.3}Sr_{0.7}Cr_{0.3}Fe_{0.7}O_{3-\delta}$ (LSCrFe) of the $La_{1-x}Sr_xCr_{1-y}Fe_yO_3$ perovskite family, which have been studied as anode materials for SOFCs and catalysts for hydrocarbon reforming and oxidation.[83,126–129] Compared to the Ti-containing perovskite oxides, Cr and Fe in the perovskite lattice allows B cation reduction and oxygen release at relatively lower temperatures, which may facilitate the cation exsolution process. The Fe

metal exsolved from LSCrFe was observed in extremely reducing atmospheres (pO_2 = $10^{-21.5}$ atm) at 800 °C.[128] In our study here, 10 at. % Co is doped to give LSCrFeCo10 due to the high reducibility of Co for decreasing the exsolution temperature and enhancing the catalytic activity. A-site deficient $(La_{0.3}Sr_{0.7})_{0.95}Cr_{0.3}Fe_{0.6}Co_{0.1}O_{3-\delta}$ (A-LSCrFeCo10) is also studied for accelerating the exsolution.[66] Furthermore, the performance enhancement, redox stability, tolerance to sulfur impurity, resistance to coking, and long-term performance of the electrolyte-supported single cell with exsolved Co-Fe nanocatalysts on the LSCrFeCo10 anode are evaluated to demonstrate the potential of the LSCrFeCo10 anode in practical SOFCs at relatively low temperatures.

5.2 Experimental Section

5.2.1 Materials synthesis and characterization

The perovskite anode materials, including LSCrFe, LSCrFeCo10, and A-LSCrFeCo10, were synthesized by SSR of stoichiometric ratios of La_2O_3, $SrCO_3$, Cr_2O_3, Fe_3O_4, and Co_3O_4. After mixing the precursor chemicals with ethanol in a mortar and pestle, the raw materials were calcined at 1000 °C. The calcined powder was pressed into a pellet and sintered at 1350 °C with intermediate grinding and mixing. The cathode material $La_{0.6}Sr_{0.4}Co_{0.2}Fe_{0.8}O_3$ (LSCF) was prepared by an EDTA–citric acid complexing method. A proper amounts of $La(NO_3)_2{\cdot}6H_2O$, $Sr(NO_3)_2$, $Co(NO_3)_2{\cdot}9H_2O$, and $Fe(NO_3)_3{\cdot}9H_2O$ were dissolved and mixed in deionized water, and then citric acid and EDTA were added into the solution as chelating agents. The molar ratio of citric acid, EDTA, and total amount of metal ions (La, Sr, Co, and Fe) was 1.5 : 1 : 1. After adjusting the pH value to 7 with NH_4OH, the solution was continuously stirred at room temperature for 12 h. The water was slowly evaporated by stirring and heating at 120 °C overnight, and

the gel was further dried at 200 °C and calcined at 600 °C. Then, the powder was ground and sintered at 1000 °C to achieve a single-phase material.

The phase evolution and redox stability of the anode materials were analyzed by XRD after annealing the powder at 700 and 800 °C for 24 h under 5% H_2 – Ar and ambient air, respectively, as reducing and oxidizing atmospheres. The heating and cooling rates of the annealing processes was 2 °C min^{-1}. The bulk samples for conductivity and thermal expansion evaluation were made by pressing the ball-milled powder into a pellet or bar shape and sintering at 1350 °C for 12 h. The elemental compositions were identified by an inductively coupled plasma – optical emission spectrometry (ICP-OES) (Varian 715-ES). The thermal behavior was evaluated by TGA with 5 % H_2 – Ar gas to simulate the anodic environment.

The morphology of the annealed samples was observed with a field emission SEM (Hitachi S5500). All SEM samples were examined by 5 - 10 kV electron beam to reduce the surface charging, and no conductive material, such as Au or Pt, was deposited in order to reveal the true morphology. The structural characterization and elemental distribution were determined, respectively, by high resolution transmission electron microscopy (HR-TEM) and scanning transmission electron microscopy (STEM) (JEOL 2010F), along with EDX (Bruker Quantax 4010).

5.2.2 Single cell evaluation

The fabrication method of an electrolyte-supported single cell was detailed in Chapter 2.4. The electrochemical performance of the electrolyte-supported single cells was evaluated from 700 to 850 °C with a homemade testing system. The cathode was exposed to ambient air and the anode was tested with various fuels, including H_2 – 3 % H_2O, H_2 –

27 ppm of H_2S, and C_3H_8 – 3 % H_2O. The humidified fuel was made by passing the fuel through a water bubbler at room temperature. Since H_2S is able to dissolve into water, the hydrogen with 27 ppm of H_2S was applied without moisture. The polarization curve and single-cell impedance were recorded, respectively, with an Arbin cycler (BT-G) and EIS (Solartron 1260 FRA). The scanning frequency of the EIS was 10^6 to 10^{-1} Hz, and the amplitude was 10 mV under open-circuit condition. The redox cycle of the anode was conducted by replacing the fuel gas with dry N_2 for 5 mins and switching to dry air for various times, and a cycle was completed by reversing the above step. Due to the short interval of N_2 gas, the description of the redox cycle in the content will briefly note the fuel and air without indicating the N_2 gas.

5.3 Results and Discussions

5.3.1 Phase Characterization of Perovskite Oxides

In order to achieve the phase purity of LSCrFe, LSCrFeCo10, and A-LSCrFeCo10, the materials were all synthesized by repeating a sintering process at 1350 °C and pulverization at least two times. Figure 5.1 shows that the XRD patterns of pristine LSCrFeCo10 and LSCrFe with a fit to rhombohedral symmetry ($R\bar{3}c$), which coincides with the structure of the $La_{1-x}Sr_xCr_{1-y}Fe_yO_3$ perovskite family.[128,130,131] A trace amount of $SrCrO_4$ impurity ($P12_1/c1$) is detected in pristine LSCrFe, suggesting that the Cr content is slightly above the Cr solubility limit in $La_{0.3}Sr_{0.7}Cr_xFe_{1-x}O_{3-\delta}$. Based on the ICP-OES result, the actual cation ratio of La : Sr : Cr : Fe in LSCrFe is 0.294 : 0.701 : 0.302 : 0.698, and the deviation of La content from the nominal composition might be due to the rapid moisture absorption of the La_2O_3 reagent. The slight A-site deficiency is also observed in LSCrFeCo10 where the actual cation ratio of La : Sr : Cr : Fe : Co determined by ICP-OES

is 0.295 : 0.698 : 0.294 : 0.603 : 0.103. Although there is no $SrCrO_4$ phase in the XRD data of pristine LSCrFeCo10, this impurity phase is still found in the later redox stability evaluation. The low-intensity peaks of the $SrCrO_4$ phase in both the LSCrFe and LSCrFeCo10 materials show that the limited amount of $SrCrO_4$ is close to the detection limitation of XRD. Compared to the estimated Cr solubility value of 0.33 in $La_{0.33}Sr_{0.67}Cr_xFe_{1-x}O_3$ perovskite[128,132], the Cr solubility in $La_{0.3}Sr_{0.7}Cr_xFe_{1-x}O_3$ perovskite might be shifted to about 0.3 due to the higher Sr content and slight A-site deficiency.

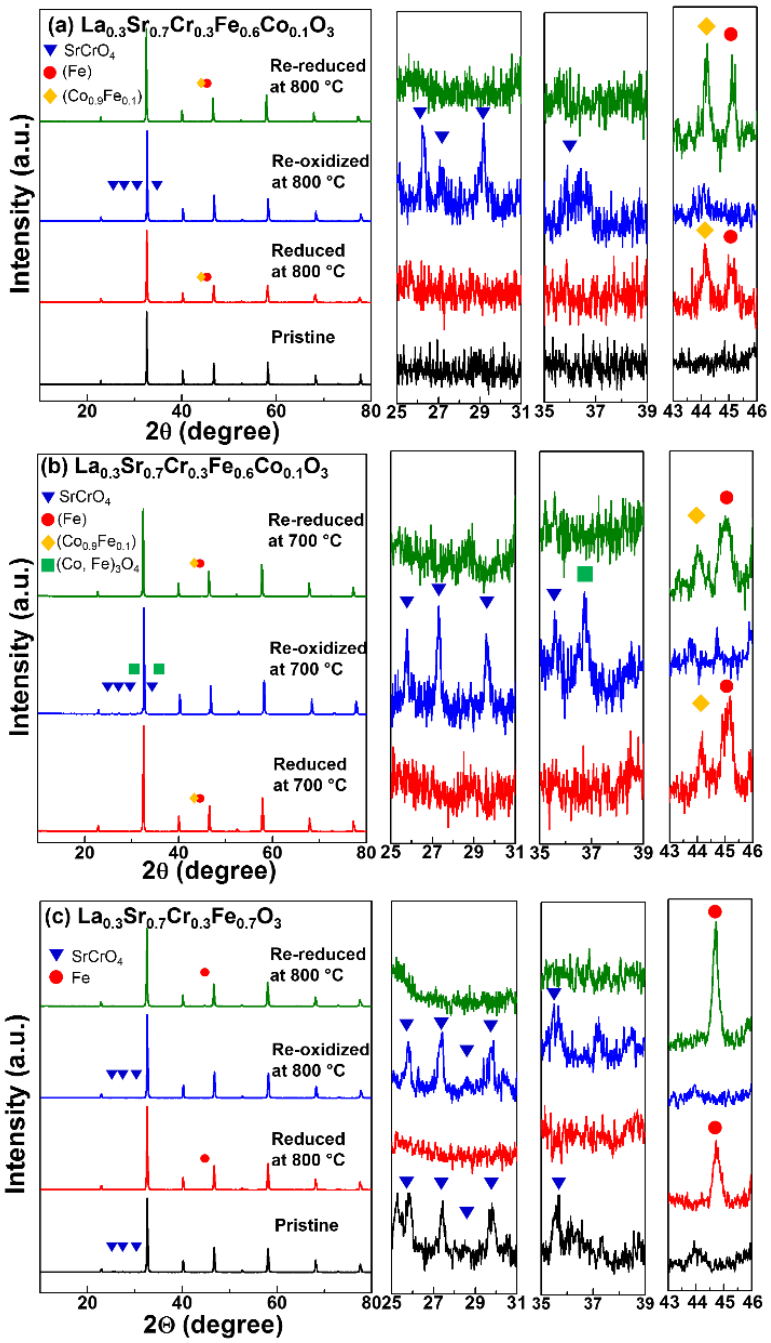

Figure 5.1 Room-temperature (RT) XRD patterns of the pristine and annealed LSCrFeCo10 powder with the redox temperatures of (a) 800 °C and (b) 700 °C and (c) the pristine and annealed LSCrFe powder with a redox temperature of 800 °C. (Fe) and ($Co_{0.9}Fe_{0.1}$) are, respectively, Co-Fe alloy in body-centered and face-centered cubic structures.

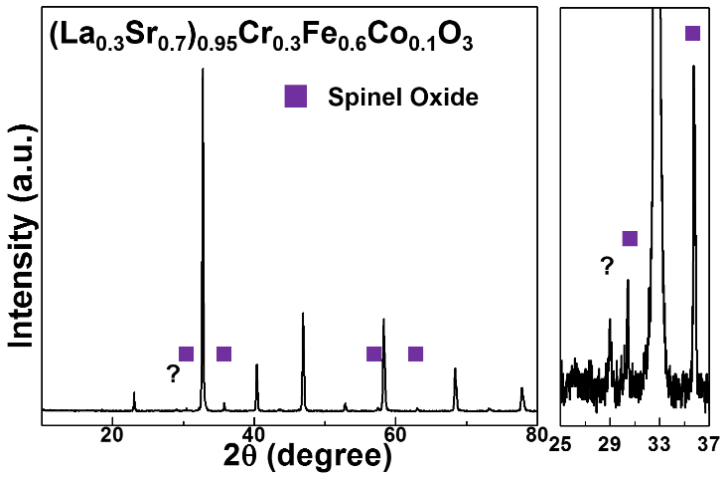

Figure 5.2 RT-XRD pattern of the pristine A-LSCrFeCo10.

On the other hand, Fe-rich $(Fe,Cr)_3O_4$ spinel oxide ($Fd\bar{3}m$) appears as an impurity phase in pristine A-LSCrFeCo10, which is displayed in Figure 5.2, and it indicates that single phase A-LSCrFeCo10 cannot be formed with 5 % A-site deficiency. In order to maintain charge neutrality, the compensation of non-stoichiometric deficiency is achieved either by forming built-in oxygen vacancies or increasing average cation oxidation state. Based on the iodometric titration, LSCrFe and LSCrFeCo10 only have less than 0.03 of oxygen deficiency (δ) at room temperature. The limited built-in oxygen vacancies in this $La_{1-x}Sr_xCr_{1-y}Fe_yO_{3-\delta}$ family is commonly found, and our data are consistent with limited oxygen vacancies in $La_{0.3}Sr_{0.7}Cr_{0.3}Fe_{0.7}O_{2.97}$ ($\delta = 0.03$), which was determined by refinement calculation of room-temperature neutron diffraction data.[83] In addition, Lü et al. reported that $(La_{0.75}Sr_{0.25})_{0.95}Cr_{0.6}Fe_{0.4}O_{3-\delta}$ had a very low amount of oxygen vacancies because no penta-coordinated Fe^{3+} was detected in the room-temperature Mössbauer spectra.[130] The charge compensation of the Sr^{+2} dopant and 5 % A-site cation deficiency in $(La_{0.75}Sr_{0.25})_{0.95}Cr_{0.6}Fe_{0.4}O_{3-\delta}$ was fulfilled mainly by oxidizing Cr^{+3} to Cr^{+4}. In comparison

to $(La_{0.75}Sr_{0.25})_{0.95}Cr_{0.6}Fe_{0.4}O_{3-\delta}$, the 5 % A-site cation deficiency in A-LSCrFeCo10 might be beyond the compensation ability of B-site cation oxidation due to higher Sr content and lower Cr content. Since Fe-rich $(Fe,Cr)_3O_4$ is formed as the secondary phase, the composition of this rhombohedral perovskite phase should be close to stoichiometric. A similar mechanism of rutile secondary phase formation was also found in $La_{0.4}Sr_{0.4}Ti_{1-x}Ni_xO_{3-\delta}$ when the incomplete compensation of charge neutrality was induced by substituting aliovalent cations or introducing cation deficiency.[66] Since the single phase A-LSCrFeCo10 with a desired composition cannot be achieved, only LSCrFe and LSCrFeCo10 are evaluated as anode materials in the following experiments.

5.3.2 Phase Stability and Reversibility

The redox stability and phase reversibility were evaluated by annealing the powder samples alternatively under 200 mL min^{-1} of 5 % H_2 – Ar and ambient air for 24 h, respectively, as reducing and oxidizing environment. Figure 5.1 also displays the room-temperature XRD (RT-XRD) patterns of LSCrFeCo10 and LSCrFe after redox tests. The excellent stability of the perovskite phase in both reducing and oxidizing environments is indicated by the preservation of the rhombohedral structure after annealing at 700 and 800 °C for 24 h. Figure 5.3 shows the thermal behaviors of LSCrFeCo10 and LSCrFe in 5 % H_2 – Ar. The TGA evaluation was conducted with a heating rate of 4 °C min^{-1} and an annealing process at 800 °C for 2 h, and the initial oxygen content was determined by iodometric titration at room temperature. Although both materials have a similar behavior for losing their lattice oxygen with increasing temperatures, LSCrFeCo10 has a lower starting temperature at 340 °C for a rapid oxygen loss and a lower oxygen content of 2.54 at 800 °C due to the 10 at. % substitution of highly reducible Co. Among the $LaBO_3$ (B =

Cr, Mn, Fe, Co, and Ni) perovskite oxides, the relative resistance to structural decomposition, which has an opposite trend for material reducibility, decreases in the order Cr > Fe > Mn > Co > Ni when the partial oxygen pressure decreases.[133,134] Importantly, the oxygen content of LSCrFeCo10 and LSCrFe becomes stable after 1 h of the annealing process at 800 °C and the limited lattice oxygen loss suggests that both materials have a good thermal stability in the reducing operation environment.

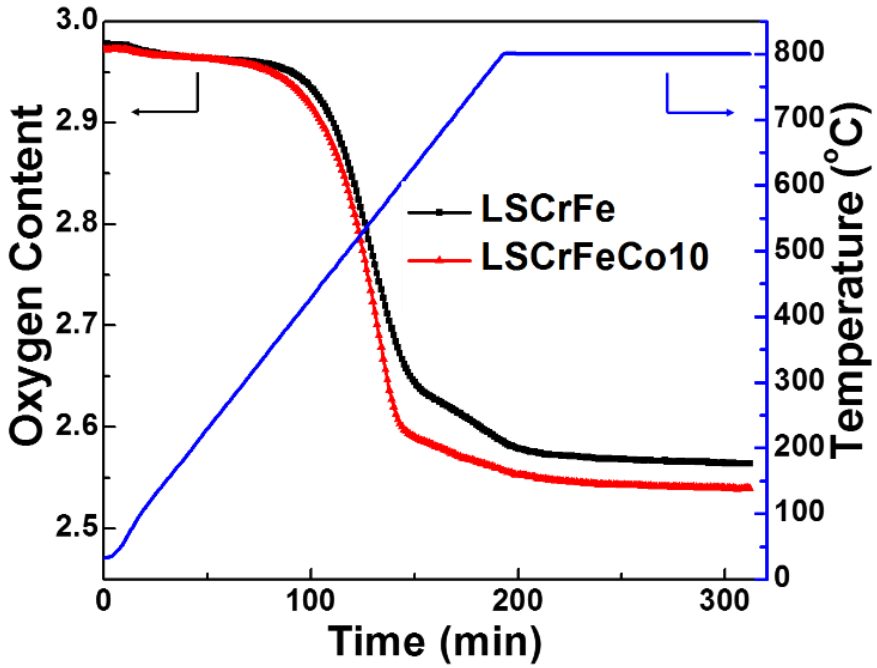

Figure 5.3 The TGA results of LSCrFe and LSCrFeCo10 with 5 % H_2 – Ar. The initial oxygen content of the powder samples was determined by iodometric titration at room temperature.

$SrCrO_4$ is a common impurity of the reoxidized LSCrFeCo10 and LSCrFe samples after annealing at 700 and 800 °C, and this phase was also observed in the other chromite perovskite materials after a reoxidizing process in the literature.[71,129] Fortunately, $SrCrO_4$

completely decomposes in the reducing atmosphere above 600 °C and cannot be observed in the reduced samples.[71] Another impurity, $(Co, Fe)_3O_4$ spinel phase ($Fd\bar{3}m$), only appears in the reoxidized LSCrFeCo10 at 700 °C, and it might be the result of sluggish cation reincorporation rate to the perovskite lattice. Nonetheless, except for the Co-Fe alloy in face-centered cubic structure and the Fe metal / Co-Fe alloy in body-centered cubic structure as the exsolved species, no other secondary phase is detected after the rereducing process.[135] Therefore, among the samples annealed in 5 % H_2 – Ar, their matched perovskite phase and secondary phases suggest excellent phase reversibility of LSCrFeCo10 at 700 and 800 °C during a redox process.

Figure 5.4 shows the morphology of the exsolved nanoparticles on the perovskite oxide surface after annealing with 5 % H_2 – Ar for 24 h. The nanoparticles exsolved at 700 °C in the reduced and rereduced LSCrFeCo10 samples are randomly distributed on the oxide surface with a similar sphere shape, and their sizes are about 30 nm. In Figure 5.4(b), most of the exsolved particles on the surface of the reduced powder sample disappear after annealing in air. The rough surface with the eliminated nanoparticles indicates that the exsolved particles reincorporate back into the perovskite lattice at 700 °C. The surface dents are a result of nanoparticle exsolution during the initial reduction process.[67,136] However, some particles remain on the reoxidized surface, and these particles might suggest an incomplete cation reincorporation process. Figure 5.5(a) displays the same position as in Figure 5.4(b) with a lower magnification. Figure 5.5(b) shows another position with more irregular-shaped particles.

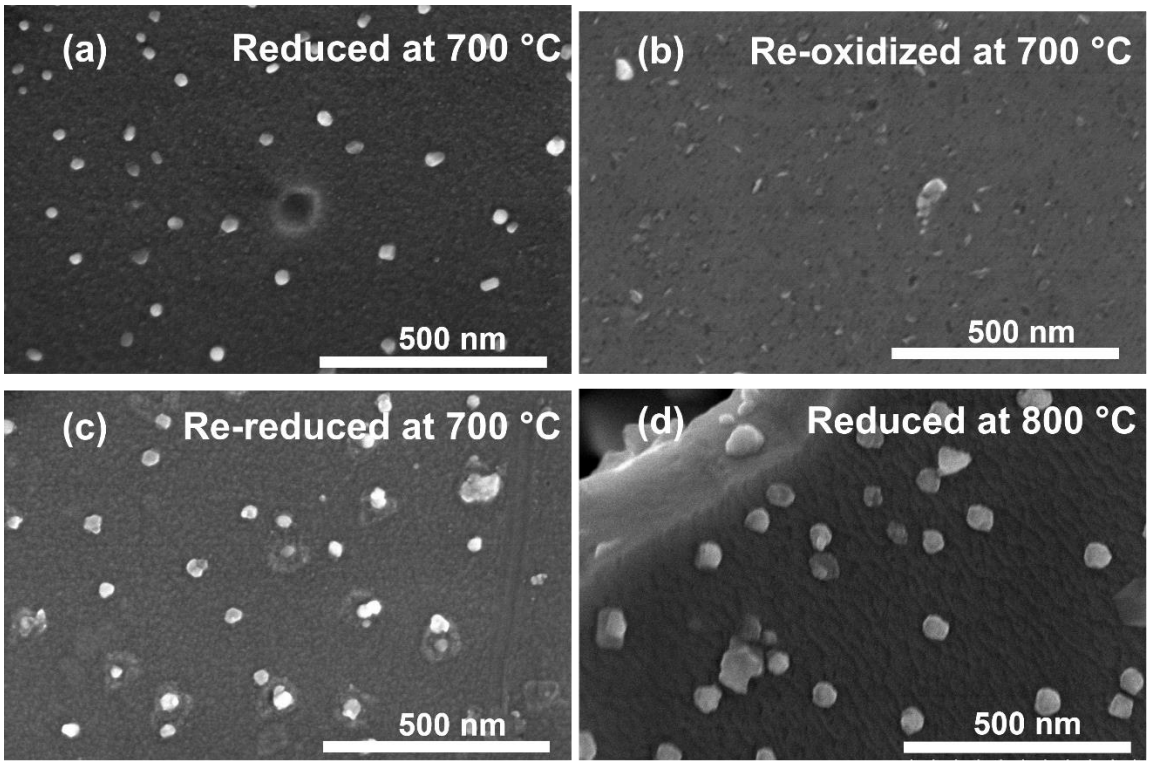

Figure 5.4 SEM images of the surface morphology on the LSCrFeCo10 powder sample after (a) a reducing process at 700 °C for 24 h, (b) a reoxidizing process at 700 °C in air for 24 h, (c) a rereducing process at 700 °C for 24 h, and (d) a reducing processing at 800 °C for 24 h. The reducing process is in 5 % H_2 – Ar gas.

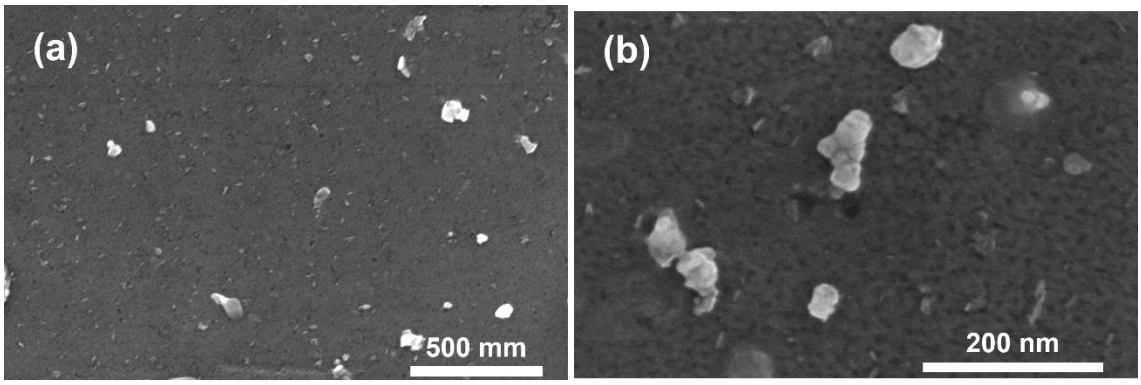

Figure 5.5. SEM images of the surface morphology on the LSCrFeCo10 powder sample after reoxidizing in air at 700 °C for 24 h. Images (a) and (b) were taken at different magnifications.

The estimated diameter of the irregular-shaped particles generally as displayed in Figure 5.4(b) and 5.5 is over 1.5 times of that of the exsolved particles shown in Figure 5.4(a) and 4(c). The volume of Co_3O_4 spinel phase is theoretically double the volume of Co metal, and the corresponding diameter change from Co to Co_3O_4 should be 126 %. Thus, the irregular-shaped particle formation might be due to the oxidized nanoparticle growth. Also, another question that arises is how the self-regeneration of nanoparticles occurs from coarsened spinel particles in the reducing atmosphere.

In order to answer the above question, the surface morphology evolution of the cross-sectional surface of a dense sample during the redox cycle was carefully examined, and the analysis is detailed in our other paper.[135] Since powder samples often have inclined and uneven surfaces, a bulk sample provides more precise observation of the morphology evolution of nanoparticles. In contrast to the complete cation reincorporation after a reoxidation process at 800 °C, large Co-rich $(Co, Fe)_3O_4$ particles of the spinel phase are found to remain on the LSCrFeCo10 surface at 700 °C. Although the transition-metal oxide coarsens quickly in air, the disintegration of a spinel particle and the redispersion of the metal nanoparticles lead to complete self-regeneration when the reducing gas is supplied again at 700 °C. With the assistance of the strong metal-oxide interaction between the metallic particles and the perovskite oxide, the hemispherical-like nanoparticles are formed from reduced spinel oxide by minimizing the metallic surface and surface energy. The consistency in the phase, morphology, and size and distribution of the nanoparticles before and after the redox process (Figure 5.4(a) and 5.4(c)) indicates that the exsolved nanoparticles are self-regeneratable even at 700 °C.

The nanoparticle size strongly depends on the annealing temperature. In Figure 5.4(c), the larger nanoparticle size on the reduced LSCrFeCo10 sample at 800 °C suggests higher particle growth rate is induced by a higher annealing temperature. The particle

density on the reduced oxide surface of a dense sample decreases significantly from ~ 160 μm^{-2} to ~ 25 μm^{-2} when the reducing temperature increases from 700 to 800 °C.[135] About 6 % of the reduced oxide surface is covered by nanoparticles regardless of the annealing temperature. Since smaller nanoparticles have a higher area-to-volume ratio and longer metal-oxide-gas boundary, the nanoparticles exsolved at 700 °C might provide more catalytically active sites for fuel oxidation reaction. Therefore, with more active sites and slower particle growth rate of the exsolved nanoparticles, the lower operation temperature ensures better long-term performance stability.

Figure 5.6 shows the STEM images and the EDX elemental mapping images of the LSCrFeCo10 powder, which was reduced at 800 °C for 24 h. The Co-rich nanoparticles are clearly observed and there is no other noticeable segregated element on the mapping images. Although exsolved Fe metal is found in the XRD, the high concentration of Fe in the perovskite matrix might obscure the signal of Fe nanoparticles in the EDX mapping result. The area without significant Co segregation only contains trace amounts of Co signal and it suggests that most Co in LSCrFeCo10 is exsolved on the surface to form nanoparticles in the diameter of 40 – 80 nm after reducing at 800 °C. Figure 5.6(b) displays the HR-TEM image of a Co-rich nanoparticle and the perovskite matrix. The lattice fringe spacing of 0.212 nm is closest to the (1 0 1) plane of the $Co_{0.95}Fe_{0.05}$ hexagonal phase ($P6_3/mmc$), and this result also verifies the composition variation of Co-Fe nanoparticles in a small range. Meanwhile, the 0.278 nm spacing of the other fringes matches well with the (1 1 0) plane of reduced LSCrFeCo10.

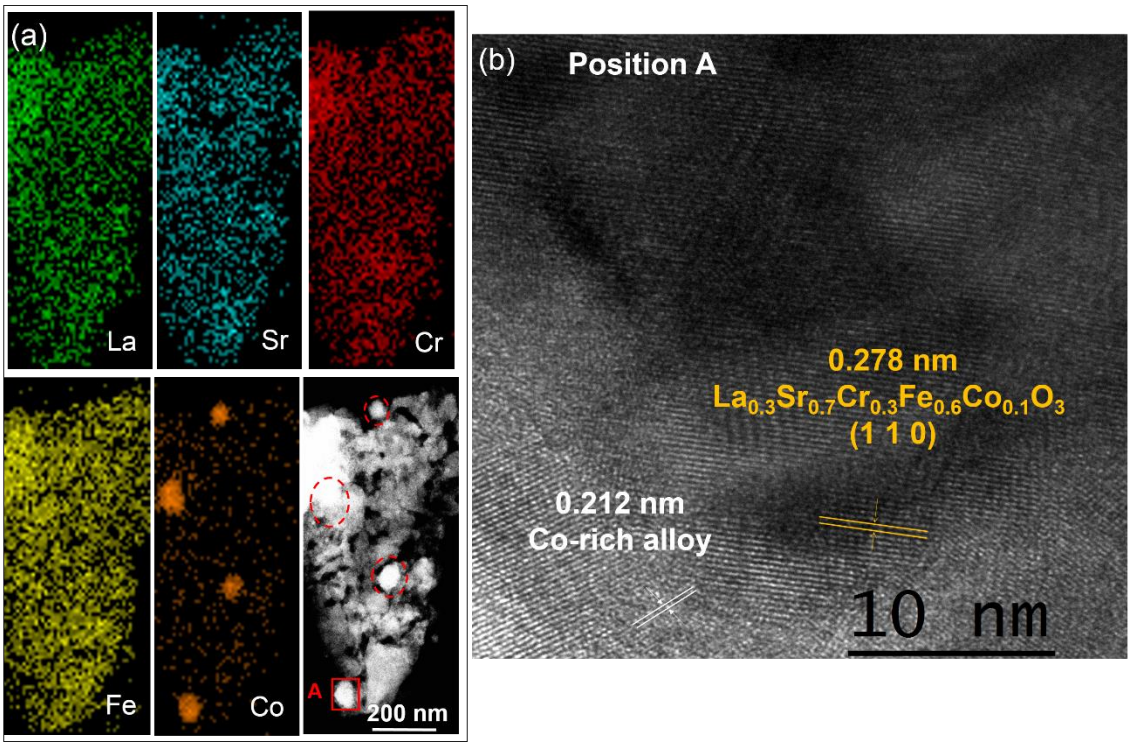

Figure 5.6 (a) EDX mapping results and STEM image of reduced LSCrFeCo10 powder sample at 800 °C. The Co-rich nanoparticles are marked with red dashed circles. (b) HR-TEM image of the exsolved nanoparticle and its perovskite matrix on Position A, which is marked with a red square.

5.3.3 Electrical Conductivity and Thermal Expansion Behavior

Electrical conductivity was measured by van der Pauw method in air and 5 % H_2 – Ar at a rate of 3 °C min^{-1}. Figure 5.7 shows the electrical conductivity of LSCrFeCo10 at 500 – 900 °C in both oxidizing and reducing atmospheres. The total conductivity continuously increases in air from room temperature and reaches its highest value of 100 S cm^{-1} at 520 °C. LSCrFeCo10 then exhibits a slowly decreasing conductivity to 52 S cm^{-1} while the temperature increases to 900 °C. The temperature dependence of the electrical

conductivity above 500 °C in air might be the result of the oxygen vacancy formation, the B-site cation reduction, and the charge carrier decrease.

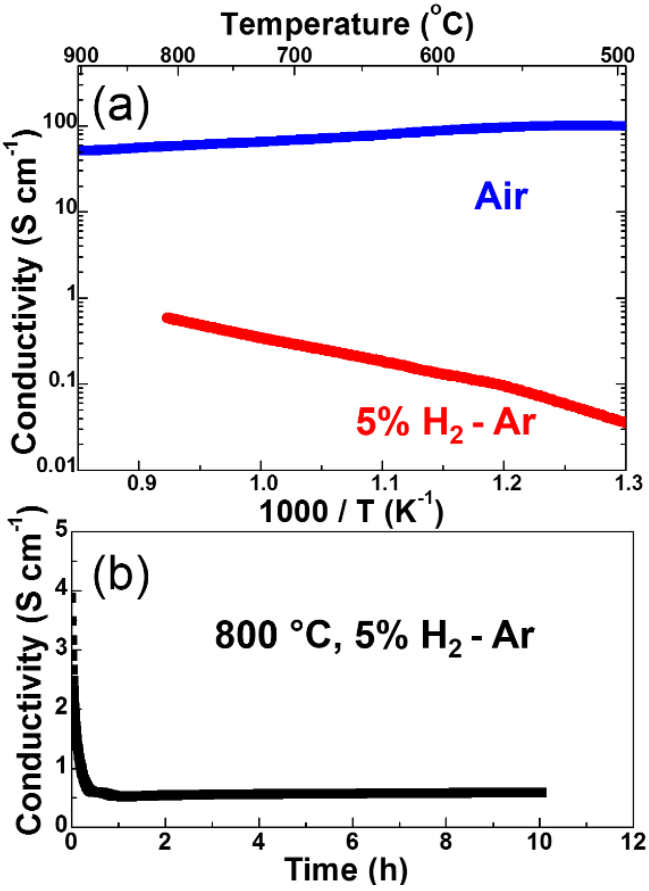

Figure 5.7 (a) Electrical conductivity of LSCrFeCo10 versus temperature in air and 5 % H_2 – Ar with a heating rate of 3 °C min^{-1}. (b) Conductivity of LSCrFeCo10 versus time during the annealing process at 800 °C in 5 % H_2 – Ar for achieving the equilibrium of a dense pellet sample.

In order to achieve the equilibrium in the reducing atmosphere, the pellet sample was annealed in 5 % H_2 – Ar for 10 h before the temperature-dependent measurement. Figure 5.7(b) displays that the conductivity during the annealing process drops quickly in

the first hour and becomes stable in the following time. Compared to the conductivity in air, LSCrFeCo10 has much lower electrical conductivity with a range of 0.04 to 0.59 S cm^{-1} at 500 to 800 °C in 5 % H_2 – Ar. The increasing conductivity with temperature could be explained by the small polaron hopping mechanism, which is consistent with the conductivity behavior of LSCrFe in the reducing atmosphere.[132]

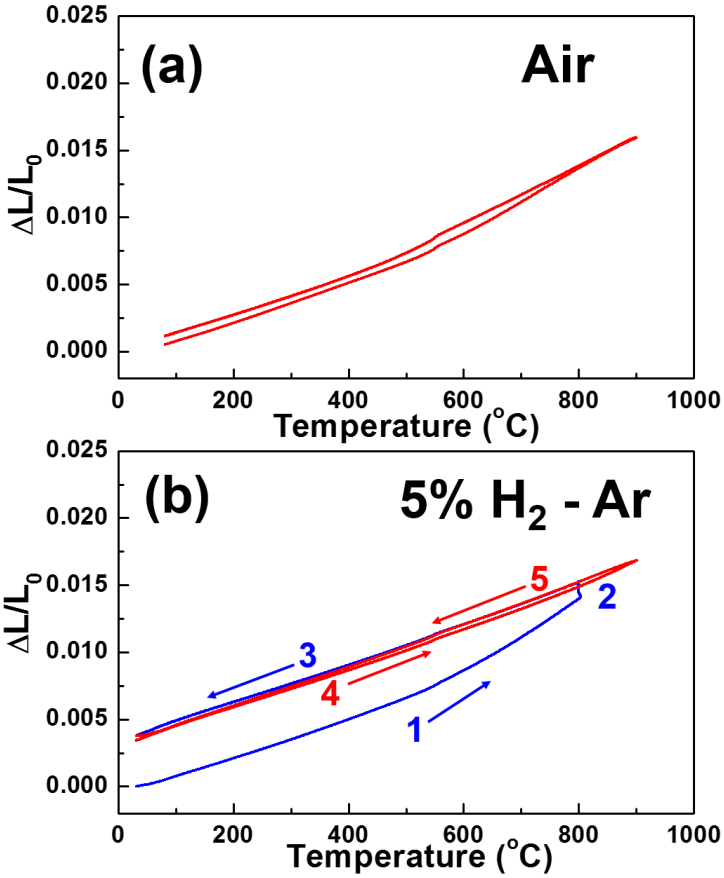

Figure 5.8 Thermal expansion curves of a dense LSCrFeCo10 bar sample in (a) air and (b) 5 % H_2 – Ar with heating and cooling rates of 3 °C min^{-1}. In order to achieve equilibrium in the reducing atmosphere, the bar sample was annealed at 800 °C for 10 h in the step 2. The thermal expansion coefficients under reducing conditions were calculated using the second cycle, which is displayed as curves 4 and 5 in red color.

Figure 5.8 shows the thermal expansion behaviors of LSCrFeCo10 in air and 5 % H_2 – Ar with heating and cooling rates of 3 °C min^{-1}. The thermal expansion coefficient (TEC) of LSCrFeCo10 is 11.5 – 17.4 × 10^{-6} K^{-1} and 12.5 – 15.0 × 10^{-6} K^{-1}, respectively, in air and 5 % H_2 – Ar from 200 to 900 °C. In order to achieve the equilibrium, the bar sample was annealed at 800 °C in 5 % H_2 – Ar for 10 h, and then the thermal behavior was measured in the same atmosphere. Although the TECs are slightly higher than the LSGM electrolyte, the composite anode with GDC could mitigate the TEC mismatch and lessen the thermal stress during cell operation and redox process.

5.3.4 Electrochemical Performance

To evaluate the catalytic enhancement of Co-Fe exsolved nanoparticles, LSGM electrolyte-supported single cells with LSCrFe and LSCrFeCo10 composite anodes were tested. The composite anode was made by mixing the perovskite oxide material with GDC in a weight ratio of 50 : 50 to increase the three phase boundary and provide a pathway with high oxide-ion conductivity.[83] In addition, GDC is well-known to resist coking and H_2S poisoning. The single cell performance with an LSCrFe composite anode, seen in Figure 5.9(a), reaches 0.20, 0.34, 0.43, and 0.50 W cm^{-2}, respectively, at 700, 750, 800, and 850 °C with 30 mL min^{-1} of H_2 – 3 % H_2O.

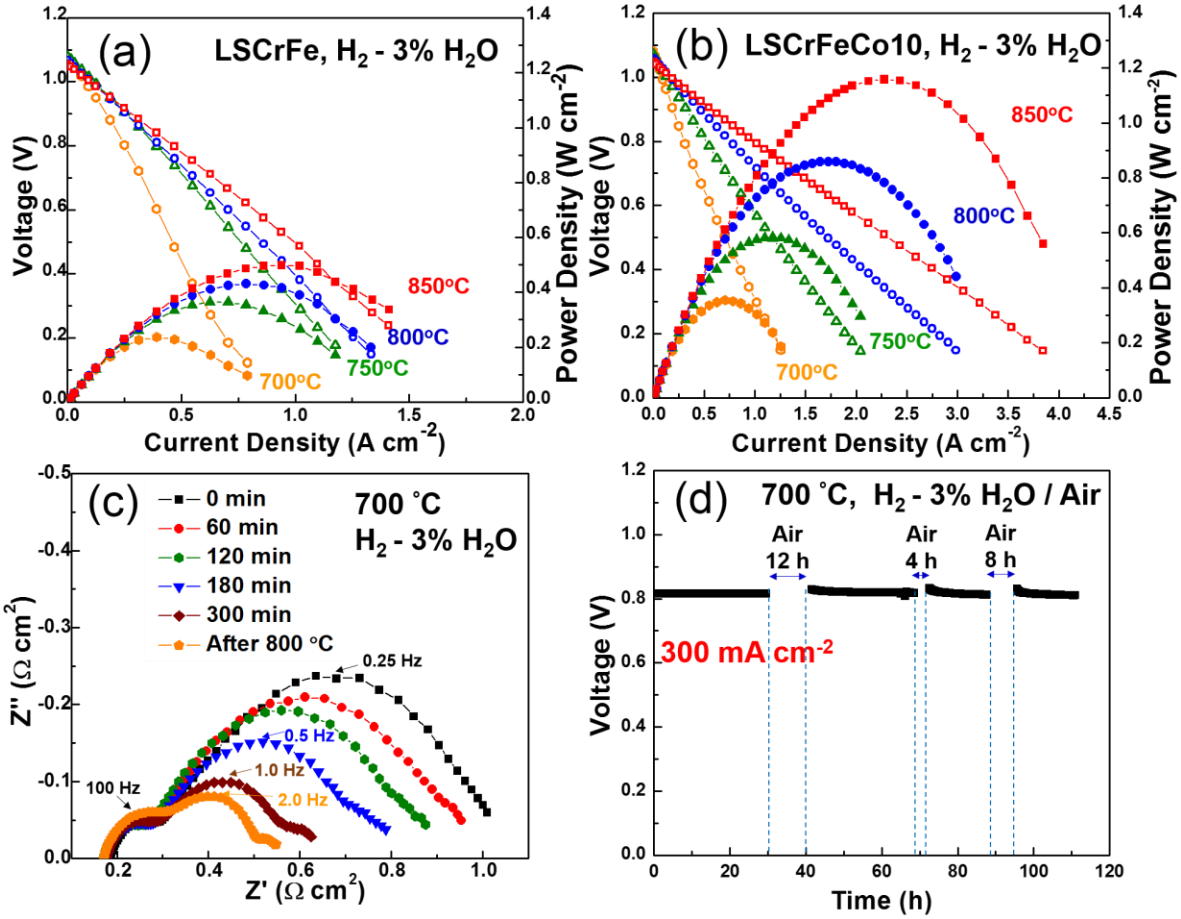

Figure 5.9 Electrochemical performance evaluation of an electrolyte-supported single cells with (a) LSCrFe – GDC composite anode and (b) LSCrFeCo10 – GDC composite anode under H_2 – 3 % H_2O. (c) Nyquist diagram of the electrochemical impedance data for an electrolyte-supported single cell with LSCrFeCo10 – GDC composite anode under open-circuit voltage at 700 °C. The activation time started when 30 mL min^{-1} H_2 – 3 % H_2O was applied. The annealing process at 800 °C for 1 h was conducted with heating and cooling rates of 2 °C min^{-1} after the activation process at 700 °C for 5 h. (d) The redox stability evaluation under a constant current density of 300 mA cm^{-2} at 700 °C under H_2 – 3 % H_2O and air, respectively, as the fuel and the oxidant. The three redox cycles were conducted with various oxidation times.

The performance with an LSCrFe composite anode is slightly higher than the performance reported by Haag due to the thinner LSGM electrolyte.[83] Figure 5.9(b) shows

that the maximum power density of the single cell with the LSCrFeCo10 composite anode achieves 0.36, 0.60, 0.86, and 1.16 W cm^{-2}, respectively, at 700, 750, 800, and 850 °C with H_2 – 3 % H_2O. Compared to the performance with LSCrFe and LSCrFeCo10 anodes, more than 75 % and 100 % of the performance enhancement is, respectively, catalytically activated by the Co-Fe exsolved nanoparticles at below and above 800 °C. In this study, two identical single cells with the LSCrFeCo10 composite anode were tested and they had consistent maximum power densities under H_2 – 3 % H_2O at 700 – 850 °C. The single cell #1 was used in the performance evaluation with H_2 – 3 % H_2O and H_2 – 27 ppm of H_2S, and single cell #2 was measured with propane fuel to avoid the influence from H_2S.

It is worth noting that the initial anode activation of the LSCrFeCo10 composite anode at 700 °C is required for Co-Fe nanoparticle formation. Figure 5.9(c) displays the EIS results under open-circuit voltage with respect to activation time with H_2 – 3 % H_2O. According to Fowler's observation with similar anode materials and single cell configuration, the high-frequency (HF) and low-frequency (LF) semi-circle in the Nyquist diagram represents, respectively, the cathode and anode reaction.[131] Our data show that the dominant low-frequency semi-circle becomes smaller with time and the high-frequency semi-circle remains unchanged. After 5 h of the initial activation process, the total polarization resistance (R_p) from both the cathode and anode is about 0.46 Ω cm^{-2}. In addition, the R_p at 700 °C is further reduced to 0.39 Ω cm^{-2} after a short annealing process at 800 °C for 1 h with 2 °C min^{-1} heating and cooling rates, which could be the result of more Co-Fe exsolution and faster exsolution kinetics at 800 °C.

In order to verify the redox reversibility and cyclability of the LSCrFeCo10 composite anode, three redox cycles with 30 mL min^{-1} of air and different reoxidation times were conducted. Figure 5.9(d) demonstrates that the short-term performance at 700 °C under a constant current density of 300 mA cm^{-2} stays unchanged before and after the

reoxidation process with various processing times. In addition, another activation process was not needed when the atmosphere was switched from air to H_2 in a redox cycle. These results indicate that LSCrFeCo10 has excellent redox reversibility and cyclability regardless of oxidation time, and there is no detrimental effect on the performance after a redox process at 700 °C.

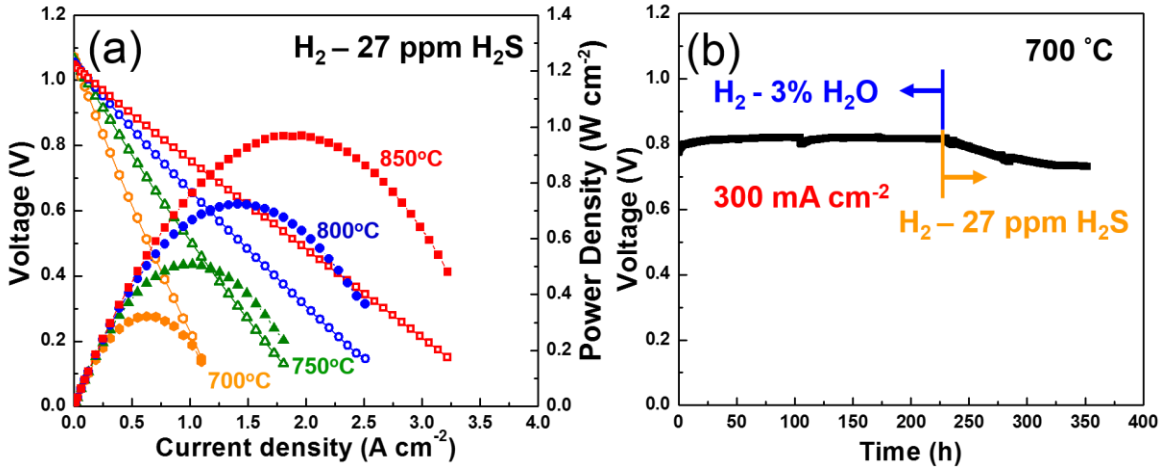

Figure 5.10 (a) The electrochemical performance evaluation of an electrolyte-supported single cell with LSCrFeCo10 – GDC composite anode under H_2 – 27 ppm of H_2S. (b) The long-term performance evaluation under a constant current density of 300 mA cm^{-2} at 700 °C with H_2 – 3 % H_2O and H_2 – 27 ppm of H_2S. These measurements were tested on single cell #1.

One of the advantages in using oxides as anode materials is their high tolerance of H_2S poisoning, so to verify this, the single cell performance of LSCrFeCo10 with 27 ppm of H_2S was also measured. The 30 ml min^{-1} of H_2 – 27 ppm of H_2S was applied for at least 30 mins under open-circuit voltage to achieve equilibrium before the performance evaluation at each operation temperature. Figure 5.10(a) demonstrates that the open-circuit voltage decreased less than 3 mV with the H_2S impurity present; however, the maximum

power density with H_2 – 27 ppm of H_2S was 12 - 14 % lower than the power density without H_2S impurity. The long-term performance with and without H_2S on the same single cell at 700 °C was also tested to understand the long-term effect of H_2S poisoning. It can be seen in Figure 5.10(b) that the performance under a constant current density of 300 mA cm^{-2} with H_2 – 3 % H_2O remained stable without noticeable degradation for more than 210 h.

When the fuel switched to H_2 – 27 ppm of H_2S, the voltage under the constant density slowly decreased from 0.82 to 0.73 V and became stabilized. This behavior matches Haag's observation on LSCrFe composite anode with H_2 – 22 ppm of H_2S, and it indicates that the LSCrFeCo10 perovskite with Co-Fe exsolved nanoparticles exhibits high H_2S tolerance just as its parent perovskite, LSCrFe, does. In addition, the ~11 % voltage drop under 300 mA cm^{-2} after 100 h is consistent with the range of maximum power density drop in the single cell-performance evaluation between H_2 – 3 % H_2O and H_2 – 27 ppm of H_2S.

Figure 5.11 shows the evolution of the SOFC's impedance after the (1) redox cycling with H_2 – 3 % H_2O and air, (2) long-term performance evaluation with H_2 – 3 % H_2O, and (3) long-term performance evaluation with H_2 – 27 ppm of H_2S. As the activation process shown in Figure 5.9(c), the HF and LF semicircles are easy to distinguish before the redox cycling, and the center of the LF semicircle gradually shifts from 0.25 to 2 Hz, causing the overlap between the two semicircles to increase. After the 3 redox cycles, the HF and LF semicircles shown in Figure 5.11 can no longer be easily distinguished. However, the value of R_p does not change significantly after the redox cycling. Following > 200 h of long-term performance evaluation with H_2 – 3 % H_2O, the impedance shape and R_p value remain unchanged. This agrees with no significant performance degradation from operation with H_2 – 3 % H_2O shown in Figure 5.10(b). On the other hand, the R_p value increases after operation with the H_2S impurity. The similar in shape between the HF

semicircles with and without H_2S impurity confirms that the HF semicircle pertains to oxygen reduction at the cathode. The LF intercept increases from 0.58 to 0.64 Ω cm^2 after applying H_2 – 27 ppm of H_2S. The shape change in the LF region indicates an increase in anode polarization due to H_2S poisoning, leading to performance degradation.

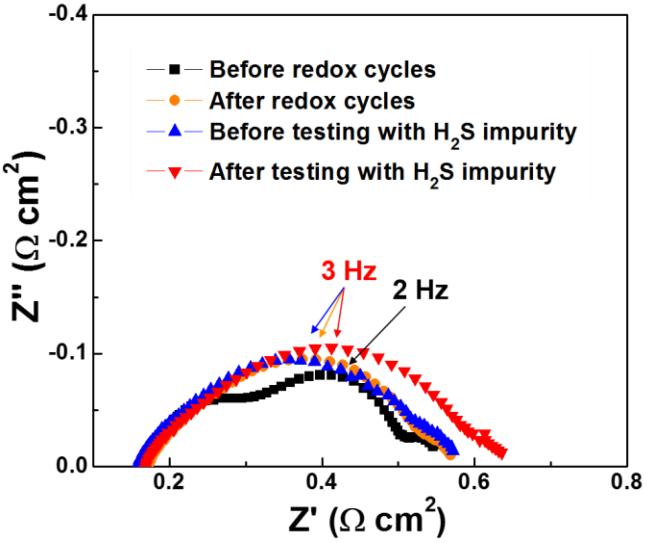

Figure 5.11 Nyquist plot of the electrochemical impedance data for an electrolyte-supported single cell with LSCrFeCo10 – GDC composite anode under open-circuit voltage at 700 °C. The redox cycles were conducted first, and the performance stability was subsequently evaluated with H_2 – 3 % H_2O and H_2 - 27 ppm of H_2S.

The coking resistance of the LSCrFeCo10 perovskite with Co-Fe alloy nanoparticles was evaluated with propane fuel. Figure 5.12 demonstrates the single cell performance and the long-term performance with 20 mL min^{-1} C_3H_8 – 3 % H_2O. The maximum power density under C_3H_8 – 3 % H_2O was 0.15, 0.35, 0.49, and 0.70 W cm^{-2}, respectively, at 700, 750, 800, and 850 °C. The long-term performance was first conducted at 750 °C under a constant current density of 300 mA cm^{-2}, and there was no significant

degradation after testing for 130 h. However, the long-term performance at 700 °C under a constant current density of 200 mA cm^{-2} exhibited slow degradation, which might be the result of limited carbon deposition on the anode.

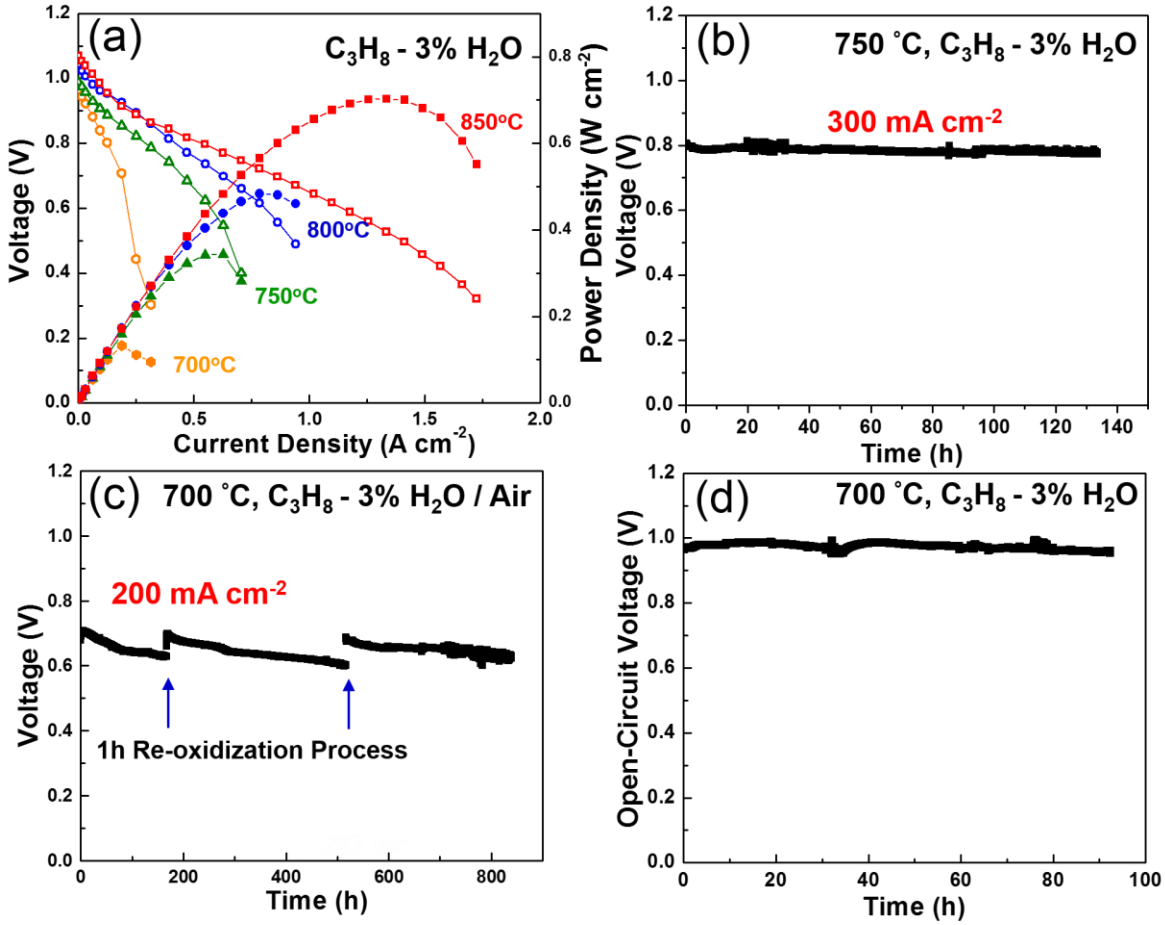

Figure 5.12 Electrochemical performance evaluation of an electrolyte-supported single cell with LSCrFeCo10 – GDC composite anode under C_3H_8 – 3 % H_2O. (a) I-V curve and its corresponding power density. (b) Long-term performance evaluation under a constant current density of 300 mA cm^{-2} at 750 °C. (c) Long-term performance evaluation under a constant current density of 200 mA cm^{-2} at 700 °C. The two redox cycles were conducted when the voltage was below 0.62 V and the reoxidation process was with 100 mL min^{-1} air for 1 h. (d) Open-circuit voltage versus time at 700 °C. These measurements were tested on the single cell #2.

Although carbon deposition is often considered a more serious problem at higher operation temperatures, the current density, which controls the oxygen amount transferring from the cathode strongly affects the carbon formation on the anode from a kinetic point of view.[137,138] With the consideration of the cracking reaction, steam reforming reaction, and Boudouard reaction of hydrocarbon fuel, carbon formation is unavoidable when the oxygen is not sufficient in the anode.[138] Thus, the reason for the noticeable degradation rate at 700 °C could be that 200 mA cm^{-2} is lower than the critical current density for fully preventing solid carbon formation on anode surface. The carbon deposition might grow from the nanoparticles and gradually occupy some of the active sites on these nanoparticles.[67] Nonetheless, the LSCrFeCo10 perovskite anode with Co-Fe exosluted nanoparticles still exhibited proper coking resistance with propane fuel. Moreover, based on the excellent redox reversibility and cyclability of LSCrFeCo10, the carbon deposition can be removed by the reoxidation process. Figure 5.12(c) depicts two cycles of catalytic reactivation of the LSCrFeCo10 composite anode by the reoxidation process for 1 h under air. The long-term performance behavior remains the same after redox cycles and the total operation time was over 840 h.

The single cell was also tested under open-circuit voltage with propane fuel, which is the most reducing atmosphere and most preferred condition for solid carbon formation and accumulation. Although Figure 5.12(d) shows that the open-circuit voltage remains between 0.98 – 0.95 V for over 90 h at 700 °C, the single cell performance is too small to be measured immediately after the test at open-circuit voltage. The fuel transportation pathway to the anode surface might be blocked by the accumulated carbon due to the propane cracking reaction. However, the maximum power density can be recovered after a 6 h reoxidation process to remove the accumulated carbon. The following short-term

performance at 200 mA cm^{-2} for 10 h at 700 °C still gives a similar result to the previous long-term performance evaluation in Figure 5.12(c). Therefore, a redox process not only benefits the self-regeneration of the anode surface morphology with exsolved nanoparticles, but it also becomes an excellent strategy to remove unwanted products and recover the catalytic activity of anode.

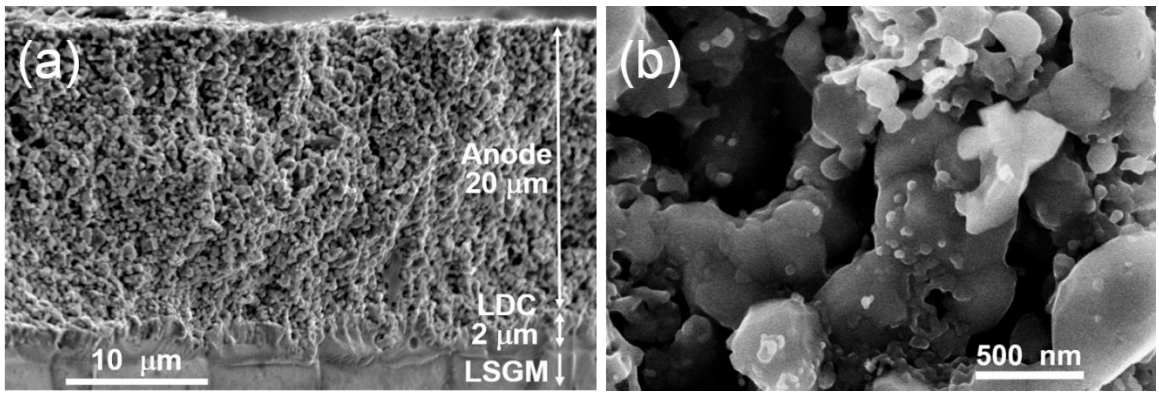

Figure 5.13 SEM images of the anode tested with propane fuel. (a) Cross-sectional image displaying the composite anode layer, LDC barrier layer, and LSGM electrolyte. (b) The zoomed-in image of the internal anode.

The internal microstructure of the tested LSCrFeCo10 composite anode was observed by SEM, and the images are displayed in Figure 5.13 After the last short-term performance evaluation at 700 °C with propane for 10 h, the single cell was cooled with N_2 to avoid further oxidation or carbon formation. There were no observable cracks or delamination on the anode layer, which means that the LSCrFeCo10 composite anode is mechanically robust in long-term operation and redox cycles. The zoomed-in image of the tested anode in Figure 5.13(b) shows that the diameter of nanoparticles is mostly smaller than 50 nm, and the random distribution of independent nanoparticles confirms that the surface morphology is well maintained after the long-term test and the redox cycles at 700

°C. Although the inner wall of the alumina tube in the testing system was deposited with carbon, distinct carbon filaments, which commonly appear in the conventional Ni cermet anode, were not observed inside the anode layer. In addition, the carbon signal in the EDX result was small.

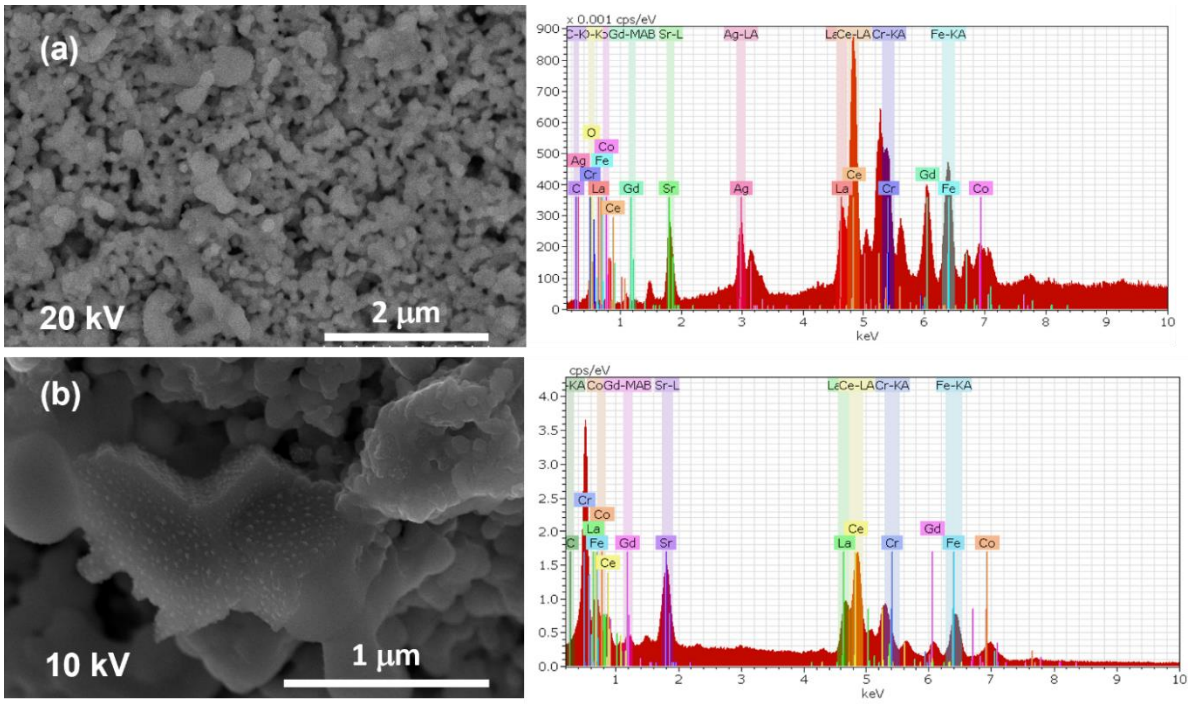

Figure 5.14 SEM images and EDX results of the anode that was tested with propane fuel. The anode surface was observed after the Ag current collector was peeled off. Images (a) and (b) were taken at different magnifications.

Figure 5.14 shows the top surface morphology of the tested composite anode after the Ag current collector was peeled off. Again, there is no obvious carbon fiber and filament formation on the anode surface. The Ag signal in the EDX result (Figure 5.14(a)) could be a result of the residual Ag particles. The carbon signal is very weak, which suggests the carbon deposition is scarce. In Figure 5.14(b), the nanoparticles remain on the

particle surface after the performance evaluation with propane after several redox cycles, and the EDX diagram indicates the absence of carbon element in this local region. These evidence verify that the LSCrFeCo10 perovskite anode with Co-Fe nanoparticles maintains proper coking resistance with propane and very limited carbon deposition may occur on the anode.

5.4 CONCLUSION

In this work, the phase characterization analysis and nanoparticle morphology observation have confirmed that the exsolved Co-Fe nanoparticles on the LSCrFeCo10 perovskite is self-regeneratable at 700 °C while the parent perovskite phase remains stable in the reducing and oxidizing atmospheres. The smaller nanoparticle size and the slower particle growth rate on the perovskite surface may benefit the long-term operation at relatively low temperatures. The maximum power density of an electrolyte-supported single cell with the LSCrFeCo10 – GDC composite anode reaches 0.86 W cm^{-2} with humidified H_2 at 800 °C, which represents over 100 % performance enhancement in comparison to that with the LSCrFe – GDC composite anode. The redox and long-term performance evaluations also demonstrate the redox reversibility and cyclability, excellent activity stability, good H_2S poisoning tolerance, and proper coking resistance of the LSCrFeCo10 – GDC composite anode. Most importantly, the performance evaluation with propane for over 800 h at 700 °C confirms that a redox process benefits catalytic activity recovery and carbon deposition elimination of the LSCrFeCo10 composite anode with exsolved Co-Fe nanoparticles for practical applications.

Chapter 6: Evolution of Exsolved Nanoparticles on a Perovskite Oxide Surface during a Redox Process

6.1 INTRODUCTION

Metal catalysts on oxides are widely applied in many chemical and electrochemical processes, but they often suffer from lifetime limitation and catalytic deactivation due to particle growth or unwanted reactions, such as carbon deposition and impurity poisoning. Self-regenerable metal nanoparticles on the oxide surface show great potential to overcome these challenges. By controlling the operational atmosphere or applied potential, easily-reducible cations in the oxide can exsolve from the lattice and precipitate as nanoparticles on the surface under the reducing condition, and dissolve back to the oxide lattice under the oxidizing environment.[62,66,68] The nanoparticles are reversibly regenerated after switching back to the reducing atmosphere, and the reconstructed surface morphology induces catalytic reactivation. Perovskites are often used as the matrix oxide because they allow for a variety of substitutions and have a high structure tolerance under reducing and oxidizing (redox) atmospheres.[4] For example, Nishihata et al. first reported the self-regeneration of Pd nanoparticles on the perovskite oxide as three-way catalysts for automotive emission control,[62] and Kobsiriphat et al. demonstrated Ru-containing perovskite oxides as anode materials in SOFCs.[70] However, exsolution or self-regeneration temperatures are generally between 800 °C and 1000 °C in the literature.[62–68,70,136] High-temperature processing accelerates microstructural coarsening, leads to undesired interactions between adjacent components in the system, increases system costs, and

---

Lai, K.-Y.; Manthiram, A. Evolution of Exsolved Nanoparticles on a Perovskite Oxide Surface during a Redox Process. *Chem. Mater.* 2018. Manthiram, A. supervised the project.

induces irreversible device performance degradation, thereby hindering the practical application of self-regenerating exsolved nanocatalysts.

Thus, we aim to evaluate the self-regeneration feasibility of exsolved nanoparticles and explore the evolution of nanoparticle morphology and phase on the perovskite surface at a relatively lower temperature of 700 °C. $La_{0.3}Sr_{0.7}Cr_{0.3}Fe_{0.6}Co_{0.1}O_{3-\delta}$ (LSCrFeCo10) is investigated here as a model material, since this perovskite oxide, as an anode material in SOFCs, exhibited enhanced catalytic activity, reasonable H_2S tolerance, excellent redox stability, and proper coking resistance with exsolved Co-Fe nanoparticles.[139] The Fe in the parent perovskite oxide, $La_{0.3}Sr_{0.7}Cr_{0.3}Fe_{0.7}O_{3-\delta}$ (LSCrFe), is partially substituted by easily-reducible Co with the goal of decreasing the exsolution and self-regeneration temperature. The phase and surface morphology of LSCrFeCo10 are analyzed after annealing the powder and bulk samples at 700 and 800 °C under 5 % H2 – Ar and ambient air as a redox environment.

A surface evolution mechanism is discussed with the considerations of the reincorporation rate and interaction between surface particles and the perovskite oxide at the relatively lower temperature. Several questions about the self-regeneration behavior will be addressed: (1) what is the effect of temperature on surface morphology evolution; (2) does the size of exsolved nanoparticles depend strongly on temperature; (3) is the cation reincorporation process complete at lower temperatures; and (4) is nanoparticle redispersion still possible when reincorporation is incomplete during a redox process.

6.2 Experimental Section

A SSR was used for the synthesis of the LSCrFeCo10 and LSCrFe perovskite oxides by first mixing a stoichiometric ratio of La_2O_3, $SrCO_3$, Cr_2O_3, Fe_3O_4, and Co_3O_4 in

ethanol. Then, the raw chemicals were calcined at 1000 °C, pressed into a pellet, and sintered at 1350 °C for 24 h. The phase of the pulverized materials was determined by XRD. The actual cation ratio was measured by ICP-OES (Varian 715-ES). To evaluate the phase evolution during a redox process, the powder samples were annealed at 700 and 800 °C with 5% H_2 – Ar and ambient air for 24 h, respectively, to simulate reducing and oxidizing conditions. The lattice parameters of the pristine and annealed powder samples were calculated by the Rietveld refinement method with GSAS software.[75] The cation occupancies in the refinement were fixed to the values from the ICP-OES results; La : Sr : Cr : Fe in LSCrFe is 0.294 : 0.701 : 0.302 : 0.698 and La : Sr : Cr : Fe : Co in LSCrFeCo10 is 0.294 : 0.698 : 0.294 : 0.603 : 0.103. Oxygen vacancies were not introduced into the refinement calculation because the small scattering cross section of the oxygen makes the XRD insensitive to oxygen occupancy.

In order to prevent interference of the A-site cation segregation on the surface during the exsolution process, the fractured surface of a broken dense pellet was observed.[66] The ball-milled materials were uniaxially pressed and sintered at 1350 °C for 12 h to form a dense pellet. The surface morphology of the annealed bulk samples was observed with a field emission SEM (Hitachi S5500) without depositing a conductive layer. The surface specimen of the rereduced LSCrFeCo10 sample was further prepared by a multi-beam focused ion beam (FIB) – SEM system (FEI Strata DB235). The exsolved species on the oxide surface were preserved by the deposition of a protective Au layer, and a gallium focused ion beam was used for cutting and thinning the specimen. The phase and elemental distribution were further analyzed with HR-TEM and STEM (JEOL 2010F) along with EDX.

6.3 RESULTS AND DISCUSSIONS

6.3.1 Phase characterization of powder samples during a redox process

The XRD patterns of the LSCrFeCo10 and LSCrFe samples annealed at 700 and 800 °C for 24 h were collected at room temperature, and their lattice parameters and fractions of rhombohedral perovskites ($R\bar{3}c$) and secondary phases were calculated with Rietveld refinement and summarized in Tables 6.1 and 6.2. The details of the refinement results are shown in the Appendix B (Figures B1 – B3). The excellent stability of the perovskite phase in both the oxidizing and reducing environments is evidenced by the presence of over 96 % fraction of the rhombohedral phase, and the small deviation in lattice parameters after annealing in both environments. The lattice expansion of all reduced perovskite samples is due to the overall effect of B-site cation reduction, cation exsolution, and lattice oxygen loss.

Table 6.1 Lattice parameters and fraction of LSCrFe and impurity phase during the redox process at 800 °C

		Lattice Parameters			Fraction
Process	Phase	a (Å)	b (Å)	c (Å)	(wt.%)
LSCrFe powder annealed at 800 °C for 24 h					
Pristine	Perovskite	5.5056(5)		13.4845(2)	98.2
	$SrCrO_4$	7.0091(6)	7.3061(6)	6.6782(5)	1.8
Reduced	Perovskite	5.5043(2)		13.4832(1)	99.4
	(Fe)	2.8644(6)			0.6
Reoxidized	Perovskite	5.4951(1)		13.4607(5)	98.1
	$SrCrO_4$	7.0635(1)	7.3657(9)	6.7192(8)	1.9
Rereduced	Perovskite	5.5041(1)		13.4821(6)	98.9
	(Fe)	2.8571(3)			1.1

Table 6.2 The lattice parameters and phase fractions of LSCrFeCo10 and impurity phases during the redox process at 700 and 800 °C.

Process	Phase	Lattice Parameters a (Å)	Lattice Parameters c (Å)	Fraction (wt. %)
Pristine	perovskite	5.4934(4)	13.4531(2)	100
LSCrFeCo10 powder annealed at 800 °C for 24 h				
Reduce	perovskite	5.5071(7)	13.4840(3)	98.4
	(Fe)**	2.8420(8)		0.5
	($Co_{0.9}Fe_{0.1}$)	3.5657(7)		1.1
Reoxidize	perovskite	5.4913(1)	13.4517(6)	98.4
		7.0435(1);		
	$SrCrO_4$*	7.3578(1)	6.7248(5)	1.6
Rereduce	perovskite	5.5116(4)	13.4998(2)	98.6
	(Fe)**	2.8439(5)		0.4
	($Co_{0.9}Fe_{0.1}$)	3.5619(3)		1.0
LSCrFeCo10 powder annealed at 700 °C for 24 h				
Reduce	perovskite	5.5246(6)	13.5321(3)	98.8
	(Fe)**	2.8466(8)		0.8
	($Co_{0.9}Fe_{0.1}$)	3.5580(3)		0.4
Reoxidize	perovskite	5.484(1)	13.4286(5)	96.1
		7.0821(4);		
	$SrCrO_4$*	7.3967(3)	6.7589(3)	2.2
	$(Co,Fe)_3O_4$	8.0781(1)		1.7
Rereduce	perovskite	5.5281(2)	13.5349(1)	98.8
	(Fe)**	2.8428(1)		0.8
	($Co_{0.9}Fe_{0.1}$)	3.5595(7)		0.4

* The lattice parameters, a and b, of $SrCO_4$ phase ($P12_1/c1$) are listed in the same blank for brevity.

** (Fe) indicates Co-Fe alloy in BCC structure with $Im\bar{3}m$ space group.

The consistent peak position of a secondary phase at 44.9° – 45.1° in the annealed LSCrFeCo10 and LSCrFe samples with 5 % H_2 – Ar suggests that this exsolved species is Fe metal or Co-Fe alloy in the body-centered cubic (BCC) structure with $Im\bar{3}m$ space group, denoted as (Fe). Based on the phase diagram[140,141], the (Fe) phase exists in a wide range of Co-Fe compositions. The lattice constants of pure Fe metal[142] and $Co_{0.72}Fe_{0.28}$[143] are, respectively, 2.865 Å and 2.842 Å, which are very close due to the similar atomic sizes of Co and Fe. Whereas, the lattice constant of (Fe) in the reduced LSCrFe samples (Table 6.1) matches very well with that of pure Fe metal, and this also agrees with the *in-situ* neutron diffraction analysis of LSCrFe under $pO_2 = 10^{-21.5}$ atm at 800 °C and the XRD analysis of $La_{0.75}Sr_{0.25}Cr_{0.5}Fe_{0.5}O_{3-\delta}$ anode.[126,128] On the other hand, the lattice constant of (Fe) in the reduced LSCrFeCo10 samples, which lies in a range of 2.842 to 2.846 Å (Table 6.2), is close to that of $Co_{0.72}Fe_{0.28}$. This similarity suggests that (Fe) is a Co-rich Co-Fe alloy. Although Fe has a higher content than Co in LSCrFeCo10, the Co cation is much more reducible than the Fe cation.[133] Thus, it is reasonable to have a higher Co content in the alloy when Co and Fe cations are exsolved together in a reducing atmosphere.

The other exsolved phase in the reduced and rereduced LSCrFeCo10 samples is determined to be a Co-rich Co-Fe alloy in face-centered cubic (FCC) structure with the $Fm\bar{3}m$ space group, which is denoted as ($Co_{0.9}Fe_{0.1}$).The lattice constant of the FCC Co-Fe alloy lies in a range of 3.558 Å to 3.565 Å, which is close to that of $Co_{0.9}Fe_{0.1}$ (3.547 Å) and $Co_{0.82}Fe_{0.18}$ (3.561 Å).[144,145] Since the strongest diffraction peak of the pure Co hexagonal phase ($P6_3/mmc$) cannot be found, most of the exsolved phases are Co-Fe alloys with BCC and FCC structures depending on their compositions.

The total fraction of exsolved phases (($Co_{0.9}Fe_{0.1}$) + (Fe)) at 800 °C is higher than that at 700 °C due to the stronger reduction capability of 5 % H_2 – Ar at higher temperature. In addition, higher temperature promotes much faster kinetics of the exsolution process.

As discussed earlier, the Fe cation is less reducible than the Co cation in the reducing atmosphere, so only limited Fe cations could be exsolved. Hence, the total difference in the fraction between 700 and 800 °C could be mainly attributed to Co exsolution content. With higher Co content in exsolved phases, the fraction of ($Co_{0.9}Fe_{0.1}$) alloy becomes higher than that of (Fe) alloy in the LSCrFeCo10 samples reduced at 800 °C.

It is worthwhile to note that the fraction of the exsolved phases is low and close to the XRD detection limit, which might reduce the accuracy of the refinement results. Meanwhile, the peak broadening effect due to small exsolved particle size (as shown in the following section) and slight compositional variation among the nanoparticles might induce refinement error, especially when the peak has a low signal-to-noise ratio. However, the similarity of the phase fractions and their lattice parameters between reduced and rereduced samples at the same annealing temperature indicates phase consistency in the reducing atmosphere before and after the 24 h reoxidation process.

A $SrCrO_4$ impurity ($P12_1/c1$) was identified in the pristine and reoxidized LSCrFe and LSCrFeCo10 samples and its existence is commonly found in the chromite perovskite oxides due to the limited solubility of Cr.[71,128] In addition, $SrCrO_4$ prefers to form at relatively low temperature and high partial oxygen pressure and only fully dissolves back into the perovskite phase above 1200 °C.[127,146] Although the $SrCrO_4$ phase is an insulator without catalytic activity for the fuel oxidation reaction, the complete decomposition of $SrCrO_4$ in a reducing atmosphere above 600 °C eliminates this impurity in the anodic operation condition.[71]

The secondary phases in the LSCrFeCo10 sample reoxidized at 700 °C not only includes $SrCrO_4$ but also $(Co, Fe)_3O_4$. The $(Co, Fe)_3O_4$ spinel phase ($Fd\bar{3}m$) is only detected after reoxidizing at 700 °C, because the reincorporation of exsolved metal into the B site of the LSCrFeCo10 perovskite lattice is kinetically retarded by a lower reoxidation

temperature. The lattice constant of Co_3O_4 and Co_2FeO_4 is, respectively, 8.054 Å and 8.242 Å.[147,148] Thus, the lattice constant of 8.078 Å, as calculated by Reitveld Refinement and shown in Table 6.2, suggests that $(Co, Fe)_3O_4$ in the reoxidized LSCrFeCo10 sample at 700 °C is highly Co rich. In terms of phase analysis, the $(Co, Fe)_3O_4$ phase does not interfere with the phase consistency in the reduced and rereduced samples at 700 °C, but the influence of the $(Co, Fe)_3O_4$ phase on the surface morphology is uncertain and is discussed in the following section.

Figure 6.1 presents a STEM image with EDX elemental mapping results and HR-TEM images of LSCrFeCo10 reoxidized at 700 °C for 24 h. The homogeneously distributed Co signals in LSCrFeCo10 in the EDX mapping image confirm the reincorporation process in LSCrFeCo10 at 700 °C. A cobalt-segregated particle is identified as the $(Co, Fe)_3O_4$ spinel phase ($Fd\bar{3}m$) whose lattice fringe spacing of 0.288 nm agrees with the interplanar distance of its (2 2 0) plane. Based on the similar ionic radii of Fe and Co cations, a small amount of Fe may be doped into the spinel phase, and the exact composition is difficult to identify via EDX. The over 200 nm $(Co, Fe)_3O_4$ particle size is significantly larger than that of the exsolved Co-Fe nanoparticles on the reduced sample surface shown in Figure 6.2, suggesting that the $(Co, Fe)_3O_4$ particle growth on LSCrFeCo10 is very rapid. Consistent with the XRD result, $SrCrO_4$ is also observed in the EDX mapping image in Figure 6.1, and the HR-TEM image (Figure 6.1 (c)) shows its interplanar distance of 0.327 nm, which matches with the (0 1 2) plane of the $SrCrO_4$ phase ($P12_1/c1$). The Sr and Cr segregations occur together with diminishing La, Fe, and Co signals. Unlike the $(Co, Fe)_3O_4$ particle that appears to be on the perovskite matrix, the $SrCrO_4$ phase does not overlap with LSCrFeCo10 (Figure 6.1(a)) and is circled with a white dashed line.

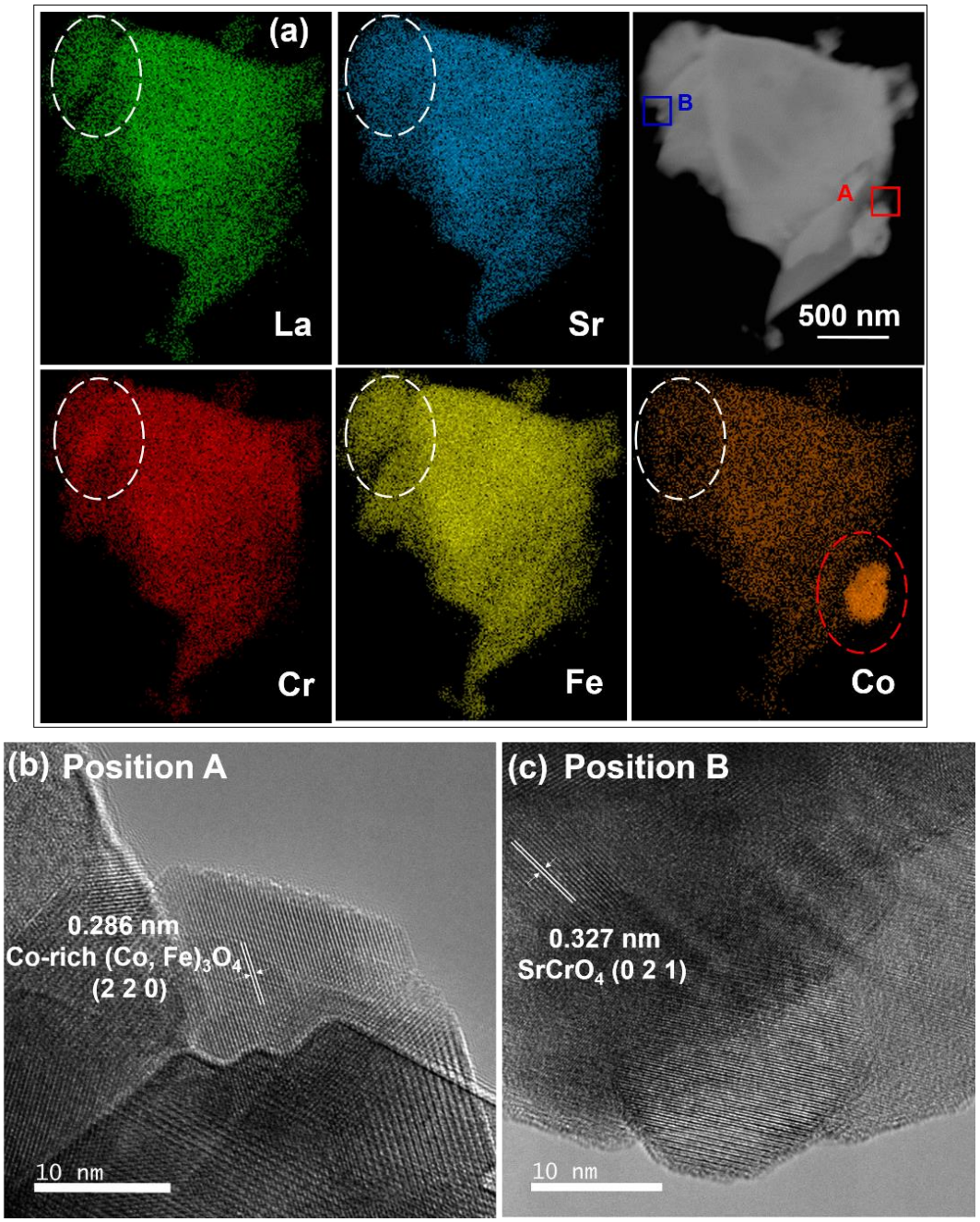

Figure 6.1 (a) EDX mapping results and STEM image of the reoxidized LSCrFeCo10 powder sample after annealing at 700 °C. The Co and Sr-Cr segregations are, respectively, circled with red and white dashed lines. (b) HR-TEM image of the $(Co, Fe)_3O_4$ spinel phase on position A. (c) The HR-TEM image of the $SrCrO_4$ phase on position B.

6.3.2 Surface Morphology Evolution during a redox process at 800 °C

Figure 6.2 displays the SEM images of the fractured surface of the broken dense sample after annealing in 5 % H_2 – Ar or ambient air at 800 °C for 24 h. Compared to the smooth and clean surface of the pristine sample in Figures 2(a, b), Figures 2(c, d) shows that the surface becomes rough and pitted with nanoparticles partially socketed on the perovskite matrix after reducing at 800 °C. In addition, most of the nanoparticle diameters are larger than 50 nm and several pairs of nanoparticles are closely attached to each other, which indicates that the small nanoparticles may increase their size by coalescence or Ostwald ripening during the annealing process at 800 °C. Figure 6.2(e, f) demonstrates that after reoxidation at 800 °C, a complete reincorporation reaction occurs, with no nanoparticles left on the perovskite surface.

The pore displayed in Figure 6.2(f) was naturally formed when the pellet was sintered, and was exposed on the cross-sectional surface after breaking the pellet open. Although $SrCrO_4$ is identified by XRD in an oxidizing atmosphere, the clean surface implies that this secondary phase does not prefer to form on the surface. After the rereducing process, the nanoparticles are self-regenerated and the surface morphology becomes similar to that of the reduced surface.

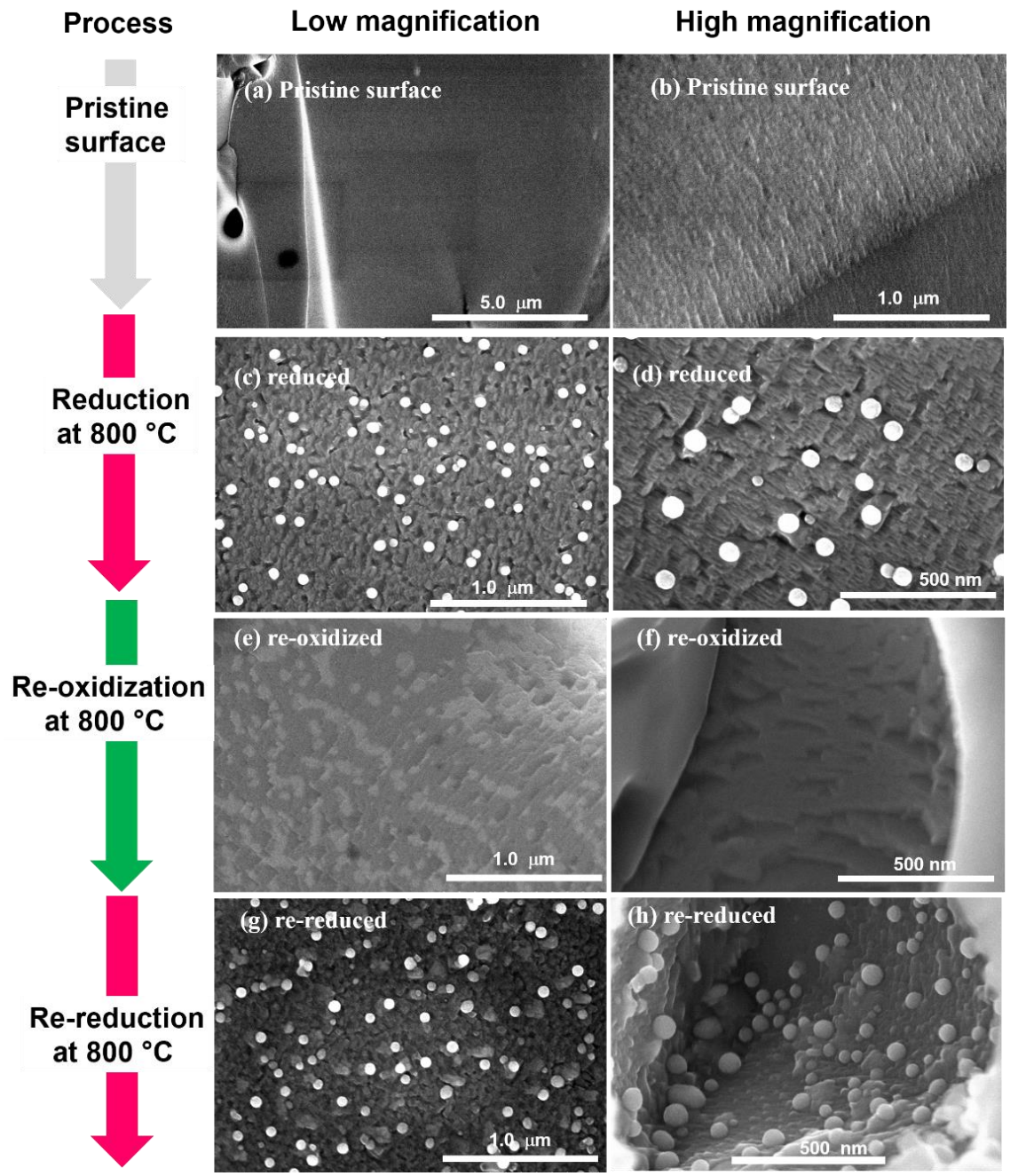

Figure 6.2 Surface morphology evolution of LSCrFeCo10 during the redox process at 800 °C. (a, b) pristine surface at different magnifications; (c, d) flat surface after reducing with 5% H_2 – Ar for 24 h at different magnifications; (e) flat surface and (f) inner surface of a pore after reoxidizing under ambient air for 24 h; (g) flat surface and (h) inner surface of a pore formed after rereducing for 24 h

6.3.3 Surface Morphology Evolution during a redox process at 700 °C

Figures 6.3 and 6.4 shows the surface morphology evolution during a redox process at 700 °C, which is very different from the morphology evolution at 800 °C. The nanoparticles not only exsolve directly from the perovskite oxide surface, but they also nucleate from a flat particle, which is marked with a black dashed circle in Figure 6.3(b). These flat particles strongly attach to the perovskite surface with an irregular shape in a sub-μm size. Meanwhile, Figure 6.5 displays a similar morphology of nanoparticle nucleation from a flat particle on the LSCrFe surface after reducing at 800 °C for 24 h. In the initial stage of nanoparticle formation, a protrusion appears on the flat particle as shown in Figure 6.5(a) and 6.5(c). Then, a nanoparticle grows to a spherical shape with a strong connection to the flat particles (Figure 6.5(b) and 6.5(d)). Based on the diminishing edge of the parent flat particle, the nanoparticle might have a similar composition to the flat particle.

Unlike the clean surface of the LSCrFeCo10 sample reoxidized at 800 °C, the nanoparticles and sub-μm particles shown in Figures 6.3(c-f) remain on the surface after reoxidizing at 700 °C due to sluggish and incomplete cation reincorporation back to the perovskite lattice. This phenomenon is consistent with the experimental observation in Irvine's group that the transition-metal oxide phase may exist during a reoxidation process at the relatively lower temperatures.[69]

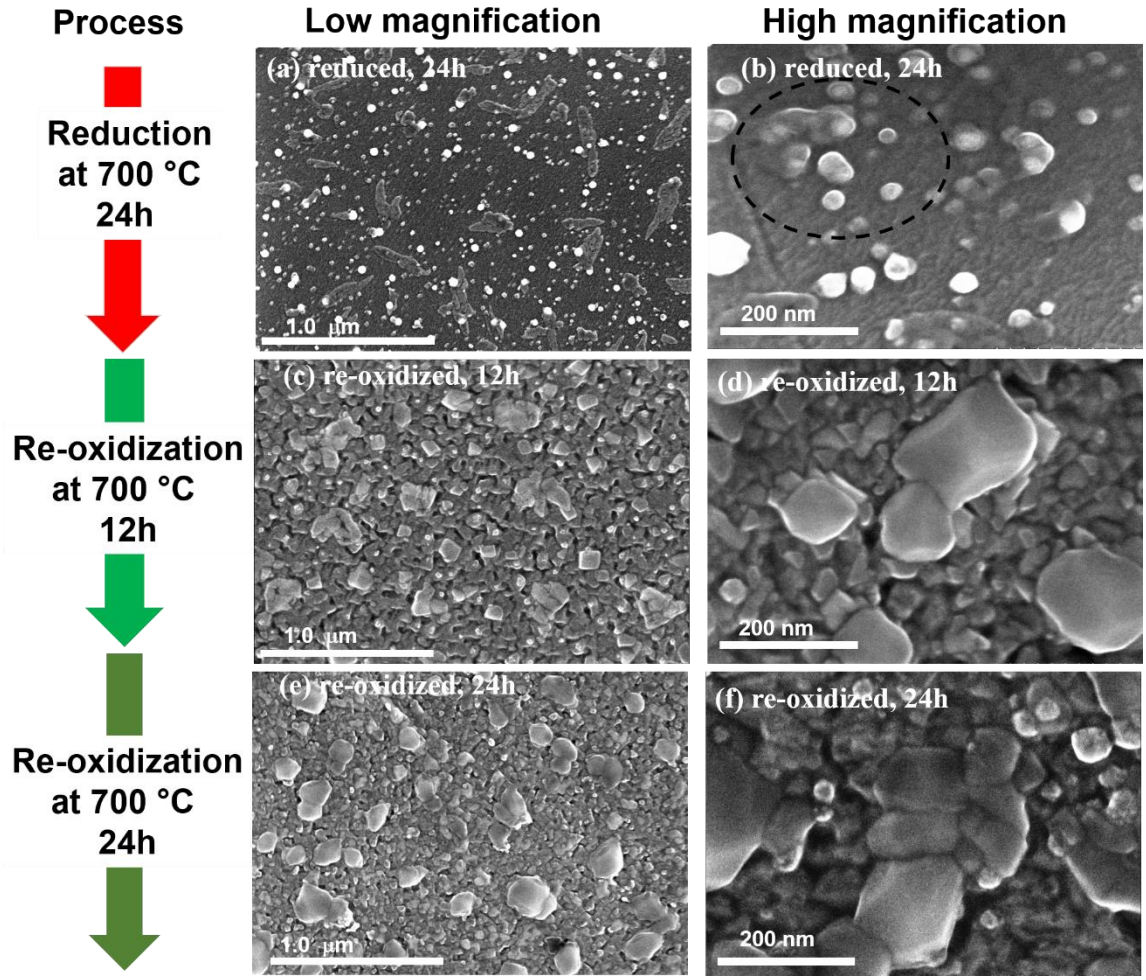

Figure 6.3 Surface morphology evolution of LSCrFeCo10 during the reduction and reoxidation process at 700 °C. (a, b) The surface after reducing in 5% H_2 – Ar for 24 h. The nanoparticles formed from the flat particles are marked by the black dashed circles. The surface after reoxidizing in ambient air for (c, d) 12 h and (e, f) 24 h.

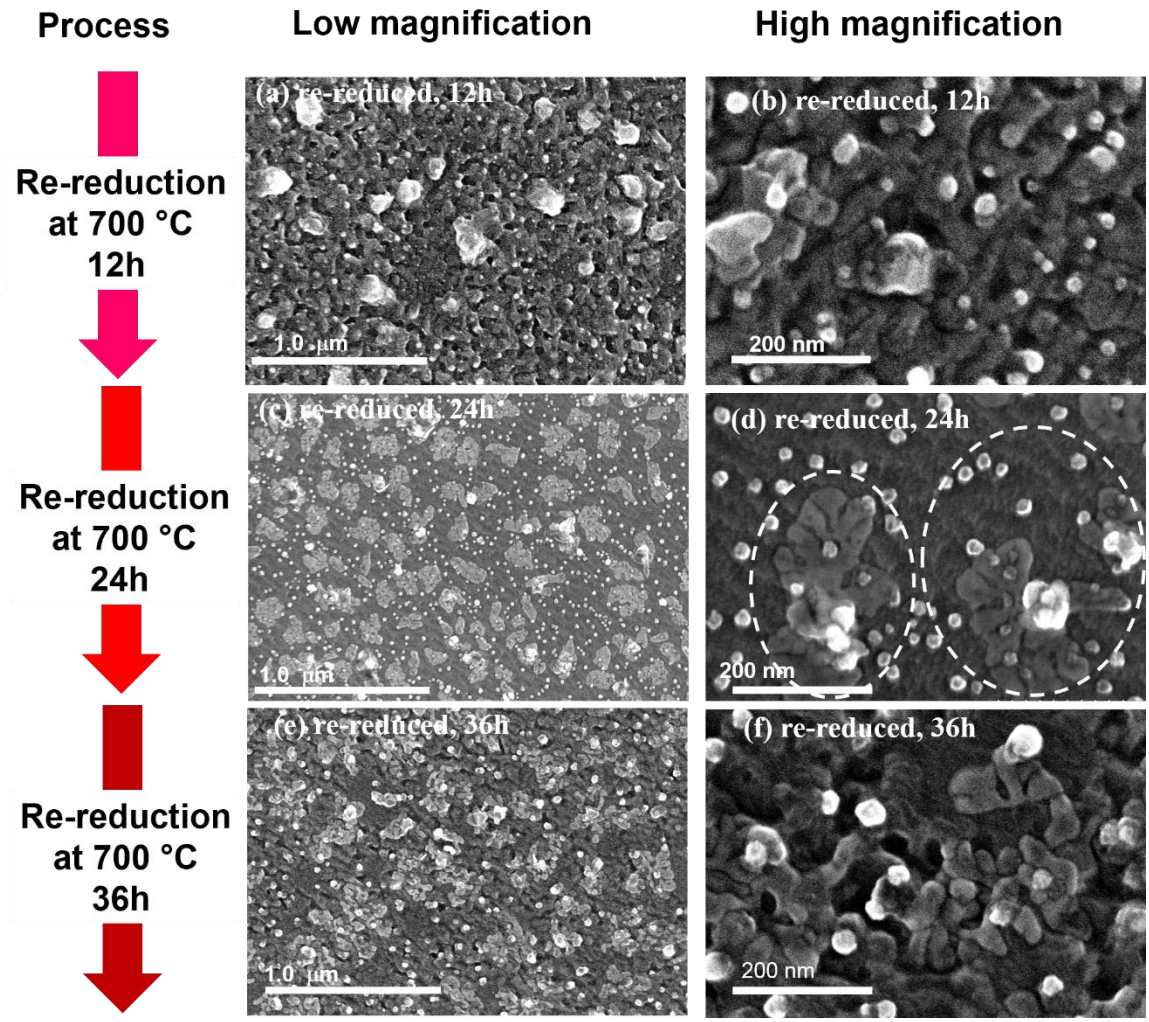

Figure 6.4 Surface morphology evolution of LSCrFeCo10 during the rereduction process at 700 °C, which follows the reoxidation process at 700 °C for 24 h in Figure 6.3 (e, f). The surface after rereducing in 5% H_2 – Ar for (a, b) 12 h, (c, d) 24 h, and (e, f) 36 h. The flat particle disintegration and nanoparticle formation are circled with white dashed line.

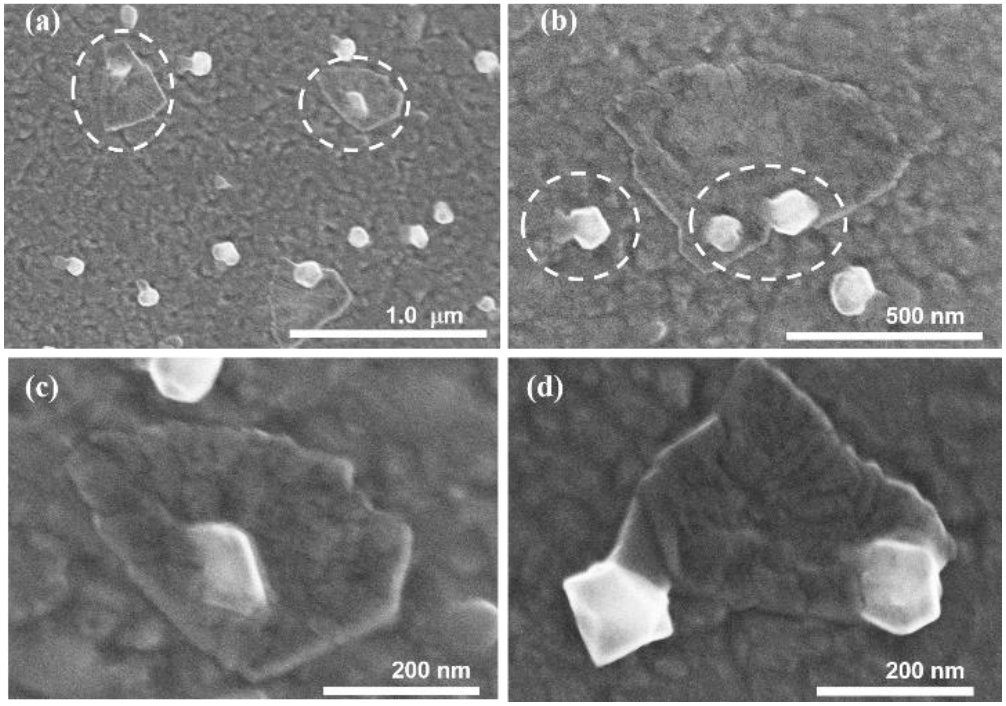

Figure 6.5 SEM images of reduced LSCrFe surface at different magnifications. The LSCrFe bulk sample was reduced with 5% H_2 – Ar at 800 °C for 24 h. Nanoparticle nucleation and growth from flat particles are indicated by the white dashed circles.

The increasing size of sub-μm particles with time might be caused by a fast particle growth rate in the oxidizing atmosphere, and their sizes agree with the size of the Co-rich spinel particle in the reoxidized powder sample shown in Figure 6.1(a).With the consideration of the evidence of secondary phase analysis and particle size similarity, the sub-μm particles may be $(Co, Fe)_3O_4$.

Although rapid $(Co, Fe)_3O_4$ particle growth changes the surface morphology of the perovskite oxide significantly during reoxidation at 700 °C, the nanoparticle is still self-regenerable in the reducing atmosphere. Besides the direct nanoparticle exsolution from the perovskite, Figures 3(g-l) demonstrate another pathway of nanoparticle formation in

which the sub-μm $(Co, Fe)_3O_4$ particle is reduced and disintegrated into several Co-Fe nanoparticles. In Figure 6.4(d), the nanoparticles form on the edge or center of a flat particle, and the same phenomenon is observed in the reduced LSCrFeCo10 sample (Figure 6.3(a, b)) and the reduced LSCrFe sample (Figure 6.5(a-d)). Finally, flat particles are disintegrated into dispersed nanoparticles over a longer rereducing time as shown in Figure 6.4(e, f). Therefore, the $(Co, Fe)_3O_4$ particles formed during the reoxidation process at 700 °C does not impede the nanoparticle redispersion in the following reducing process. The self-regeneration behavior and the redispersion mechanism are discussed in the following section.

6.3.4 Compositional variations among the nanoparticles

The surface specimen of the LSCrFeCo10 bulk surface rereduced at 700 °C for 24 h was further prepared by FIB and analyzed by STEM and HR-TEM. Based on Figure 6.4(c, d), a large nanoparticle with a diameter of over 40 nm always sits in the middle of a flat particle with a strong and clear connection, so the composition of the flat particle may be correlated to that of the large nanoparticle. Figure 6.6(a) displays the STEM and EDX results of a large nanoparticle surrounded by several smaller nanoparticles, and this arrangement is very similar to the nanoparticle distribution on a flat particle shown in Figure 6.4(d). The EDX line scan along the two nanoparticles demonstrates that the Fe and Co signals fluctuate together while the Cr signal remains flat, and the low Cr concentration profile without Cr segregation excludes the possibility of a $SrCrO_4$-derived phase being the flat particle on the surface. The lattice fringe spacing of the large nanoparticle in the HR-TEM image is 0.205 nm and close to the (1 1 1) interplanar distance of $Co_{1-x}Fe_x$ ($Fm\bar{3}m$, x = 0.1 to 0.2). Due to the similar atomic sizes of Co and Fe, Fe content in the Co-Fe alloy

is determined to be from 10 % to 20 %. Based on the geometric relationship between a flat particle and a relatively large nanoparticle, this result confirms our speculation of the flat particle as Co-Fe alloy, which is the reduced product of a sub-μm (Co, Fe)$_3$O$_4$ spinel particle as show in Figure 6.1 and 6.3(c-f). Thus, the nanoparticle formation from the transition-metal oxide on the surface as an indirect process provides another pathway of exsolved nanoparticle regeneration, which is different from the direct formation from the perovskite in the literature.[66,67,136]

The EDX line scan of two nanoparticles as displayed in Figure 6.6(b) shows that the nanoparticle composition varies from one to another. The synchronous variation of the Co and Fe signal indicates that the larger nanoparticle is Co-Fe alloy, which agrees with the interplanar distance analysis in the HR-TEM result (Figure 6.6(c)). In contrast, the smaller nanoparticle, whose diameter is about 20 nm, shows only a clear Co signal in the line scan and has less Fe content than the larger nanoparticle. This provides direct evidence that the nanoparticle composition is not constant. The Fe nanoparticle density on the reduced LSCrFe sample (Figure 6.5(a)) is much less than the Co-Fe nanoparticle density (Figure 6.3(a)). This phenomenon suggests that the exsolution amount of Fe is much less than that of Co, which is consistent with the discussion on Co-rich Co-Fe alloy phase in the XRD results. Due to the lower amount of exsolved Fe and the random distribution of the nanoparticles, it is reasonable that different nanoparticles have slightly varying Fe contents. Even in a coarsened (Co, Fe)$_3$O$_4$ particle, the composition could be slightly varying among different grains.

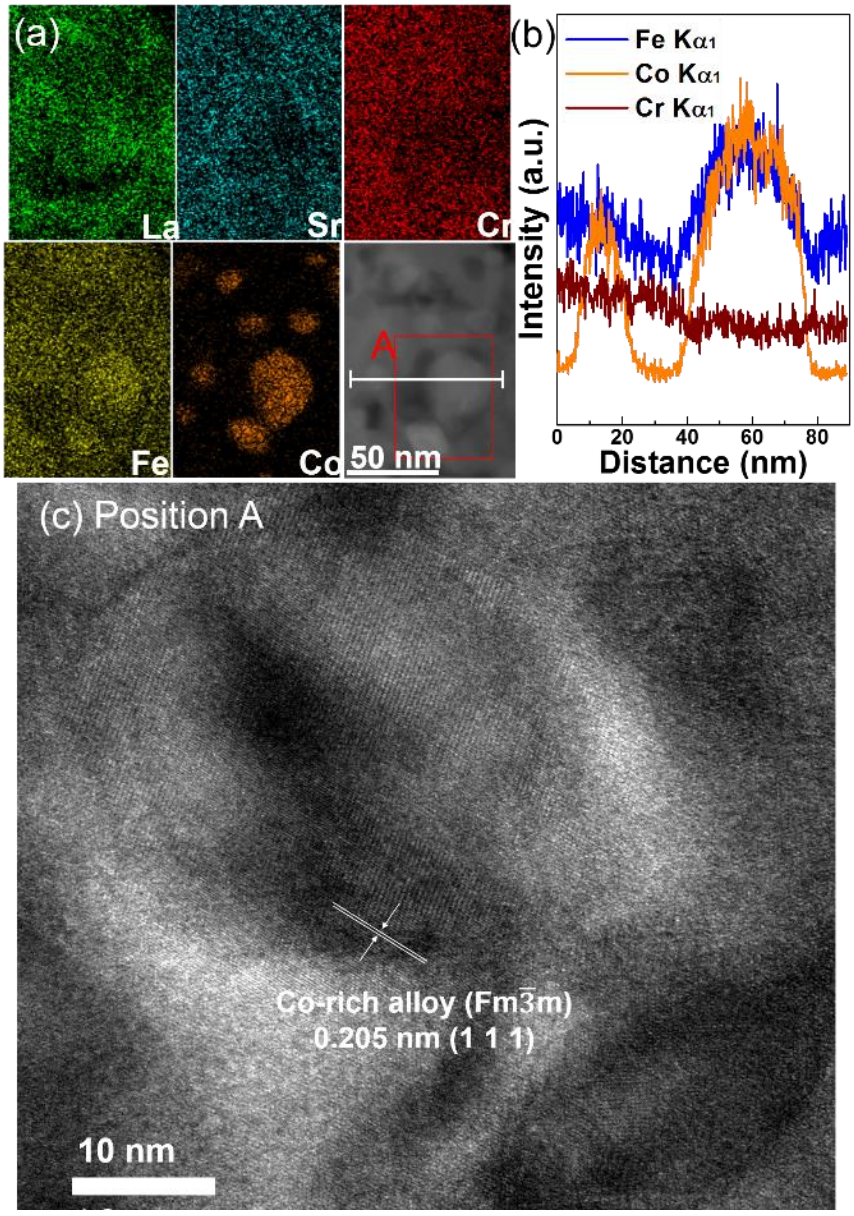

Figure 6.6 (a) STEM image with EDX mapping results of the surface specimen prepared by FIB. The LSCrFeCo10 sample was rereduced at 700 °C for 24 h. (b) Elemental variation of the EDX line scan in which the scan crossed two Co-Fe nanoparticles (scanning position marked with white line in (a)). (c) An HR-TEM image of Co-Fe nanoparticles on position A.

6.3.5 Nanoparticle distribution analysis

Severe particle growth occurs rapidly at the relatively high temperature.[123] The nanoparticle size distribution and particle density on the perovskite surface (on Figure 6.2(c), 6.2(g), 6.3(a) and 6.4(e)) were analyzed with ImageJ software. We make the assumption that the nanoparticle shape is hemispherical, and the restrictions that the nanoparticle area is larger than 80 nm^2 (diameter > 10 nm) and circularity is 0.2 – 1.0 were applied for avoiding overestimation. Figure 6.7 shows the size distribution histograms for the samples reduced and rereduced at 700 and 800 °C, and the calculated results are presented in Figures B4 and B5. The surface coverage is the ratio of the total projected area occupied by the nanoparticles to the total projected surface area of the perovskite oxide. Although the surface coverages of these four samples are within 5.9 – 6.9 %, the main nanoparticle size distribution shifts from 60 – 70 nm to 10 – 30 nm due to the slower particle growth rate when temperature decreases from 800 to 700 °C. Accordingly, the particle areal density (number of particles) on the perovskite surface decreases significantly from about 160 to 25 particles per μm^{-2} with a temperature increase of 100 °C.

The potential mechanisms of nanoparticle growth include (1) coalescence, (2) Ostwald ripening, and (3) evaporation-condensation growth. These mechanisms are all thermally activated, and evaporation-condensation growth requires much higher temperatures, which are close to the melting temperatures of metallic nanoparticles. Although the melting temperature drops with decreasing particle size, this becomes less significant for nanoparticles whose diameter is larger than 10 nm.[149] Thus, the evaporation-condensation growth mechanism is ruled out in the current case of nanoparticle growth from 700 to 800 °C.

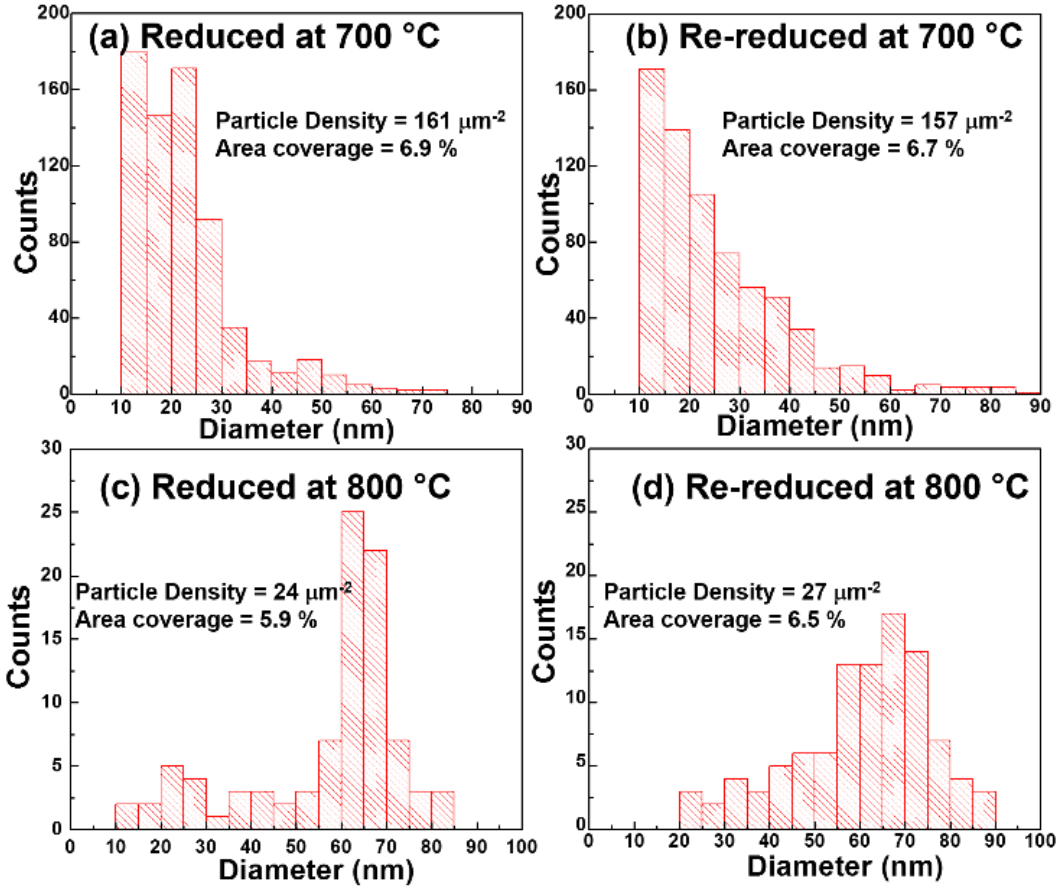

Figure 6.7 The size distribution histograms of the exsolved nanoparticles on the LSCrFeCo10 samples, which were (a) reduced at 700 °C for 24 h, (b) rereduced at 700 °C for 36 h, (c) reduced at 800 °C for 24 h, and (d) rereduced at 800 °C for 24 h.

In this study, coalescence can occur when nanoparticles are very close to each other as shown in Figure 6.2(d, f), but it may not be the dominant mechanism due to the enhanced interaction between nanoparticles and the perovskite oxide matrix. The metallic nanoparticle shape on an oxide support can be strongly affected by the metal-oxide interfacial interaction.[150–153] When the interaction is weak, the driving force to reduce the metallic surface energy makes the nanoparticle approach to a spherical shape, which is generally observed in the conventional infiltration-prepared nanoparticles on an oxide

support. However, strong metal-oxide interaction changes the nanoparticle shape to hemispherical or even flat on the support. The hemispherical shape of the exsolved nanoparticles here (Figure 6.2(h)) indicates enhanced metal-oxide interaction, which agrees with the shape of other exsolved nanoparticles in the literature.[67,136] The pinning effect induced by strong oxide-metal interaction makes the nanoparticles much less mobile on the oxide surface, and particle migration and coalescence rates are considerably decreased.[154]

Ostwald ripening process describes the growth of a larger particle by consuming a smaller particle without direct connection. The clusters of the adatoms from a small particle migrate on the oxide support surface and merge into another large particle.[155] In the case with strong metal-oxide interaction, Ostwald ripening often becomes the main mechanism of particle growth due to more sluggish coalescence rate. Since the cluster migration rate on the surface strongly depends on temperature, particle growth through Ostwald ripening becomes much more severe at elevated temperatures.[155] Interestingly, clusters of atoms could also migrate from a large particle to a small particle, which was observed by *in-situ* TEM and STEM.[155] The cluster migration between two close nanoparticles could also initialize the coalescence and form an observable inter-particle neck region.

The over five-fold higher number of exsolved nanoparticles at 700 °C in comparison to that at 800 °C ensures more catalytically active sites for the fuel oxidation reaction in SOFC applications. More importantly, in comparison to the size distribution before and after the redox process, over 80 % of nanoparticles have diameters smaller than 30 nm in both cases at 700 °C. This consistent nanoparticle size distribution suggests that the redox process does not affect the exsolved nanoparticle redispersion on the perovskite surface and reactivation is feasible even at the lower temperature.

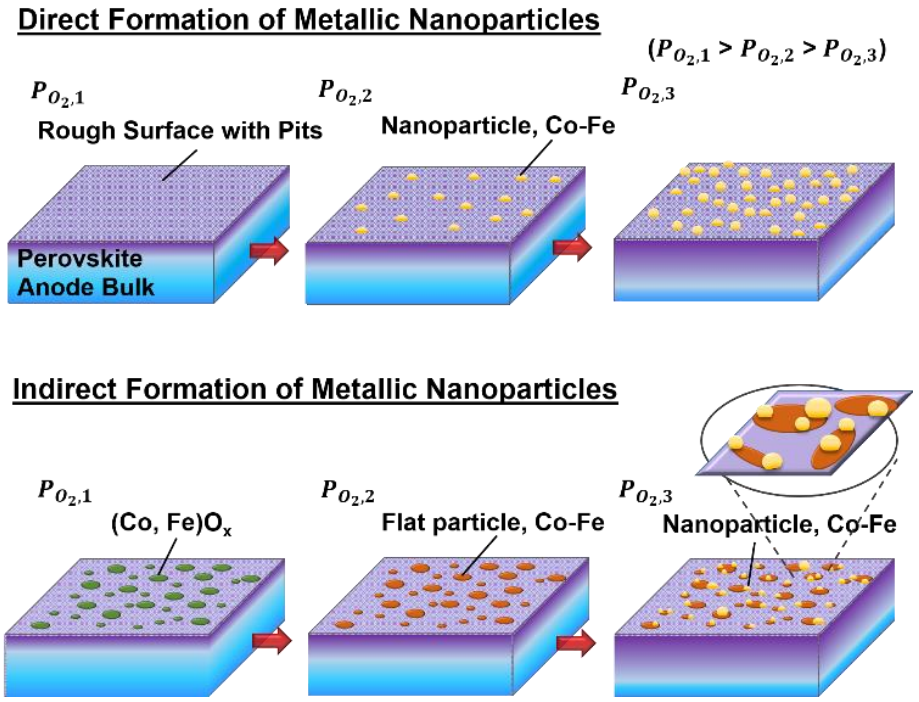

Figure 6.8 Schematic diagram of exsolution mechanism for LSCrFeCo10 with respect to oxygen partial pressure.

6.3.6 Self-regeneration mechanism

In order to understand the evolution of metallic nanoparticles on the perovskite surface during the redox process, the defect reactions behind the exsolution and reincorporation processes are described as follow:

$$2M_B^{\times} + O_O^{\times} \leftrightarrow 2M_B' + V_O^{\bullet\bullet} + \frac{1}{2}O_2 \quad \text{(eq. 6.1)}$$

$$M_B' + O_O^{\times} \leftrightarrow MO + V_B''' + V_O^{\bullet\bullet} \quad \text{(eq. 6.2)}$$

$$MO \leftrightarrow M + \frac{1}{2}O_2 \quad \text{(eq. 6.3)}$$

where $M_B^{\times}$ is the transition-metal ion, such as Fe^{3+} and Co^{3+}, on the B site of the perovskite oxide with neutral charge, $O_O^{\times}$ is the oxygen atom on the oxygen lattice site of the perovskite oxide with zero net charge, M_B' is the reduced cation, *e.g.*, Fe^{2+} and Co^{2+} on the B site with a -1 net charge, $V_O^{\bullet\bullet}$ is the oxygen vacancy with +2 net charge, V_B''' is the cation vacancy on the B site with a -3 net charge, MO is the transition-metal oxide, and M is the metallic phase of the transition metals. Figure 6.8 illustrates the direct and indirect formation of metallic nanoparticles in the exsolution process.

The direct process describes the most common nanoparticle formation process at relatively high temperatures. In principle, when the cations on the B site of the perovskite are reduced to their lowest oxidation states in the lattice, the oxygen vacancy cannot be simply created while maintaining a single-phase perovskite as Eq. 6.1 states. As a result, the oxygen vacancy generation is further accompanied with cation vacancy formation and phase separation, *e.g.*, transition-metal oxide formation, which is described by Eq. 6.2 However, the intermediate metal oxide with a very short lifetime is barely observed due to the rapid reduction reaction in Eq. 6.3 before the particle growth on the surface.

On the other hand, the transition-metal oxide, in both crystalline and amorphous phases, can be formed with an observable size at relatively low temperatures in the indirect process. The interaction between the transition-metal oxide and the perovskite oxide is relatively strong, so the contact area between the two phases could be large with good wetting. However, the interaction becomes weaker when the transition-metal oxide is further reduced to a metallic phase due to the relatively weaker interaction between the metal particles and the perovskite oxide in comparison to oxide-oxide interaction. As a result, metallic nanoparticles nucleate and grow from a flat particle, which is the reduced product of the intermediate oxide phase. The final nanoparticle shape is determined by

balancing two driving forces: (1) maintaining strong metal-oxide interaction and (2) reducing total metallic surface energy by minimizing the surface area.

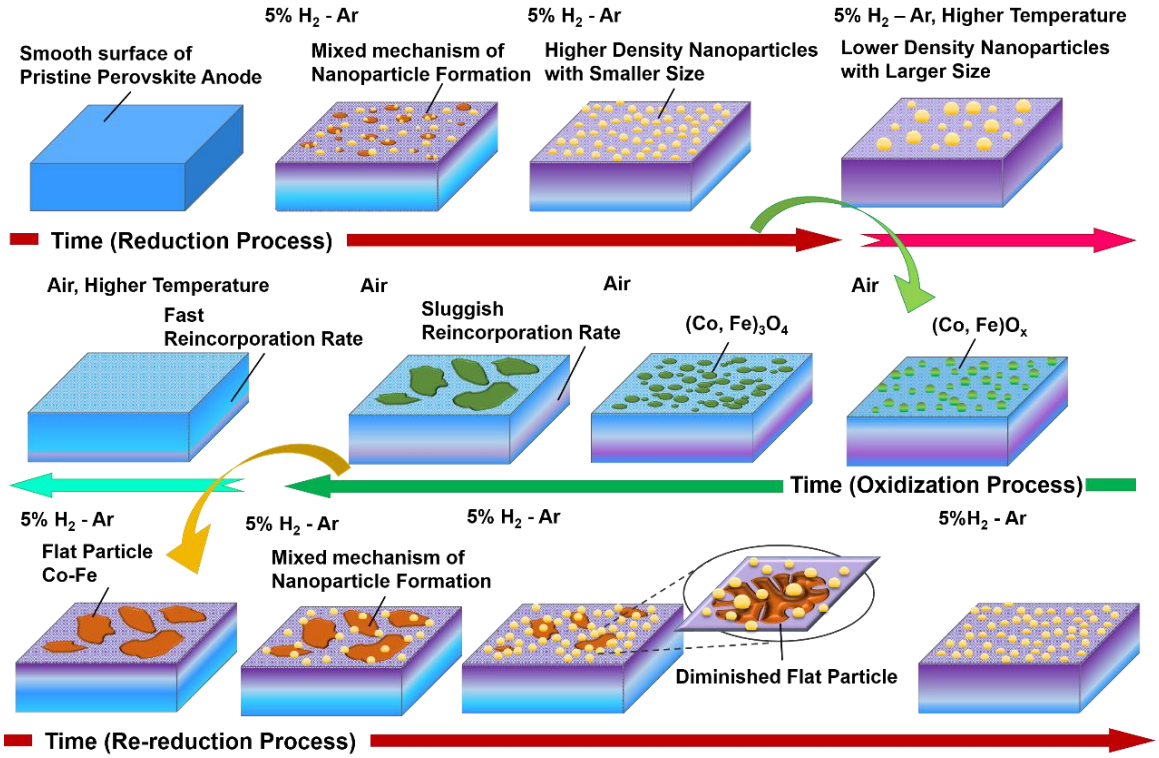

Figure 6.9 Schematic diagram of self-regeneration mechanism for LSCrFeCo10 with respect to processing time and temperature.

Figure 6.9 illustrates the perovskite oxide surface evolution during a redox process depending on processing time and temperature. The self-regeneration of exsolved nanoparticles is controlled by the oxygen partial pressure, temperature, inherent material reducibility, and non-stoichiometry of the parent oxide. With constant oxygen partial pressures for the reducing or oxidizing conditions, the lower temperature leads to slower kinetics in the exsolution and reincorporation reactions, especially in eq. 2 and 3. Thus, the

mixed exsolution mechanism, including direct and indirect nanoparticle formation, during reducing and rereducing processes is observable. Moreover, the existence of intermediate phase ($(Co, Fe)_3O_4$) in the self-regeneration process is also found. However, the defect reactions do not describe the morphology of the exsolved phases and the intermediate phase on the surface.

The nanoparticle shape and distribution strongly depend on the metal-oxide interaction and particle growth rate. Based on our observation, the enhanced metal-oxide interaction is not affected much by temperature due to the similar nanoparticle morphology at 700 and 800 °C, whereas the lower temperature slows down the particle growth rate with higher areal particle density and smaller size of the exsolved nanoparticle. Even though the transition-metal oxide as an intermediate phase particle grows much faster in the oxidizing atmosphere, the redispersion of Co-Fe nanoparticles is still achievable by disintegrating the reduced product of a large spinel oxide particle. The redispersion phenomena has also been observed in oxide-supported noble metal nanoparticles.[156–158] The mechanism of nanoparticle redispersion from reduced spinel oxide is similar to the indirect nanoparticle formation mechanism. With strong metal-oxide interaction in the reducing atmosphere, nanoparticle nucleation still occurs and pins on the surface while total metallic surface energy is minimized by decreasing the metallic surface area and forming a hemispherical-like shape.

6.4 CONCLUSION

In this work, surface morphology evolution and phase characterization analysis have confirmed that the self-regeneration of exsolved Co-Fe nanoparticles on the LSCrFeCo10 perovskite is reversible at both 700 and 800 °C, while the parent perovskite

phase remains stable. The transition-metal oxide particles are observed on the surface after a reoxidation process at 700 °C, since the cation reincorporation rate becomes sluggish. The intermediate phase of the transition-metal oxide demonstrates an alternative pathway for nanoparticle self-regeneration even with incomplete reincorporation at the lower temperature during the reoxidizing process. The nanoparticles are redispersed by a disintegration of the reduced spinel oxide. With a strong interaction between the metal particles and the perovskite oxide, the hemispherical-like nanoparticle forms through minimizing the metallic surface energy. Furthermore, the smaller nanoparticle size and the higher areal particle density on the perovskite surface with slower particle growth rate enhance the long-term performance stability at the lower operation temperature. The consistent phase and surface morphology before and after a redox process at 700 °C also ensure catalytic reactivation for practical applications.

Chapter 7: Summary

The objective of this dissertation is to develop electrode materials fulfilling the requirements of highly robust SOFCs. Increasing SOFC performance and extending system lifetime are two of the most effective strategies to reduce the cost of the IT-SOFC system and facilitate large-scale manufacturing. As a result, new alternative materials with high phase stability, enhanced electrocatalytic activity, and TECs matched to corresponding electrolyte materials are necessary to overcome the challenges of conventional SOFCs. This dissertation systematically investigates eight series of swedenborgite oxides with relatively low TECs as cathode candidates for alleviating the thermal stresses in SOFCs during operation. In addition, the redox stable Co-doped chromite perovskite oxide with exsolved nanoparticles is synthesized as a catalytically active anode candidate which has moderate TECs, proper coking resistance, and acceptable H_2S impurity tolerance.

Chapter 3 studied $RBaCo4O_{7+\delta}$-based samples with a co-substitution in the R site with Y, In, and Ca and Ga substitution in the Co site to enhance the high-temperature phase stability, oxygen-storage capability, and electrocatalytic activity in IT-SOFCs. $YBaCo_{4-y}Ga_yO_{7+\delta}$, $Y_{1-x}In_xBaCo_{3.3}Ga_{0.7}O_{7+\delta}$, $Y_{1-x}Ca_xBaCo_{3.3}Ga_{0.7}O_{7+\delta}$, $In_{1-x}Ca_xBaCo_{3.3}Ga_{0.7}O_{7+\delta}$, and $Y_{0.5}In_{0.5}BaCo_{4-y}Ga_yO_{7+\delta}$ series of materials have been synthesized by a SSR and the phase stabilities have been assessed by long-term testing at 600 – 800 °C for 120 h. The substitution of In for Y mitigates the phase decomposition but decreases the oxygen-storage capacity and electrochemical performance in IT-SOFCs. With In and Y co-dopants, $Y_{0.5}In_{0.5}BaCo_{3.5}Ga_{0.5}O_{7+\delta}$ remains stable even with a lower amount of Ga. In contrast, Ca-doping reduces the phase stability regardless of its content. By optimizing the compositions, $Y_{0.9}In_{0.1}BaCo_{3.3}Ga_{0.7}O_{7+\delta}$ is found to exhibit the highest electrochemical

performance without decomposition in the long-term test at 600 – 800 °C. The anode-supported single cell with the $Y_{0.9}In_{0.1}BaCo_{3.3}Ga_{0.7}O_{7+\delta}$ + GDC (50 : 50 wt.%) composite cathode reaches a maximum power density of 0.91 W cm^{-2} at 700 °C. Moreover, the ideal matching of the relatively low TEC of $Y_{0.9}In_{0.1}BaCo_{3.3}Ga_{0.7}O_{7+\delta}$ ($7.5 – 9.2 \times 10^{-6}$ K^{-1}) with those of common electrolytes alleviates the thermal stress during long-term operation in IT-SOFCs. The combination of long-term phase stability, high oxygen-storage, and electrocatalytic properties makes the $Y_{0.9}In_{0.1}BaCo_{3.3}Ga_{0.7}O_{7+\delta}$ + GDC composite cathodes appealing for practical application in IT-SOFCs.

In order to understand the doping and co-doping effects of trivalent cations (Al^{3+}, Ga^{3+}, and Fe^{3+}) in the Co-containing swedenborgite oxide as a cathode in IT-SOFCs, Chapter 4 investigated four series of $YBaCo_4O_7$-based materials, including $YBaCo_{4-x}Al_xO_{7+\delta}$, $YBaCo_{4-x-y}Ga_xAl_yO_{7+\delta}$, $YBaCo_{3.2}Ga_{0.8-x}Fe_xO_{7+\delta}$, and $YBaCo_{3.5-x}Al_{0.5}Fe_xO_{7+\delta}$. Although Al has been suggested to have better phase stabilization capability than Ga in the literature, severe decomposition above 700 °C occurs in all the $YBaCo_{4-x}Al_xO_{7+\delta}$ samples. Fe has much weaker phase stabilization capability than Al and Ga, but excellent phase stability is still maintained with a small substitution of Fe for Ga. All the materials with a stable phase at high temperatures exhibit well-matched TECs ($8.0 – 9.5 \times 10^{-6}$ K^{-1}) with common electrolyte materials, which alleviates the thermal stress during SOFC operation. In comparison to $YBaCo_{3.2}Ga_{0.8}O_{7+\delta}$, a partial substitution of Ga by Fe enhances the catalytic activity for the oxygen reduction reaction. In addition, the performance of the anode-supported single cell with the $YBaCo_{3.2}Ga_{0.7}Fe_{0.1}O_7$ – $Ce_{0.8}Gd_{0.2}O_{1.9}$ composite cathode reached 1.0 W cm^{-2} with H_2 fuel at 700 °C. Thus, this work provides a guideline on trivalent dopants for developing swedenborgite-based cathode materials with a high phase stability and catalytic activity in IT-SOFC.

Chapter 5 presented a perovskite anode material, $La_{0.3}Sr_{0.7}Cr_{0.3}Fe_{0.6}Co_{0.1}O_{3-\delta}$, which allows Co-Fe nanoparticles exsolved on the oxide surface at intermediate operation temperatures (700 °C). The perovskite oxide exhibits excellent phase stability during the redox process, and the exsolved nanoparticles show good self-regeneration capacity by the phase characterization and the nanoparticle morphology observation. The $La_{0.3}Sr_{0.7}Cr_{0.3}Fe_{0.6}Co_{0.1}O_{3-\delta}$ has a slightly higher TEC (15.0×10^{-6}) than those of common electrolyte materials, but the anode composited with GDC could mitigate the TEC mismatch. The electrochemical performance has been evaluated by an electrolyte-supported single cell with hydrogen and propane fuels. The Co-Fe nanocatalysts enhance the maximum power density of the $La_{0.3}Sr_{0.7}Cr_{0.3}Fe_{0.6}Co_{0.1}O_{3-\delta}$ – GDC composite anode more than 75 % in comparison to that of the cobalt-free $La_{0.3}Sr_{0.7}Cr_{0.3}Fe_{0.7}O_{3-\delta}$ – GDC composite anode with hydrogen. The self-regeneratable anode drives off carbon deposition with hydrocarbon fuels and facilitates catalytic reactivation by the redox cycles without requiring a higher-temperature process. Additionally, the dispersed Co – Fe nanoparticles with a random distribution and slow particle growth rate ensure long-term performance. The single-cell SOFC evaluation demonstrates that $La_{0.3}Sr_{0.7}Cr_{0.3}Fe_{0.6}Co_{0.1}O_{3-\delta}$ with Co–Fe nanoparticles exhibits acceptable H_2S tolerance, excellent redox reversibility, and stable long-term performance for more than 200 h with H_2 and over 800 h with propane at 700 °C.

To evaluate the self-regeneration feasibility of exsolved Co-Fe nanoparticles on the $La_{0.3}Sr_{0.7}Cr_{0.3}Fe_{0.6}Co_{0.1}O_{3-\delta}$ perovskite at intermediate operation temperature (700 °C), Chapter 6 analyzed the evolution of surface morphology and particle phases during a redox process with scanning and transmission electron microscopy. Unlike the complete reincorporation of the exsolved metals back to the perovskite lattice at 800 °C during the reoxidation process, the transition-metal oxide remains on the surface as an intermediate

phase because of a sluggish reincorporation rate at 700 °C. Although the transition-metal oxide particles grow and coarsen quickly in an oxidizing atmosphere, the nanoparticles could still be formed by a disintegration of the reduced spinel oxide in a reducing atmosphere. The hemispherical-like shape of the nanoparticles can be achieved by minimizing metallic surface energy and maintaining the strong metal-oxide interaction. The redispersion of Co-Fe nanoparticles completes the self-regeneration process at 700 °C. The exsolved nanoparticle size distribution is strongly affected by temperature but not by a redox process, which improves performance stability and reactivation at the relatively lower temperature during long-term operation.

Overall, this dissertation describes the successful development of $YBaCo_4O_7$-based swedenborgite oxides as cathode materials for IT-SOFCs with excellent phase stability, high catalytic activity, relatively low TECs, sufficient electrical conductivity, and good chemical compatibility with the GDC electrolyte. The comprehensive study of the cation effect in $YBaCo_4O_7$-based materials provides a guideline for material selection and development. At the anode, the Co-doped chromite perovskite oxide with self-regenerating metallic nanoparticles developed in this dissertation overcomes the redox instability of the conventional Ni – GDC cermet anode and the poor catalytic activity of perovskite-related oxide materials. In addition, with the use of Cr and Fe as the main B-site dopants, the exsolution and self-regenerating temperatures of the nanoparticles on the $La_{0.3}Sr_{0.7}Cr_{0.3}Fe_{0.6}Co_{0.1}O_{3-\delta}$ surface are relatively lower than those of other perovskite oxides in the literature. The high power performance and stability of the alternative electrode candidates described herein demonstrate great promise toward fulfilling the requirements of IT-SOFCs.

The lab-scale results presented in this dissertation have demonstrated the unique materials advantages of the Co-containing swedenborgite oxide and the chromite

perovskite oxide with self-regenerating nanoparticles, respectively, as cathode and anode candidates. For future work, the phase stability, surface morphology evolution, and chemical compatibility testing for > 1000 h are still needed. In addition, the material synthesis methods, electrode fabrication method, and electrode microstructure should be further optimized to enhance device performance. An intense degradation evaluation with numerous redox cycles, chromia gas poisoning from the metallic interconnect, and rapid thermal cycling are also desired. Moreover, fundamental studies can provide more insights into the reaction kinetics of these alternative materials and benefit future material modification. The author sincerely hopes that the strategies and results presented in this dissertation will incentivize more studies on catalysts and accelerate novel material development for commercialization of SOFCs.

Appendix A: Supporting Information for Chapter 3

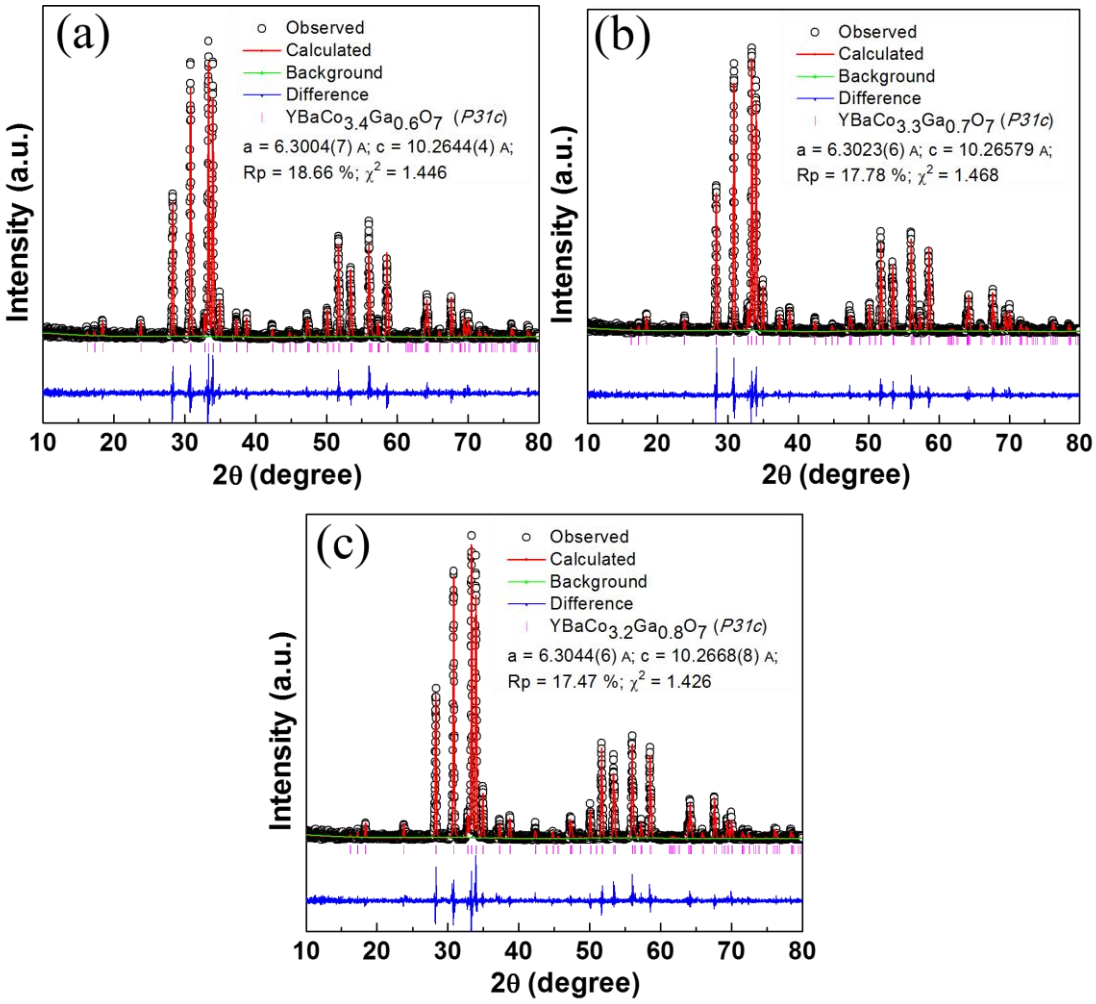

Figure A1 Powder XRD Rietveld refinement results of (a) $YBaCo_{3.4}Ga_{0.6}O_{7+\delta}$, (b) $YBaCo_{3.3}Ga_{0.7}O_{7+\delta}$, and (c) $YBaCo_{3.2}Ga_{0.8}O_{7+\delta}$.

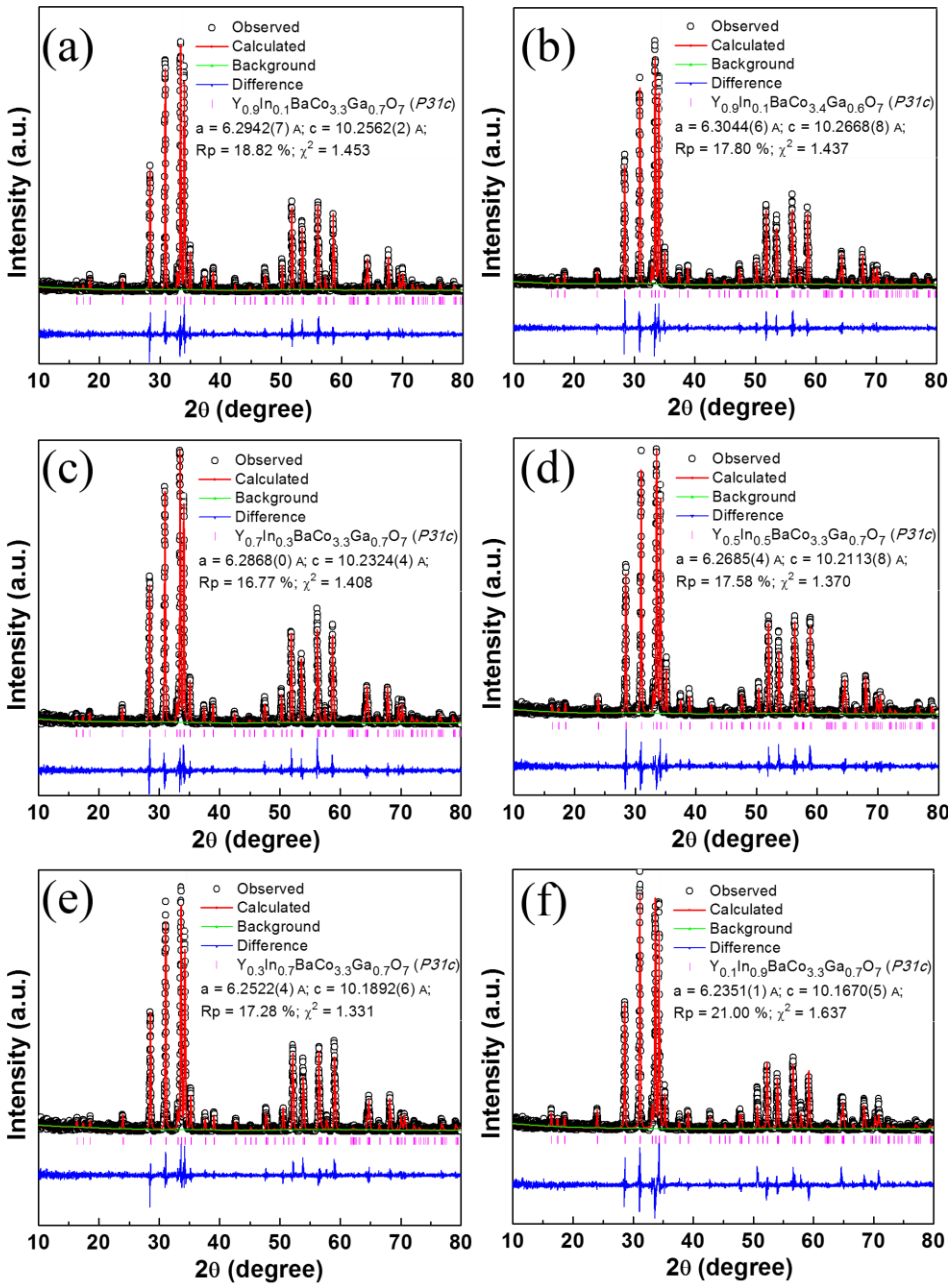

Figure A2 Powder XRD Rietveld refinement results of (a) $Y_{0.9}In_{0.1}BaCo_{3.3}Ga_{0.7}O_{7+\delta}$, (b) $Y_{0.9}In_{0.1}BaCo_{3.4}Ga_{0.6}O_{7+\delta}$, (c) $Y_{0.7}In_{0.3}BaCo_{3.3}Ga_{0.7}O_{7+\delta}$, (d) $Y_{0.5}In_{0.5}BaCo_{3.3}Ga_{0.7}O_{7+\delta}$, (e) $Y_{0.3}In_{0.7}BaCo_{3.3}Ga_{0.7}O_{7+\delta}$, and (f) $Y_{0.1}In_{0.9}BaCo_{3.5}Ga_{0.5}O_{7+\delta}$.

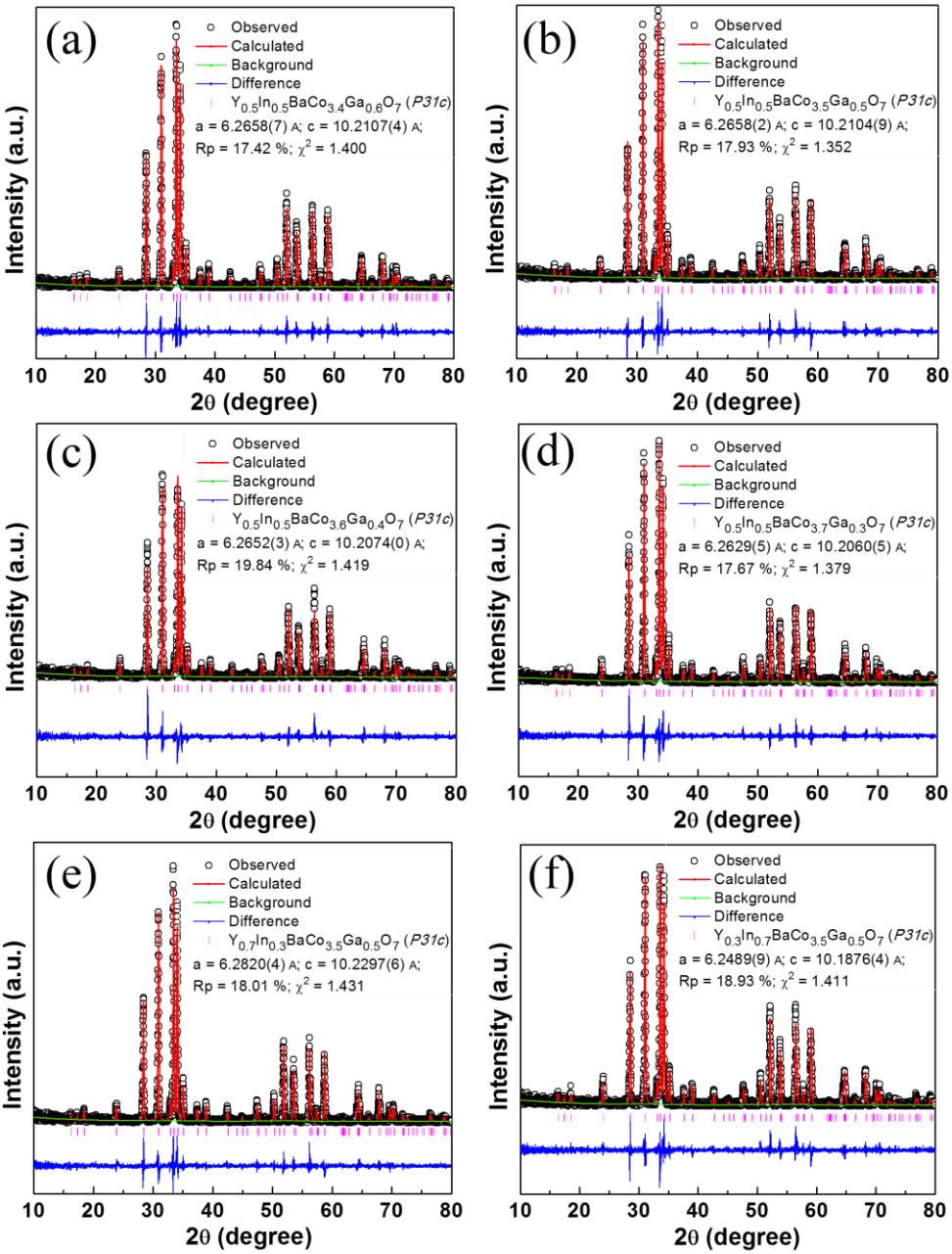

Figure A3 Powder XRD Rietveld refinement results of (a) $Y_{0.5}In_{0.5}BaCo_{3.4}Ga_{0.6}O_{7+\delta}$, (b) $Y_{0.5}In_{0.5}BaCo_{3.5}Ga_{0.5}O_{7+\delta}$, (c) $Y_{0.5}In_{0.5}BaCo_{3.6}Ga_{0.4}O_{7+\delta}$, (d) $Y_{0.5}In_{0.5}BaCo_{3.7}Ga_{0.3}O_{7+\delta}$, (e) $Y_{0.7}In_{0.3}BaCo_{3.5}Ga_{0.5}O_{7+\delta}$, and (f) $Y_{0.3}In_{0.7}BaCo_{3.5}Ga_{0.5}O_{7+\delta}$.

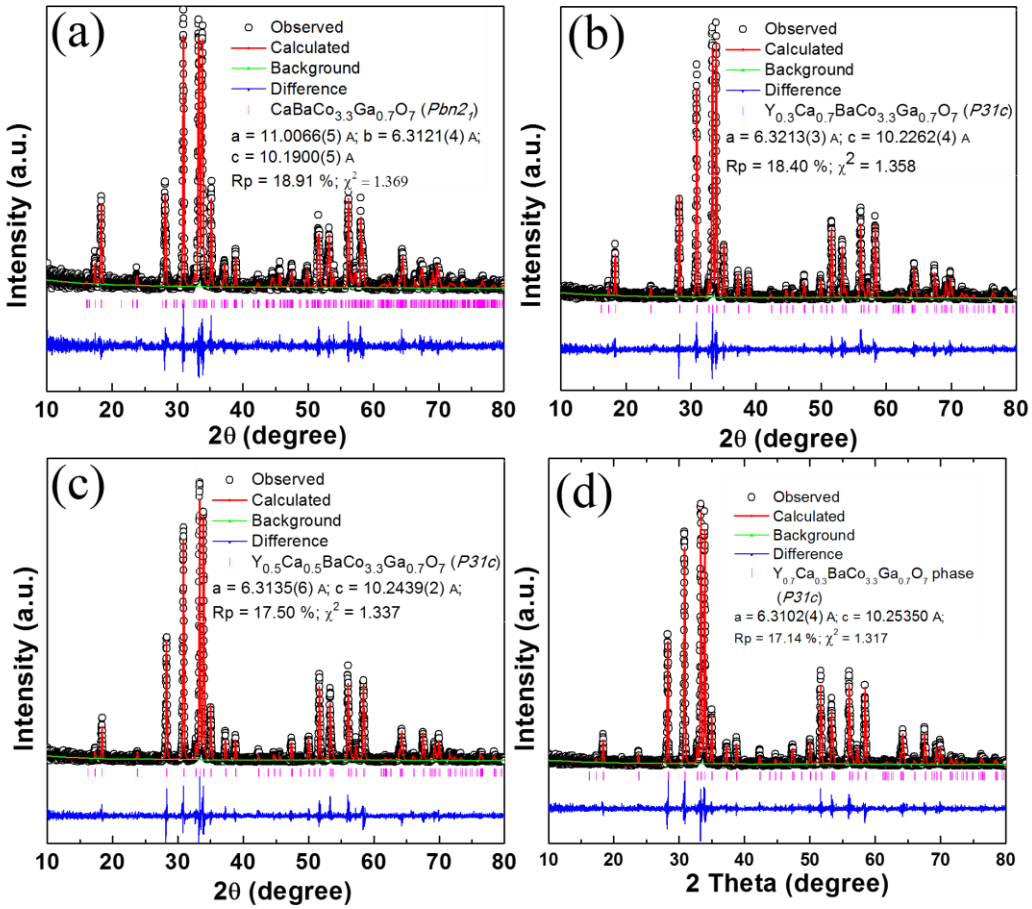

Figure A4 Powder XRD Rietveld refinement results of (a) $CaBaCo_{3.3}Ga_{0.7}O_{7+\delta}$, (b) $Y_{0.3}Ca_{0.7}BaCo_{3.3}Ga_{0.7}O_{7+\delta}$, (c) $Y_{0.5}Ca_{0.5}BaCo_{3.3}Ga_{0.7}O_{7+\delta}$, and (d) $Y_{0.7}Ca_{0.3}BaCo_{3.3}Ga_{0.7}O_{7+\delta}$.

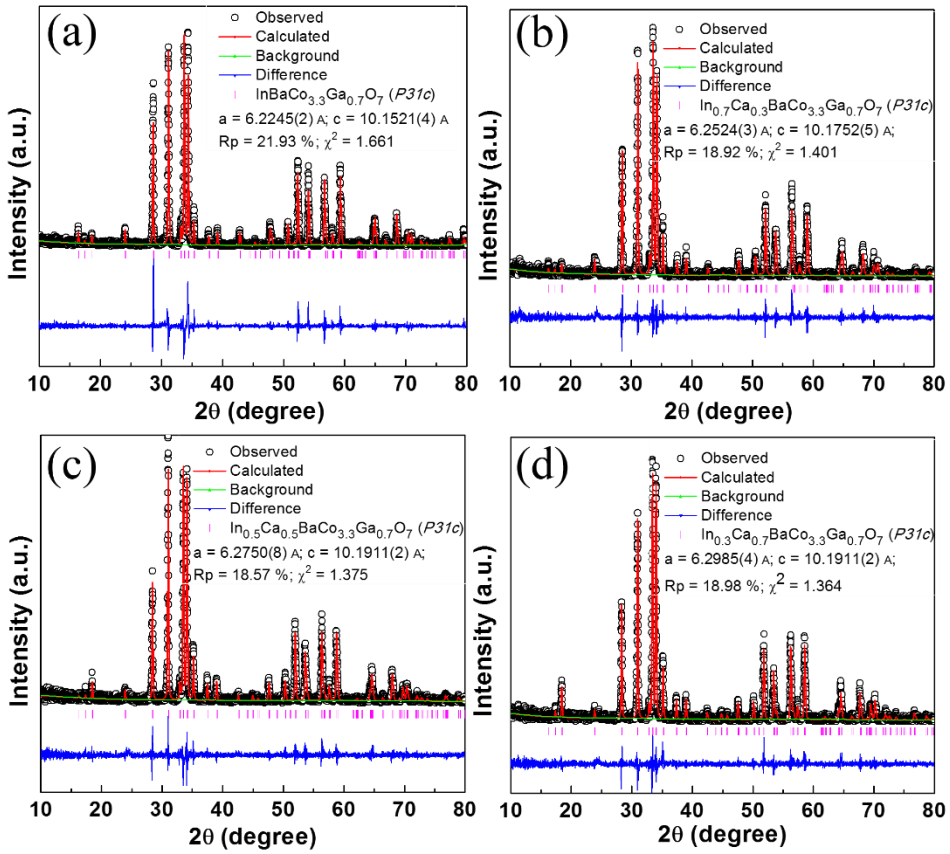

Figure A5 Powder XRD Rietveld refinement results of (a) $InBaCo_{3.3}Ga_{0.7}O_{7+\delta}$, (b) $In_{0.7}Ca_{0.3}BaCo_{3.3}Ga_{0.7}O_{7+\delta}$, (c) $In_{0.5}Ca_{0.5}BaCo_{3.3}Ga_{0.7}O_{7+\delta}$, and (d) $In_{0.3}Ca_{0.7}BaCo_{3.3}Ga_{0.7}O_{7+\delta}$.

Appendix B: Supporting Information for Chapter 6

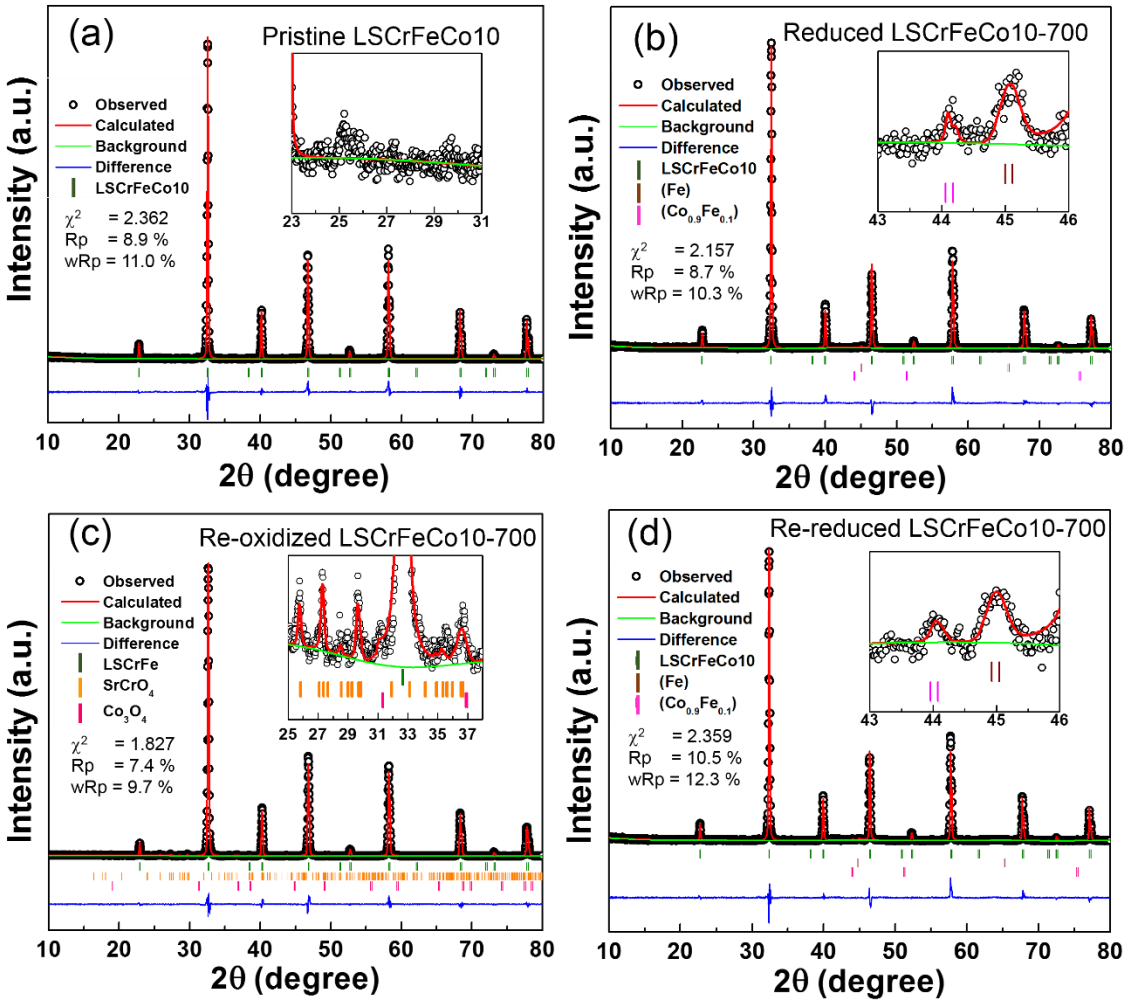

Figure B1 XRD refinement results of (a) pristine LSCrFeCo10, (b) reduced LSCrFeCo10, (c) reoxidized LSCrFeCo10, and (d) rereduced LSCrFeCo10 samples where the redox temperature is 700 °C. The inset shows the selective 2θ range of major peaks for the impurity phase.

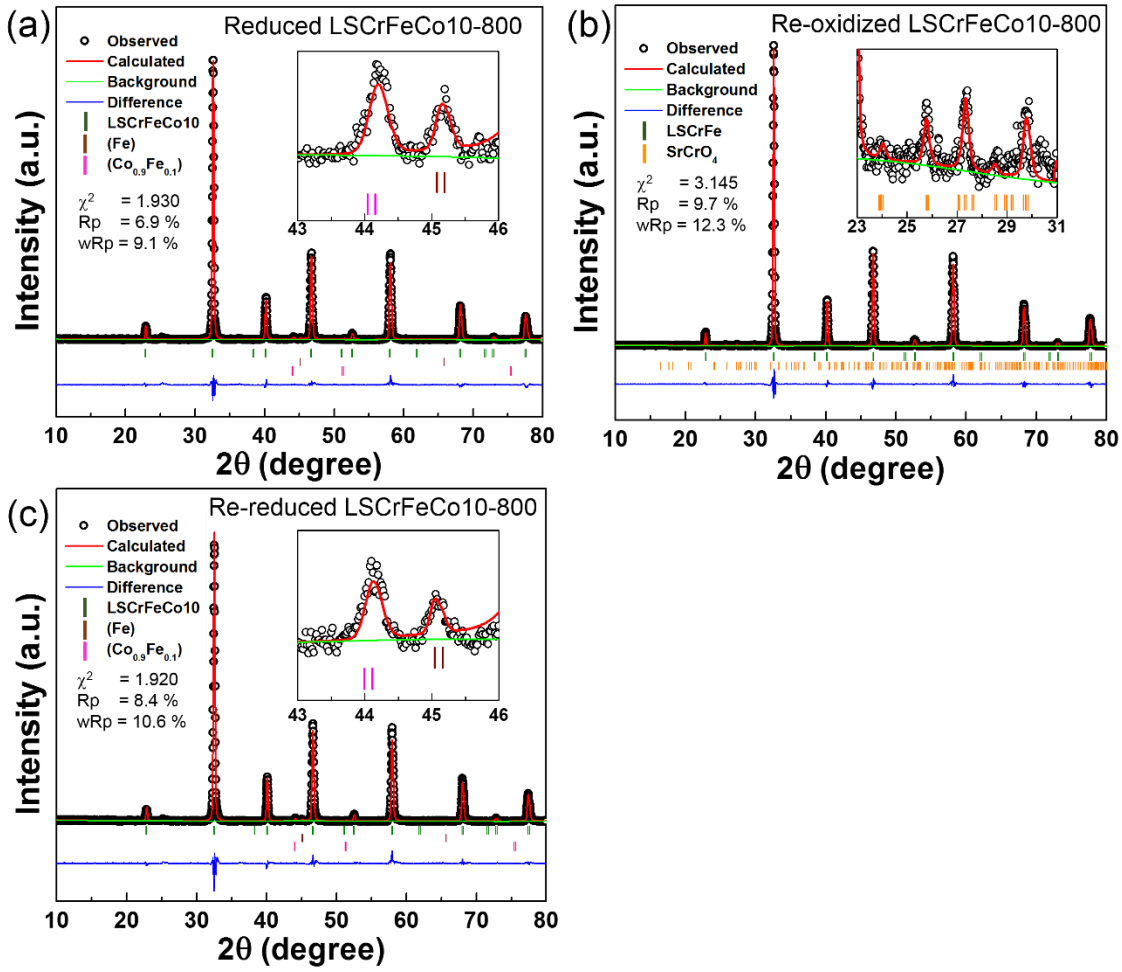

Figure B2 XRD refinement results of (a) reduced LSCrFeCo10, (b) reoxidized LSCrFeCo10, and (c) rereduced LSCrFeCo10 samples where the redox temperature is 800 °C. The inset shows the selective 2θ range of major peaks for the impurity phase.

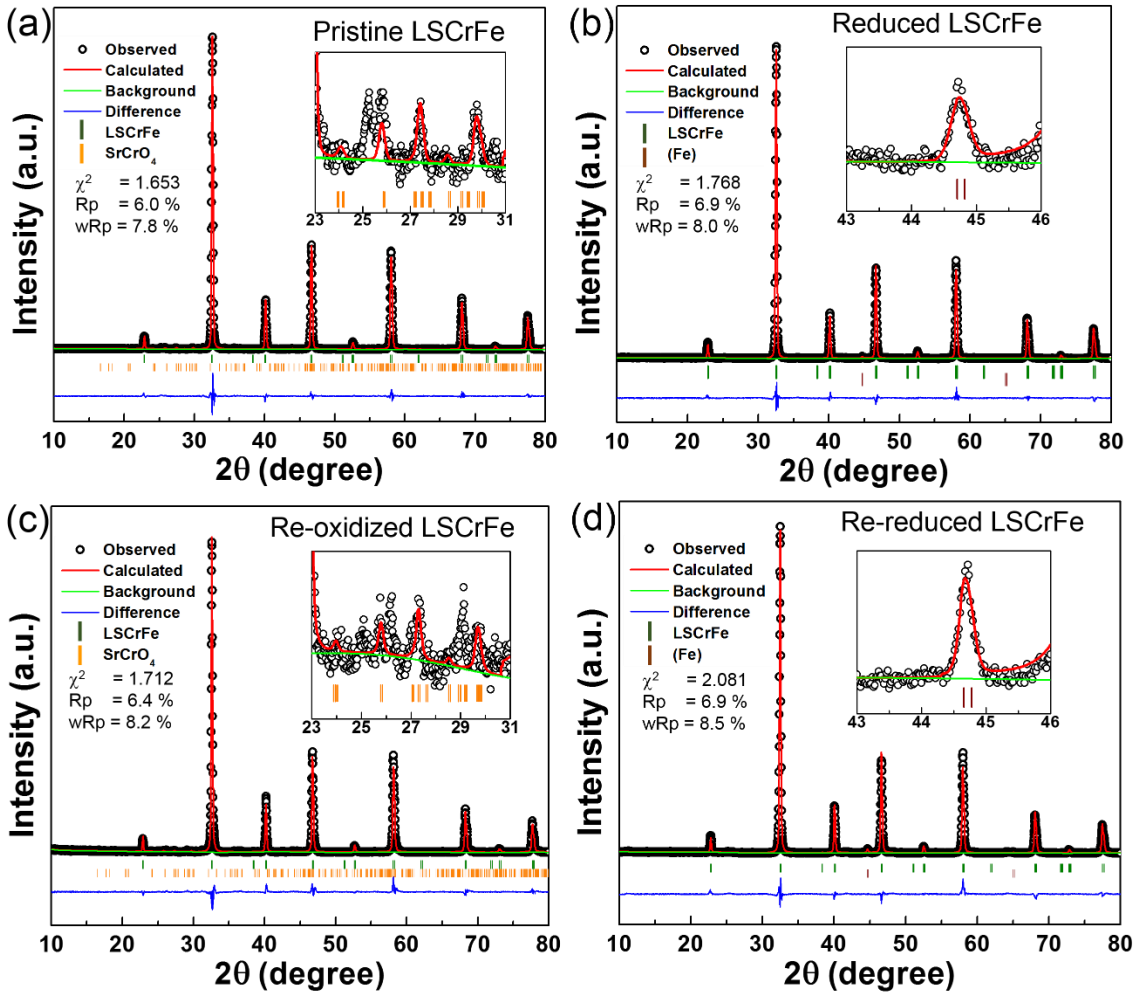

Figure B3. XRD refinement results of (a) pristine LSCrFe, (b) reduced LSCrFe, (c) reoxidized LSCrFe, and (d) rereduced LSCrFe samples where the redox temperature is 800 °C. The inset shows the selective 2θ range of major peaks for the impurity phase.

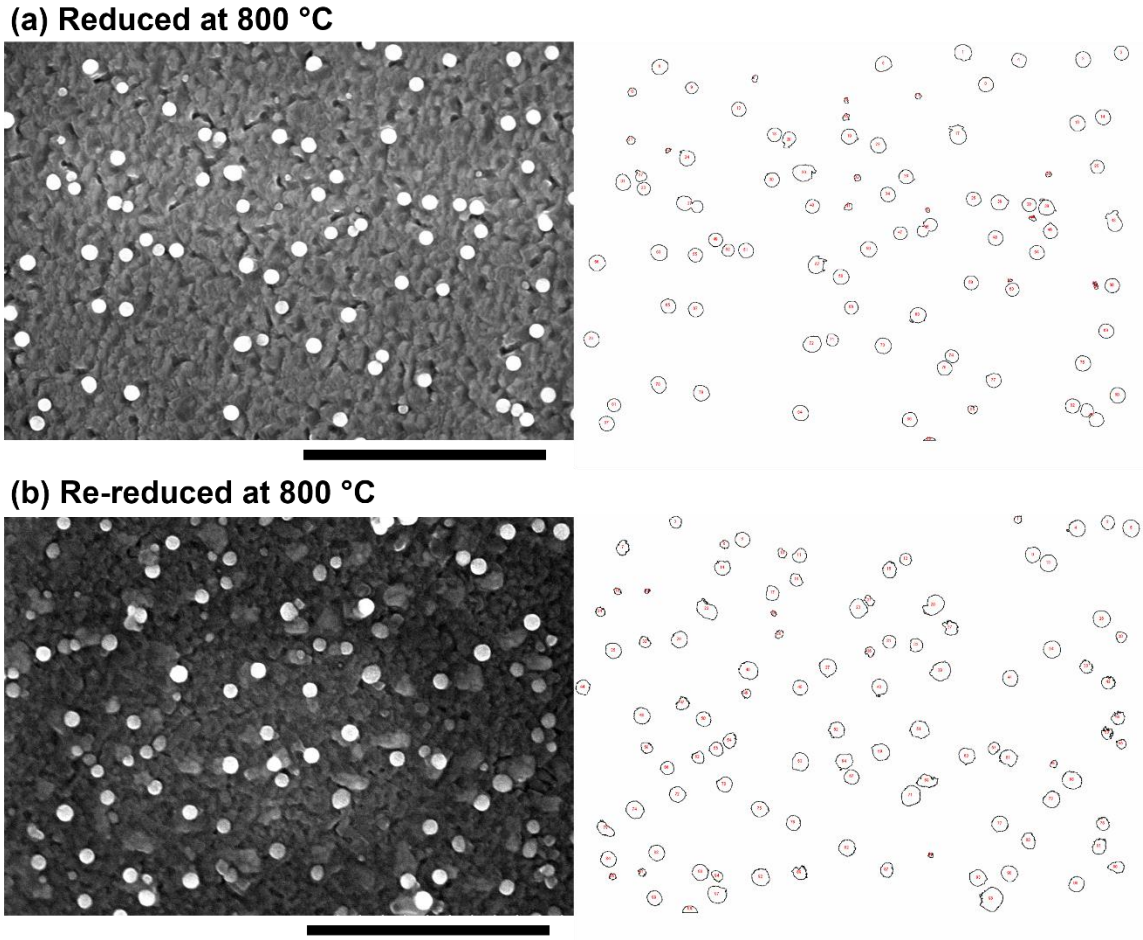

Figure B4 Particle size analysis for the LSCrFeCo10 samples which were (a) reduced and (b) rereduced at 800 °C for 24 h. The scale bar is 1 μm.

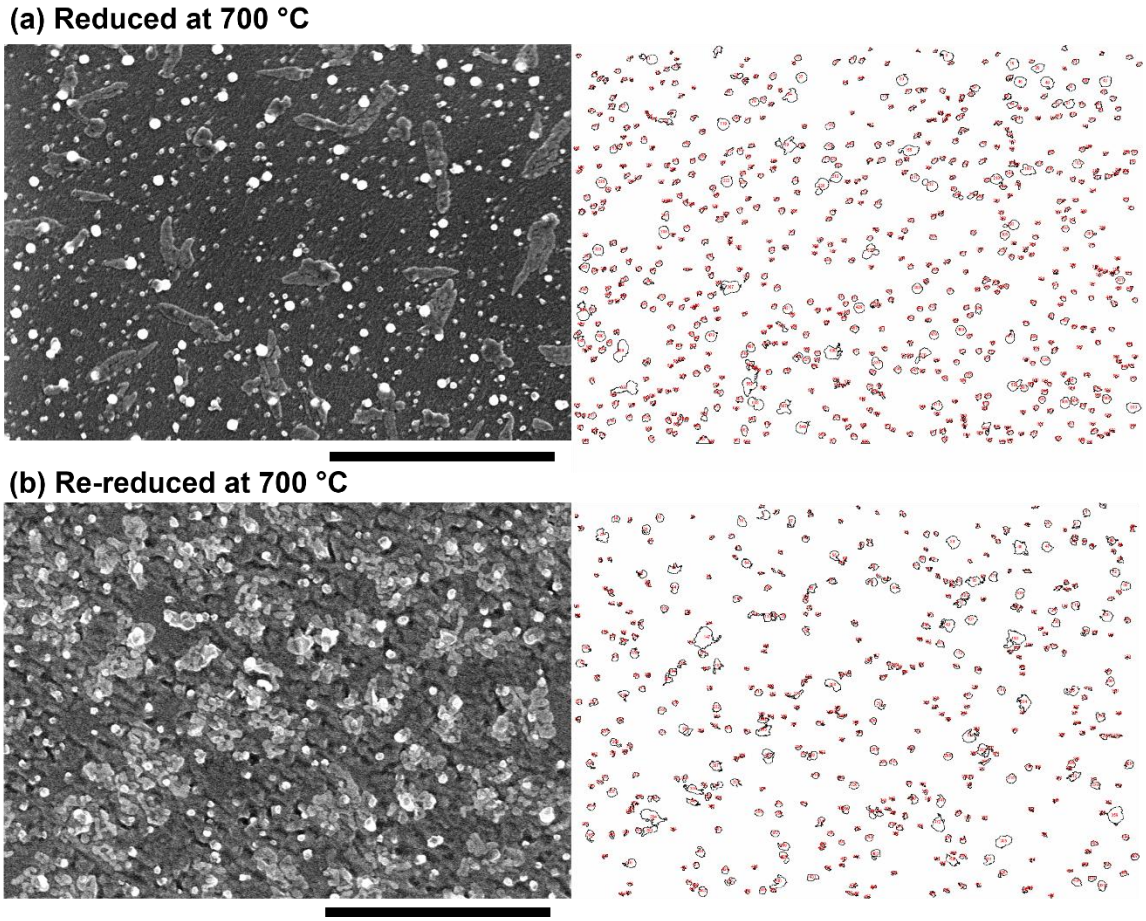

Figure B5 Particle size analysis for the LSCrFeCo10 samples which were (a) reduced and (b) rereduced at 700 °C, respectively, for 24 h and 36 h. The scale bar is 1 μm.

References

(1) Huang, K.; Goodenough, J. B. *Solid Oxide Fuel Cell Technology: Principles, Performance and Operations*; Elsevier, 2009.

(2) Curzon, F. L.; Ahlborn, B. Efficiency of a Carnot Engine at Maximum Power Output. *Am. J. Phys.* **1975**, *43*, 22–24.

(3) Stambouli, A. B.; Traversa, E. Solid Oxide Fuel Cells (SOFCs): A Review of an Environmentally Clean and Efficient Source of Energy. *Renew. Sustain. Energy Rev.* **2002**, *6*, 433–455.

(4) Braun, R. J.; Klein, S. A.; Reindl, D. T. Evaluation of System Configurations for Solid Oxide Fuel Cell-Based Micro-Combined Heat and Power Generators in Residential Applications. *J. Power Sources* **2006**, *158*, 1290–1305.

(5) Ahmed, K.; Foger, K. Kinetics of Internal Steam Reforming of Methane on Ni/YSZ-Based Anodes for Solid Oxide Fuel Cells. *Catal. Today* **2000**, *63*, 479–487.

(6) Gorte, R. J.; Park, S.; Vohs, J. M.; Wang, C. Anodes for Direct Oxidation of Dry Hydrocarbons in a Solid-Oxide Fuel Cell. *Adv. Mater.* **2000**, *12*, 1465–1469.

(7) Kim, H.; Park, S.; Vohs, J. M.; Gorte, R. J. Direct Oxidation of Liquid Fuels in a Solid Oxide Fuel Cell. *J. Electrochem. Soc.* **2001**, *148*, A693–A695.

(8) Steele, B. C. H.; Heinzel, A. Materials for Fuel-Cell Technologies. *Nature* **2001**, *414*, 345–352.

(9) Hoogers, G. *Fuel Cell Technology Handbook*; CRC Press, 2002.

(10) Mogensen, M.; Kammer, and K. Conversion of Hydrocarbons in Solid Oxide Fuel Cells. *Annu. Rev. Mater. Res.* **2003**, *33*, 321–331.

(11) Xu, J.; Froment, G. F. Methane Steam Reforming, Methanation and Water-Gas Shift: I. Intrinsic Kinetics. *AIChE J.* **1989**, *35*, 88–96.

(12) Arora, S.; Prasad, R. An Overview on Dry Reforming of Methane: Strategies to Reduce Carbonaceous Deactivation of Catalysts. *RSC Adv.* **2016**, *6*, 108668–108688.

(13) Hanna, J.; Lee, W. Y.; Shi, Y.; Ghoniem, A. F. Fundamentals of Electro- and Thermochemistry in the Anode of Solid-Oxide Fuel Cells with Hydrocarbon and Syngas Fuels. *Prog. Energy Combust. Sci.* **2014**, *40*, 74–111.

(14) Gaskell, D. R. *Introduction to the Thermodynamics of Materials*, 5 edition.; CRC Press: Boca Raton, FL, 2008.

(15) Bard, A. J.; Faulkner, L. R. *Electrochemical Methods: Fundamentals and Applications*, 2 edition.; Wiley: New York, 2000.

(16) Adler, S. B. Factors Governing Oxygen Reduction in Solid Oxide Fuel Cell Cathodes. *Chem. Rev.* **2004**, *104*, 4791–4844.

(17) Iwai, H.; Shikazono, N.; Matsui, T.; Teshima, H.; Kishimoto, M.; Kishida, R.; Hayashi, D.; Matsuzaki, K.; Kanno, D.; Saito, M.; et al. Quantification of SOFC Anode Microstructure Based on Dual Beam FIB-SEM Technique. *J. Power Sources* **2010**, *195*, 955–961.

(18) L. Brett, D. J.; Atkinson, A.; P. Brandon, N.; J. Skinner,S. Intermediate Temperature Solid Oxide Fuel Cells. *Chem. Soc. Rev.* **2008**, *37*, 1568–1578.
(19) Goodenough, J. B. Oxide-Ion Electrolytes. *Annu. Rev. Mater. Res.* **2003**, *33*, 91–128.
(20) Kharton, V. V.; Figueiredo, F. M.; Navarro, L.; Naumovich, E. N.; Kovalevsky, A. V.; Yaremchenko, A. A.; Viskup, A. P.; Carneiro, A.; Marques, F. M. B.; Frade, J. R. Ceria-Based Materials for Solid Oxide Fuel Cells. *J. Mater. Sci.* **2001**, *36*, 1105–1117.
(21) Ishihara, T.; Matsuda, H.; Takita, Y. Doped LaGaO3 Perovskite Type Oxide as a New Oxide Ionic Conductor. *J. Am. Chem. Soc.* **1994**, *116*, 3801–3803.
(22) Feng, M.; Goodenough, J. B. A Superior Oxide-Ion Electrolyte. *Eur. J. Solid State Inorg. Chem.* **1994**, *31*, 663–672.
(23) Tsipis, E. V.; Kharton, V. V. Electrode Materials and Reaction Mechanisms in Solid Oxide Fuel Cells: A Brief Review. III. Recent Trends and Selected Methodological Aspects. *J. Solid State Electrochem.* **2011**, *15*, 1007–1040.
(24) Irvine, J. T. S.; Connor, P. *Solid Oxide Fuels Cells: Facts and Figures: Past, Present and Future Perspectives for SOFC Technologies*; Springer, 2013.
(25) Simner, S. P.; Anderson, M. D.; Engelhard, M. H.; Stevenson, J. W. Degradation Mechanisms of La – Sr – Co – Fe – O3 SOFC Cathodes. *Electrochem. Solid-State Lett.* **2006**, *9*, A478–A481.
(26) Schlegl, H.; Dawson, R. Finite Element Analysis and Modelling of Thermal Stress in Solid Oxide Fuel Cells. *Proc. Inst. Mech. Eng. Part J. Power Energy* **2017**, *231*, 654–665.
(27) McIntosh, S.; Vente, J. F.; Haije, W. G.; Blank, D. H. A.; Bouwmeester, H. J. M. Oxygen Stoichiometry and Chemical Expansion of Ba0.5Sr0.5Co0.8Fe0.2O3-δ Measured by in Situ Neutron Diffraction. *Chem. Mater.* **2006**, *18*, 2187–2193.
(28) Aguadero, A.; Calle, C. de la; Alonso, J. A.; Escudero, M. J.; Fernández-Díaz, M. T.; Daza, L. Structural and Electrical Characterization of the Novel SrCo0.9Sb0.1O3–δ Perovskite: Evaluation as a Solid Oxide Fuel Cell Cathode Material. *Chem. Mater.* **2007**, *19*, 6437–6444.
(29) Sarantaridis, D.; Atkinson, A. Redox Cycling of Ni-Based Solid Oxide Fuel Cell Anodes: A Review. *Fuel Cells* **2007**, *7*, 246–258.
(30) Cowin, P. I.; Petit, C. T. G.; Lan, R.; Irvine, J. T. S.; Tao, S. Recent Progress in the Development of Anode Materials for Solid Oxide Fuel Cells. *Adv. Energy Mater.* **2011**, *1*, 314–332.
(31) Fouquet, D.; Müller, A. C.; Weber, A.; Ivers-Tiffée, E. Kinetics of Oxidation and Reduction of Ni/YSZ Cermet; European Solid Oxide Fuel Cell Forum; European Fuel Cell Forum: Oberrohrdorf, Switzerland, 2002; 467–474.
(32) Ettler, M.; Blaß, G.; Menzler, N. H. Characterisation of Ni–YSZ-Cermets with Respect to Redox Stability. *Fuel Cells* **2007**, *7*, 349–355.
(33) Vaßen, R.; Simwonis, D.; Stöver, D. Modelling of the Agglomeration of Ni-Particles in Anodes of Solid Oxide Fuel Cells. *J. Mater. Sci.* **2001**, *36*, 147–151.

(34) Sfeir, J.; van herle, J.; McEvoy, A. J. Stability of Calcium Substituted Lanthanum Chromites Used as SOFC Anodes for Methane Oxidation. *J. Eur. Ceram. Soc.* **1999**, *19*, 897–902.
(35) Tao, S.; Irvine, J. T. S. A Redox-Stable Efficient Anode for Solid-Oxide Fuel Cells. *Nat. Mater.* **2003**, *2*, 320–323.
(36) Haag, J. M.; Madsen, B. D.; Barnett, S. A.; Poeppelmeier, K. R. Application of LaSr2Fe2CrO9 − δ in Solid Oxide Fuel Cell Anodes. *Electrochem. Solid-State Lett.* **2008**, *11*, B51–B53.
(37) Slater, P. R.; Fagg, D. P.; Irvine, J. T. S. Synthesis and Electrical Characterisation of Doped Perovskite Titanates as Potential Anode Materials for Solid Oxide Fuel Cells. *J. Mater. Chem.* **1997**, *7*, 2495–2498.
(38) Huang, Y.-H.; Dass, R. I.; Xing, Z.-L.; Goodenough, J. B. Double Perovskites as Anode Materials for Solid-Oxide Fuel Cells. *Science* **2006**, *312*, 254–257.
(39) Sengodan, S.; Choi, S.; Jun, A.; Shin, T. H.; Ju, Y.-W.; Jeong, H. Y.; Shin, J.; Irvine, J. T. S.; Kim, G. Layered Oxygen-Deficient Double Perovskite as an Efficient and Stable Anode for Direct Hydrocarbon Solid Oxide Fuel Cells. *Nat. Mater.* **2015**, *14*, 205–209.
(40) Wei, M.; Smith, S. J.; Sohn, M. D. Experience Curve Development and Cost Reduction Disaggregation for Fuel Cell Markets in Japan and the US. *Appl. Energy* **2017**, *191*, 346–357.
(41) Valldor, M.; Andersson, M. The Structure of the New Compound YBaCo4O7 with a Magnetic Feature. *Solid State Sci.* **2002**, *4*, 923–931.
(42) Karppinen, M.; Yamauchi, H.; Otani, S.; Fujita, T.; Motohashi, T.; Huang, Y.-H.; Valkeapää, M.; Fjellvåg, H. Oxygen Nonstoichiometry in YBaCo4O7+δ: Large Low-Temperature Oxygen Absorption/Desorption Capability. *Chem. Mater.* **2006**, *18*, 490–494.
(43) Valldor, M. Syntheses and Structures of Compounds with YBaCo4O7-Type Structure. *Solid State Sci.* **2004**, *6*, 251–266.
(44) Tsipis, E. V.; Kharton, V. V.; Frade, J. R.; Núñez, P. High-Temperature Transport and Electrochemical Properties of YBaCo4O7+δ. *J. Solid State Electrochem.* **2004**, *9*, 547–557.
(45) Kadota, S.; Karppinen, M.; Motohashi, T.; Yamauchi, H. R-Site Substitution Effect on the Oxygen-Storage Capability of RBaCo4O7+δ. *Chem. Mater.* **2008**, *20*, 6378–6381.
(46) Parkkima, O.; Karppinen, M. The YBaCo4O7+δ-Based Functional Oxide Material Family: A Review. *Eur. J. Inorg. Chem.* **2014**, *2014*, 4056–4067.
(47) Markina, M.; Vasiliev, A. N.; Nakayama, N.; Mizota, T.; Yeda, Y. Structural and Magnetic Phase Transitions of Kagome-like Compounds REBaCo4O7 (RE=Dy, Ho, Er, Tm, Yb, Lu). *J. Magn. Magn. Mater.* **2010**, *322*, 1249–1250.
(48) Maignan, A.; Caignaert, V.; Pralong, V.; Pelloquin, D.; Hébert, S. Impact of Metal Substitutions for Cobalt in YBaCo4O7. *J. Solid State Chem.* **2008**, *181*, 1220–1226.

(49) Valldor, M. Magnetic Investigations on Six Compounds with the General Formula (Ca,Y)Ba(Co,Fe,Al,Zn)4O7 and the Structures of YBaCoFeZn2O7 and YBaCo2FeZnO7. *Solid State Sci.* **2005**, *7*, 1163–1172.
(50) Hao, H.; Zhang, X.; He, Q.; Chen, C.; Hu, X. Effect of Zn Substitution for Co on the Transport Properties of Y BaCo4O7. *Solid State Commun.* **2007**, *141*, 591–594.
(51) Kim, J.-H.; Manthiram, A. Low Thermal Expansion RBa(Co,M)4O7 Cathode Materials Based on Tetrahedral-Site Cobalt Ions for Solid Oxide Fuel Cells. *Chem. Mater.* **2010**, *22*, 822–831.
(52) Räsänen, S.; Motohashi, T.; Yamauchi, H.; Karppinen, M. Stability and Oxygen-Storage Characteristics of Al-Substituted YBaCo4O7+δ. *J. Solid State Chem.* **2010**, *183*, 692–695.
(53) Kim, J.-H.; Kim, Y. N.; Bi, Z.; Manthiram, A.; Paranthaman, M. P.; Huq, A. High Temperature Phase Stabilities and Electrochemical Properties of InBaCo4−xZnxO7 Cathodes for Intermediate Temperature Solid Oxide Fuel Cells. *Electrochimica Acta* **2011**, *56*, 5740–5745.
(54) Kim, Y. N.; Kim, J.-H.; Manthiram, A. Characterization of (Y1-XCax)BaCo4-YZnyO7 as Cathodes for Intermediate Temperature Solid Oxide Fuel Cells. *Int. J. Hydrog. Energy* **2011**, *36*, 15295–15303.
(55) Kim, Y. N.; Kim, J. H.; Huq, A.; Paranthaman, M. P.; Manthiram, A. (Y0.5In0.5)Ba(Co,Zn)4O7 Cathodes with Superior High-Temperature Phase Stability for Solid Oxide Fuel Cells. *J. Power Sources* **2012**, *214*, 7–14.
(56) Räsänen, S.; Parkkima, O.; Rautama, E.-L.; Yamauchi, H.; Karppinen, M. Ga-for-Co Substitution in YBaCo4O7+δ: Effect on High-Temperature Stability and Oxygen-Storage Capacity. *Solid State Ion.* **2012**, *208*, 31–35.
(57) Parkkima, O.; Yamauchi, H.; Karppinen, M. Oxygen Storage Capacity and Phase Stability of Variously Substituted YBaCo4O7+δ. *Chem. Mater.* **2013**, *25*, 599–604.
(58) West, M.; Manthiram, A. Improved Phase Stability and Electrochemical Performance of (Y,In,Ca)BaCo3ZnO7+δ Cathodes for Intermediate Temperature Solid Oxide Fuel Cells. *Int. J. Hydrog. Energy* **2014**, *39*, 19722–19730.
(59) West, M.; Sher, S.-J.; Manthiram, A. Effects of In Substitution in Y1−xInxBaCo3ZnO7+δ ($0 \leq x \leq 0.5$) Cathodes for Intermediate Temperature Solid Oxide Fuel Cells. *J. Power Sources* **2014**, *271*, 252–261.
(60) West, M.; Ortiz, C.; Manthiram, A. High-Performance Y0.9In0.1BaCo3(Zn,Fe)O7 + δ Swedenborgite-Type Oxide Cathodes for Reduced Temperature Solid Oxide Fuel Cells. *Int. J. Hydrog. Energy* **2015**, *40*, 1186–1194.
(61) Kan, W. H.; Lai, K.-Y.; Huq, A.; Manthiram, A. Unravelling the Low Thermal Expansion Coefficient of Cation-Substituted YBaCo4O7+δ. *J. Power Sources* **2016**, *307*, 454–461.

(62) Nishihata, Y.; Mizuki, J.; Akao, T.; Tanaka, H.; Uenishi, M.; Kimura, M.; Okamoto, T.; Hamada, N. Self-Regeneration of a Pd-Perovskite Catalyst for Automotive Emissions Control. *Nature* **2002**, *418*, 164–167.
(63) Tanaka, H.; Taniguchi, M.; Uenishi, M.; Kajita, N.; Tan, I.; Nishihata, Y.; Mizuki, J.; Narita, K.; Kimura, M.; Kaneko, K. Self-Regenerating Rh- and Pt-Based Perovskite Catalysts for Automotive-Emissions Control. *Angew. Chem. Int. Ed.* **2006**, *45*, 5998–6002.
(64) Katz, M. B.; Zhang, S.; Duan, Y.; Wang, H.; Fang, M.; Zhang, K.; Li, B.; Graham, G. W.; Pan, X. Reversible Precipitation/Dissolution of Precious-Metal Clusters in Perovskite-Based Catalyst Materials: Bulk versus Surface Re-Dispersion. *J. Catal.* **2012**, *293*, 145–148.
(65) Yang, C.; Yang, Z.; Jin, C.; Xiao, G.; Chen, F.; Han, M. Sulfur-Tolerant Redox-Reversible Anode Material for Direct Hydrocarbon Solid Oxide Fuel Cells. *Adv. Mater.* **2012**, *24*, 1439–1443.
(66) Neagu, D.; Tsekouras, G.; Miller, D. N.; Ménard, H.; Irvine, J. T. S. In Situ Growth of Nanoparticles through Control of Non-Stoichiometry. *Nat. Chem.* **2013**, *5*, 916–923.
(67) Neagu, D.; Oh, T.-S.; Miller, D. N.; Ménard, H.; Bukhari, S. M.; Gamble, S. R.; Gorte, R. J.; Vohs, J. M.; Irvine, J. T. S. Nano-Socketed Nickel Particles with Enhanced Coking Resistance Grown in Situ by Redox Exsolution. *Nat. Commun.* **2015**, *6*, 8120.
(68) Myung, J.; Neagu, D.; Miller, D. N.; Irvine, J. T. S. Switching on Electrocatalytic Activity in Solid Oxide Cells. *Nature* **2016**, *537*, 528–531.
(69) Neagu, D.; Papaioannou, E. I.; Ramli, W. K. W.; Miller, D. N.; Murdoch, B. J.; Ménard, H.; Umar, A.; Barlow, A. J.; Cumpson, P. J.; Irvine, J. T. S.; et al. Demonstration of Chemistry at a Point through Restructuring and Catalytic Activation at Anchored Nanoparticles. *Nat. Commun.* **2017**, *8*, 1855.
(70) Kobsiriphat, W.; Madsen, B. D.; Wang, Y.; Marks, L. D.; Barnett, S. A. La0.8Sr0.2Cr1 − XRuxO3 − Δ–Gd0.1Ce0.9O1.95 Solid Oxide Fuel Cell Anodes: Ru Precipitation and Electrochemical Performance. *Solid State Ion.* **2009**, *180*, 257–264.
(71) Vert, V. B.; Melo, F. V.; Navarrete, L.; Serra, J. M. Redox Stability and Electrochemical Study of Nickel Doped Chromites as Anodes for H2/CH4-Fueled Solid Oxide Fuel Cells. *Appl. Catal. B Environ.* **2012**, *115–116*, 346–356.
(72) Chick, L. A.; Pederson, L. R.; Maupin, G. D.; Bates, J. L.; Thomas, L. E.; Exarhos, G. J. Glycine-Nitrate Combustion Synthesis of Oxide Ceramic Powders. *Mater. Lett.* **1990**, *10*, 6–12.
(73) Yoon, D.; Su, Q.; Wang, H.; Manthiram, A. Superior Power Density Solid Oxide Fuel Cells by Enlarging the Three-Phase Boundary Region of a NiO–Ce0.8Gd0.2O1.9 Composite Anode through Optimized Surface Structure. *Phys. Chem. Chem. Phys.* **2013**, *15*, 14966–14972.
(74) Rietveld, H. M. A Profile Refinement Method for Nuclear and Magnetic Structures. *J. Appl. Crystallogr.* **1969**, *2*, 65–71.

(75) Toby, B. H. EXPGUI, a Graphical User Interface for GSAS. *J. Appl. Crystallogr.* **2001**, *34*, 210–213.
(76) Lai, K.-Y.; Manthiram, A. Phase Stability, Oxygen-Storage Capability, and Electrocatalytic Activity in Solid Oxide Fuel Cells of (Y, In, Ca)BaCo4–yGayO7+δ. *Chem. Mater.* **2016**, *28*, 9077–9087.
(77) Vickerman, J. C.; Gilmore, I. S. *Surface Analysis: The Principal Techniques*; John Wiley & Sons, 2011.
(78) Gabbott, P. *Principles and Applications of Thermal Analysis*; John Wiley & Sons, 2008.
(79) van der Pauw, L. J. A Method of Measuring Specific Resistivity and Hall Effect of Discs of Arbitrary Shape. *Philips Res. Rep.* **1958**, *13*, 1–9.
(80) Chwang, R.; Smith, B. J.; Crowell, C. R. Contact Size Effects on the van Der Pauw Method for Resistivity and Hall Coefficient Measurement. *Solid-State Electron.* **1974**, *17*, 1217–1227.
(81) Riess, I.; Tannhauser, D. S. Application of the van Der Pauw Method to Conductivity Measurements on Mixed Ionic-Electronic Solid Conductors. *Solid State Ion.* **1982**, *7*, 307–315.
(82) Gong, Y.; Qin, C.; Huang, K. Can Silver Be a Reliable Current Collector for Electrochemical Tests? *ECS Electrochem. Lett.* **2013**, *2*, F4–F7.
(83) Haag, J. M.; Bierschenk, D. M.; Barnett, S. A.; Poeppelmeier, K. R. Structural, Chemical, and Electrochemical Characteristics of LaSr2Fe2CrO9-δ-Based Solid Oxide Fuel Cell Anodes. *Solid State Ion.* **2012**, *212*, 1–5.
(84) Nagai, Y.; Yamamoto, T.; Tanaka, T.; Yoshida, S.; Nonaka, T.; Okamoto, T.; Suda, A.; Sugiura, M. X-Ray Absorption Fine Structure Analysis of Local Structure of CeO2–ZrO2 Mixed Oxides with the Same Composition Ratio (Ce/Zr=1). *Catal. Today* **2002**, *74*, 225–234.
(85) Hayashi, H.; Kanoh, M.; Quan, C. J.; Inaba, H.; Wang, S.; Dokiya, M.; Tagawa, H. Thermal Expansion of Gd-Doped Ceria and Reduced Ceria. *Solid State Ion.* **2000**, *132*, 227–233.
(86) Hao, H.; Cui, J.; Chen, C.; Pan, L.; Hu, J.; Hu, X. Oxygen Adsorption Properties of YBaCo4O7-Type Compounds. *Solid State Ion.* **2006**, *177*, 631–637.
(87) Tsipis, E. V.; Kharton, V. V.; Frade, J. R. Transport Properties and Electrochemical Activity of YBa(Co,Fe)4O7 Cathodes. *Solid State Ion.* **2006**, *177*, 1823–1826.
(88) Wang, S.; Hao, H.; Zhu, B.; Jia, J.; Hu, X. Modifying the Oxygen Adsorption Properties of YBaCo4O7 by Ca, Al, and Fe Doping. *J. Mater. Sci.* **2008**, *43*, 5385–5389.
(89) Hao, H.; Zhao, L.; Hu, X.; Hou, H. Effect of Metal Substitution for Cobalt on the Oxygen Adsorption Properties of YBaCo4O7. *J. Therm. Anal. Calorim.* **2009**, *95*, 585–588.
(90) Komiyama, T.; Motohashi, T.; Masubuchi, Y.; Kikkawa, S. Synthesis, Thermal Stability, and Oxygen Intake/Release Characteristics of YBa(Co1−xAlx)4O7+δ. *Mater. Res. Bull.* **2010**, *45*, 1527–1532.

(91) Ye, F.; Zhou, Q.; Xu, K.; Zhang, Z.; Han, X.; Yang, L.; Xu, J.; Xu, H.; Wu, K.; Guan, Y. Phase Stability and Electrochemical Performance of Y0.5Ca0.5−xInxBaCo3.2Ga0.8O7+δ (x = 0 and 0.1) as Cathodes for Intermediate Temperature Solid Oxide Fuel Cells. *J. Alloys Compd.* **2016**, *680*, 163–168.
(92) Manthiram, A.; Swinnea, J. S.; Sui, Z. T.; Steinfink, H.; Goodenough, J. B. The Influence of Oxygen Variation on the Crystal Structure and Phase Composition of the Superconductor Yttrium Barium Copper Oxide (YBa2Cu3O7-X). *J. Am. Chem. Soc.* **1987**, *109*, 6667–6669.
(93) Xia, C.; Liu, M. A Simple and Cost-Effective Approach to Fabrication of Dense Ceramic Membranes on Porous Substrates. *J. Am. Ceram. Soc.* **2001**, *84*, 1903–1905.
(94) Caignaert, V.; Pralong, V.; Hardy, V.; Ritter, C.; Raveau, B. Magnetic Structure of CaBaCo4O7: Lifting of Geometrical Frustration towards Ferrimagnetism. *Phys. Rev. B* **2010**, *81*, 094417.
(95) Sarkar, T.; Caignaert, V.; Pralong, V.; Raveau, B. Hysteretic "Magnetic−Transport−Structural" Transition in "114" Cobaltites: Size Mismatch Effect. *Chem. Mater.* **2010**, *22*, 6467–6473.
(96) Shannon, R. D. Revised Effective Ionic Radii and Systematic Studies of Interatomic Distances in Halides and Chalcogenides. *Acta Crystallogr. Sect. A* **1976**, *32*, 751–767.
(97) Zhou, W.; Ran, R.; Shao, Z.; Jin, W.; Xu, N. Evaluation of A-Site Cation-Deficient (Ba0.5Sr0.5)1−xCo0.8Fe0.2O3−δ (x > 0) Perovskite as a Solid-Oxide Fuel Cell Cathode. *J. Power Sources* **2008**, *182*, 24–31.
(98) Kim, J. H.; Irvine, J. T. S. Characterization of Layered Perovskite Oxides NdBa1−xSrxCo2O5+δ (x = 0 and 0.5) as Cathode Materials for IT-SOFC. *Int. J. Hydrog. Energy* **2012**, *37*, 5920–5929.
(99) Nirasawa, H. Current Status of National SOFC Projects in Japan. *ECS Trans.* **2017**, *78*, 33–40.
(100) McPhail, S. J.; Kiviaho, J.; Conti, B. *The Yellow Pages of SOFC Technology*; ENEA, 2017.
(101) Montross, C. S.; Yokokawa, H.; Dokiya, M. Thermal Stresses in Planar Solid Oxide Fuel Cells Due to Thermal Expansion Differences. *Br. Ceram. Trans.* **2002**, *101*, 85–93.
(102) Selimovic, A.; Kemm, M.; Torisson, T.; Assadi, M. Steady State and Transient Thermal Stress Analysis in Planar Solid Oxide Fuel Cells. *J. Power Sources* **2005**, *145*, 463–469.
(103) Nakajo, A.; Stiller, C.; Härkegård, G.; Bolland, O. Modeling of Thermal Stresses and Probability of Survival of Tubular SOFC. *J. Power Sources* **2006**, *158*, 287–294.
(104) Hayashi, H.; Saitou, T.; Maruyama, N.; Inaba, H.; Kawamura, K.; Mori, M. Thermal Expansion Coefficient of Yttria Stabilized Zirconia for Various Yttria Contents. *Solid State Ion.* **2005**, *176*, 613–619.

(105) Du, Y.; Sammes, N. M.; Tompsett, G. A.; Zhang, D.; Swan, J.; Bowden, M. Extruded Tubular Strontium- and Magnesium-Doped Lanthanum Gallate, Gadolinium-Doped Ceria, and Yttria-Stabilized Zirconia Electrolytes Mechanical and Thermal Properties. *J. Electrochem. Soc.* **2003**, *150*, A74–A78.
(106) Mori, M. Mechanisms of Thermal Expansion and Shrinkage of La0.8Sr0.2MnO3 + δ Perovskites with Different Densities during Thermal Cycling in Air. *J. Electrochem. Soc.* **2005**, *152*, A732–A739.
(107) Park, K.; Yu, S.; Bae, J.; Kim, H.; Ko, Y. Fast Performance Degradation of SOFC Caused by Cathode Delamination in Long-Term Testing. *Int. J. Hydrog. Energy* **2010**, *35*, 8670–8677.
(108) Fischer, W.; Malzbender, J.; Blass, G.; Steinbrech, R. W. Residual Stresses in Planar Solid Oxide Fuel Cells. *J. Power Sources* **2005**, *150*, 73–77.
(109) Valldor, M.; Hollmann, N.; Hemberger, J.; Mydosh, J. A. Structure and Properties of the Kagome Compound YBaCo3AlO7. *Phys. Rev. B* **2008**, *78*, 024408.
(110) Hao, H.; He, Q.; Cheng, Y.; Zhao, L. Oxygen Adsorption and Electronic Transport Properties of Fe-Substituted YBaCo4O7 Compounds. *Mater. Res. Bull.* **2014**, *53*, 84–88.
(111) Hollmann, N.; Hu, Z.; Valldor, M.; Maignan, A.; Tanaka, A.; Hsieh, H. H.; Lin, H.-J.; Chen, C. T.; Tjeng, L. H. Electronic and Magnetic Properties of the Kagome Systems YBaCo4O7 and YBaCo3MO7 (M=Al, Fe). *Phys. Rev. B* **2009**, *80*, 085111.
(112) Waerenborgh, J. C.; Tsipis, E. V.; Pereira, L. C. J.; Avdeev, M.; Naumovich, E. N.; Kharton, V. V. Magnetization, Mössbauer and Isothermal Dilatometric Behavior of Oxidized YBa(Co,Fe)4O7+δ. *Dalton Trans.* **2011**, *41*, 667–678.
(113) Tsipis, E. V.; Khalyavin, D. D.; Shiryaev, S. V.; Redkina, K. S.; Núñez, P. Electrical and Magnetic Properties of YBaCo4O7+δ. *Mater. Chem. Phys.* **2005**, *92*, 33–38.
(114) Atkinson, A.; Barnett, S.; Gorte, R. J.; Irvine, J. T. S.; McEvoy, A. J.; Mogensen, M.; Singhal, S. C.; Vohs, J. Advanced Anodes for High-Temperature Fuel Cells. *Nat. Mater.* **2004**, *3*, 17.
(115) Gross, M. D.; Vohs, J. M.; Gorte, R. J. A Strategy for Achieving High Performance with SOFC Ceramic Anodes. *Electrochem. Solid-State Lett.* **2007**, *10*, B65–B69.
(116) Comotti, M.; Li, W.-C.; Spliethoff, B.; Schüth, F. Support Effect in High Activity Gold Catalysts for CO Oxidation. *J. Am. Chem. Soc.* **2006**, *128*, 917–924.
(117) Faes, A.; Nakajo, A.; Hessler-Wyser, A.; Dubois, D.; Brisse, A.; Modena, S.; Van herle, J. RedOx Study of Anode-Supported Solid Oxide Fuel Cell. *J. Power Sources* **2009**, *193*, 55–64.
(118) Ruiz-Morales, J. C.; Canales-Vázquez, J.; Savaniu, C.; Marrero-López, D.; Zhou, W.; Irvine, J. T. S. Disruption of Extended Defects in Solid Oxide Fuel Cell Anodes for Methane Oxidation. *Nature* **2006**, *439*, 568–571.

(119) Vernoux, P. Lanthanum Chromite as an Anode Material for Solid Oxide Fuel Cells. *Ionics* **1997**, *3*, 270–276.
(120) Kim, J.-S.; Nair, V. V.; Vohs, J. M.; Gorte, R. J. A Study of the Methane Tolerance of LSCM–YSZ Composite Anodes with Pt, Ni, Pd and Ceria Catalysts. *Scr. Mater.* **2011**, *65*, 90–95.
(121) Gross, M. D.; Vohs, J. M.; Gorte, R. J. A Study of Thermal Stability and Methane Tolerance of Cu-Based SOFC Anodes with Electrodeposited Co. *Electrochimica Acta* **2007**, *52*, 1951–1957.
(122) Bierschenk, D. M.; Potter-Nelson, E.; Hoel, C.; Liao, Y.; Marks, L.; Poeppelmeier, K. R.; Barnett, S. A. Pd-Substituted (La,Sr)CrO3−δ–Ce0.9Gd0.1O2−δ Solid Oxide Fuel Cell Anodes Exhibiting Regenerative Behavior. *J. Power Sources* **2011**, *196*, 3089–3094.
(123) Kobsiriphat, W.; Madsen, B. D.; Wang, Y.; Shah, M.; Marks, L. D.; Barnett, S. A. Nickel- and Ruthenium-Doped Lanthanum Chromite Anodes: Effects of Nanoscale Metal Precipitation on Solid Oxide Fuel Cell Performance. *J. Electrochem. Soc.* **2010**, *157*, B279–B284.
(124) Adijanto, L.; Padmanabhan, V. B.; Küngas, R.; Gorte, R. J.; Vohs, J. M. Transition Metal-Doped Rare Earth Vanadates: A Regenerable Catalytic Material for SOFC Anodes. *J. Mater. Chem.* **2012**, *22*, 11396–11402.
(125) Irvine, J. T. S.; Neagu, D.; Verbraeken, M. C.; Chatzichristodoulou, C.; Graves, C.; Mogensen, M. B. Evolution of the Electrochemical Interface in High-Temperature Fuel Cells and Electrolysers. *Nat. Energy* **2016**, *1*, 15014.
(126) Tao; Irvine, J. T. S. Catalytic Properties of the Perovskite Oxide La0.75Sr0.25Cr0.5Fe0.5O3-δ in Relation to Its Potential as a Solid Oxide Fuel Cell Anode Material. *Chem. Mater.* **2004**, *16*, 4116–4121.
(127) Oishi, M.; Yashiro, K.; Sato, K.; Mizusaki, J.; Kawada, T. Oxygen Nonstoichiometry and Defect Structure Analysis of B-Site Mixed Perovskite-Type Oxide (La, Sr)(Cr, M)O3−δ (M=Ti, Mn and Fe). *J. Solid State Chem.* **2008**, *181*, 3177–3184.
(128) Haag, J. M.; Barnett, S. A.; Richardson, J. W.; Poeppelmeier, K. R. Structural and Chemical Evolution of the SOFC Anode La0.30Sr0.70Fe0.70Cr0.30O3−δ upon Reduction and Oxidation: An in Situ Neutron Diffraction Study. *Chem. Mater.* **2010**, *22*, 3283–3289.
(129) Fowler, D. E.; Messner, A. C.; Miller, E. C.; Slone, B. W.; Barnett, S. A.; Poeppelmeier, K. R. Decreasing the Polarization Resistance of (La,Sr)CrO3−δ Solid Oxide Fuel Cell Anodes by Combined Fe and Ru Substitution. *Chem. Mater.* **2015**, *27*, 3683–3693.
(130) Lü, M. F.; Tsipis, E. V.; Waerenborgh, J. C.; Yaremchenko, A. A.; Kolotygin, V. A.; Bredikhin, S.; Kharton, V. V. Thermomechanical, Transport and Anodic Properties of Perovskite-Type (La0.75Sr0.25)0.95Cr1−xFexO3−δ. *J. Power Sources* **2012**, *206*, 59–69.
(131) Fowler, D. E.; Haag, J. M.; Boland, C.; Bierschenk, D. M.; Barnett, S. A.; Poeppelmeier, K. R. Stable, Low Polarization Resistance Solid Oxide Fuel Cell

Anodes: La1–xSrxCr1–xFexO3-δ (x = 0.2–0.67). *Chem. Mater.* **2014**, *26*, 3113–3120.
(132) Kozhevnikov, V. L.; Leonidov, I. A.; Bahteeva, J. A.; Patrakeev, M. V.; Mitberg, E. B.; Poeppelmeier, K. R. Disordering and Mixed Conductivity in the Solid Solution LaSr2Fe3-YCryO8+δ. *Chem. Mater.* **2004**, *16*, 5014–5020.
(133) Nakamura, T.; Petzow, G.; Gauckler, L. J. Stability of the Perovskite Phase LaBO3 (B = V, Cr, Mn, Fe, Co, Ni) in Reducing Atmosphere I. Experimental Results. *Mater. Res. Bull.* **1979**, *14*, 649–659.
(134) Konysheva, E.; Irvine, J. T. S. Thermochemical and Structural Stability of A- and B-Site-Substituted Perovskites in Hydrogen-Containing Atmosphere. *Chem. Mater.* **2009**, *21*, 1514–1523.
(135) Lai, K.-Y.; Manthiram, A. Evolution of Exsolved Nanoparticles on a Perovskite Oxide Surface during a Redox Process. *Chem. Mater.* **2018**.
(136) Oh, T.-S.; Rahani, E. K.; Neagu, D.; Irvine, J. T. S.; Shenoy, V. B.; Gorte, R. J.; Vohs, J. M. Evidence and Model for Strain-Driven Release of Metal Nanocatalysts from Perovskites during Exsolution. *J. Phys. Chem. Lett.* **2015**, *6*, 5106–5110.
(137) Lin, Y.; Zhan, Z.; Liu, J.; Barnett, S. A. Direct Operation of Solid Oxide Fuel Cells with Methane Fuel. *Solid State Ion.* **2005**, *176*, 1827–1835.
(138) Lee, W. Y.; Hanna, J.; Ghoniem, A. F. On the Predictions of Carbon Deposition on the Nickel Anode of a SOFC and Its Impact on Open-Circuit Conditions. *J. Electrochem. Soc.* **2013**, *160*, F94–F105.
(139) Lai, K.-Y.; Manthiram, A. Self-Regenerating Co-Fe Nanoparticles on Perovskite Oxides as a Hydrocarbon Fuel Oxidation Catalyst in Solid Oxide Fuel Cells. *Chem. Mater.* **2018**.
(140) Nishizawa, T.; Ishida, K. The Co−Fe (Cobalt−Iron) System. *Bull. Alloy Phase Diagr.* **1984**, *5*, 250.
(141) Ohnuma, I.; Enoki, H.; Ikeda, O.; Kainuma, R.; Ohtani, H.; Sundman, B.; Ishida, K. Phase Equilibria in the Fe–Co Binary System. *Acta Mater.* **2002**, *50*, 379–393.
(142) Ohba, S.; Saito, Y.; Noda, Y. A Measurement of Charge Asphericity in Iron Metal. *Acta Crystallogr. A* **1982**, *38*, 725–729.
(143) Pourroy, G.; Läkamp, S.; Vilminot, S. Stabilization of Iron-Cobalt Alloy Isomorphous of α-Mn in a Metal Ferrite Composite. *J. Alloys Compd.* **1996**, *244*, 90–93.
(144) Ellis, W. C.; Greiner, E. S. Equilibrium Relations in the Solid State of the Iron-Cobalt System. *Trans Am Soc Met* **1941**, *29*, 415–434.
(145) Schlosser, W. F. Calculation of the Atomic Volumes of Fe-Ni and Fe-Co Alloys. *Phys. Status Solidi A* **1973**, *17*, 199–205.
(146) Mori, M.; Yamamoto, T.; Ichikawa, T.; Takeda, Y. Dense Sintered Conditions and Sintering Mechanisms for Alkaline Earth Metal (Mg, Ca and Sr)-Doped LaCrO3 Perovskites under Reducing Atmosphere. *Solid State Ion.* **2002**, *148*, 93–101.

(147) Smith, W. L.; Hobson, A. D. The Structure of Cobalt Oxide, Co3O4. *Acta Crystallogr. B* **1973**, *29*, 362–363.
(148) Ferreira, T. A. S.; Waerenborgh, J. C.; Mendonça, M. H. R. M.; Nunes, M. R.; Costa, F. M. Structural and Morphological Characterization of FeCo2O4 and CoFe2O4 Spinels Prepared by a Coprecipitation Method. *Solid State Sci.* **2003**, *5*, 383–392.
(149) Mirjalili, M.; Vahdati-Khaki, J. Prediction of Nanoparticles' Size-Dependent Melting Temperature Using Mean Coordination Number Concept. *J. Phys. Chem. Solids* **2008**, *69*, 2116–2123.
(150) Simoens, A. J.; Baker, R. T. K.; Dwyer, D. J.; Lund, C. R. F.; Madon, R. J. A Study of the Nickel-Titanium Oxide Interaction. *J. Catal.* **1984**, *86*, 359–372.
(151) Haruta, M.; Tsubota, S.; Kobayashi, T.; Kageyama, H.; Genet, M. J.; Delmon, B. Low-Temperature Oxidation of CO over Gold Supported on TiO2, α-Fe2O3, and Co3O4. *J. Catal.* **1993**, *144*, 175–192.
(152) Gonzalez-DelaCruz, V. M.; Holgado, J. P.; Pereñíguez, R.; Caballero, A. Morphology Changes Induced by Strong Metal–support Interaction on a Ni–ceria Catalytic System. *J. Catal.* **2008**, *257*, 307–314.
(153) Dulub, O.; Hebenstreit, W.; Diebold, U. Imaging Cluster Surfaces with Atomic Resolution: The Strong Metal-Support Interaction State of Pt Supported on TiO2(110). *Phys. Rev. Lett.* **2000**, *84*, 3646–3649.
(154) Palasantzas, G.; Vystavel, T.; Koch, S. A.; De Hosson, J. T. M. Coalescence Aspects of Cobalt Nanoparticles during in Situ High-Temperature Annealing. *J. Appl. Phys.* **2006**, *99*, 024307.
(155) Asoro, M. A.; Ferreira, P. J.; Kovar, D. In Situ Transmission Electron Microscopy and Scanning Transmission Electron Microscopy Studies of Sintering of Ag and Pt Nanoparticles. *Acta Mater.* **2014**, *81*, 173–183.
(156) Baker, R. T. K.; Prestridge, E. B.; Garten, R. L. Electron Microscopy of Supported Metal Particles II. Further Studies of Pt/TiO2. *J. Catal.* **1979**, *59*, 293–302.
(157) Baker, R. T. K.; Prestridge, E. B.; Garten, R. L. Electron Microscopy of Supported Metal Particles: I. Behavior of Pt on Titanium Oxide, Aluminum Oxide, Silicon Oxide, and Carbon. *J. Catal.* **1979**, *56*, 390–406.
(158) Straguzzi, G. I.; Aduriz, H. R.; Gigola, C. E. Redispersion of Platinum on Alumina Support. *J. Catal.* **1980**, *66*, 171–183.